EXPERIMENTAL AND COMPUTATIONAL DOSIMETRY OF LASER-DRIVEN RADIATION BEAMS

by

FRANCESCA FIORINI

A thesis submitted to the
University of Birmingham
for the degree of
DOCTOR OF PHILOSOPHY

School of Physics and Astronomy
College of Engineering and Physical Sciences
University of Birmingham
March 2012

EXPERIMENTAL AND COMPUTATIONAL DOSIMETRY OF LASER-DRIVEN RADIATION BEAMS

ABSTRACT

Laser-driven particle acceleration is an area of increasing research interest given the recent development of short pulse high intensity lasers. A significant difficulty in this field is given by the exceptionally large instantaneous dose rates which such particle beams can produce. This represents a challenge for standard dosimetry techniques and more sophisticated procedures need to be explored. In this thesis I present novel detection and characterisation methods using a combination of GafChromic films, TLD chips, nuclear activation and Monte Carlo simulations, applicable to laser-driven beams. Part of the work is focused on the detection of laser-driven protons used to irradiate V79 cells in order to determine the feasibility of laser-driven proton therapy. A dosimetry method involving GafChromic films and numerical simulations has been appositely developed and used to obtain cell survival results, which are in agreement with those obtained by conventionally accelerated proton beams. Another part is dedicated to the detection and characterisation of laser-driven electron and X-ray beams. An innovative simulation method to obtain the temperature of the electrons accelerated by the laser, and predict the subsequently generated X-ray beam, has been developed and compared with the acquired experimental data.

This thesis is dedicated to the memory
of my beloved grandfather
Giovanni Illuminati.

ACKNOWLEDGEMENTS

I could not have accomplished the work presented in this thesis without the help of some remarkable people. The first acknowledgement goes to my supervisor Prof. Stuart Green, first of all for selecting me and taking me in his group, then for his suggestions, advise, help and support. I thank him for having introduced me to the world of laser-driven particle acceleration and for his guide into this field. A second and large thanks goes to the cyclotron team of the University of Birmingham and in particular to Prof. David Parker and Mike Smith: their advice and willingness have been a huge help for all the works performed using the cyclotron. Another equally big thanks goes to Dr. Daniel Kirby, friend, colleague and at times teacher. I would also like to thank Prof. David Neely for his help with the laser-driven electron and X-ray part of the work and for giving me the opportunity to work on this topic. Another thanks goes to Dr. Rob Clarke and Dr. James Green for their help during the laser experiments at RAL and for providing very useful advise; another to Prof. Marco Borghesi and his team at the University of Belfast for the help during the radiobiological experiment at the TARANIS facility and in general to each component of the LIBRA group for their contribution to the project. A thanks goes again to LIBRA and to EPSRC for providing my doctoral bursary. Then I would like to express my gratitude to Dr. Cecile Wojnecki for her help with the implant CT at the Queen Elisabeth Hospital and to her, Dr. Spyros Manolopoulos, Zamir Ghani and Ben Phoenix for their company and always interesting conversations.

I would really like to thank my parents, all my family and friends for their support or even only for their important presence in my life. A final thanks goes to Dr. Sam Vinko, for his patience during the last stressful months and for his very useful explanations about laser interactions.

Contents

List of Tables

List of Figures

ACRONYMS

CLF	Central Laser Facility
FWHM	Full Width at Half Maximum
FLUKA	FLUktuierende KAskade
IAEA	International Atomic Energy Agency
LET	Linear Energy Transfer
LDPB	Laser-Driven Particle Beam
LDPrB	Laser-Driven Proton Beam
LDXrB	Laser-Driven X-ray Beam
OD	Optical density
PAW	Physics Analysis Workstation
PMMA	Poly(Methyl MethAcrylate)
PV	Pixel Value
RAL	Rutherford Appleton Laboratory
TLD	ThermoLuminescent dosimeter

NOTATION

quantity	symbol(s)	value / preferred units
Boltzmann's constant	k_B	1.381×10^{-23} m^2 kg s^{-2} K^{-1}
charge number	Z	-
coordinate	x, y, z	cm
cross section	σ	1 b (10^{-24} cm^2)
decay constant	λ	s^{-1}
density	ρ	g cm^{-3}
dose	d, D	Gy
electron charge	e	1.602×10^{-19} C
energy	E	MeV or J
half life	$t_{1/2}$	ln(2) τ^{-1}
laser intensity	I	W cm^{-2}
mean lifetime	τ	s
number	n, N	-
speed of light	c	2.9979×10^8 m s^{-1}
temperature	T	K
thermal energy	$k_B T$	MeV
time	t	s

CHAPTER 1

INTRODUCTION

Recent improvements in laser technology, particularly the development of PetaWatt lasers, has allowed the irradiation of solid and gaseous targets with intensities higher than 10^{18} W/cm^2, leading to the creation of secondary particle beams. These electron, photon, proton and ion beams have characteristics different from those accelerated by conventional particle accelerators, opening the field to new and very promising applications, but also creating problems in their detection and dosimetry.

In this thesis experimental and computational studies of proton, electron and X-ray beams that could be used for medical purposes such as particle therapy and imaging will be presented. In particular, this first chapter is focused on the theory underlining the acceleration of these beams and on the possible developments of proposed applications. All the studies in this thesis have been implemented using different dosimetry techniques which had to be adapted to the unusual characteristics of the beams. For this reason the second chapter is focused on the explanation of the basic operating principles of the dosimeters used or which could be used

in the presence of these beams. The third is focused on the operating principles of the Monte Carlo code Fluka used throughout the thesis to expand the information gained from the used dosimeters or to characterise the accelerated beams. The fourth chapter presents a dosimetry method implemented for a radiobiology experiment of hamster cells irradiated by a laser-driven proton beam: the results of the experiment showing, for the first time, that laser-driven proton therapy is actually feasible, are also shown. The fifth chapter presents another detection method for proton and ion beams involving nuclear activation of metal foils. Chapter six and seven are focused on simulation studies for the characterisation of laser-driven electron and X-ray beams. In particular, in the sixth chapter a simulation method is presented to recognise the electron beam energy and in the seventh the analysis of experimental data sets is reported and used to benchmark the simulation method. To conclude, a summary of the topics presented in this thesis and an explanation of the most promising directions of future work needed to further advance this line of research are given in chapter eight.

The code written to produce the work described in this thesis is available on request[1].

1.1 LASER-DRIVEN BEAMS

In a typical laser-particle acceleration experiment, a high power laser pulse (of intensity above 10^{18} W/cm^2) is focused onto a solid or gaseous target. Pedestal (due to incoherent spontaneous emissions of the crystal generating the pulse amplified mainly in the pre-amplification stage) and prepulses (of the duration of picoseconds and due to time re-compression effects of the bunch) anticipating the main pulse, create plasma on the surface of the target. When the main pulse arrives, it interacts preferentially with this plasma and a population of hot electrons with a

[1] Requests to francesca.fiorini83@gmail.com

Maxwellian-type distribution is generated. These electrons traverse the target and build up a high electrostatic field, up to the order of TV/m, capable of accelerating particles on the rear surface of the target. Photons, mainly due to bremsstrahlung and characteristic inner-shell line emission, are also produced as the electron beam crosses the target.

In order to understand the importance of the pulse shape, it has to be specified that a laser pulse does not have a Gaussian temporal profile, but is characterised by the presence of prepulses and the pedestal. In particular, the pedestal, being due to random effects, does not have a fixed relation with the spectrum of the main pulse, so it cannot be compressed in the re-compression stage. For this reason it maintains its original duration of usually a few nanoseconds (in contrast to the main pulse which can be compressed to duration of the order of femtoseconds). Another consequence of it being an aleatory phenomenon is that it changes at each shot causing different effects in the final interaction of the main pulse with the target. In a laser-solid interaction the pedestal and/or the prepulses can be so intense to ionise a large part of the front surface of the target before the main pulse arrives (see figure 1.1). In this case, when the main pulse arrives, it will not interact with the solid, but with an already expanded plasma.

1.1.1 Driving forces

Supposing that the target is irradiated normal to the surface, when the main pulse arrives on the plasma created by the prepulse, the electrons feel the strong electric field, $\vec{E}$, carried by the pulse and start to oscillate on the target surface with velocity $\vec{v}$ parallel to $\vec{E}$ (and opposite sense). These moving electrons feel also the magnetic field, $\vec{B}$, carried by the pulse, so that Lorentz force starts acting. Being $\vec{F} = -e\,\vec{v} \times \vec{B}$, the electrons start drifting across the target parallel to the laser direction ($\vec{k_L}$). The combined force of the electric and magnetic field of the laser is called *ponderomotive*

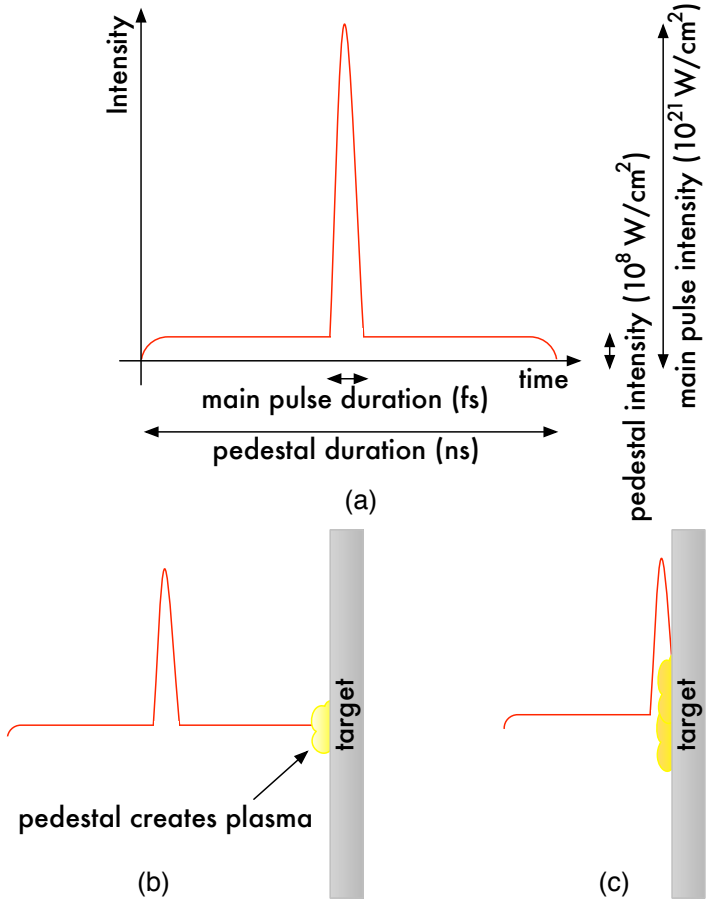

Figure 1.1 – (a) Schematic view of the temporal composition of a laser pulse (example of contrast $= \frac{\text{main pulse intensity}}{\text{pedestal intensity}} = 10^{13}$): for simplicity prepulses are not represented in this scheme. (b) The pedestal interacts with the target creating plasma. (c) When the main pulse arrives, it interacts with an already expanding plasma.

force [1] and as can be seen its direction does not depend on the charge of the accelerated particle, so that if protons and ions were accelerated directly by the laser pulse, they would move in the same direction and sense as the electrons.

In the case of a single particle the equation of motion can be easily solved. In the case of a plasma the conditions are more complex because the distribution of the plasma fluctuates with the oscillating electric field. Wilks in [2] found that due to the ponderomotive force the electrons spectrum resembles a relativistic Maxwellian

distribution with an effective temperature, T_{PM}, given by equations 1.1:

$$k_B T_{PM} \simeq m_e c^2 \left[\left(1 + \frac{I\lambda^2}{1.37 \times 10^{18}} \right)^{1/2} - 1 \right] \tag{1.1}$$

where $k_B T_{PM}$ is the effective electron energy measured in MeV, m_e is the electron mass in MeV, I is the laser intensity in W/cm^2 and λ its wavelength in μm. Therefore this cloud of hot electrons is pushed forward creating a strong electric field (up to the order of TV/m). The build up of such high current must be opposed by an inductively or electrostatically generated electric field which confines the fast electrons near the surface of the target, or else the background thermal plasma must supply a balancing return current. So, upon reaching the rear surface of the target some of the hottest electrons escape, but most of them are attracted back into the target. A similar situation later occurs at the front of the target: most of the electrons return to the front surface and some escape. This phenomenon is called electron refluxing [3]. The percentage of refluxing electrons and the number of refluxes change with the target and laser beam characteristics [4, 5]. During its multiple paths inside the target, the electron beam generates an X-ray beam (mostly bremsstrahlung), strictly dependent on target and laser properties.

If the target is extremely thin (a few μm at maximum), since the accelerated electrons are very energetic, the target will be transparent for them because the energy loss will be negligible: the electron cloud will reach the back of the target, where it will ionise and accelerate the proton layer on the back of the target. The cause for this proton acceleration is traced to a thin layer of contaminants (water vapour or hydro carbons), a large fraction of which are hydrogen atoms deposited everywhere around the target. Due to their higher charge-to-mass ratio, protons are more efficiently accelerated than any other ion species, reducing the effectiveness of the approach for heavier ion acceleration, but oxygen and carbon ions present in the contaminants can also be accelerated. This mechanism is called Target Normal Sheath

Acceleration (TNSA) [6] and it is so far the only established mechanism to accelerated protons and ions using a laser beam. The word 'normal' is due to the fact that protons and ions feel the strong electric field all around them and so they are accelerated straight, normally to the surface where they lie. One of the methods to improve the acceleration of ions to the detriment of protons, is to preheat the metal target [7, 8], above 1000 K, so that the loosely bound hydrogens of the C_xH_y contaminants are driven out of the target surface, allowing for other heavier contaminants or some target ions (increasing even more the preheating temperature) to be accelerated. The produced proton/ion beams exhibit advantageous characteristics, such as short pulse lengths, high currents and low transverse emittance, but they also show exponential energy spectra with almost 100% energy spread (typical proton and ion spectra are shown in figure 1.2 (a) and (b)). This large energy spread remains the biggest impediment which makes the TNSA technique still not properly usable on large-scale (see section 1.1.2). For the proton beams the maximum energy achieved so far has been ∼60 MeV [9]: see figure 1.2 (c) for the maximum achieved proton energy as a function of the laser irradiance ($I\lambda^2$) and (d) for the proton energy as a function of the target thickness. Irradiating solid targets, the maximum ion energy detected so far has been ∼10 MeV/n [10] involving mainly C and O from the contaminants but also a few ions of the target material. Irradiation of gas jets rather than solid targets has been proved to be more advantageous for ion acceleration: so far the maximum detected energy has been 20 MeV/n [11].

If the target is not extremely thin, then it will not appear transparent to the electron cloud and during its multiple paths inside the target, decreasing its energy, will generate X-rays, mostly bremsstrahlung and shell emissions (but also gammas from photo-nuclear reactions and pair production if the electron energy is high enough), strictly dependent on target and laser properties. Proton and ion acceleration at this point will be drastically reduced (see figure 1.2 (d)).

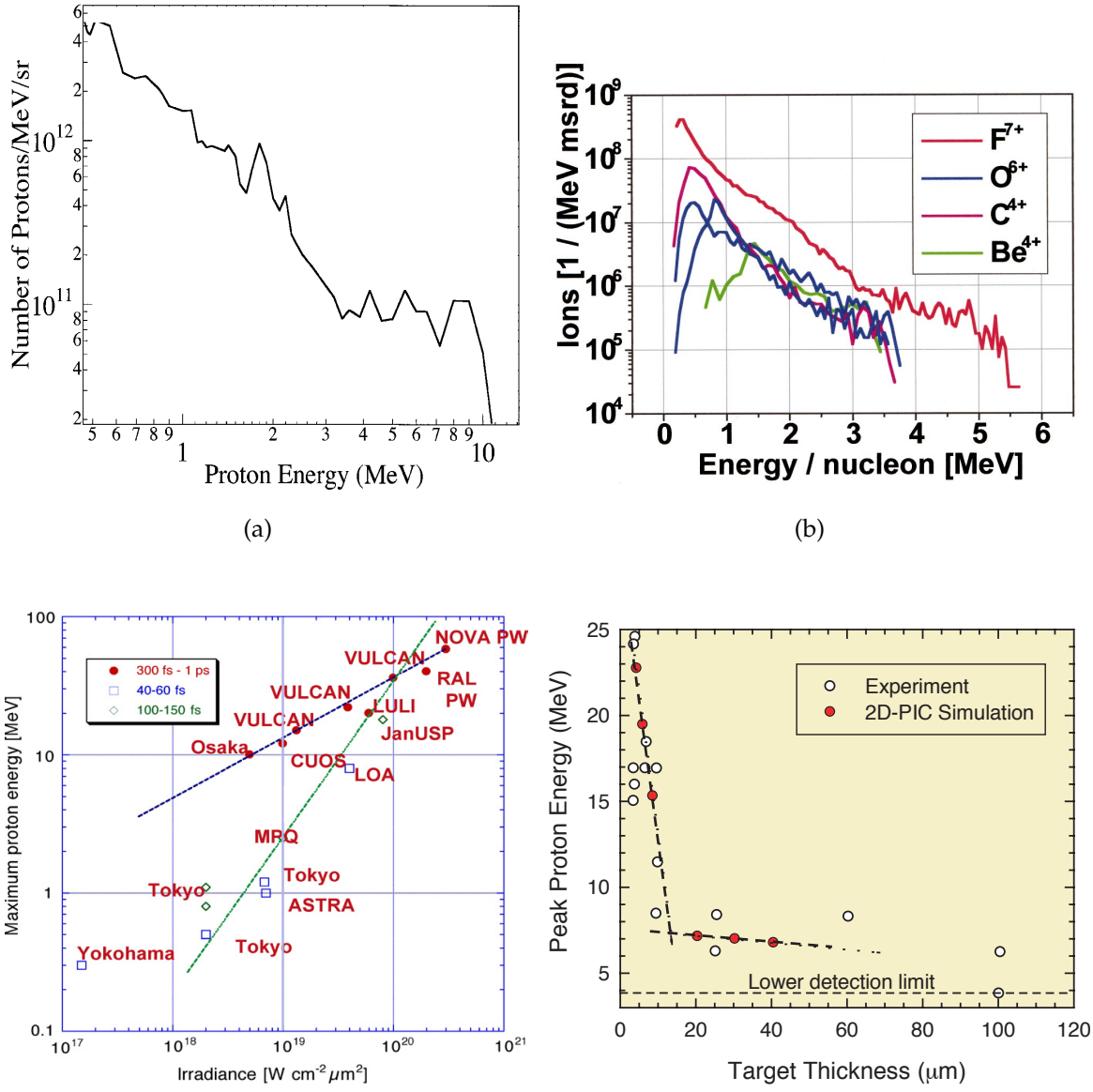

Figure 1.2 – (a) Typical spectrum of protons accelerated through TNSA. (b) Spectra of ions accelerated through TNSA pre-heating the target before laser irradiation. (c) Maximum achieved proton energy as a function of the laser irradiance ($I\lambda^2$) of the world wide facilities. (d) Maximum achieved proton energy as a function of the target thickness (data from different experiments). From (a) to (d) the images are taken and readapted respectively from reference [12, 8, 13] and [14].

If the target is not irradiated perpendicularly, the electric field, and in particular the component parallel to the plasma cloud, will still act as the starter of the ponderomotive force accelerating the electrons along the laser axis, but also another phenomenon will become relevant. Resonance absorption is the consequence of a singularity, due to the laser incidence angle θ, in the wave equation when the electron plasma frequency is equal to the laser frequency [15]. In this case the laser drives a plasma wave at the critical density surface in a plasma density gradient [16], i.e. along the normal to the target. Beg et al in [17] explained that the temperature of the electrons accelerated by the resonance absorption is given by equation 1.2:

$$k_B T_{res} \simeq 0.24 \left(\frac{I \lambda^2}{10^{18}} \right)^{1/3} \tag{1.2}$$

where $k_B T_{res}$ is the effective electron energy measured in MeV, I the laser intensity in W/cm^2 and λ its wavelength in μm. As documented in the paper by Cho [18], who irradiate a solid target at 45°, these two mechanisms can occur together in the target, causing the acceleration of two separate beams which can be detected simultaneously. The one due to the resonance absorption, which shows the characteristic laser frequency, was seen to be almost an order of magnitude more intense than the beam accelerated by the ponderomotive force. It also exhibited a greater divergence. At the same time the temperatures of these two beams were estimated to be different and in good agreement with those expected using equations 1.1 and 1.2. From this derives the fact that, when a target is irradiated non perpendicularly, photons, protons and ions are accelerated by two different sources, therefore they'll show different energetic spectra, but in the particular case of protons and ions, since they are accelerated from the contaminant sheath deposited on the target rear surface the result will always be a beam moving perpendicularly from the target surface. Figure 1.3 shows a simplified scheme of the TNSA mechanism in the case of a target irradiated non perpendicularly.

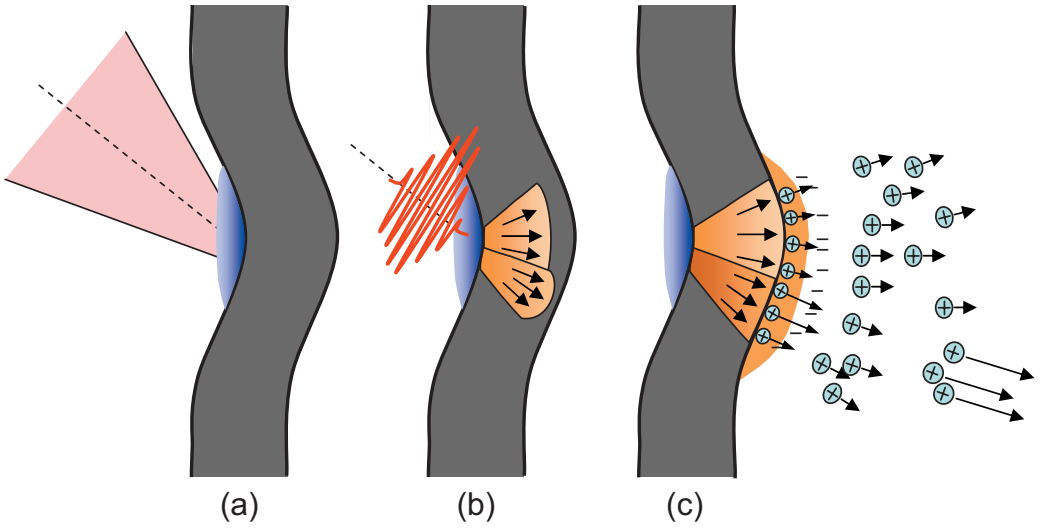

Figure 1.3 – Schematic representation of the TNSA mechanism for target irradiated non perpendicularly. Before the arrival of the main pulse, the pressure induced by the prepulse creates the plasma in the target (a). When the pulse arrives it accelerates the electrons of the plasma in two directions: along laser axis due to the ponderomotive force and along target normal due to the resonance absorption. The most energetic and less divergent electrons are along the direction of the laser axis (b). Reaching the surface the electric field generated is of the order of several TV/m. Protons and ions of the contaminated rear surface are accelerated by this electric field. As for the electrons the most energetic protons, ions and photons will be detected along the laser axis (c). Image taken from [20].

Other techniques, such as radiation pressure acceleration (RPA) [19], are still nascent and so far not possible to be applied in full. RPA in particular requires more powerful lasers and ultra high contrast pulses that are still not entirely attainable. In fact, to be applied, the theory makes the assumption that the laser momentum is efficiently coupled to the ion population, an assumption which is not trivial because, until now, the laser primarily interacts with the pre-plasma electrons, and then leads the proton and ion acceleration, preventing the entire foil from being uniformly accelerated. In contrast with TNSA, in the RPA mechanism there is no dependence on ion charge, so the acceleration of protons or ions have no priority: their acceleration depends only on their presence in the foil.

1.1.2 LASER-DRIVEN PROTON AND ION THERAPY

Once the technology to accelerate light and heavy particles is improved and higher energies are delivered, there will be many potential applications. Among the most promising ones are: the creation of compact accelerators or injectors for larger scale accelerators [21], fast ignitor for inertial confinement [22], fusion induced by laser-accelerated heavy ions, transmutation of nuclear waste. Also medical applications will be possible: laser-driven proton and ion therapy [23], laser-driven $(p-n)$ and $(p-\alpha)$ reactions to produce short-lived isotopes for use in positron emission tomography (PET) [24] and laser-driven X-ray source for radiobiological applications [25]. The creation of laser-induced X-rays useful for imaging [26] will be either of medical and industrial interest according to the intensity and energy of the delivered beams.

At present there are 34 particle therapy centres working worldwide (with only one in UK) and another 22 have been proposed. All of them use either cyclotrons or synchrotrons to accelerate the proton and/or ions. The use of protons and ions in radiotherapy has several advantages [27]. First of all the lateral scattering on the atomic electrons is weak (it decreases with the mass of the accelerated particle) so that they produce a much lower irradiation of healthy tissues in the vicinity of the tumour. Second, the range of these particles with a given energy is known and fixed: this again minimises undesired irradiation of healthy tissues at the rear side of the tumour. Third, the well localised maximum of the proton energy loss in matter (Bragg peak) leads to a considerable increase of the delivered dose in the vicinity of the stopping point (calculable through the Bethe-Block formula [28]) which has to be chosen to be the tumour. Fourth, their Relative Biological Effectiveness (RBE, defined as the ratio of the photon dose to the particle dose necessary to produce the same biological effect, as for example the inactivation of 90% of the irradiated cells) is greater than 1 (and up to 3 for carbon ions), so that the local ionisation density and hence the density of complex DNA lesions becomes so high that repair fails [29]: the

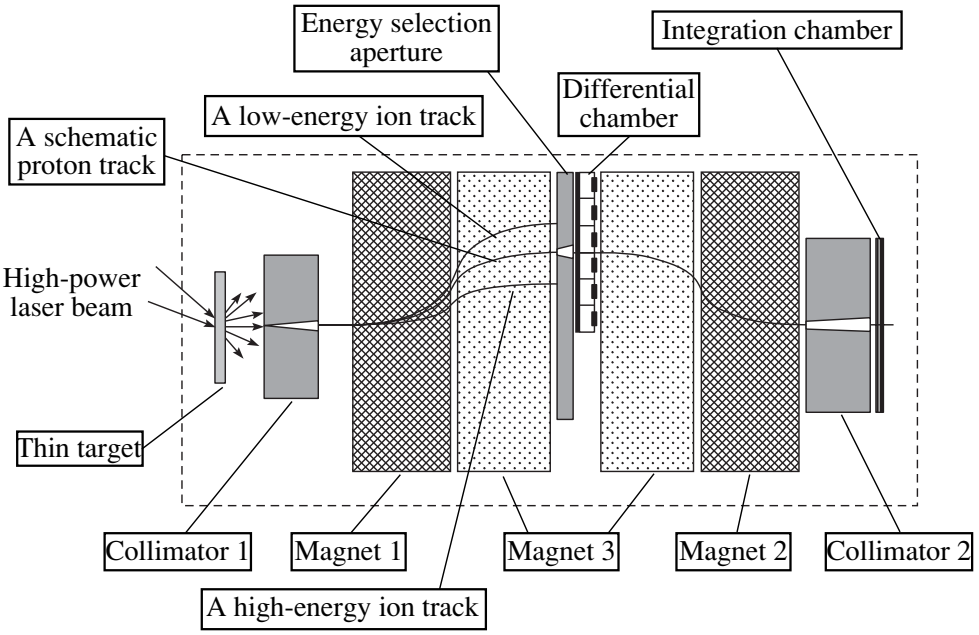

Figure 1.4 – Energy selection system designed to deliver to the patient only those protons useful for the therapy. It is intended to select only the desired particle species and energies (image taken from [31]).

reproduction of the tumour cells is inhibited and the tumour stops growing. For more information about the physics of particle therapy see Appendix A.

Despite these recognised benefits, the deployment of such facilities has been slow mainly because of the large construction and maintenance costs and their enormous sizes. A conventional proton therapy facility can cost up to $\sim$ £ 100M and one for combined protons and heavy ions up to $\sim$ £ 140M [30]. By building a laser-driven proton/ion beam facility, both the costs and size could be significantly reduced. So far, several proposals on how to build such facilities have been discussed, but, since the achieved energy spectra are still not useful for therapy (too low energy and 100% energy spread), none of them has been constructed. The projects see the large accelerators replaced by lasers, the large magnetic system to deliver the beams to the treatment rooms substituted by mirrors to deliver the laser and consequently the radiation shielding reduced. Ideally the laser would be transported (through mirrors and lenses) to the treatment room (even in a gantry) and only there the particle beam

would be created, particle type and energy selected, and immediately delivered to the patient. One design for the particle and energy selection system [31], is shown in figure 1.4: a collimator (collimator 1) selects only the part of the proton/ion beam that is supposed to be more energetic, blocking the particles emitted with a larger divergence and lower energy; a first pair of magnets is used to separate the particles in the beam, not only the type but partially also the energy; another collimator (energy selection aperture) is used to select the required beam and a differential chamber (consisting of multiple electrodes to collect ionisation from different parts of the cavity volume) to monitor its energy and fluence in order to predict the dose rate and dose distribution; a second pair of magnets is used to focus the selected beam into another collimator (collimator 2) and into an integral chamber, installed to monitor the beam based on the information from the differential chamber. This system, built to deliver always the same beam, protons, with always the same energy, would be used in conjunction with a passive scattering system [27] (made of a collimator and absorbers to change the lateral profile and the energy of each single particle of the beam) to conform the beam's spatial and energy distribution to the shape and depth of the tumour. In order to use this energy selection system with an active scanning system [32], the energy selection aperture has to be replaced by a mobile collimator, which from shot to shot would move to select a different energy beam in order to irradiate deeper or more superficial parts of the tumour. The active scanning system, essentially made of a set of magnets, would then deliver the incoming particles to the different volumetric regions (voxels) in which the tumour can be divided.

The main product of all of this will be a drastic reduction in the cost of a facility but also in its size, which could allow more centres to accommodate a proton facility within an already existing building. Also the cost of imaging will be reduced: simply developing more than one laser line, it will be possible to produce short-lived

low Z isotopes for PET and X-ray beams for computer tomography. Prototypes of delivery rooms of the facilities presented in [33, 34] are shown in figure 1.5.

So a compact laser-driven proton or ion therapy facility, in order to be completely laser sustained, would include at least three laser beam lines: one for the therapy room to deliver the particle beam to the patient and irradiate the tumour, another

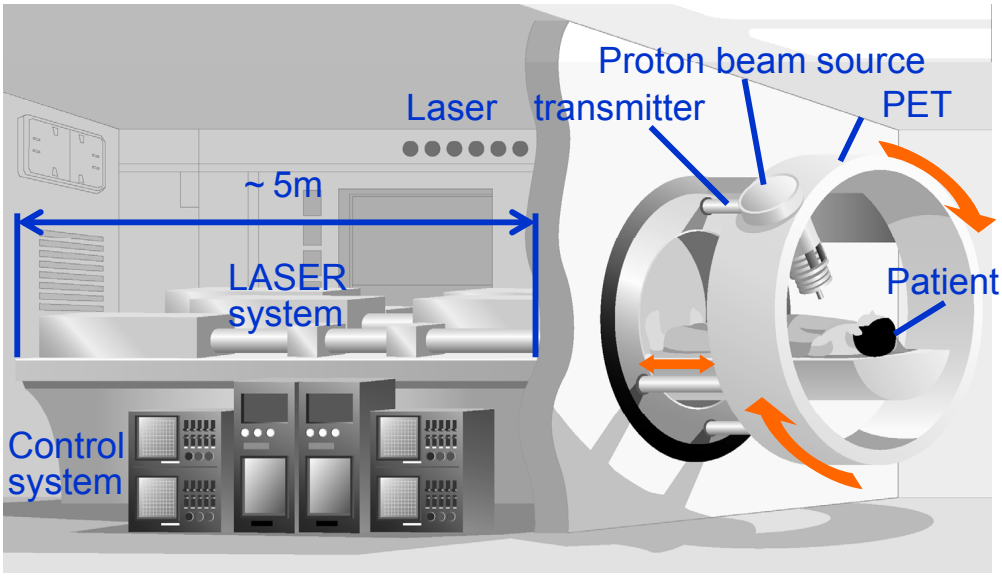

(a)

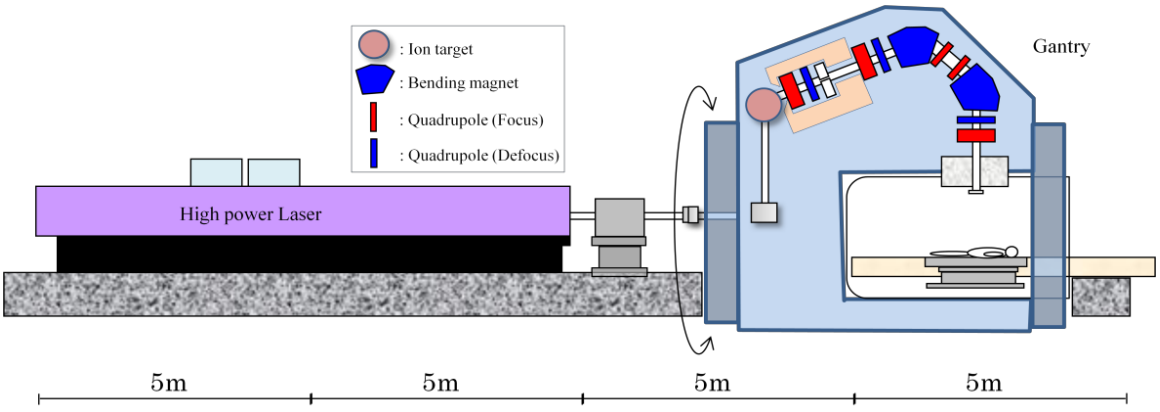

(b)

Figure 1.5 – (a) Conceptual design of a compact laser-driven proton therapy room combined with an in-situ real-time PET camera (image taken from [33]). (a) Schematic overview of a beam-line for acceleration and delivery of laser-driven protons embedded in gantry (image taken from [34]). Both the beam-lines imply the use of the energy selection system shown in figure 1.4.

one to produce short-lived isotopes (as for example the most commonly used ^{18}F included in the radiopharmaceutical 2-fluoro-2-deoxyglucose) to be for use in PET, and a third one (at lower power) to produce the X-ray beam with which to irradiate the patient for radiography.

1.1.3 LASER-DRIVEN X-RAY IMAGING

Glinec at al. in 2004 [26] proved the feasibility of high resolution imaging with laser-driven X-rays using a low energy and low intensity (10^{18} W/cm^2) laser focused on a 3mm-diameter helium gas jet and a conversion target with high atomic number. The laser, irradiating the gas jet, accelerated an escaping electron beam, which irradiating a tantalum target (conversion target) created an X-ray beam used to irradiate a complex tungsten object placed in the beam line. The out-coming radiation was then detected by an imaging system and the experimental image processed, resulting in a final submillimetre resolution image.

The technique used in that experiment could be used for nondestructive material or mechanical inspection of objects, but not of living creatures, because the energy of the accelerated X-rays reached hundreds of MeV which would produce a high dose deposition inside the irradiated body (the highest doses delivered with conventional computer tomography are usually lower than 30 mSv and much lower for radiography procedures). By using a different configuration, such as the one explained in chapter 7 not including gas jets and conversion targets but directly irradiating a solid target with low intensity lasers, the energy and the intensity of the X-ray beam can be successfully decreased. Unfortunately the characterisation of the out-coming electron and X-ray beams and the laser conditions useful to produce the beams needed for medical imaging are still not completely understood. This justifies a large part of this thesis which is devolved to the characterisation of these beams.

In any case tomography of objects (small and large) does not require low doses and high intensity beams are usually required, so that high power lasers could be useful for security applications ranging from high speed imaging of objects in motion to airpot or container imaging.

1.2 LIBRA PROJECT

All the work explained in this thesis has been developed in the context of the LIBRA project (http://www.qub.ac.uk/sites/LIBRA/). The Laser Induced Beams of Radiation and their Applications (LIBRA), is a British consortium including several Universities and Laboratories along the UK which aims to develop the relevant technology for high-flux/high-repetition source delivery and characterise the produced beams, while achieving the quality and reliability essential for some medical and non medical applications of laser-driven beams. This will be achieved via a combination of innovative developments in target production and delivery, detector technology, beam property optimisation and control.

Most of the efforts of the LIBRA collaboration are therefore focused on: developing new target technologies to facilitate laser interactions for the production of beams of high-energy ions, protons and X-rays; experimentally and theoretically optimising new and novel target materials, constructions, shapes, techniques, processes etc, using existing systems supported by state-of-the-art modelling, to tailor the properties of these beams; developing new, novel and comprehensive diagnostics that are capable of measuring the parameters of interest for each type of particle beam; demonstrating particle source properties suitable for use in scientific, technological or medical applications; and on demonstrating the suitability of ions sources for medical applications via biological and dose deposition tests.

The task of the Medical Physics group of the University of Birmingham involved in LIBRA has been fundamental for the development of the dosimetry techniques

used to detect the produced beams and to demonstrate via radiobiological experiments the feasibility of particle therapy using laser-driven proton beams.

CHAPTER 2

DOSIMETRY OF LDPBS

The main aim in radiotherapy is the irradiation of cancer tissues, delivering the right amount of dose to damage the cells' DNA and avoiding damage as much as possible to the surrounding healthy tissues. This requires a very accurate treatment plan where the patient information (CT and MRI) are carefully taken into account: the treatment plan is developed *ad personam*. Before arriving at this point, many years of experiments and tests have passed, but even now when the treatment planning programs have become more and more accurate, it is still often the case that the delivered dose is checked on each patient at several places of the body. Dose is defined as the amount of energy deposited per unit mass and, since more than 70% of the human body is made of water and the overall average density is close to 1 g/cm^3, it is usually standardised in terms of absorbed dose-to-water.

Dosimetry is not only important during treatments. Experimental studies of new techniques and quality assurance require very precise dosimetric techniques because their future application on patients depends on the accuracy of the data

gathered.

In the case of LDPBs, not only the application to particle therapy is still nascent, but the beams still have to be fully developed and characterised. The acceleration of these beams is improving with the laser technology: not only the maximum energy is increasing with the laser power, but also the possibility to obtain monoenergetic beams is getting closer with the exploration of the approach of the Radiation Pressure Acceleration method. For a precise analysis of the accelerated beams it is mandatory to obtain a full set of information about the particle conditions in each single shot. Of primary interest are the measurements of the source size, divergence, transverse emittance and the angular and energetic distribution. All of this means that the accuracy of the detection systems is vital to understand the characteristics of the beams and eventually to make sure that the requirements for particle therapy are fully achieved. The difficulty with these kind of experiments, though, is that the large instantaneous dose rate of the LDPBs (higher than 10^9 Gy/s) is a challenge for commonly used detection techniques, so that other procedures need to be explored.

In this chapter the bases of some dosimetry techniques are explained. One of these is a standard technique and can be used only for commonly accelerated beams, while others can also be used in the presence of LDPBs. The description of the standard technique was necessary because it was intensively used in the process of testing and understanding the development of some of the techniques applied to LDPBs. Some simple applications and calibrations are also described. More accurate explanations of the techniques used for LDPBs and the experiments in which they were used are better illustrated in chapters 4, 5 and 7.

2.1 IONISATION CHAMBERS

Ionisation chambers are widely used in radiotherapy dosimetry and consist of two electrodes with a voltage across them, separated by a small collecting volume of gas.

As an ionising particle passes through a gas, it ionises atoms along its path and the ion pairs move to the electrodes where they are collected. The pulse of current due to the movement of charges is measured. Ion pairs can be formed either by direct interaction with the incident particle or through a secondary process in which some of the particle energy is firstly transferred to an electron. Regardless of the mechanism involved, the practical quantity of interest is the total number of ion pairs created along the track of the radiation. At a minimum, the particle must transfer an amount of energy equal to the ionising energy of the gas molecule to allow the ionisation process to occur. However, there are other mechanisms by which the incident particles may lose energy within the gas without creating ion pairs. Examples are excitation processes in which an electron may be elevated to a higher bound state in the molecule without being completely removed. Therefore, the average energy lost, called *W-Value*, is always substantially greater than the ionisation energy. The W-Value is dependent on the species of gas involved, on the type of incident radiation and its energy. However, empirical observations show that this value is not a strong function of any of these variables and is remarkably constant for many gases and types of radiation. Assuming that W is constant for a given type of radiation, the deposited energy will be proportional to the number of formed ion pairs, so that a calibration to primary standards will give the relation between dose and measured charge.

Collision between positive ions and free electrons may result in recombination in which the electron is captured by the positive ion recreating a state of charge neutrality. Alternatively, the positive ion may undergo a collision with a negative ion in which the extra electron is transferred to the positive ion and both ions are neutralised. In either case, the charge represented by the original ion pair is lost and cannot contribute any longer to the signal in detectors based on collection of the ionisation charge. There are two types of recombination loss: columnar and volu-

metric recombination. The first type (called also initial recombination) arises from the fact that ion pairs are first formed in a column along the track of the ionising particle. The local density of ion pairs is therefore high along the track until the ion pairs are drifted or diffused away from their point of formation. Columnar recombination is most severe for densely ionising particles such as light or heavy ions compared with fast electrons which deposit their energy over a much longer track, and it is dependent only on the local conditions along individual tracks and does not depend on the rate at which such tracks are formed within the detector volume. In contrast, volume recombination is due to encounters between ions and or electrons after they have left the immediate location of the track. Since many tracks are typically formed over the time taken for ions to drift all the way to the collecting electrodes, it is possible for ions and/or electrons from independent tracks to collide and recombine. Volume recombination, therefore, increases in importance with irradiation rate. Charge separation and collection should be as rapid as possible in order to minimise the recombination, and reasonably high electric fields (100 V/cm) are indicated for this purpose. A laser-ion source delivers many Grays in less than a nanosecond, so that the recombination would be so high even if very strong electric fields are applied. This makes these chambers highly unsuitable for laser-driven particle measurements.

2.1.1 Corrections to be applied to obtain the dose

Suppose we have a cell dish irradiated by a proton beam and the measurement of the dose on the cells is required. In the case of conventionally accelerated proton beams the easiest way to obtain the dose is using an ionisation chamber, placed on the beam line in front of the cell dish, for which the calibration factor to relate measured charge–dose to water is known. A primary standard dosimetry laboratory can calibrate several types of dosimeters via calorimetry in standard reference con-

ditions, so that the dose to water calibration factor, $N_{D,w,Q}$ (measured in Gy/nC), is known for a specific radiation quality, Q. When this quantity is not known for the required beam quality, it is possible to obtain it taking the calibration factor for another known beam quality, Q_0, and then multiplying it by a beam quality correction factor:

$$N_{D,w,Q} = N_{D,w,Q_0}\, k_{Q,Q_0} \tag{2.1}$$

where k_{Q,Q_0} corrects for the effects of the difference between the reference beam quality Q_0 and the actual user quality Q.

The calculation of the dose on the cells then becomes a product of the charge reading on the chamber, Ch_Q, the calibration factor and other correction factors for which the calibration factor is valid, depending on:

- temperature and pressure conditions, $k_{T,P}$;
- ion recombination, k_{ion};
- different dose deposition due to the different position and possibly material composition of the chamber and cell dish, k_{pos}:

$$D_{w,Q} = Ch_Q\, N_{D,w,Q_0}\, k_{Q,Q_0}\, k_{T,P}\, k_{ion}\, k_{pos} \tag{2.2}$$

k_{Q,Q_0} determination

This beam quality correction factor is due to the fact that calibration is currently not available for protons, so the Code of Practice TRS-398 [35] from IAEA recommends to use a calibration based on γ-rays from ^{60}Co. For this reason, from now on the calibration beam quality, Q_0, will refer to γ-rays from ^{60}Co.

The beam quality correction factor, k_{Q,Q_0}, is defined as the ratio, at the qualities Q and Q_0, of the calibration factors in terms of absorbed dose to water of the ionisation chamber:

$$k_{Q,Q_0} = \frac{N_{D,w,Q}}{N_{D,w,Q_0}} = \frac{D_{w,Q}/Ch_Q}{D_{w,Q_0}/Ch_{Q_0}} \tag{2.3}$$

As this factor has not been experimentally determined in the case of protons, it can be calculated theoretically applying the Bragg–Gray (B–G) cavity theory [36, 37]. According to this theory, it is possible to define the dose in a medium as:

$$D_{med} = \Phi_{med} \left(\frac{S_{coll}}{\rho} \right)_{med} \tag{2.4}$$

where Φ_{med} is the fluence of identical particles with energy E and $\left(\frac{S_{coll}}{\rho}\right)_{med}$ is the collision stopping power of those particles with that energy in the medium. If the particles cross a boundary between two different media (for example the media surrounding the chamber and the gas inside the chamber), then the ratio in equation 2.5 is valid :

$$\frac{D_{med}}{D_{gas}} = \frac{\Phi_{med} \left(\frac{S_{coll}}{\rho} \right)_{med}}{\Phi_{gas} \left(\frac{S_{coll}}{\rho} \right)_{gas}} = \frac{\left(\frac{S_{coll}}{\rho} \right)_{med}}{\left(\frac{S_{coll}}{\rho} \right)_{gas}} = s_{m,g} \tag{2.5}$$

where it has been possible to simplify the fluences, assuming that the particle fluence changes negligibly in the two materials (undisturbed medium). In the case of a non-monochromatic beam, then the ratio becomes a ratio of integrals where the quantity at numerator and denominator are integrated across the entire spectrum.

If the gas is a thin layer immersed in the medium, such as for example the gas cavity in air, then it can be considered a Bragg–Gray cavity if its presence does not disturb the particle fluence (including the distribution in energy) existing in the medium in the absence of the cavity, i.e. it must be small if compared to the particle range in the medium. This condition is called B-G condition and it depends on the scattering properties of the two materials (to be similar) or on the thickness of the cavity. A second B-G condition implies that the absorbed dose in the cavity must be deposited entirely by the charged particles crossing it: all the charged particles in the cavity must be originated outside it and they must not stop in it.

At the same time, since the radiation ionises the gas crossing the cavity, the mea-

sured dose in Grays will be:

$$D_{gas} = \frac{Ch}{m} W_{gas} \tag{2.6}$$

where Ch is the produced charge (in Coulombs), m the mass (in grams) and W_{gas} is the W-Value (in J/C) of the gas in the cavity. Using equation 2.5, equation 2.6 becomes:

$$D_{med} = \frac{Ch}{m} W_{gas}\ s_{m,g} \tag{2.7}$$

In reality the chamber includes also the very thin walls which contain the gas: an additional correction due to the wall perturbation has to be calculated. Substituting 2.7 in 2.3, k_{Q,Q_0} can be expressed as:

$$k_{Q,Q_0} = \frac{(s_{m,g})_Q\ (W_{gas})_Q\ p_Q}{(s_{m,g})_{Q_0}\ (W_{gas})_{Q_0}\ p_{Q_0}} \tag{2.8}$$

where p_Q and p_{Q_0} represent the perturbation corrections of the specific used chamber for Q and Q_0 quality respectively: $p_Q = (p_{cav}\ p_{wall}\ p_{dis}\ p_{cel})_Q$ and the corresponding for Q_0. p_{cav} is a factor predominantly due to the in-scattering of electrons that makes the electron fluence inside a cavity different from that in the surrounding medium in the absence of the cavity. p_{wall} is a factor that corrects the response of the chamber for the non-medium equivalence of the chamber walls. p_{dis} is a factor that accounts for the effect of replacing a volume of water with the detector cavity when the reference point of the chamber is taken to be at the chamber centre. p_{cel} is a factor that corrects the response of the chamber for the effect of the central electrode during in-phantom measurements in high-energy photon, electron and proton beams.

The chamber used at the University of Birmingham to measure the dose is a Markus chamber (serial number 478) which is a 2 mm air cavity with 0.03 mm graphited polyethylene foil window. Equation 2.8 can be rewritten as:

$$k_{Q,Q_0} = \frac{(s_{w,air})_Q\ (W_{air})_Q\ p_Q}{(s_{w,air})_{Q_0}\ (W_{air})_{Q_0}\ p_{Q_0}} \tag{2.9}$$

since the required dose is dose to water. Moreover, as the Markus is a plane-parallel ionisation chambers, p_{dis} and p_{cel} are not required.
Values for Markus chambers irradiated by ^{60}Co (Q_0) are as follows:

- the value $s_{w,air} = 1.133$ was calculated by Andreo et al. [38]. As a consequence of spectral differences between ^{60}Co beams, the systematic uncertainty in assigning a stopping-power ratio to a particular ^{60}Co beam is estimated to be 0.1%;

- the value for W_{air} in ^{60}Co, for dry air, is taken to be 33.97 J/C. The uncertainty of this value was estimated by Niatel et al. [39] to be 0.2%;

- since transient electronic equilibrium exists in ^{60}Co the value for $(p_{cav})_{Q_0}$ is taken to be unity. The uncertainty associated with this assumption is negligible ($< 0.1\%$);

- the value used for $(p_{wall})_{Q_0}$ is reported in the Code of Practice [35] and it is estimated to be 1.009. The associated uncertainty is 1.5%.

Multiplying $(p_{wall})_{Q_0}$ and $(p_{cav})_{Q_0}$ one obtains $p_{Q_0} = 1.009$ with 1.6% of uncertainty. Considering all the factors in the denominator in 2.9 the value 38.8 J/C is obtained with an associated uncertainty equal to 1.7%.
Values for Markus chambers irradiated by proton beams:

- The value for $s_{w,air}$ is derived from the proton beam quality specifier R_{res} according to:

$$s_{w,air} = a + b\, R_{res} + \frac{c}{R_{res}} \tag{2.10}$$

where a = 1.137, b = -4.3×10^{-5} cm^2/g and c =1.84×10^{-3} g/cm^2. In the Code of Practice [35] the residual range, R_{res}, is chosen as the beam quality index with the advantage of being easily measurable. It is measured in g cm^{-2} and it calculated through: $R_{res} = R_p - z$, where z is the depth of measurement

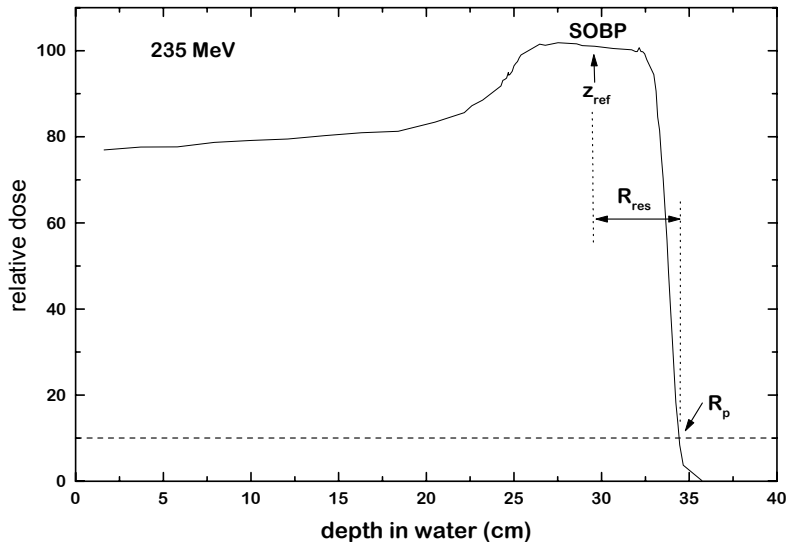

Figure 2.1 – R_{res} determined from the depth-dose deposition. Image taken from the Code of Practice TRS-398 [35] by IAEA.

and R_p is the practical range (both in water and expressed in g/cm^2), which is defined as the depth at which the absorbed dose beyond the Bragg peak or SOBP falls to 10% of its maximum value (see figure 2.1) (a). This means that R_{res} is an indirect expression of the beam energy at the depth of measurement. The uncertainty of $s_{w,air}$ is estimated to be within 1%;

- the value of W_{air} for protons can be considered constant and so not dependent on the beam energy. 34.23 J/C and a standard uncertainty of 0.4% [40], are the values recommended by IAEA;

- the value of p_{cav} is taken to be unity. Its uncertainty may be considered in two parts, corresponding to the contributions of secondary electrons and of heavier secondary particles. The slowing down of the secondary electrons generated in a proton beam is similar to that for γ-rays from ^{60}Co and so the negligible uncertainty assumed for the photon case may also be assumed for protons. The uncertainty of the heavier particle contribution is taken to be 0.3%, for both plane-parallel and cylindrical chambers [35];

- Monte Carlo calculations by Palmans and Verhaegen [41] indicate a possible effect on p_{wall} due to the influence of secondary electrons. An experimental study [42] confirmed these calculations for certain wall materials, however the effect is seen not to be larger than 0.5%. Therefore p_{wall} is currently taken to be equal to unity, and its total uncertainty is estimated to be 0.6%.

Multiplying $(p_{wall})_Q$ and $(p_{cav})_Q$ one obtains $p_Q = 1$ with 0.7% of uncertainty.
Table 2.2 summarises the values and the uncertainties taken into account to calculate k_{Q,Q_0} for a Markus chamber.

Quantity	value for ^{60}Co	uncertainty for ^{60}Co (%)	value for p	uncertainty for p (%)
$s_{w,air}$	1.133	0.1	depending on E_p	1
(W_{air}/e)	33.97 J/C	0.2	34.23 J/C	0.4
p	1.009	1.6	1	0.7
combining	38.8	1.7	–	–

Table 2.2 – Values and uncertainties of the quantities for γ-rays from ^{60}Co and for protons used to calculate k_{Q,Q_0} for a Markus chamber.

$k_{T,P}$ determination

$k_{T,P}$ is a factor which corrects the response of the chamber for the effect of the difference that may exist between the standard reference temperature and pressure specified by the standards laboratory and the temperature and pressure of the chamber in the user facility during the irradiation. This is a consequence of the fact that the chamber is open to the ambient air, so the mass of air in the cavity volume is subject to atmospheric variations. The correction factor is given by:

$$k_{T,P} = \frac{(273.2 + T)P_0}{(273.2 + T_0)P} \tag{2.11}$$

where T and P are the temperature (in degrees) and pressure (in Pa) of the room where the chamber is in use, and T_0 and P_0 are the reference temperature and pressure applied at the time of the calibration, respectively 20°C and 101.3 kPa.

k_{ion} determination

Incomplete collection of charge (when this is small enough to be calculated and corrected) in the chamber cavity due to the recombination of ions requires the use of this correction factor. As already mentioned, two separate effects take place: the recombination of ions formed by separate ionising particle tracks, volume recombination, which is dependent on the density of ionising particles and therefore on the dose rate; and the recombination of ions formed by a single ionising particle track, initial recombination, which is independent on the dose rate, but highly dependent on the linear energy transfer (LET). Both effects depend on the chamber geometry and on the applied voltage. For beams other than heavy ions, initial recombination is generally lower than 0.2%.

In pulsed radiation, the dose rate during a pulse is relatively high and general recombination is not negligible and it is possible to derive a correction factor using the theory of Boag [43]. In his theory Boag shows that the inverse of the ionisation current is proportional to the inverse of the square of the applied voltage for non-pulsed beams, or proportional to the inverse of the applied voltage for pulsed beams. A beam is classified as continuous (non-pulsed) when the pulse duration is larger than the charge collecting time and the time between two pulses much shorter. A cyclotron beam, even if usually considered pulsed, has a frequency of ∼20 MHz, but the collecting time of a typical chamber is 0.25 ms [44], so that, in this context, the beam from a cyclotron can be considered continuous. From [44] it is possible to derive the useful formula to be applied for continuous beams:

$$k_{ion} \approx 1 + \frac{A}{V} + \frac{m^2 g}{V^2} I_V \tag{2.12}$$

where A and m^2 are parameters to be experimentally determined at each irradiation. For plane-parallel chambers $g = d^4/6v$, where d is the distance between the electrodes and v is the air collecting volume. V is the voltage applied to the chamber and I_V is the ionisation current that would be measured if there was a 100% collecting efficiency. In equation 2.12 the term inversely proportional to the voltage is the component due to the initial recombination and the term inversely proportional to the square of the voltage is the component due to volume recombination. Even if A and m^2 should be experimentally derived for each irradiation because they depend on R_{res}, this would be impractical at each measurement, so the generic values have been used: A=0.515 V and m^2g=12.5 V^2/A. As mentioned by the author the overall experimentally derived correction (k_{ion}) was always within 0.1% of the correction obtained using the general values for A and m^2.

k_{pos} determination

Once all the corrections described previously have been applied, the obtained dose is the dose to water which would be measured in the chamber. The dose absorbed by a cell layer placed in front of the chamber is not yet determined. k_{pos} is the correction factor which transforms the dose to water measured by the chamber to the dose absorbed by the cells. For this reason it also takes into account the different composition of the two considered objects.

Suppose that the cell layer is a thin water thickness and the protons pass through it and then through the chamber. Simulating with a Monte Carlo code the beam and the experimental setup it is possible to obtain the dose per initial proton deposited in the cell layer and in the air cavity of the chamber. Once the cavity and the cell layer are simulated and the doses inside them measured (for example using the USRBIN card of the Monte Carlo code Fluka [45, 46], see chapter 3 for more information

about the code), k_{pos} can be calculated as:

$$k_{pos} = \frac{(D_{cell}/N_p)}{(D_{ch}/N_p)} \tag{2.13}$$

where D_{cell} is the simulated dose measured in the cell layer and D_{ch} is the simulated dose measured in the chamber air cavity. By multiplying k_{pos} by all the other corrections and chamber reading, the real dose absorbed by the cells is obtained.

This correction determination using a simulation of the experiment has to be repeated for each irradiation because it is strictly dependent on the positions and composition of the objects on the beam line and on the initial particle energy. Almost any experimental disposition can be used: the dish can be placed far away or very close to the chamber, several dishes can be irradiated at the same time (in this case there will be as many k_{pos} to be calculated as the number of cell layers) or absorbers can be used, as long as two conditions are always fulfilled:

1. the experimental setup has to be exactly reproduced by the simulation;
2. regardless of the number or type of objects placed along the beam line, there must be protons reaching the chamber so that a charge can be measured.

2.1.2 Measurements using the cyclotron beam line of the University of Birmingham

Several works have been performed using ionisation chambers and the proton beam accelerated by the cyclotron of the University of Birmingham. So far the characteristics of the Markus chamber (in figure 2.2 (a)) have been described, but another transmission chamber has also been largely used. It is a PTW monitor ionisation chamber model 7862: a circular plane parallel chamber, 2.4 mm thick and 96.5 mm of diameter (see figure 2.2 (b)). The chamber walls are made of double layers of graphited polyimide films (Kapton), each 0.05 mm thick. The ionising gas is air,

2.2 mm thick.

It was always used in combination with the Markus chamber, but since only the latter is calibrated ($N_{D,w,Q_0} = 0.5563$ Gy/nC), the monitor chamber was not used to give any dose measurement, unless the ratio between the experimental charge reading of the Markus and of the monitor chamber, $R\left(\frac{Ch_{Mark}}{Ch_{mon}}\right)$, was calculated and saved. The value of this quantity corresponds to the average of several ratios calculated from readings taken at the same beam conditions (energy, chamber position, fixed absorber thickness placed between the chambers, current, pressure, temperature...). The uncertainty is instead the standard deviation calculated from these ratios. Knowing the relation between the readings of both the chambers for a fixed R_{res}, the dose can be calculated using the charge from the monitor using the 2.14:

$$D_{w,Q} = N_{D,w,Q_0}\, k_{Q,Q_0}\, k_{T,P}\, k_{ion}\, k_{pos}\, R\left(\frac{Ch_{Mark}}{Ch_{mon}}\right) Ch_{mon} \tag{2.14}$$

where the charge Ch_Q in 2.2 from the Markus chamber has been replaced with $R\left(\frac{Ch_{Mark}}{Ch_{mon}}\right) Ch_{mon}$, with Ch_{mon} the monitor chamber reading. Equation 2.14 is highly useful in case of high current irradiations which could damage the more sensitive Markus chamber, or simply when it is requested to know the dose in a particu-

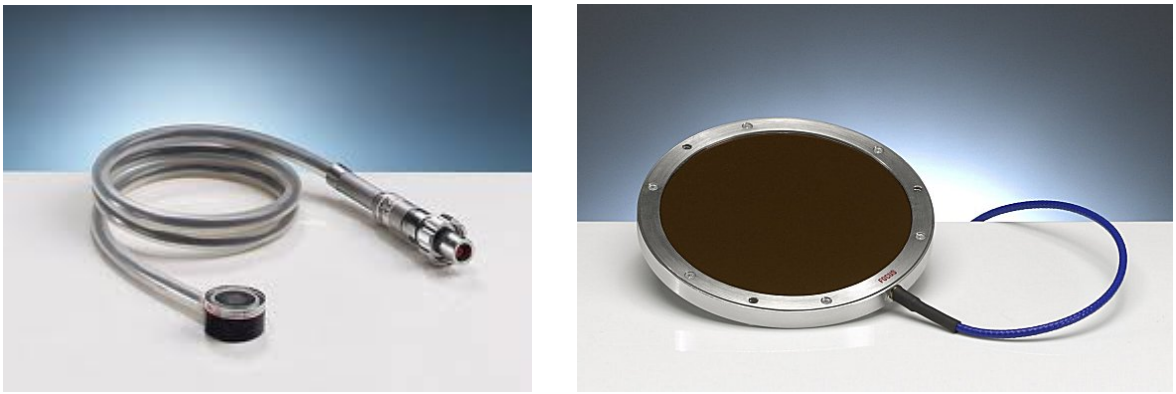

(a) (b)

Figure 2.2 – Markus (a) and monitor (b) chambers.

lar thickness of a much thicker object. In this case $R\left(\frac{Ch_{Mark}}{Ch_{mon}}\right)$ is calculated for a thickness similar to the one where the dose is needed, then the Markus chamber is removed and the final dose is calculated using 2.14. While k_{pos} and k_{Q,Q_0} (due to its dependence on R_{res}) will be calculated for each used absorber thickness, the other components in 2.14 will not change, because even if using the reading from the monitor chamber, it is the calibration of the Markus which gives the dose.

Determination of the beam energy

The beam accelerated by the cyclotron of the University of Birmingham is affected by fluctuations in energy (up to ± 0.5 MeV). These fluctuations are mostly due to the way the proton are extracted from the source or to objects which interfere with the beam before it reaches the chambers. For this reason, before performing any accurate measurement, it is necessary to find the proton energy, so that the subsequent measurements can be carried out according to the obtained beam characteristics. Both the chambers have also been used for other works explained in the following pages, for example during Gafchromic film calibration (see section 2.2.1), cell irradiation (see section 4.1.8) and nuclear activation of metal targets (see section 5.1), but since the energy check is common to all these works, it is explained here.

In order to determine the energy of the beam both the chambers, PMMA absorbers and simulations performed with the Monte Carlo code Fluka are used. Figures 2.3 (a) and (b) show the arrangement of the chambers and absorbers, respectively outside and on the beam line, supported by a PMMA jig. The procedure consists in measuring the depth dose curve in PMMA, gradually changing the thickness of the absorbers (the total thickness takes into account also the front wall of the Markus chamber) placed between the chambers. The depth dose points are then fit using the output of Fluka simulations, where the proton energy and its spread are changed until the best fit of the experimental points is obtained. Since the cur-

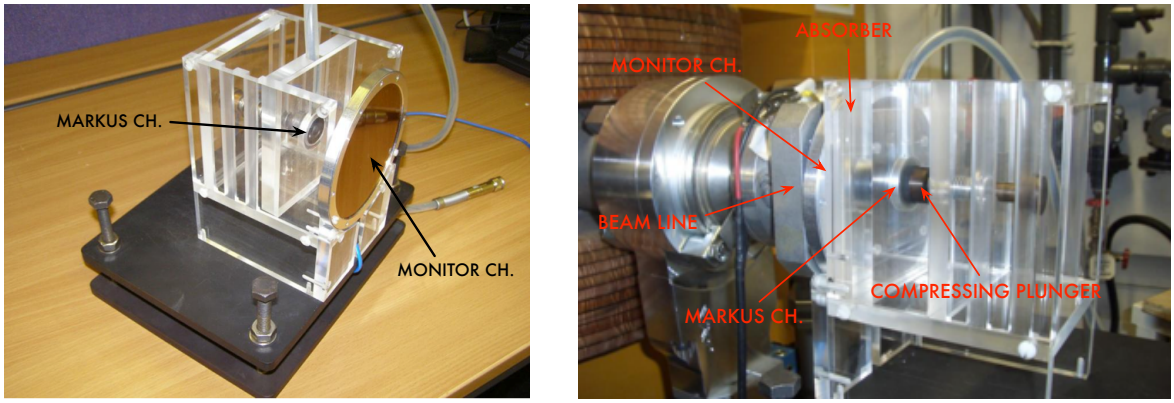

(a) (b)

Figure 2.3 – PMMA jig supporting the chambers and the absorbers, before using it in the beam line (a) and in the beam line placed immediately beyond the beam vacuum window (b).

rent could change during the irradiation (there is no necessity to keep it constant at this stage), the depth dose points were calculated taking the ratio between the charge measured by the Markus chamber and by the monitor chamber. This ratio, $R\left(\frac{Ch_{Mark}}{Ch_{mon}}\right)$, is not affected by the variation of current, and even if it is not a measure of dose (because it is not a charge multiplied by a calibration factor), it is still representative of the dose deposition. If the current were constant the monitor chamber would always measure the same charge (because it is irradiated by protons with always the same energy) and the Markus would measure a charge which is proportional to the dose absorbed by the air cavity after the protons have crossed the PMMA thickness, which is modified at each irradiation. If the current is variable, both the chambers measure a charge which is proportional to the current, regardless of their position. By considering $R\left(\frac{Ch_{Mark}}{Ch_{mon}}\right)$, the dependence on the current is eliminated and the comparison with the simulated curve becomes possible. The output from Fluka is the dose deposited (or energy loss) in bins of a thick PMMA absorber. The geometry of the beam line is reproduced up to the absorber. The Markus chamber is not exactly simulated: the wall is simulated as PMMA, with its equivalent

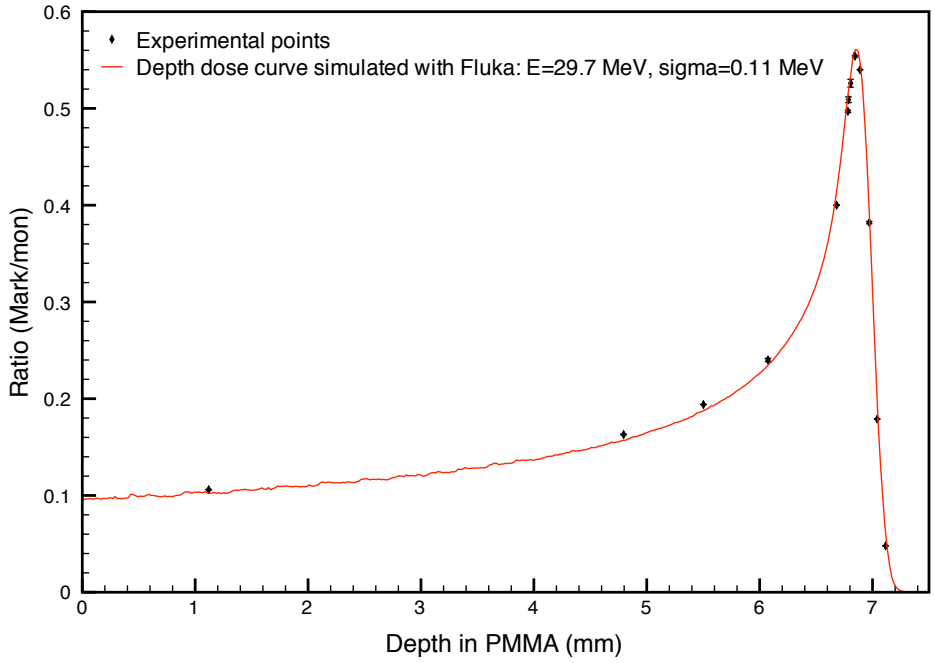

Figure 2.4 – Example of depth dose curve to determine the energy of the proton beam. The uncertainty of R $\left(\frac{Ch_{Mark}}{Ch_{mon}}\right)$ values is not well visible in the graph because it varied in the range 0.2–0.7%. The best fit curve from Fluka simulations revealed a proton spectrum with $\overline{E} = 29.7$ MeV and $\sigma_E = 0.11$ MeV.

thicknesses, so that the final absorber thickness includes also the thickness of the chamber window. The scoring card used in Fluka to have the dose in PMMA is USRBIN and the binning is usually cartesian, with bins 0.2 mm thick along Z (which is the beam direction). Along X and Y the beam is assumed to be circular. In the BEAM card, energy and momentum spread (and so energy spread) are varied until the depth dose curve from USRBIN fits the experimental points. Once this is obtained, the energy and spread used in the BEAM card to do the simulation are the experimental proton energy and sigma. In figure 2.4 an example is shown of approximate best fits for a proton beam where the energy spectrum was found to have $\overline{E} = 29.7$ MeV and $\sigma_E = 0.11$ MeV.

2.2 RADIOCHROMIC FILMS

Radiochromic (RCF) films are plastic films with self-developing active layers which change colour when exposed to ionising radiation. The darkening effect of the active layer is caused by the presence in it of an organic monomer which polymerise under irradiation, showing a significant optical absorption. The amount of colouring, depending on the amount of absorbed dose, is express in optical density (OD), which is a quantification of the transmission level of the film in presence of light: the higher the optical density, the lower is the transmitted light:

$$OD = \log_{10} \frac{I_0}{I} \tag{2.15}$$

where I_0 is the light intensity in absence of film and I is the transmitted light through a film. When the irradiated film is scanned in a CCD scan, the pixel value for a particular colour channel (or greyscale) represents I and the maximum transmission value (65535 for 16-bit channel) is used for I_0. In order to be used for dosimetry, the OD has to be related to the dose absorbed by the film. The relation between dose and OD is given by the calibration (see section 2.2.1). Once this is known, RCF films can give a 2D map of the absorbed dose in the overall range mGy–10kGy. Several type of GafChromic (from the name of the producing manufacturer) films are available on the market: the difference between them is the range of dose where they can be applicable (EBT, MD-55, HD-810). The active material of all these films is a crystalline diacetylene monomer (PCDA) suspended in gelatine. In particular, for the EBT films used in this work this monomer is modified by the presence of Lithium, which interacting with PCDA forms the salt LiPCDA, giving to the active material a higher sensitivity if compared to the other two types of film. This particular type of film becomes blue when irradiated and the absorption has a peak in the red part of the visible spectrum. By measuring the amount of darkening in the red channel,

it is possible to increase the sensitivity of the measurement.

These films are quite sensitive and temperature can produce undesirable effects, both during irradiation and scanning. While the effects of temperature during irradiation are permanent, during scanning the effect on the measured transmission light are reversible [47]. For this reason it is always preferable to irradiate the films at around 25°C, or lower temperatures, where the OD of EBT is seen to be quite stable [48], and to scan the films using always the same scanner used to obtain the calibration. This last assumption is particularly important also to avoid effects due to polarisation [49]: PCDA acid has a preferred orientation and so do the molecules within the active layer. For this reason, in order to avoid inconsistency in the OD it is required to always orient the films in the same direction, with respect to the particle source and to the scanning light. The simplest expedient is to mark each film before irradiation to help to remember the orientation.

It is important to remember that RCFs are LET dependent. This means that they show a different response depending on the particle energy and on the energy transferred from the particles to the active material. This effect has been noticed as a response reduction at low energies for both high and low LET particles. The under-response for X-ray radiation can be explained by the value of the cross section of the interactions occurring at low energies. At energies of the order of 100 keV the dominant interaction is the photoelectric effect which has $\sigma_{ph} \propto Z^n E_\gamma^{-m}$, with $n = [4, 4.5]$ and $m = [3, 3.5]$. Since Z_{eff} of the films is lower than the Z_{eff} of water ($Z_{eff_{EBT}} = 6.84$ and $Z_{eff_w} = 7.3$) the resultant cross section is $\sigma_{EBT} < \sigma_w$. This results in the dose response of the film looking reduced if compared with the response of water. At higher energies, once Compton scattering becomes the dominant interaction ($\sigma_C \propto ZE^{-1}$), this effect decreases. The under-response for heavy charged particles seems instead due to the fact that the high LET of these particles, which is highest near the range, causes a local dose release which is so high that exceed the dose

range of the film: the polymerisation of the film is locally saturated and part of the particle energy loss becomes unmeasurable. This means that the higher the particle LET, the higher is the under-response. With regard to the film EBT and EBT2:

- proton energies up to 30 MeV, have been investigated by Kirby [50] who found an under-response up to ∼50% of the nominal response for the lowest energies;
- proton energies higher than 50 MeV have been investigated by Martišíková [51] who found no under-response at all;
- carbon ion energies in the therapeutic range 100–400 MeV/u have been investigated by Martišíková [51] who found an overall under-response between 25 and 35%.

A final and important point is the dose-rate dependence. Until now it is not 100% clear whether GafChromic films can be safely used with the high dose-rate of LDPBs. This is due not only to the fact that the nominal uncertainty could cover this dependence, but also to the fact that in order to prove such dependence, another dosimetry method, non dose-rate dependent, should be used for the comparison. So far X-ray dose-rates up to 4×10^8 Gy/s have been used to test EBT films and the results have shown no significant difference in the response [52]. It could be assumed that even for higher dose-rates, up to the LDPB dose-rate (higher than 10^9 Gy/s) the response does not vary with the rate. In section 2.4 and in chapter 5 a technique which is not dependent on the dose-rate of the pulse is described: nuclear activation of metal foils. The comparison of the results from the two techniques has been proposed, but so far an experimental test in a LDPB has not been possible.

2.2.1 EBT2 FILMS AND CALIBRATION

EBT2 films are an improved version of EBT films using the same active component, but containing a yellow marker dye which provides two benefits. Firstly, if an EBT2

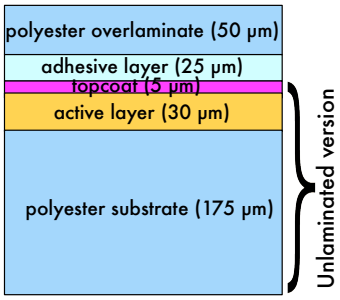

(a)

layer	thickness (μm)	density g/cm^2	ATOMIC COMPOSITION (%) H	Li	C	N	O	Cl	K	Br
Polyester overlaminate	50	1.35	36.4	-	45.5	-	18.2	-	-	-
Adhesive	25	1.2	57.1	-	33.3	-	9.5	-	-	-
Topcoat	5	1.2	56.9	0.9	25.7	-	15.6	0.9	-	-
Active layer	30	1.2	58.3	0.8	29.6	0.1	10.7	0.3	0.1	0.1
Polyester substrate	175	1.35	36.4	-	45.5	-	18.2	-	-	-

(b)

Figure 2.5 – (a) EBT2 film geometry: the geometry of the used unlaminated version is pointed out by the brace. (b) composition of EBT2 films: the composition of the unlaminated version is in the yellow rows.

film is measured on a colour scanner, the signal provided by the dye in the blue colour channel can be used to improve dose accuracy by adjusting for small differences in response over the area of a film. Secondly, the yellow dye protects the active layer from exposure by UV and visible light, reducing effect from these sources by about 10 times. Another difference from the previous EBT films is that the active part of the film has been reduced to a single layer about 30 μm thick, placed between a thin topcoat layer, 5 μm, and polyester substrate layer, 175 μm. The coated layers are: an over-laminated polyester layer, 50 μm and a pressure-sensitive adhesive layer, 25 μm. During my work for dosimetry of cell irradiation, I used a special edition of EBT2 films, where the polyester overlaminate and the adhesive layers were absent. This fact did not affect the functionality of the EBT2, but it was useful because of the very low beam energy, improving the detection of the particles. Figure 2.5 (a) shows the geometry of laminated and unlaminated EBT2 films and (b) shows their atomic composition, which is important in the simulation phase.

Like its predecessor, the response of EBT2 is dependent on orientation: all films must be irradiated and then scanned in the same orientation. The dose varies in the range $10^{-2} - 10$ Gy if the optical density is measured through the red channel and up to 40 Gy if it is measured through the green channel. Another characteristic is

that the EBT2 films develop in real time: there is no post-exposure treatment and the density changes stabilise rapidly after exposure, so that there is no waste of time between irradiation and scanning.

Before using the films in an experiment, it is necessary to find the relation between OD and deposited dose: the calibration. This has been possible using the 29 MeV proton beam accelerated by the cyclotron of the University of Birmingham and the ionisation chambers. After the beam energy characterisation (see section 2.1.2), several films (one at the time) were irradiated: a particular dose was deposited on each one of them. They were placed between the two chambers, with the topcoat layer touching the monitor chamber and the base substrate touching the Markus. The dose absorbed by the active layer of the film was calculated from the dose measured by the Markus chamber using the 2.2, where Ch_Q was the charge measured by the Markus chamber. k_{pos} was determined from a Fluka simulation:

$$k_{pos} = \frac{(D_{act.lay}/N_p)}{(D_{Markus}/N_p)} \tag{2.16}$$

where $(D_{act.lay}/N_p)$ is the dose measured in the active layer volume of the film normalised by the number of primary protons and (D_{Markus}/N_p) is the dose per primary absorbed by the air cavity volume of the chamber. One film at a time was irradiated and the dose measured from the Markus was varied in the range 0–14 Gy. Each film was then scanned using a CCD scanner (a Nikon Super Coolscan 5000) and the red channel extracted. In figure 2.6 an example of an irradiated film scanned in white light (a) and the extracted red channel (b) are shown.

Using the program ImageJ [53], it was possible to calculate the optical density: the average pixel value of the irradiated region of the films was measured and used to calculate the optical density according to 2.15, where $I = \overline{\text{pixel value}}$ and $I_0 = 65535$. The calculation of the background, i.e. the optical density in presence of non-irradiated film, was not needed, since it was just necessary to associate each

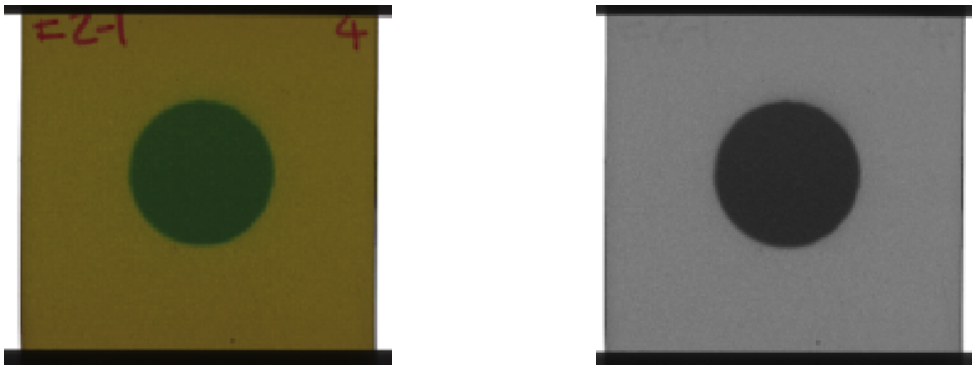

(a) (b)

Figure 2.6 – Irradiated and scanned film used for calibration: (a) in white light and (b) once the red channel was extracted. The dose absorbed by the active layer was estimate to be (7.48±0.12) Gy.

irradiated OD to the related film dose: a null dose was associated to the background. From figure 2.7 the relation (OD–dose) is visible in (a), but also the relation (pixel value–dose) in (b), which was simply obtained by relating each average pixel value to the calculated dose on the film. As it is visible from the graph in 2.7 (a) the OD of a non-irradiated film is ∼0.3 and from (b) the associated pixel value is ∼33000.

Once calibrated these films have been used in a radiobiological experiment involving laser-driven proton beams and V79 cells (see chapter 4). The dosimetry method applied has been developed specifically for this experiment taking into account the fact that the measured dose from the films was not exactly what the cells absorbed. Two corrections were required: one because of the fact that the films are LET dependent and the other because of the fact that films and cells did not have the same equivalent thickness and position with respect to the beam source (this correction is similar to k_{pos} used for the ionisation chambers).

Other types of film (HD-810, MD-55 and laminated EBT2) have also been calibrated for the LIBRA group using the described method. Once calibrated the films were used for dosimetry of LDPBs in several experiments at RAL.

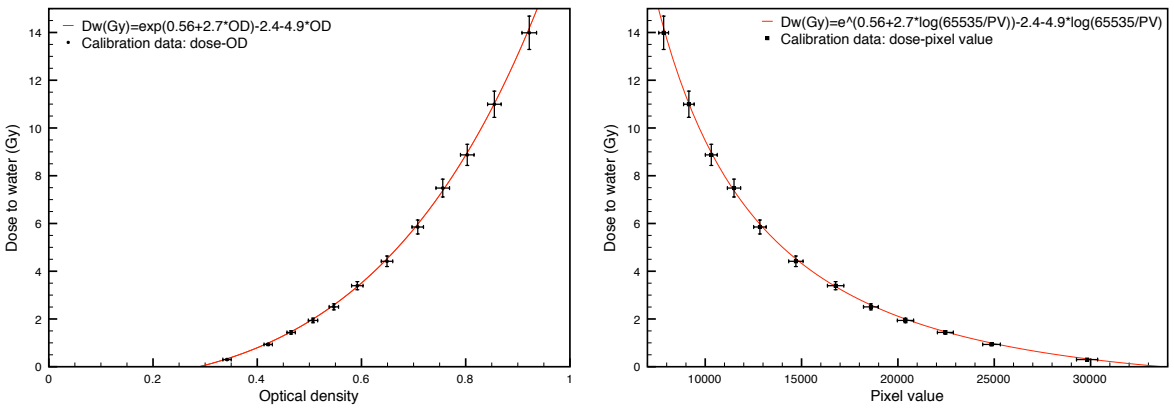

(a) (b)

Figure 2.7 – Calibration: (a) dose to water as a function of the optical density and (b) dose to water as a function of the pixel value.

2.3 THERMOLUMINESCENT DOSIMETERS

When a ionising radiation interacts with a thermoluminescent material, the electrons elevated from the valence to the conduction band are then captured at various trapping centres, due to the presence of impurities in the crystal. If the distance between the energy level of the trap and the conduction band is sufficiently large, there is only a small probability per unit time at ordinary room temperatures that the electron will escape the trap by being thermally excited back to the conduction band. For this reason, exposure of this kind of material to a continuous source of radiation leads to a progressive buildup of trapped electrons. Holes can also be trapped in a similar process: an original hole created by the incident radiation can migrate through the crystal until reaching a hole trap with an energy above the top of the valence band. If this energy difference is large enough, the hole will stop migrating and will remain locked in the trap unless an additional thermal energy is given to the crystal. Therefore, a TLD crystal will work as an integrating detector in which the number of trapped holes and electrons is proportional to the original number of electron-hole pair generated by the crossing radiation. Figure 2.8 (a)

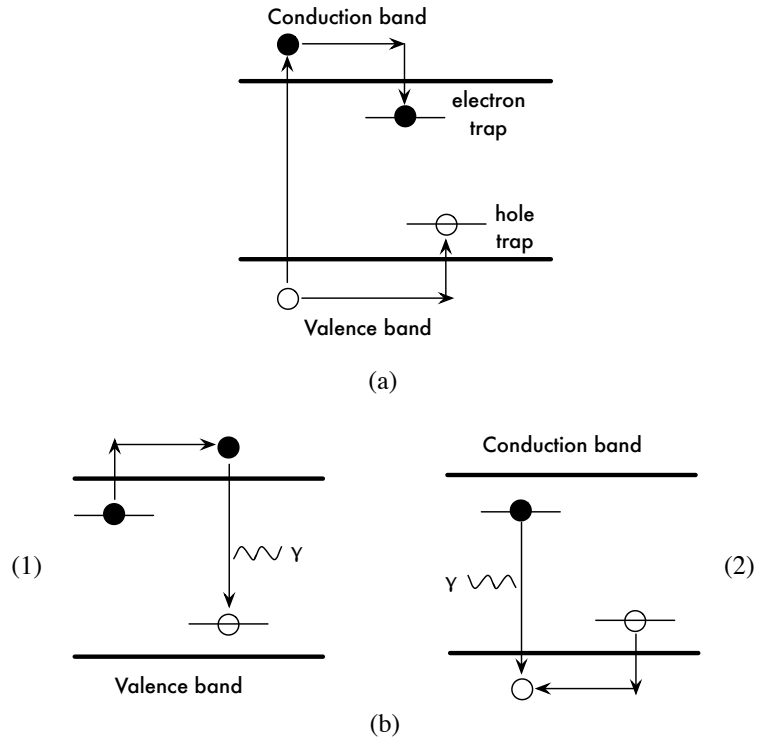

Figure 2.8 – Thermoluminescent process: (a) electron or/and hole trap, (b) two possible modes of recombination during temperature raising with consequent emission of a thermoluminescent photon.

shows the process of trapping holes and electrons.

After the exposure if the crystal is heated it is possible to have a measure of the deposited energy. The TLD material is placed in a heated support and its temperature progressively raised up to the temperature determined by the energy level of the trap: the trapped electrons acquire then enough thermal energy to be re-exited to the conduction band. Simultaneously this temperature, though, has to be low enough not to free the trapped holes, so that the liberated electrons migrating in the crystal can reach a trapped hole and recombine with the emission of a photon (see figure 2.8 (b) (1)). Alternatively the opposite process can happen: the holes are released at a lower temperature and migrating in the crystal can reach a trapped electron and recombine with the emission of a photon (see figure 2.8 (b) (2)).

In both the cases, in a TLD material the difference of energy is about 3 or 4 eV,

resulting in an emitted photon of visible light, which represents the TLD signal. The light yield is recorded as a function of the raising temperature in a glow curve (dependent on the TLD type). The signal related to the radiation deposition is the total number of emitted photons, obtainable by the area under the glow curve. This curve (intensity of the signal plotted against temperature) consists of a large number of overlapping peaks where each peak, in principle, can correspond to one or more traps. If subsequently the temperature is further raised all the traps are emptied and the sample is annealed, so that, even if TLDs have the disadvantage that the signal can be read only once, they can be reused many times for other exposures. The relation between the total signal read (usually amplified using a photomultiplier) and the energy absorbed by the crystal is determinable with a calibration process.

2.3.1 TLD 700

Several types of TLDs are on the market: the differences are on the composition of the crystal which results in a higher or lower sensitivity to the radiation. In some of them impurities are added as activators, in others the traps are created by the inherent impurities and defects in the crystal. The choice about which type to use has to be made carefully. If the energy levels of the traps are very near the edge of the bandgap, the number of trapped electrons and holes per unit exposure can be very large. This makes the material very sensitive to exposure (down to 10^{-7} Gy for $CaSO_4$:Mn), but also makes the traps unstable even at an ordinary room temperature. This kind of TLD can lose up to 85% of the trapped carriers over a few days. Other types of TLD like LiF: Mg,Ti, with deeper traps are better suited for longer term exposure, but the sensitivity will be several orders of magnitude lower.

In the case of our experiment with LDXrB, we opted for a lower sensitivity but a higher stability with the advantage that the dosimeter could be read without rush and without the necessity to make corrections due to signal loss. The choice went

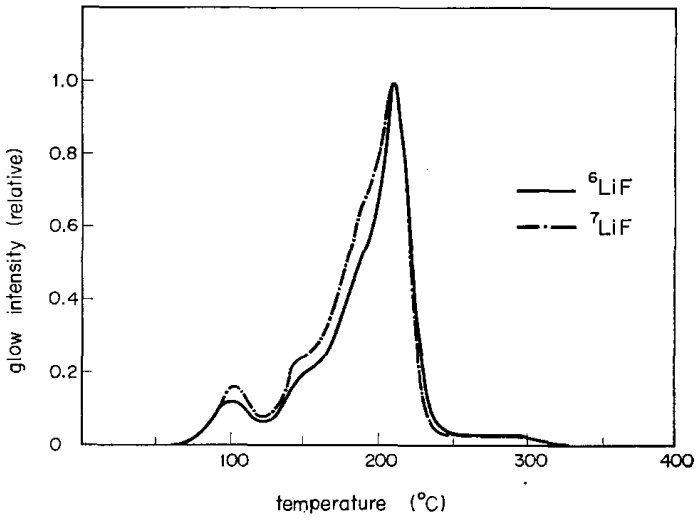

Figure 2.9 – Typical glow curve of TLD-600 and TLD-700 exposed to ^{60}Co gamma rays: the curves are normalised to the value of the main peak at 210°C. Image taken from [54].

on LiF:Mg,Ti and in particular on the type enriched with ^{7}Li (^{7}Li: 99.993% and ^{6}Li: 0.007%), also known as TLD-700 manufactured by Thermo-Fisher Scientific. The concentration of the impurities is 300 ppm of Mg, added to serve as the primary trapping centres, and 11 ppm of Ti added to provide luminescent recombination centres at which the detrapped electrons and holes recombine after being released from the trapping centres during the readout process. The useful range of this TLD type is 10 μGy–10 Gy, with a fading factor of 5% per year after exposure. The typical TLD-700 glow curve is shown in figure 2.9 (a), where it is compared with the glow curve of TLD-600 (^{6}Li enriched TLD) [54].

The heating/reading and annealing process was structured as follow: after the exposure the TLD chips were placed on a reader (figure 2.10 (a)) where the temperature was increased up to 270°C. The actual signal acquisition was between 180°C and 260°C. Afterwards the TLDs were placed in a metal case (see figure 2.10 (b)) and annealed in a TLD oven (figure 2.10 (c)): the heating process lasted about 12 hours, during which the temperature was increased with a velocity of ∼5°C/s up to 400°C, kept it constant for one hour, quickly decreased it to 80°C, kept it constant for

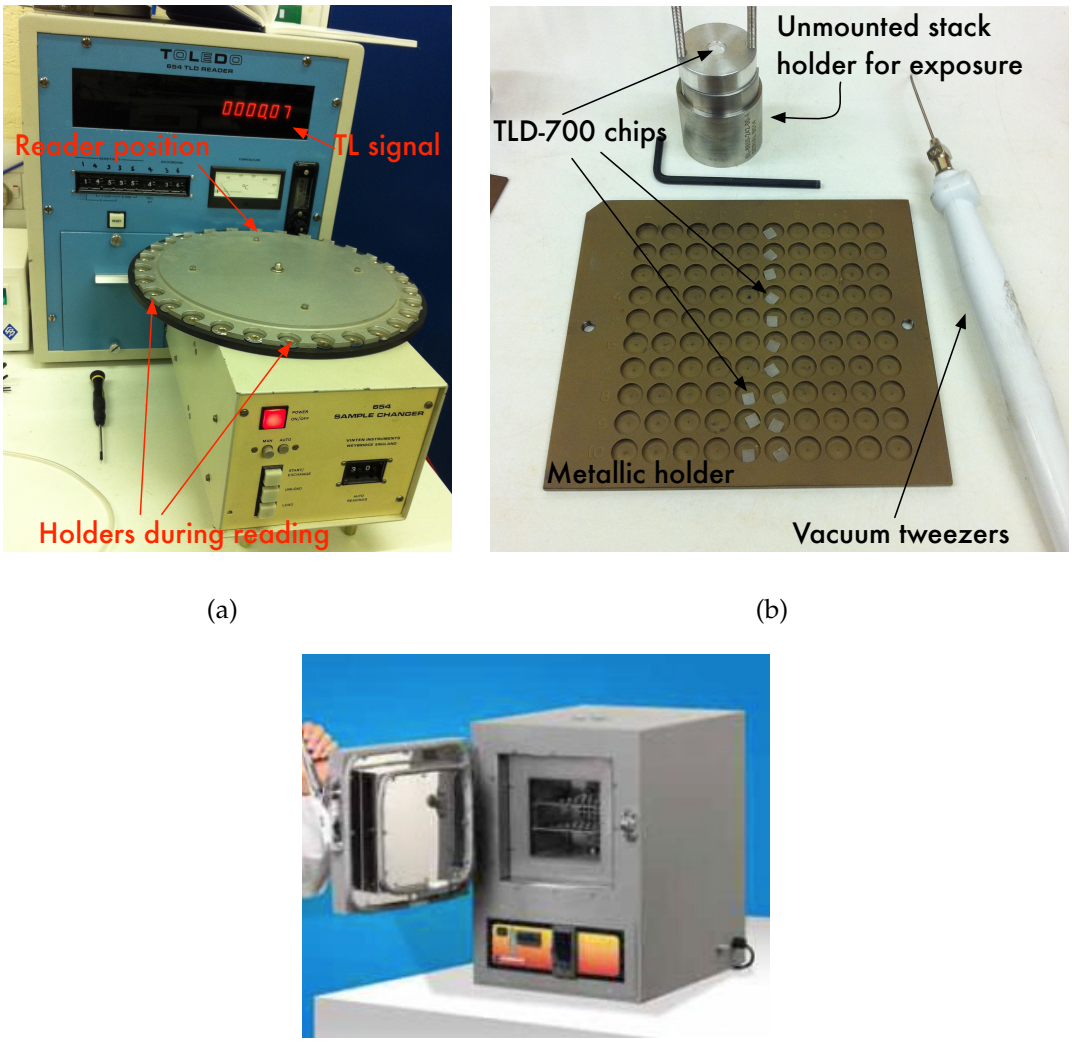

(a) (b)

(c)

Figure 2.10 – Experimental instruments: (a) TLD reader, (b) TLD-700 chips in the holder used for storing and annealing and (c) annealing oven.

8 hours and then decreased to room temperature. The presence on the glow curve of other peaks between 250°C and 400°C is the reason why the annealing has to be done up to 400°C: once this temperature is reached, all the traps are emptied. The other steps in temperature are instead due to the choice of preferring or not preferring the sensitivity of some peaks in the glow curve. The fast cooling rate from 400°C to 80°C is used to prevent the loss of sensitivity of the main peak (at 210°C). The long time at 80°C is used to reduce the contribution of the smaller peaks at

lower temperatures: this step is important if it is considered that only the signal between 180°C and 260°C is acquired for dosimetry [55]. Handling was always using vacuum tweezers: mechanical tweezers or fingers have to be avoided because small scratches, loss of mass or foreign deposits affect the light emission.

As in the case of Radiochromic films, TLDs are LET dependent: not only the dose response varies with the type of particle crossing the material, but also it changes with the particle energy. In the case of photon exposure, what was explained for EBTs is also valid for TLDs, but the effect is opposite since Z_{eff} is this time higher than that of water (for LiF: Mg,Ti $Z_{eff} = 8.2$). This causes an over-response for low energy photons which, according to some papers in the literature [56, 57, 58], for energies lower than 30 keV can even reach 50% of the response obtained in the calibration. Unfortunately, many of the papers quantifying this over-response give a different result and very poor uncertainty quantification. Our TLD batches were calibrated by AWE using ^{60}Co and for comparison the graph shown in figure 2.11 (a) taken from [59], gives the response relative to the response obtained for ^{60}Co exposure. This graph, showing a relative response higher than 1.4 at 30 keV, is in contrast with what is reported in the manufacturer paper where the relative response is 1.25 at that same energy.

For electron exposure the effect is seen to be almost opposite [55]: the relative response is constant at 1 until 0.5 MeV [61], then it decreases down to 0.87 at 2 MeV (lowest relative value in literature is 0.87 for 2.03 MeV), then the response starts increasing reaching 1 at ∼20 MeV as explained in [62]. In case of heavier charged particles and neutrons important references are [60, 63, 64].

The signal from X-ray and electron exposure remains linearly related to the dose up to about 4 Gy, but it can be considered to be linear up to 100 Gy (see figure 2.11 (b)). At higher doses LiF: Mg,Ti displays a nonlinear increase in response per unit exposure, a behaviour known as supralinearity, before it saturates at even higher

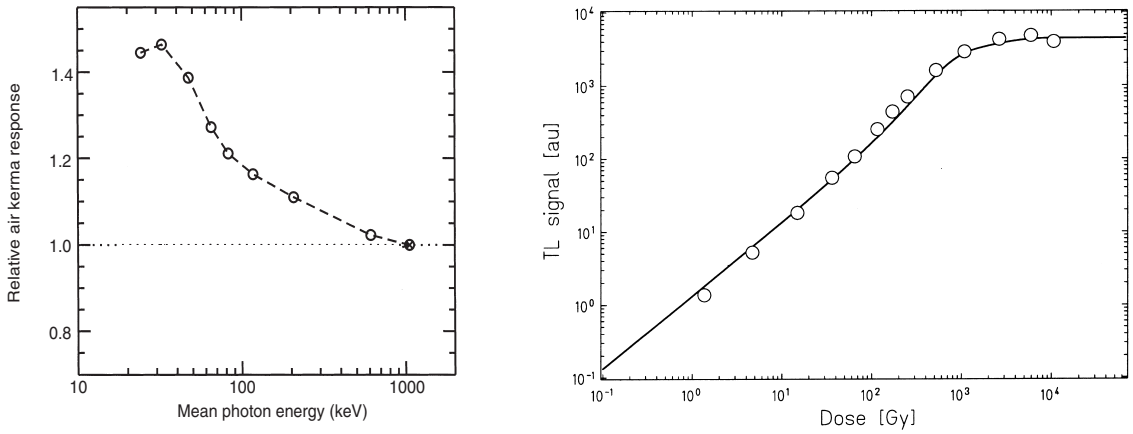

(a) (b)

Figure 2.11 – (a) LiF: Mg,Ti energy response to X-ray exposure normalised to the signal acquired for ^{60}Co exposure. Image taken from [59]. (b) Dose response for X-ray exposure: the supralinearity is well visible above 100 Gy. Image taken from [60]

doses [60]. This linear-supralinear dose response is explained to be an effect of competition between charge recombination with and without emission of light.

The dose-rate dependence is seen to be linear at least up to 10^6 Gy/s for electron and X-ray exposure [65]. At higher dose-rates the response seems to decrease by at least 11% for 3.6×10^9 Gy/s, but further studies should be done to accurately describe this dependence

As already mentioned the calibration data were taken by AWE using ^{60}Co. In figure 2.12 the data from AWE are shown as well as the linear best fit. The background, acquired from non irradiated TLD chips, was subtracted from the light signal values of the irradiated TLD chips, so that the best linear fit does not show a y-intercept value. The calibration equation is: $\mathrm{D(mGy)} = (0.99 \pm 0.02)\mathrm{LS}$, where LS is the acquired light signal. This relation was uploaded in the TLD reader, so that it could directly give the dose in mGy. As can be seen from figure 2.12 the maximum γ dose is 0.25 Gy, which is below the threshold where the linear response becomes supralinear. During the experiments at RAL the maximum acquired dose

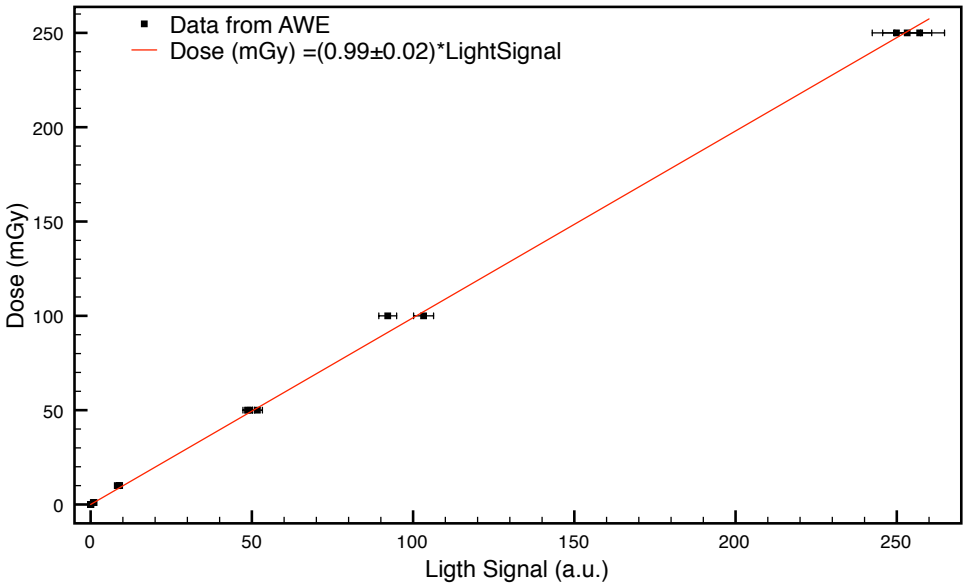

Figure 2.12 – TLD-700 calibration: the data come from AWE and the calibration linear fit is here shown.

was ∼20 Gy, which is still below the point where the dose response can no longer be considered linear.

2.4 NUCLEAR ACTIVATION

The energetic particles accelerated by a laser can induce nuclear reactions in the primarily laser-irradiated target and in secondary activation samples positioned on the beam path. Given the low reliability of the commonly used detectors to the high dose rates of the LDPB, since the first laser experiments, nuclear activation has been used to characterise the flux, the angular and energy distributions of the produced beams. Several examples can be found in literature [10, 7, 66, 67, 68, 69]. One of the results of the interaction is the fusion of projectile and nucleus target with the creation of a compound nucleus that de-excites emitting evaporation particles: α, protons, neutrons and/or photons. If the evaporation residues (the nuclei remaining after the evaporation emissions) are not stable isotopes, they decay emitting γ and β radiation. Detecting these decay particles, it is possible to obtain information about

the reactions occurred in the foil and thus about the particles accelerated by the laser which produced such reactions.

In the published literature, activation foils were usually used in stacks, so that the incident particles with their broad energy spectrum could interact with the foils and reveal from their origins their highest and lowest energy. In case of heavy ions, the procedure can be tougher: a stack of foils cannot be used because of the ions' much shorter range (considering also that usually the accelerated ion beams have low energy), so the solution is the use of a composite foil. Multiple reaction channels will occur in the foil depending on the incident ion energy [10].

This type of detection method has been preferred over the other detection instruments because under the right conditions (incident particle energy greater than the Q value of the reaction of interest) it can always be used without losses due to dead time (scintillators) or other saturation and recombination processes (RCF films and ionisation chambers). It can in principle be used with any accelerated ion beam if the cross section for production of the parental emitting radioisotopes is known. On the other hand, the reconstruction of the initial particle spectrum is complex and always requires careful considerations in the choice of the foil (or foils) in order to be able to correctly reveal the characteristics of the incident beam (as explained in chapter 5). Another drawback of the method is that the activated sample has to be removed from the interaction chamber and analysed using either a γ or α or β detector and, depending on the chosen radioisotopes' half life, it also requires more or less long counting times causing delay in the measurements.

This section has been inserted in this chapter as a continuation in the list of explanations of the detection methods used during my Ph.D. work. It is an anticipation of what is described in chapter 5, where the method and the tests using a proton beam accelerated by the cyclotron of the University of Birmingham are illustrated in much more detail.

2.5 CALORIMETERS

An ionising particle interacting with matter creates a cascade of less energetic secondary particles which eventually recombine liberating energy. This energy is partially converted to heat and can be measured as a rise of temperature. The technique of deriving the dose from a measurement of temperature rise is called calorimetry. The equation expressing the relation between heat and deposited energy is:

$$D = \frac{\Delta E}{\Delta m} = \frac{C}{\Delta m}\Delta T \tag{2.17}$$

where D is the dose in Gy, ΔE the deposited energy in J, Δm the involved medium mass in kg, C the specific heat capacity at constant pressure in J/K and ΔT the measured rise temperature in K. In the case of real calorimeter there will always be defects in the construction or dissipating objects (such as gaps, glue, wires and thermistors for the measurement of the temperature) causing a deviation from the dose that should have been measured for an homogeneous calorimeter. These deviations also called dose correction factors have to be taken into account in 2.17:

$$D = \frac{C}{\Delta m}\Delta T \prod_{i=1}^{n} k_i \tag{2.18}$$

and are evaluated either during the calibration process simply calculating the ratio between the real obtained dose and the dose that could have been measured using an homogenous calorimeter (with the same mass of the real instrument) or mathematically. In order to ensure accurate measurements, the heat insulation must be perfect and the system must operate adiabatically. This is quite simple in the case of LDPB, because the calorimeter would be placed in the vacuum interaction chamber, so that any change in temperature can be directly attributed to the incoming radiation. The rise in temperature is measured with thermistors, whose resistance varies

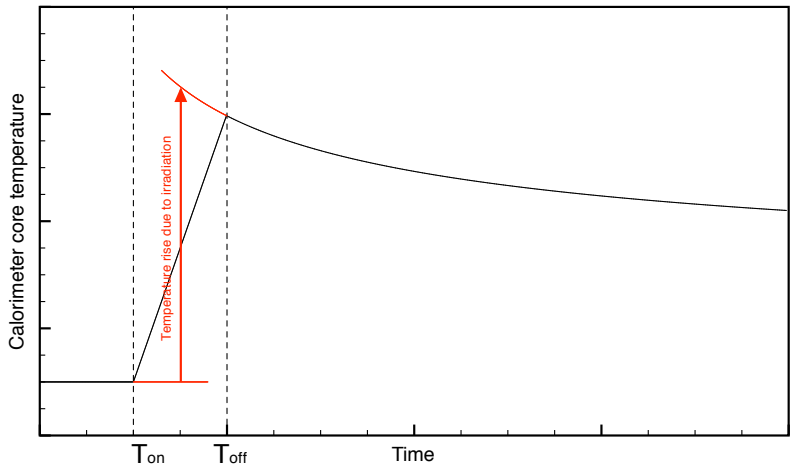

Figure 2.13 – Temperature measurement of the calorimeter core before ($t < T_{on}$), during ($T_{on} < t < T_{off}$) and after ($t > T_{off}$) irradiation.

with temperature. The usual measurement process due to irradiation is shown in figure 2.13 as a function of the time.

So far, no contraindications have been found for calorimeters to be used in LDPB: they should not be affected by the high dose-rate and there should not be saturation for high doses.

2.6 Other detectors used for LDPBs

So far, I have described the main characteristics of the commonly used detection instrument in use for radiotherapy and explained why some of them can be used for LDPB and why some others cannot. To summarise: ionisation chambers cannot be used for their high recombination in presence of high dose-rate; RCF can be used for dose up to 10 kGy applying LET corrections; TLD can be used up to 1–10 kGy being careful to the supralinear effect and to the LET response; calorimeters can in principle be used, but a test is still to be done to ensure that there are no corrections to be made in case of LDPB.

Other detectors can also been used, some of them with restrictions (such as Thomson Parabolas, CR-39, image plates) and others are in an evaluation phase

(such as plastic scintillator).

A Thomson parabola is a spectrometer consisting of electric and magnetic fields which are oriented perpendicular to the beam propagation direction. Inside the parabola, ions are deflected due to their charge-to-mass ratio, so that different isotopes can be visualised separately on a E–B graph. In the case of accelerated ion beams this instrument is of vital importance to determine the species of the accelerated particles [12], but it has the disadvantage of being a large object with a small acceptance solid angle ($\sim 10^{-5}$ sr). Consequently, it is not able to measure the overall ion flux, given that the ion expansion profile is usually not so narrow.

CR-39 is a polymer ($C_{12}H_{18}O_7$) that has been widely used as a passive, limited spectral resolution, solid state nuclear track detector. It interacts with hadrons and is insensitive to gamma or electron radiation. When a heavy charged particle crosses the detector, it causes a trail of damage along the track in the form of broken molecular chains and free radicals.The amount of local damage along the track is related to the local rate at which energy is lost by the particle, the length of the track is the range of the particle in the plastic and its diameter provides a measure of the dE/dx. Since dE/dx is different for particles of the same type but different energies, the diameter provides a measure of incident energy. dE/dx is also different for different particle types, so diameters can often be used to identify the particle type if the energy is known. In the case of LDPB, this polymer has been used mostly because of its non-reaction to photons and electrons but because of the high intensity of LDPB, irradiating CR-39 is not the best choice to take. Even if recognition of each single particle in this field is not strictly necessary (as it could be the case of very low reaction rate processes where CR-39 is widely used [70]), the higher probability to accelerate protons than ions from laser irradiated targets, makes the ion identification poor, since the radiation damage in the plastic will be dominated by damage mainly produced by protons. For this reason in case of LDPB, CR-39 is usually used

in conjunction with absorbers to stop the lower energetic particles as in [71], or to detect the particles in regions of space where their intensity is not so high [72].

Image plates (IPs) consist of an active layer of barium fluorohalide phosphor crystals [BaF(Br,I):Eu^{2+}] inserted in a plastic supportive medium. When the phosphor absorbs a photon, it promotes electrons from Eu^{2+} ions into a metastable state where they remain trapped into lattice defects appositely introduced during the manufacturing process. The trapped states will decay in a time depending on temperature and the chemical composition of the IP. Alternatively they can also decay if illuminated by light at 632.8 nm, which is the method used to read IPs in a scanning system and extract the stored data. When the metastable state decays, blue light at 400 nm is emitted and detected using a photomultiplier tube. The information stored on the IP can then be completely erased (i.e., all the Eu^{2+} ions return to their ground state) through further optical illumination to white light, allowing the IP to be reused in future irradiations. IPs have been tested for dosimetry of conventionally accelerated clinical proton beams [73, 74] and an LET dependence of the dose response has been shown. With regard to LDPBs, IPs are currently used to give 2D beam profile [75, 76], but their implementation for dosimetry is still in progress.

Characterisation of plastic scintillators has been performed by some LIBRA members using the cyclotron of the University of Birmingham. Several different scintillator samples were irradiated using a quasi mono-energetic proton beam, producing response curves describing the relationship between light output and proton energy from 2 to 28 MeV [77]. The test has recently been extended to the combined use of different scintillators in the same irradiation: the data is currently being analysed. Further tests need to be done to extend the study to high dose-rates.

Tables in figure 2.14 and 2.15 show a summary of active and passive detection instruments. Pros, cons and limitations are listed, as well as the main reasons why they can or cannot be used in presence of LDPB.

ACTIVE DETECTOR	Pros	Cons	Usable for direct dose measurements?	Dose range (Gy)	Dose-rate range (Gy/s)	Usable during cell irradiation?	Energy range	Different signal with different incident beam?	Usable with LDPB?	if yes, which are the most important limitations?
Ionisation Chamber	usable for calibration, high accuracy, instant readout, no need to be replaced after irradiation to have reading	high recombination for high dose rate or high LET, several corrections to be applied,	Yes (with corrections)	10^{-8} - 10^{5}	< 1	Yes	variable with the type	No	No	-
Plastic Scintillator	linear response with flux, no temperature correction, no direction dependent, long term stability, instant readout, no need to be replaced after irradiation to have reading	scaling non linear with particle energy, difficult spectrum reconstruction	No	-	10^{-3} - 10^{5}	No	variable with the type	No	Possibly	Method of use still in process of evaluation for LDPB
Calorimeter	total beam energy measured, instant readout, no need to be replaced after irradiation to have reading	total beam energy measured, difficult spectrum reconstruction	Yes	10^{-1} - 10^{6}	10^{-2} - 10^{6}	No	Any	No	Possibly	Method of use still in process of evaluation for LDPB
Semiconductor detector	high accuracy, instant readout, online data measurements, no need to be replaced after irradiation	possible damage with high current, temperature and energy dependent, sensitivity changes with dose accumulation, directional dependence, calibration required periodically, expensive	No	10^{-6} - 10^{2}	10^{-9} - 10^{6}	No	Any	No	No	-
Tomson Parabola/MCP	Charge and mass particle determination, single particle detection, high repetition rate detector, fast time response ~ ns, instant readout, no need to be replaced after irradiation to have reading	expensive and space consuming	No	-	-	No	Study in progress, but it depends on the applied electric and magnetic fields	Yes	Yes	Small acceptance solid angle (10^{5} sr)

Figure 2.14 – Table of active detectors commonly used: pros, cons and limitations are listed, as well as the motivations why they can or cannot be used in presence of LDPB.

PASSIVE DETECTOR	Pros	Cons	Usable for direct dose measurements?	Dose range (Gy)	Dose-rate range (Gy/s)	Usable during cell irradiation?	Energy range	Different signal with different incident beam?	Usable with LDPB?	if yes, which are the most important limitations?
RCF	2D dosimetry, readout repeatable, cuttable in any shape, several types available in dependence on the dose level	several corrections to be applied, needed calibration for each batch, LET dependence, need to be replaced after each irradiation, possible saturation at high doses, some time needed before data processing, complex spectrum reconstruction.	Yes (with corrections)	10^{-3} - 10^{4}	study in progress	Yes	Any	No	Yes	possible saturation with high doses
TLD	various types and forms available	LET dependence, signal erased during readout, long readout/erasion/calibration, needed calibration for each batch, complex spectrum reconstruction, need to be replaced after each irradiation.	Yes (with corrections)	10^{-6} - 10^{4}	10^{-11} - 10^{5}	Yes	Any	No	Yes	possible saturation with high dose
Image Plate	cuttable in any shape	difficult spectrum reconstruction, need to be replaced after each irradiation, LET dependence.	Yes (with corrections)	?	?	?	?	No	Yes	so far used only for 2D beam profile
CR 39	if the particle energy is known, it is able to distinguish different particle types, if the particle type is the same then it is possible to distinguish different energies, signal in the detector does not degrade with time, cheap	background varies from batch to batch, from foil to foil in the same batch, from one side to another of the same foil and within the same foil surface, advantageous in experiments where emissions occur sporadically or at low fluxes, limited spectral resolution.	No	-	-	No	?	Yes	it is used, but with flux limitations	only for low flux reactions
Nuclear Activation	usable with any dose-rate	needed secondary detector to measure gamma spectrum from foil, cross section reaction to be known, complex spectrum reconstruction, need to be replaced after each irradiation.	No	Any	Any	No	$E_{beam}>E_{threshold}$	Possibly but complex	Yes	$E_{beam}>E_{threshold}$

Figure 2.15 – Table of passive detectors commonly used: pros, cons and limitations are listed, as well as the motivations why they can or cannot be used in presence of LDPB.

CHAPTER 3

A BRIEF INTRODUCTION TO FLUKA

The Monte Carlo code extensively used throughout the thesis is Fluka (FLUctuating KAskad), a code for calculations of particle transport and interaction with matter [46, 45]. It covers an extended range of applications: radiation shielding, calorimetry, activation, accelerator driven systems, dosimetry, radiotherapy, detector design, cosmic rays, neutrino physics etc. The success of this program is in the improvements that the authors make to the code to update it with the most modern physical models and data. Microscopic models are adopted whenever possible and if experimental data are available the simulation results are always benchmarked. "As a result, final predictions are obtained with a minimal set of free parameters fixed for all energy/target/projectile combinations... Predictivity is provided where no experimental data are directly available, and correlations within interactions and among shower components are preserved" (cit. [46]).

Fluka can handle complex geometries using the Combinatorial Geometry (CG) package. So far the Fluka CG has been designed to correctly track particles also in

the presence of magnetic fields, however, electric fields are currently not supported. Elements, when not available among the default ones, can be easily created and merged to each other to create complex materials. For the simplest applications, no programming is required from the user. However several user interface routines (written in Fortran77) are available and can be modified by the user for special requirements, such as the creation of peculiar beam sources or particular scorings (examples of this are given in chapter 6 and 7).

Fluka can accurately simulate the interaction and propagation in matter of 62 different particles. In table 3.1 the energy limitations in the particle transport are listed.

Particle	As primary particles	As secondary particles
charged hadrons	100 keV to 10 PeV	1 keV to 10 PeV
heavy ions	100 MeV/n to 10 PeV/n	10 MeV/n to 10 PeV/n
neutrons	thermal to 10 PeV	thermal to 10 PeV
antineutrons	10 MeV to 10 PeV	1 keV to 10 PeV
muons	100 keV to 1 PeV	1 keV to 1 PeV
electrons	30 keV to 1 PeV	1 keV to 1 PeV
photons	7 keV to 1 PeV	1 keV to 1 PeV

Table 3.1 – List of energy thresholds for particle transport in Fluka, with the differentiation for primary particles (incident beam) and for secondary particles.

The difference between Fluka and other Monte Carlo codes is mainly in the improved hadronic nuclear interactions and in the nucleus-nucleus interactions. Since these are the most important processes when proton and ion beams interact with matter, the code is ideally suited to describe such experiments. In this thesis, this is the case for the simulations of the proton beams irradiating the cells in chapter 4 or the foils for nuclear activation in chapter 5. With regard to the electron and photon beams simulated in chapter 6 and 7, Fluka has been chosen not only for the improved multiple and single scattering model, but mainly because of the clarity with

which the routines can be written and implemented in the program.

A brief introduction to the packages used in Fluka to describe hadronic and electromagnetic interactions relevant for the work described in the thesis follows in the next sections.

In any case, for a complete description of Fluka it is best to refer to the manual [46] and to all the references contained therein.

3.1 HADRON-NUCLEON AND HADRON-NUCLEUS INTERACTIONS

The Fluka hadron-nucleon interaction models are based on resonance production and decay for energies below a few GeV, and on the Dual Parton model for energies above. The same models are used also in hadron-nucleus interactions. For momenta below 5 GeV/c the PEANUT (PreEquilibrium Approach to NUclear Thermalization) package includes a very detailed Generalised Intra-Nuclear Cascade (GINC) and a pre-equilibrium stage, while at high energies the Gribov-Glauber multiple collision mechanism is included in a less refined GINC. Both modules are followed by equilibrium processes: evaporation, fission, Fermi break-up, gamma de-excitation of the residual nucleus (all these reactions are quickly explained in section A.2). Light residual nuclei are not evaporated but fragmented into a maximum of 6 bodies, according to the Fermi break-up model.

Multiple Coulomb scattering is implemented as well as ionisation fluctuations. Bethe-Block theory together with Barkas and Block corrections are used and delta-ray production can be easily activated by the interested user.

For elastic scattering processes, parameterised and tabulated nucleon-nucleon and nucleon-nucleus cross sections are used.

3.2 NUCLEAR ACTIVATION

The first Fluka code, FLUKA86-87 was a specialised program to calculate shielding of high energy protons for accelerators. The actual version has been adapted and developed for an extended range of applications and it is not any longer limited to protons, but its primary aim demonstrates how the activation feature has always been one of the main highlighted characteristics of the program.

Nuclear activation can be activated in Fluka using an apposite card called RADDECAY. This card can also activate the isomeric production, but since the present models do not distinguish among ground state and isomeric states only a rough estimate (equal sharing among states) of the production of isotopes in ground and isomeric state will be given (see examples in section 5.1.2 and Appendix B). There are several ways to score the produced residual nuclei, but the important fact to underline is that the entire process involving the generation and then the transport of decay particles or radiation is today obtainable in one single simulation, the same which produces the radio-nuclides. This has been possible using decay emission databases written appositely for Fluka using information from the NNDC (National Nuclear Data Center of the Brookhaven National Laboratory) and in some cases, when explicit data were not available, models have been used. However, this does not always create the best simulation results, as demonstrated in chapter 5 where cross sections of production of Indium from Copper at proton energies lower than 15 MeV are not in agreement with the cross sections in literature. The same has been found (but not reported in this thesis) for Nickel and Iron reactions with protons at the same low energies. This is because the models calculating the cross sections in Fluka have been written according and compared to experimental data mainly for particle energies relevant to radiological studies at CERN, where the energies usually are much higher than those used in this thesis.

Residual nuclei (and so radionuclides) are calculated in Fluka directly from the

inelastic hadronic interaction models, with the only exception of low-energy neutron interactions (E lower than 19.6 MeV), where tabulated data are used. A benchmark of these models with experimental data of radionuclide production is always required for a validation, but as already mentioned, the primary importance has been given to the benchmark of the high energy reactions. For momenta below 5 GeV/c, PEANUT is the package characterising nuclear interactions; beyond 20 TeV and for nucleus-nucleus collisions the involved packages are DPMJET [78], RQMD [79] and BME [80, 81] (respectively Dual Parton Model with jets for energies between 5 GeV/n and 10 PeV/n, Relativistic Quantum Molecular Dynamics Model for energies between 100 MeV/n and 5 GeV/n and Boltzmann Master Equation for nucleus-nucleus reaction at energies lower than 100 MeV/n) useful to describe the reactions explained in section A.2.

In a paper by Brugger et al. [82], the cross sections of production of 103 isotopes (created by the interaction of high energy protons and iron or copper) calculated by Fluka were compared for validation with experimental data taken from the literature. While it was possible that some experimental data were not always consistent (particularly for energies above few GeV), the ratios between the cross sections calculated with Fluka and the experimental ones ranged between 1.1 and 0.3, showing that Fluka results can sometimes be unreliable.

3.3 Electrons and photons

Complete multiple Coulomb scattering is implemented for all charged particles, while for low energy electrons a further switch to single scattering is available for energy close to 30 keV. Delta-ray production via Bhabha scattering, positron annihilation, electrohadron production, bremsstrahlung differential cross sections and angular distribution of bremsstrahlung photons are all reactions sampled accurately for electrons.

For photons, the following interactions are accurately implemented in Fluka: pair production with the calculation of the angular distribution of electrons and positrons, Compton effect with Doppler broadening, photoelectric effect, Rayleigh effect, photon polarisation for Compton, Rayleigh and photoelectric effects and photonuclear interaction including the giant dipole resonance.

CHAPTER 4

DOSIMETRY OF LDPRB USING GAFCHROMIC FILMS AND FLUKA SIMULATIONS

While many efforts are employed to improve the characteristics of the laser-driven beams to adapt them to the requirements of a cancer therapy treatment, so far, only a few studies have been carried out to understand whether the high dose rate of these beams might cause different biological consequences from the well known effects of conventionally accelerated ion beams [83, 84]. In these previous experiments, the total dose on the cells was obtained by using multiple laser shots: the total dose was the results of several consecutive irradiations. Knowing that the biological effectiveness (and so the survival curve) changes in the presence of fractionated irradiations, in particular if the time between two consecutive irradiations is close or higher than the cell repair time, it is obvious that to obtain the absolute effect of these beams with their characteristic pulse duration on cells, the total dose needs to be delivered in single laser shots.

In this chapter I describe a dosimetry procedure using Gafchromic films and Fluka simulations, using a radiobiological experiment to better describe the steps to follow. This procedure includes the use of a magnet (or a system of magnets) to have charge and energy separation of the laser-driven beam, Gafchromic films to have information on dose and partially on energy, and a Monte Carlo code to expand the measured data in order to obtain specific details of the proton spectrum on the cells. Two specific correction factors need to be calculated: one to take into account the variation of dose response of the films as a function of the proton energy and the other to obtain the dose to the cell layer starting from the dose measured on the films. The results of the experiment are here reported and discussed as a proof of the feasibility, not only of the developed dosimetry method, but also of the laser-driven acceleration as a source for particle therapy. A paper including only the survival results of the experiment has been published in the AIP Advances Journal [85]. The method, published in the Physics in Medicine and Biology Journal (Fiorini et al 2011 [86]), is explained in this chapter, and given its complexity it is also briefly summarised in the last section of the chapter.

The experiment described has been conducted using the Terawatt Apparatus for Relativistic and Nonlinear Interdisciplinary Science (TARANIS) laser at Queen's University of Belfast, but the used dosimetry method can be applied to any other high power laser-driven ion accelerator.

4.1 Radiobiological experiment

The radiobiological experiment was performed during the summer of 2010 using the TARANIS laser. The laser part of the experiment was carried out by the Laser Physics Group of the University of Belfast, the biology part was carried out partially by the University of Belfast and partially by the University of Surrey, and the dosimetry part was conduct by the Medical Physics Group of University of Birm-

ingham (by me in particular).

4.1.1 EXPERIMENTAL SETUP

TARANIS [87] is a Ti:Sapphire-Nd:glass laser working at a wavelength of 1053 nm with a pulse duration of 500 fs and a beam energy up to 20 J. During the experiment the laser, focused onto a 12 μm thick aluminium target, deposited on the target an energy of ∼5 J, leading an intensity of the order of 10^{19} Wcm^{-2}: through the TNSA mechanism a beam of protons (but also photons and electrons) was produced with a divergence of $\sim 20°$.The resultant typical broad spectrum is shown in figure 4.1.

The overall experimental setup is illustrated in figure 4.2, where the red beam represents the TARANIS laser focused onto the aluminium target. A collimator (500 μm wide aperture) was used to select only the low divergence particles and, also, to maintain as low as possible the irradiation time (∼ ns). Subsequently, a dipole magnet of 0.9 T, was used both to discriminate between accelerated electrons and protons and to partially resolve the proton energy spectrum. At a distance of 14 cm from the magnet, a 50 μm thick mylar foil was used as a chamber window.

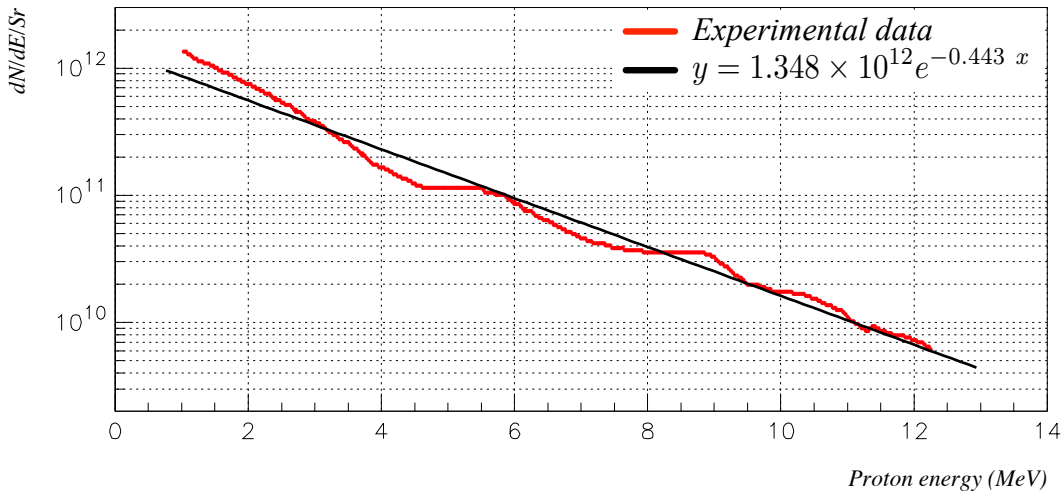

Figure 4.1 – Typical spectrum of the proton beam accelerated by the TARANIS laser. Experimental data provided by the laser group of the Queen's University ofBelfast.

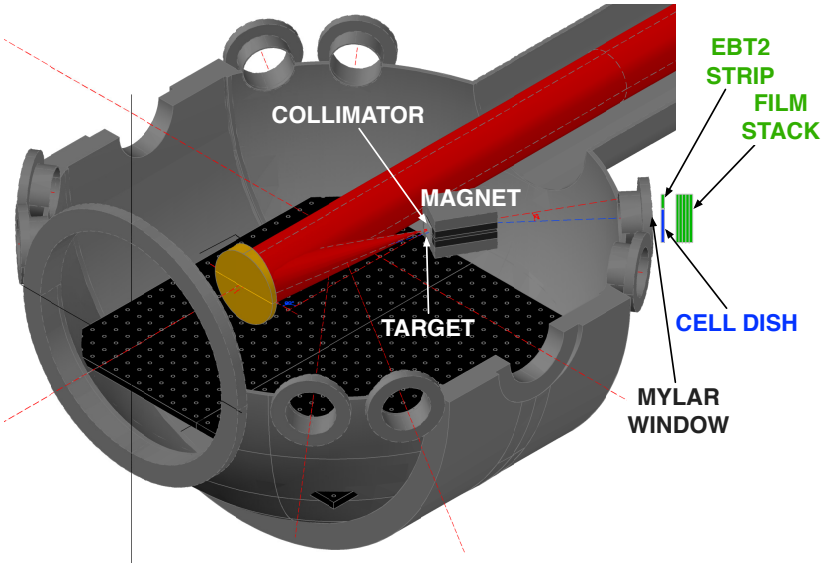

Figure 4.2 – Section of the experimental setup. In the vacuum chamber are visible: the laser beam in red, a parabola used to focus the laser beam on the Al target in yellow, a magnet used to discriminate between accelerated electrons and protons and to partially resolve the proton energy spectrum. A mylar foil was used as a vacuum window. Outside the chamber, in air, are shown: the cell dish, a film strip and a stack of films.

The dish, containing some medium and a cell monolayer, and the films, were placed vertically in air and parallel to this window.

Heavy ions were unlikely to be accelerated, in fact while in principle TARANIS can accelerate Al, C or O (the last two from contaminants), the acceleration of these species via TNSA is very inefficient, as the more mobile protons screen out the accelerating field from the other species. A relevant reference is the paper by Hegelich et al [88]. In our case the ion energy would have been lower than 4 MeV and the mylar window would have completely stopped all the accelerated ions, so that none of them could have reached the cells.

The angle between the normal to the vertical face of the magnet and the normal to the window could be varied to select the energy of the protons which perpendicularly irradiated the dish. A first configuration sees that angle fixed at 12 degrees, which allowed ∼6 MeV protons to perpendicularly strike the dish and the films (see figure 4.3). Another configuration was also used to allow ∼3.6 MeV protons to per-

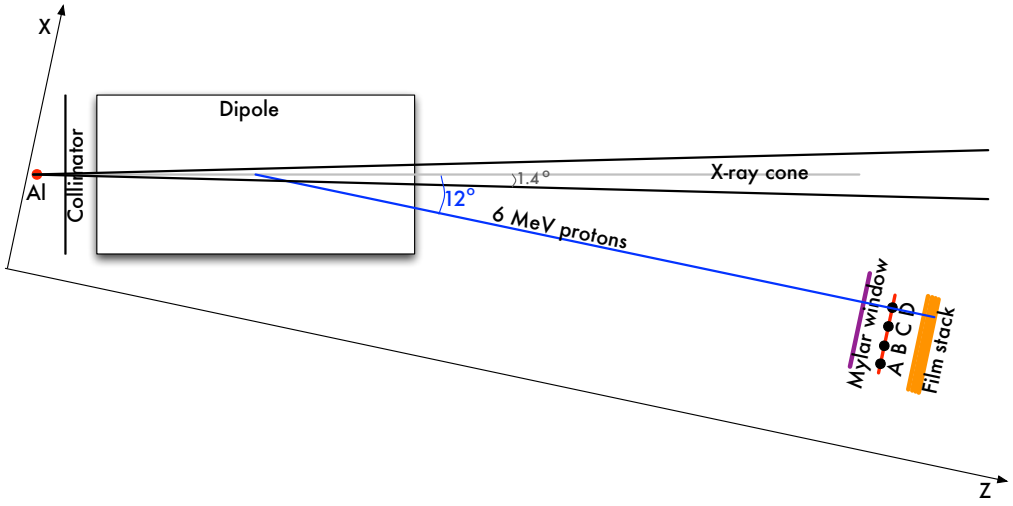

Figure 4.3 – Schematic view of the effect of magnet and collimator on the accelerated X-ray and proton beams (in scale).

pendicularly strike the cell dish. Moreover having used a magnet, electrons and the X-rays accelerated by the laser could not reach the cells: the electrons being deviated in the opposite direction and the X-rays continuing straight in the cone defined by the collimator aperture (as in figure 4.3).

The V79 cells were left to grow on a thick plastic foil which at the time of irradiation was cut in 3 mm diameter circles. Then, the cell dish was made inserting these circles between two 3 µm thick mylar foils. For the majority of the cases the average thickness of the cell monolayer and some liquid medium to keep the cells moist was (34±5) µm and for the minority it was (109±5) µm. The cell monolayer was considered to be ∼9µm thick as described in [89] and confirmed by measurements made by the Belfast team. The challenge for dosimetry was to determine the dose to cells for each laser shot. To achieve this, a stack of films was placed 1 cm behind the cell dish for all shots. An additional film strip was placed at the same distance from the window as the cells in order to measure the deposited dose on the cells in the most accurate way possible. In figure 4.4, the film stack and the strip are shown in yellow, the cells in orange and the medium in pink.

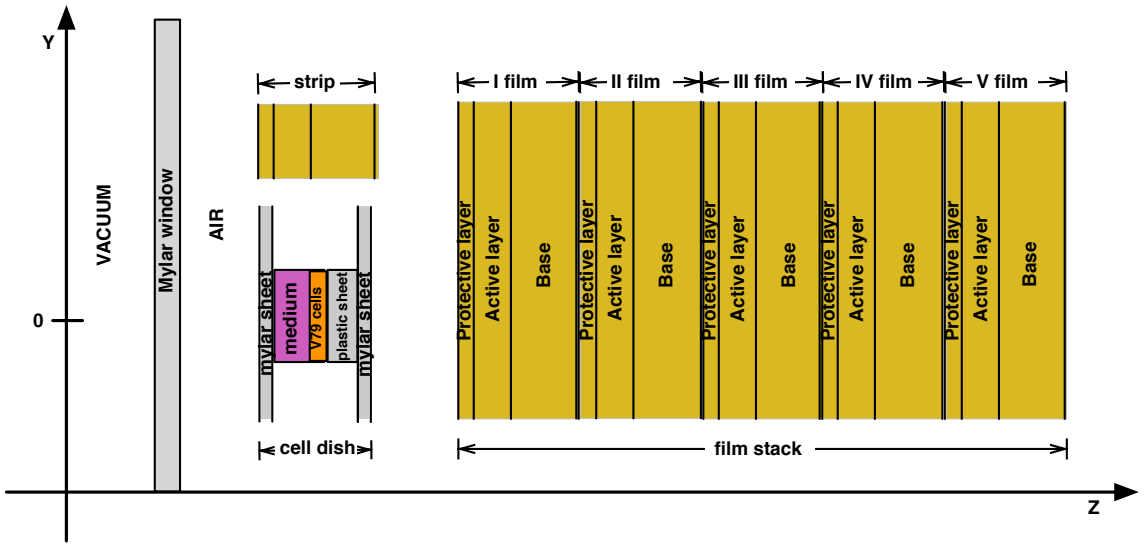

Figure 4.4 – Schematic representation on Y-Z plane (X=0) of cell dish, strip and film stack (not in scale).

4.1.2 Estimate of dose in the cell spots

The setup, from the proton source to the film stack, has been simulated using the Monte Carlo code Fluka. Distances and angles were modelled to be, as far as possible, equal to the experimental ones. The initial proton beam had a divergence of 20° and the exponential spectrum represented by the fit of the curve in figure 4.1. The simulated proton tracks are shown in figure 4.5. The very low energetic protons were stopped by the mylar window (represented by the first vertical line at ∼26 cm from the origin), but those with an initial energy higher than 2 MeV could reach the dish and the strip (represented by the second line) and then the film stack (represented by the final thicker line).

The Gafchromic films used are a special unlaminated edition of the standard EBT2 films (International Specialty Products, Wayne, NJ, USA). These special EBT2 films (lot number: A10150902), are not commercially available and have the advantage of having the active layer closer to one of the surfaces: 5 µm of top-coat layer, 30 µm of active layer and 175 µm of polyester substrate. The normal EBT2 films

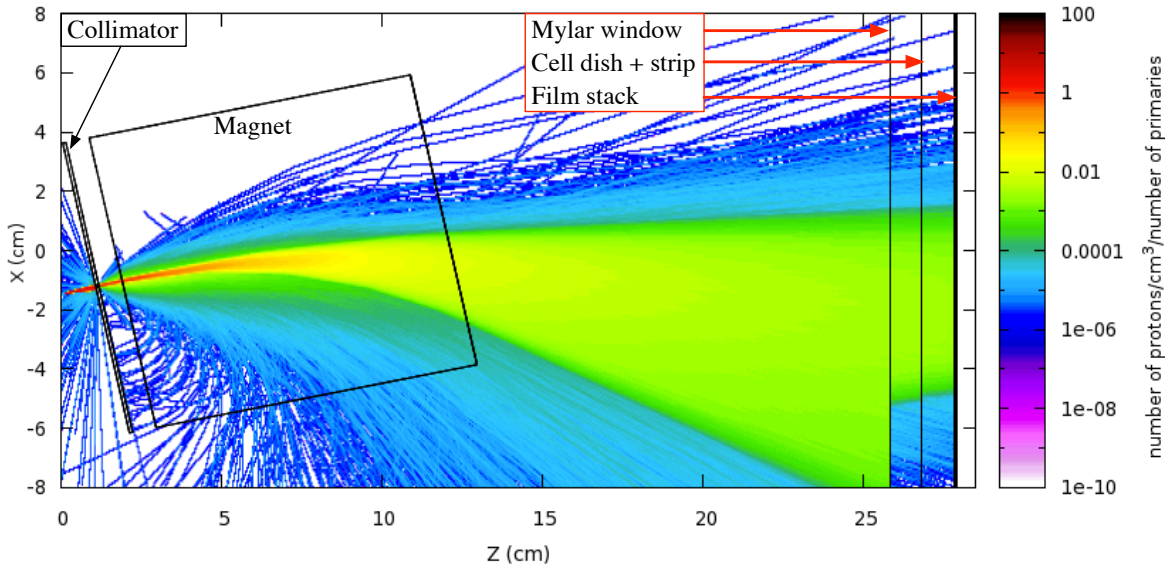

Figure 4.5 – Geometry with simulated proton tracks on X-Z plane (Y=0): only the protons with an energy higher than 2 MeV can reach the cell dish.

would have been very thick for these low proton energies and possibly a portion of information about dose and beam energy would have been lost in the non active surface layer. The films were previously calibrated using the 29 MeV beam accelerated by the cyclotron of the University of Birmingham, for doses up to 14 Gy (procedure explained in section 2.2.1). The equation of calibration is given in equation 4.1, where D indicates the dose to water in Gy, OD the optical density and PV the grey value of the pixels of the red channel scan of the film:

$$D(Gy) = e^{(a + b\,OD)} + c\,OD + d \quad \text{where} \quad OD = \log(65535/PV) \tag{4.1}$$

where: a=(0.56 ± 0.03), b=(2.70 ± 0.03), c=(-4.9 ± 0.3), d=(-2.4 ± 0.1) (as already seen in figure 2.7).

An example of irradiated films in a laser shot is shown in figure 4.6 (a). The deposited dose on the strip and on the first film of the stack decreases from the left to the right: the maximum dose corresponds to the lowest energy protons which deposit all their energy in the film. The minimum dose corresponds to the highest

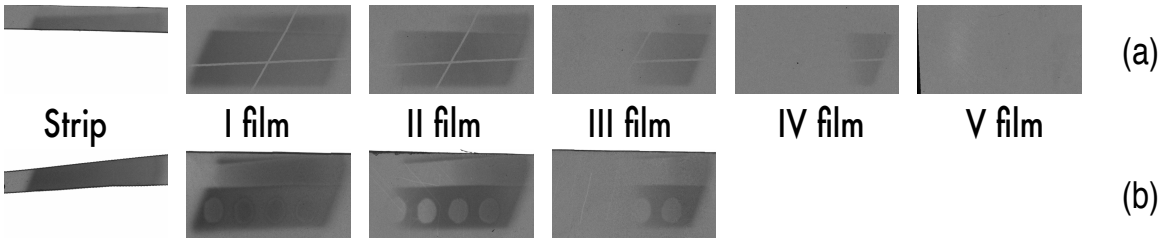

Figure 4.6 – Red channel of the scan of a stack (a) used during no cell irradiation and another one (b) used during cell irradiation. The lighter areas are the cell spot projections indicated from left to right as A, B, C and D.

energy protons which, losing energy in the films, were stopped in the last film of the stack. The protons with an initial energy higher than 4.85 MeV, 6.61 MeV, 8.13 MeV and 9.4 MeV could reach respectively the second, third, fourth and fifth film active layer. A sixth film (here not shown) would be darkened by protons having a minimum energy of 10.5 MeV. Since nothing was observed on the sixth film with any of the used configurations, the maximum energy of the protons irradiating the cell dish was between 9.4 and 10.5 MeV. As can be seen in figure 4.6 (a) during this irradiation there were no cells in the dish.

An example of the red channel scan of the films used during a cell irradiation is shown in figure 4.6 (b). The lighter areas are the projections of the cell spots. With this method it was possible to irradiate up to four cell spots (indicated from left to right as A, B, C and D), however the geometry of the vacuum chamber window meant that the optimal number was three (B, C and D). After having aligned all the films of the same stack using the TurboReg plugin [90] of ImageJ [53], the real cell locations have been evaluated for each shot considering both the projections and the position of the cross hairs (placed immediately behind the empty cell dish) which was used as a reference. For both the situations the shape of the outline of the beam on the films was due to the oblique shape of the chamber window.

Knowing the original positions of the cell circles and as there was no appreciable variation in energy or dose along the vertical axis, the first estimates of the doses (d_{ij},

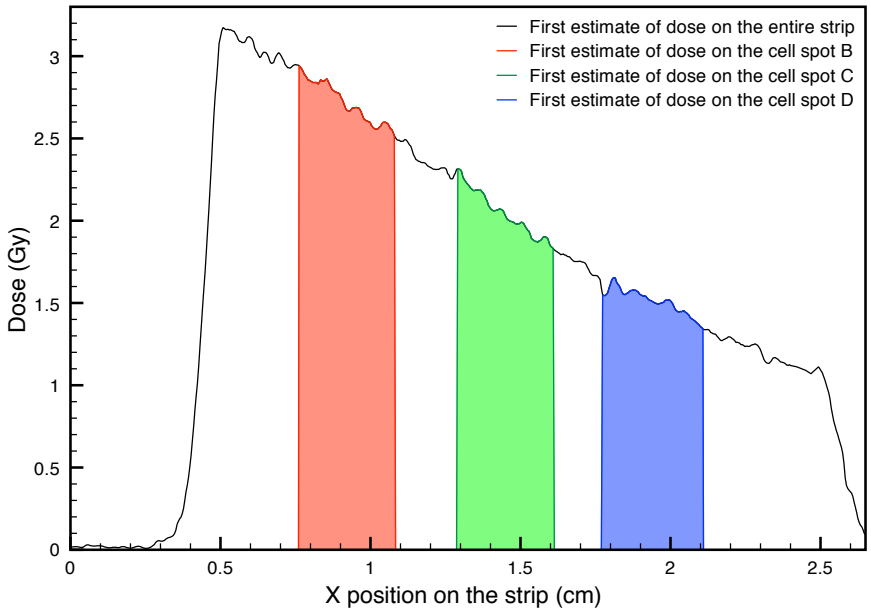

Figure 4.7 – Graph of the dose along the strip in figure 4.6 (b): the filled regions represent the doses related to the cell spot B (in red), C (in green) and D (in blue). For the cell spot A the dose cannot be measured on the strip because of the shape of the window shape.

where i is the shot and j the cell spot) were calculated using the average of the grey values of the pixels corresponding to the cell spots on the strip (see figure 4.7) and the calibration in equation 4.1. For the cell spot A the dose could not be measured, because part of the spot was outside the beam window on the strip.

This is the first step in calculating the dose: two corrections must then be made. One is due to the variation of the dose response of the films with proton energy as reported in [50], and the other is from the fact that the dose to water was measured on the strip and not on the cell layer which had a slightly different thickness and position. The first correction requires the spectrum of the protons hitting the active layer of the strip to be known and it has a particular effect on the doses due to the protons at very low energy ($E_p < 4$ MeV) as explained below. The second depends entirely on the position and on the thicknesses of the active layer of the strip and of the cell layer. In fact, using the above mentioned calibration giving directly the dose to water, the only difference between the doses we obtain after the first correction

and the doses actually absorbed by the cells is due to the position and the thickness of the materials which the protons have to cross. In order to calculate both the corrections, simulations of the experiment were indispensable.

4.1.3 Determination of the correction due to the energy response of the films

In the first part of this calculation the cell dish was simulated without cells, medium and plastic foil, but taking into account only the two thin mylar foils and the air between them. The reason for this approach is that the simulation of the films of the stack (the composition of the films is described in figure 2.5) gives the geometric relation between the simulated and the experimental reference systems, experimentally measured on the films in the region where the cells were absent (darker regions of figure 4.6 (b)). By measuring the position of the dose edges on each experimental and simulated films it was possible to relate the simulations to the experimental results. Figure 4.8 is an example of simulated protons hitting the stack: in black are the positions of the protons crossing the active layer of the first film, in red the positions of the protons crossing the active layer of the second film and so on up to the fifth film.

From the irradiated films like those in figure 4.6 (b) and from figure 4.8, it was possible to compare the distance between two different dose edges on the experimental films and on the simulated ones and find the translation value between the reference system of the experiment and of the simulation for each shot. The dose edge distances on the films were determined by the distances between the points where two different films of the same stack start darkening, except for the first film which is always dark along all its length for all the used configurations. The dose edge distances on the simulated films were obtained by the distances between the beginnings of two different colour regions, excluding the black one corresponding

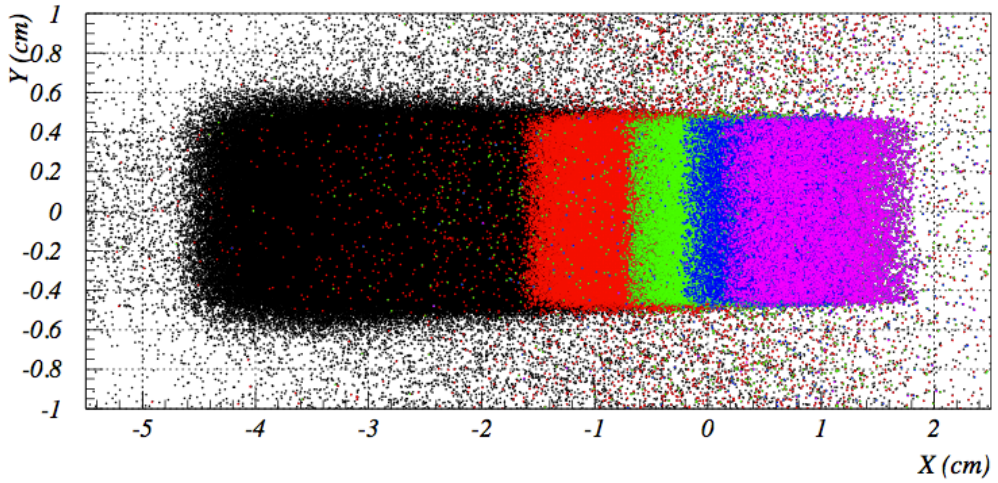

Figure 4.8 – Simulated protons crossing a stack: in black are the protons hitting the first simulated film, in red the ones hitting the second, in green the third, in blue the fourth and in pink the fifth simulated film. The colour regions on the simulated films are not affected by the shape of the chamber window which in the simulations is larger than the experimental window and rectangular.

to the first film.

If these distances were in good agreement (a tolerance of $\pm 5\%$ was used), it could be assumed that the simulated case was representative of the experimental shot. If, in a shot, the disagreement between the distances of two dose edges in the simulation and in the experimental stack was larger than 5% of the simulated value, or, the dose distribution on the strip was not as regular as in figure 4.7, it meant that the initial proton spectrum was significantly changed because of unknown factors. In these cases, obtaining the energy on the cells from the simulation is not possible. For this reason, it is preferable to use, for each shot, as many films as possible in the stack: the suggested maximum number is determined by the number of films which would be darkened by the maximum energy protons, which in our case was five. Fewer films can be used if the laser and target conditions can be kept stable.

Once the translation value between the reference system of the experimental and simulated films was known, it was possible to find the spectrum of the protons impinging on the middle of the thickness of the strip active layer along the circles

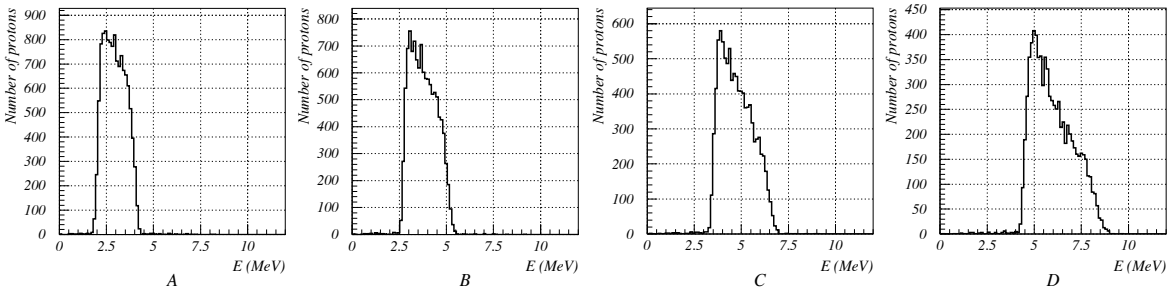

(a)

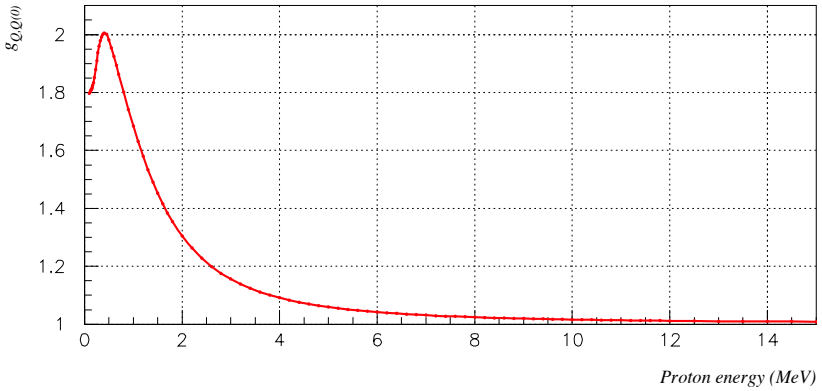

(b)

Figure 4.9 – (a) Extracted spectra of the protons crossing the strip in figure 4.6 (b) for the four cell spots. The number of simulated protons on the y axis is referred to the case where 10^7 protons were used as an initial beam. (b) Beam quality correction factor g_{Q,Q_0} curve calculated for EBT2 (D. Kirby, 2010, private communication).

corresponding to the cell spots. From this analysis it was evident that the proton spectra were not always the same changing from shot to shot. This was due not only to small movements of the magnet and of the slit holding the target, but also to varying laser pulse characteristics, such as contrast, energy and duration. These latter are conditions that cannot be simulated with Fluka, but this analysis using the dose deposition on the film stack meant it was possible to approximate the spectrum of the proton beam on the strip and on the cell dish for each shot if the 5% tolerance agreement was respected. Examples of the simulated proton spectra in the middle of the thickness of the strip active layer, with its accurate composition, are shown in figure 4.9 (a). The spectra displayed are related to the four cell spots of

the same shot with the films shown in figure 4.6 (b). In all the simulations described here the chamber window was considered to be large and rectangular (unlike the experiment) so there was no problem in simulating the spectrum also for cell spot A, even if its experimental data were not used.

The beam quality correction factor, g_{Q,Q_0}, dependent on the proton energy on the active layer of the strip, includes the relative effectiveness (RE) and the water-to-film stopping power ratio $s_{w,film}$ as defined in [50], is shown in figure 4.9 (b). The quality Q_0 refers to the calibration quality of 29 MeV protons from the Birmingham cyclotron. In the reference the author calculated the g_{Q,Q_0} values for EBT films, but it was recalculated for EBT2 appositely for this experiment. Knowing that this effect is a direct consequence of the response to the beam energy of the active material in the films, and since the used unlaminated edition of EBT2 films have the same active material as the normal EBT2 films, the g_{Q,Q_0} curve can be assumed to be the same. The average beam quality correction factor was then calculated for each shot and for each cell spot using the equation 4.2:

$$\overline{g}_{Q,Q_{0ij}} = \frac{\int_{E_{min_{ij}}}^{E_{max_{ij}}} f_{ij}(E)\, g_{Q,Q_0}(E)\, dE}{\int_{E_{min_{ij}}}^{E_{max_{ij}}} f_{ij}(E)\, dE} \tag{4.2}$$

where i represents the shot, j the cell spot, $f(E)$ the proton spectrum in the middle of the thickness of the strip active layer (like the graphs in figure 4.9 (a)), and $E_{min_{ij}}$ and $E_{max_{ij}}$ respectively the minimum and maximum energy of the proton spectrum in each spot for each shot. The corrected doses, Ds_{ij}, were subsequently calculated multiplying the correction factor $\overline{g}_{Q,Q_{0ij}}$ by the first estimates of dose, d_{ij}, obtained directly from the films.

4.1.4 Determination of the correction due to the different thickness and position of the cell spots and strip active layer

If the cell layer and the active layer of the strip have different equivalent thicknesses or/and are placed at different distances from the source, it is necessary to further correct the doses on the strip to allow for the fact that the absorbed doses in both regions are different. To achieve this the geometry of the cell dish was simulated exactly, differentiating two regions made of water for the cell monolayer and for the overlaying medium, but the active layer of the strip, on this occasion, was simulated made of water and with the equivalent water thickness. For the cell and medium layers the use of water is the usual approximation and it was applied whenever the cells and the medium were simulated. For the active layer of the strip this was due to the fact that the firstly-corrected doses are already dose to water because of the applied calibration. The ratio of the simulated dose in each cell monolayer spot and the simulated dose in the active layer is the correction. In order to have the real dose absorbed by the cell layer (Dc_{ij}), this ratio (R_{ij}) has to be multiplied by the first-corrected dose (Ds_{ij}), where i represents the shot and j the cell spot. In our case R_{ij} varied between 0.64 ± 0.05 and 1.04 ± 0.02.

4.1.5 Energy results

Once the position of the cell spots in the simulation reference system is known, it was possible to score the energy in the middle of their thickness. The graphs in figure 4.10 are an example of the simulated results for the four cell spots: they are all related to films in figure 4.6 (b). Examples of simulated results obtained for the second magnet/collimator configuration and 25µm medium layer above the cell spots are shown in figure 4.11 and with 100µm medium layer above the cell spots in figure 4.12.

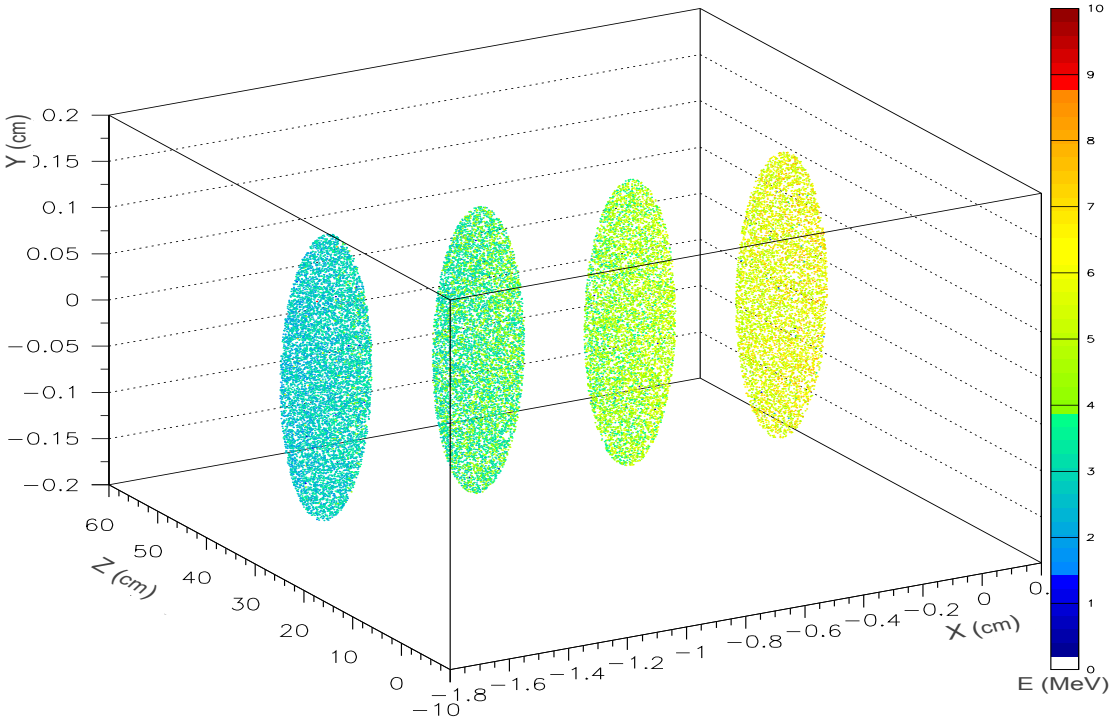

(a)

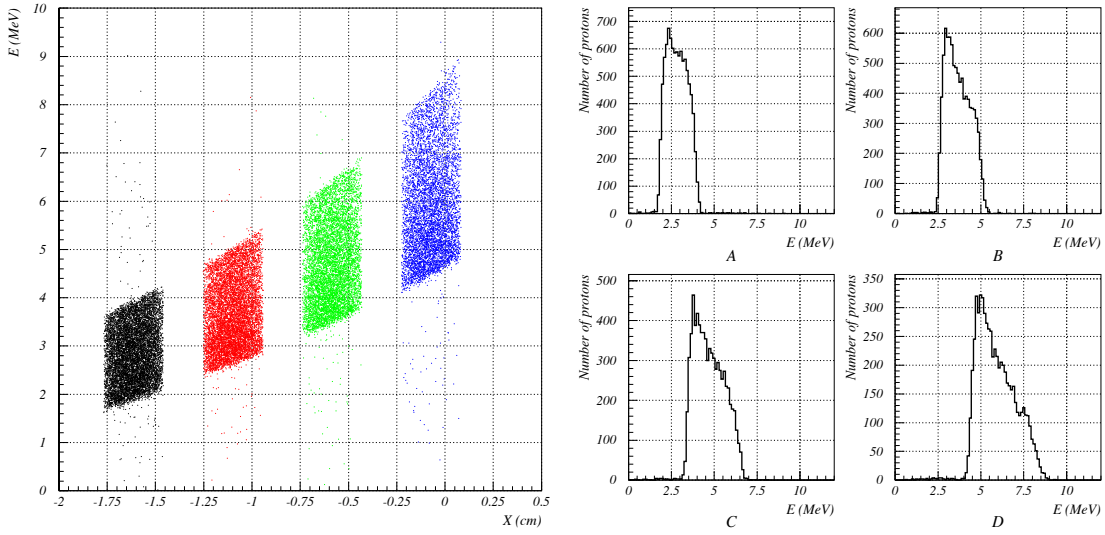

(b) (c)

Figure 4.10 – Simulated results related to the films in figure 4.6 (b): 6 MeV protons could perpendicularly strike the dish and 25µm medium was used above the cell spots. (a) 4-D graph of the simulated protons in the middle of the thickness of the cell spots. From left to right are A, B, C and D cell spot. (b) Graph of the proton energy versus the horizontal position. The points represent the protons and the different colours indicate the cell spot they are crossing: A (black), B (red), C (green) and D (blue). (c) Extracted proton spectra in the middle of the thickness of the four cell spots. Also in this case the number of simulated protons on the y axis is referred to the case where 10^7 protons were used as an initial beam.

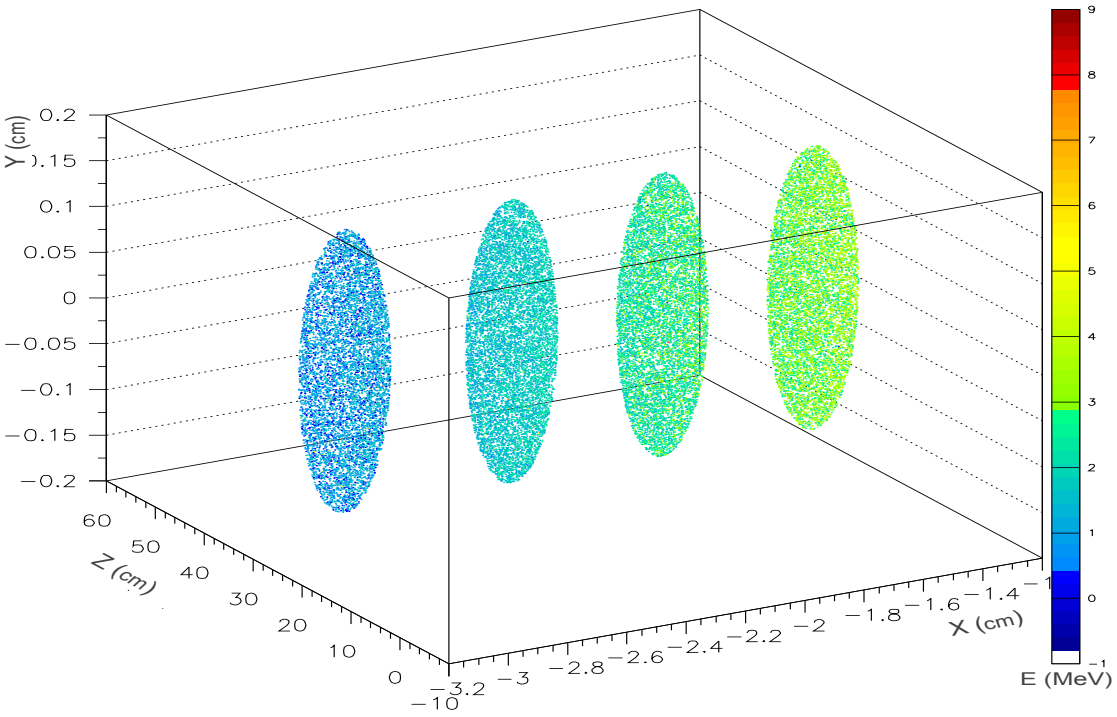

(a)

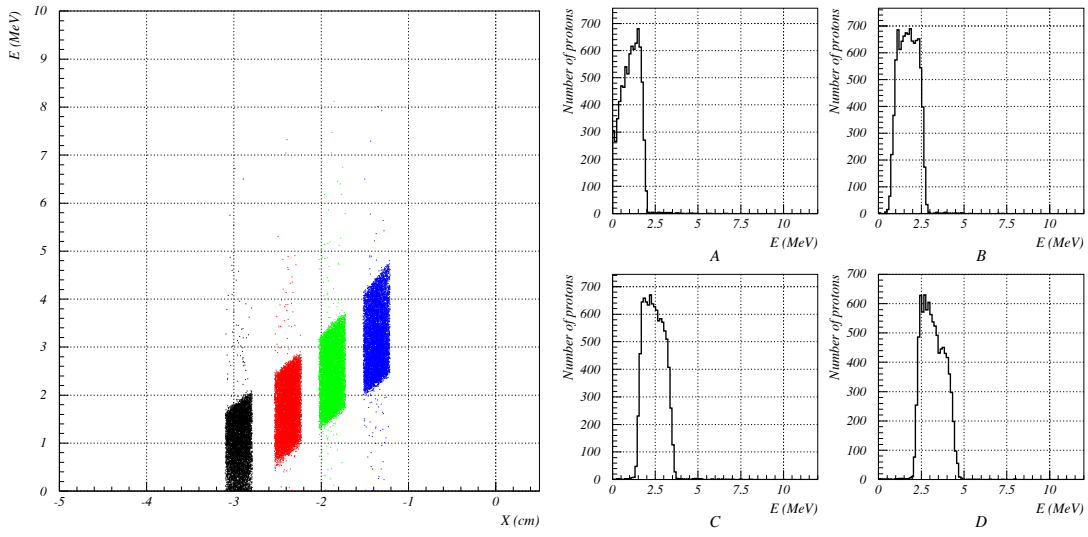

(b) (c)

Figure 4.11 – Simulated results related to the configuration where 3.6 MeV protons could perpendicularly strike the dish and where 25µm medium was used above the cell spots.(a) 4-D graph of the simulated protons in the middle of the thickness of the cell spots. From left to right are A, B, C and D cell spot. (b) Graph of the proton energy versus the horizontal position. The points represent the protons and the different colours indicate the cell spot they are crossing: A (black), B (red), C (green) and D (blue). (c) Extracted proton spectra in the middle of the thickness of the four cell spots. Also in this case the number of simulated protons on the y axis is referred to the case where 10^7 protons were used as an initial beam.

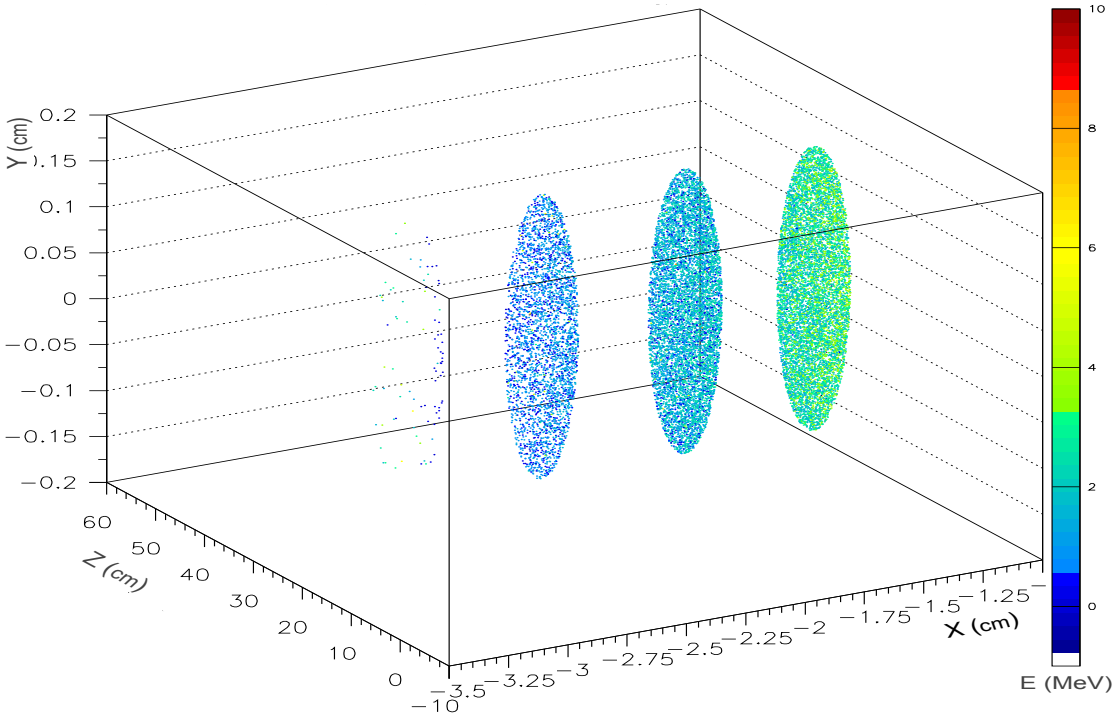

(a)

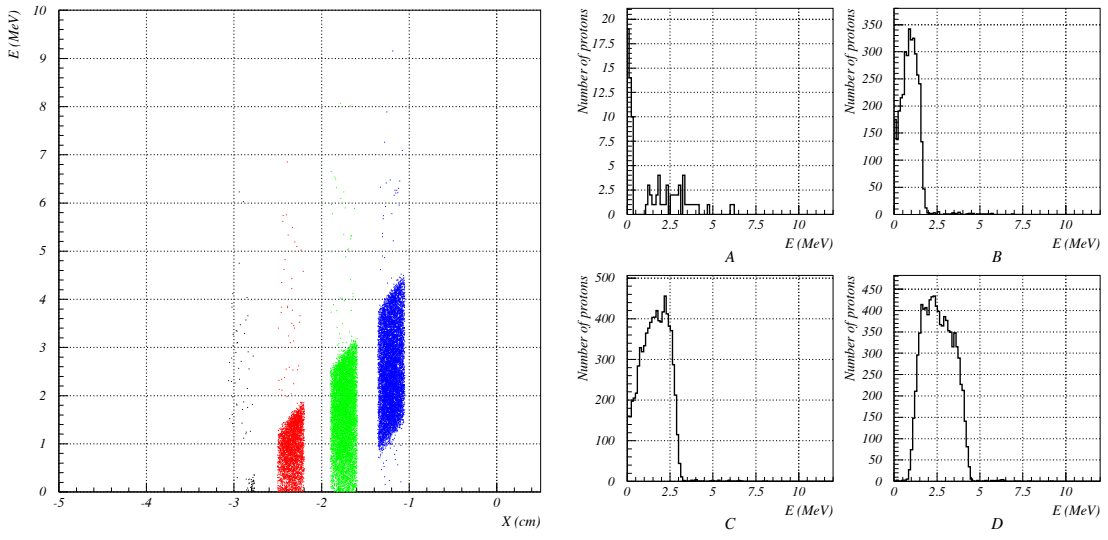

(b) (c)

Figure 4.12 – Simulated results related to the configuration where 3.6 MeV protons could perpendicularly strike the dish and where 100µm medium was used above the cell spots.(a) 4-D graph of the simulated protons in the middle of the thickness of the cell spots. From left to right are A, B, C and D cell spot. (b) Graph of the proton energy versus the horizontal position. The points represent the protons and the different colours indicate the cell spot they are crossing: A (black), B (red), C (green) and D (blue). (c) Extracted proton spectra in the middle of the thickness of the four cell spots. Also in this case the number of simulated protons on the y axis is referred to the case where 10^7 protons were used as an initial beam.

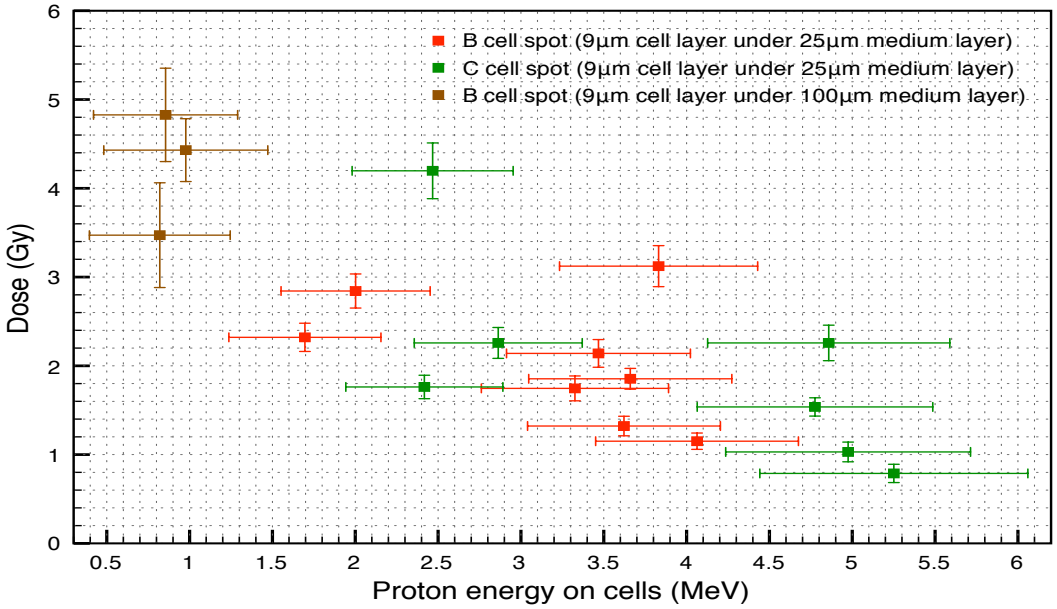

Figure 4.13 – Corrected doses as a function of the energy of the protons crossing the cell spots B and C. The spread used for the energy is one standard deviation of the gaussian fit of the spectra.

Considering both the configurations magnet/collimator and both the thicknesses of the medium above the cell layer, only for the cell spots B and C (for reasons explained later), applying a gaussian fit, the values for the mean energy varied from 0.8 to 4.0 MeV for B cell spot and from 2.4 to 5.3 MeV for C. The related σ varied from 0.4 to 0.6 MeV for B and from 0.4 to 0.8 MeV for C.

Having applied both the corrections to the first estimates of dose, it was possible to relate each dose to the mean energy of the protons crossing the corresponding cell spot. Figure 4.13 shows the corrected doses as a function of the mean beam energy for the cell spots B (in red) and C (in green). The spread of the energies is represented by one standard deviation of the gaussian fit of the spectra. In this graph the different experimental configurations of magnet and amount of medium are well differentiated. The brown data points (only for B cell spot) are due to the configuration where 100µm thick medium layer was placed above the cells and where the magnet and collimator allowed the protons with 3.6 MeV to perpendicularly strike

the cell dish. The red (for B cell spot) and green (for C cell spot) data points are both due to the configuration with lower amount of medium above the cells. In particular the data at lower energies are due to the configuration which allowed the protons with 3.6 MeV to perpendicularly strike the cell dish, and the data at higher energies are due to the configuration which allowed the protons with 6 MeV to perpendicularly strike the cell dish. The average energy for brown data points is (0.88±0.08) MeV, for red data points at low energy is (1.8±0.2) MeV and at higher energies is (3.7±0.3) MeV. The average value for C data points (green) at low energies is (2.6±0.2) MeV and at higher energies is (5.0±0.2) MeV. The fluctuation of the data around the average energy values in the graph is mainly due to the small deviations of target and laser characteristics already discussed.

Table 4.1 shows the obtained results for some laser shots. The doses, from the first estimate to the final corrected dose are inserted to show how the corrections affect the data depending on proton energy and on thickness of the medium above the cell layer.

Cell $spot_{Nshot}$	$\Delta z_{med}(\mu m)$	$\overline{E_p}$ (1σ) (MeV)	d_{ij} (Gy)	Ds_{ij} (Gy)	Dc_{ij} (Gy)
B_2	100	0.86 (0.44)	5.2 ± 0.3	6.9 ± 0.3	4.8 ± 0.5
B_4	25	1.70 (0.46)	1.64 ± 0.08	2.22 ± 0.10	2.3 ± 0.2
B_6	25	3.83 (0.60)	2.76 ± 0.15	3.06 ± 0.17	3.1 ± 0.2
B_7	25	4.06 (0.61)	1.03 ± 0.06	1.13 ± 0.07	1.15 ± 0.09
B_{11}	25	3.47 (0.56)	1.86 ± 0.10	2.09 ± 0.12	2.14 ± 0.16
C_4	25	2.42 (0.47)	1.36 ± 0.07	1.67 ± 0.08	1.76 ± 0.13
C_5	25	2.86 (0.51)	1.80 ± 0.10	2.13 ± 0.11	2.26 ± 0.17
C_7	25	4.78 (0.71)	1.42 ± 0.07	1.53 ± 0.07	1.54 ± 0.10
C_9	25	5.25 (0.81)	0.75 ± 0.08	0.80 ± 0.08	0.79 ± 0.10

Table 4.1 – Some results obtained for cell spots B and C in different laser shots. The medium thickness (Δz_{med}), the mean energy and the sigma (both with a typical uncertainty of a few %) of the gaussian fit of the spectrum of the protons irradiating the cell layers and the doses are shown for the two cell spots. The doses from the first estimate (d_{ij}) to the firstly corrected doses (Ds_{ij}) to the final corrected doses (Dc_{ij}) are displayed to illustrate the effect of the two applied corrections.

4.1.6 SURVIVAL CURVE

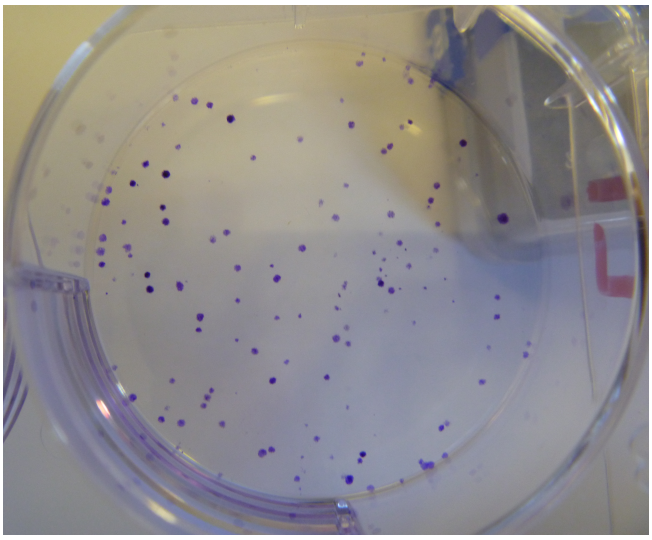

Figure 4.14 – Colonies in a petri dish stained with crystal violet during the counting process.

During each shot, while the already mentioned four cell spots were placed in the dish to be irradiated, other two were kept isolated to be used as a control during the counting process. After two hours from the irradiation (time necessary for non lethally damaged V79 cells to repair themselves) part of the irradiated cells (whose amount was decided in dependence of the first estimate of dose) and part of the control cells were plated in petri dishes and kept in an incubator at 37°C, in an atmosphere of 5% CO_2 and 95% humidification. In this environment each living cell started multiplying itself to form a colony. After a week the dishes were stained with crystal violet so that the formed colonies could be easily recognised (purple dots in figure 4.14) and counted. From the control dishes related to the same shot the average plating efficiency[1], $\overline{PE_i}$, was calculated. The typical measured plating efficiency was $\sim 60\%$. The ratio between the number of colonies counted in the dishes of the irradiated spots and the number of initial seeded cells divided by the

[1]The plating efficiency, is the ratio between the number of cells that attach and grow in the dish and the number of cells originally plated.

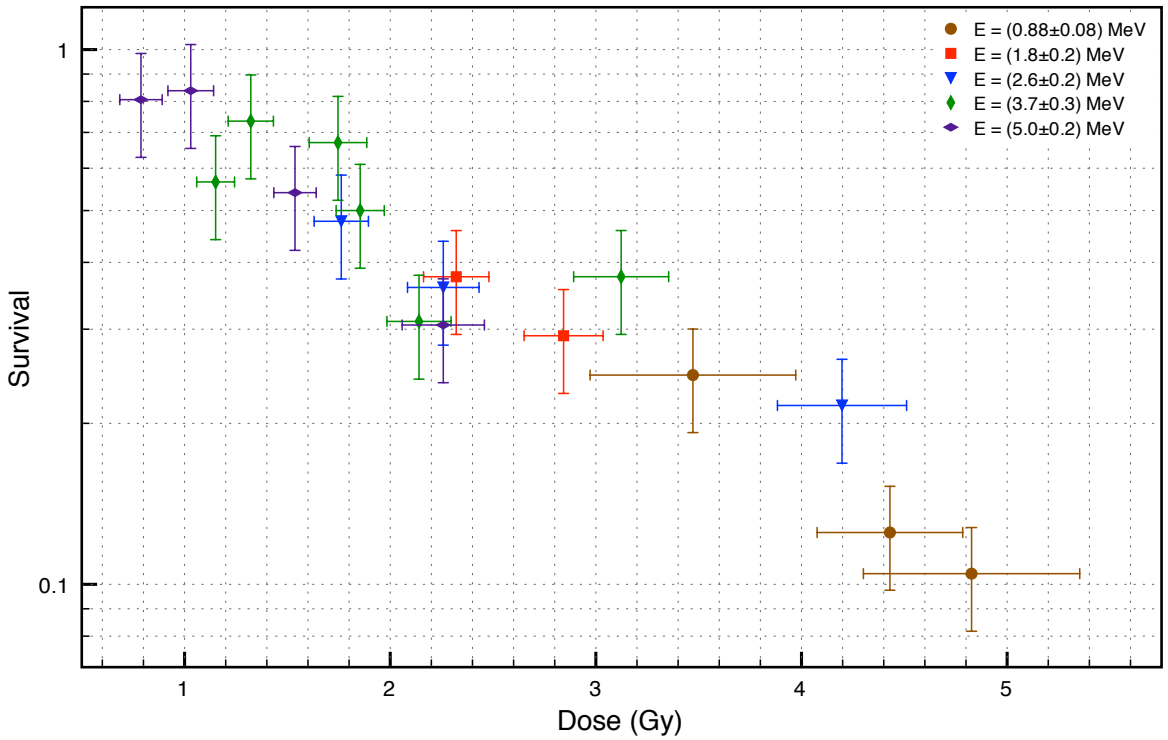

Figure 4.15 – Survival graph of the experimental data for the cell spot B and C. The colour of the points represents the average energy on the cell spot.

plating efficiency gave us the survival fraction:

$$S_{ij} = \frac{N_{counted_{ij}}}{N_{seeded_{ij}} \overline{PE_i}} \tag{4.3}$$

where i represents the shot and j the cell spot.

The data shown in figure 4.15 are those related only to the cell spots B and C. This is because for B and C we usually had: sufficient film area to measure the dose, reasonably high doses and an acceptable energy spread (the spread was in our judgement too large for cell spot D and the doses were too low to add useful survival data). For future experiments, reducing the cell spot diameter would help to decrease the energy spread of the protons crossing them, but would also reduce the number of irradiated cells, so it will need careful consideration. Rectangular cell regions (with y side longer than the x side) would probably be the best choice: the

x side could be decreased to allow a small energy spread, but by increasing the y side (along which there is no difference in particle energy and intensity) the number of irradiated cells in the spot could be kept high enough to preserve a reasonable statistic. The data in figure 4.15 are differentiated in four different colours according to the average energy of the protons crossing B and C cell spots. The graph in figure 4.15 is shown as a demonstration of the good suitability of the method. In any case, there is not sufficient statistics yet to show that different proton energies, which are expected to have different RBE values, create distinct survival curves. The number of points with similar energy should be increased in order to cover survival from 1 to 0.01 at least, something which is not easy with this kind of single-shot experiment.

4.1.7 Uncertainty discussions

Once g_{Q,Q_0} curve is known, the thickness and position of the strip active layer are important contributors to the first correction because they are necessary to determine the spectra of the protons in the cell spot positions and so to calculate $\overline{g}_{Q,Q_{0_{ij}}}$. Knowing that the cell layer is a monolayer 9 μm thick, the thickness of the medium overlaying the cell layer is the most important contributor to the second correction, affecting the position of the cells and the spectrum of the protons crossing them. Figure 4.16 shows what happens to the dose of some points of figure 4.15 when the thickness of the medium changes in the range 10 – 125 μm. This graph is used to illustrate how deeply the second correction depends on the medium thickness, so in it is not considered the obvious variations on the survival that would be caused by the different medium thickness conditions. For the same reason and for a better readability the survival uncertainties are not shown. As it can be seen, the variation in medium thickness does not strongly influence the doses at the highest proton energies, but it is crucial for the lowest energy. For these points we can see that, starting

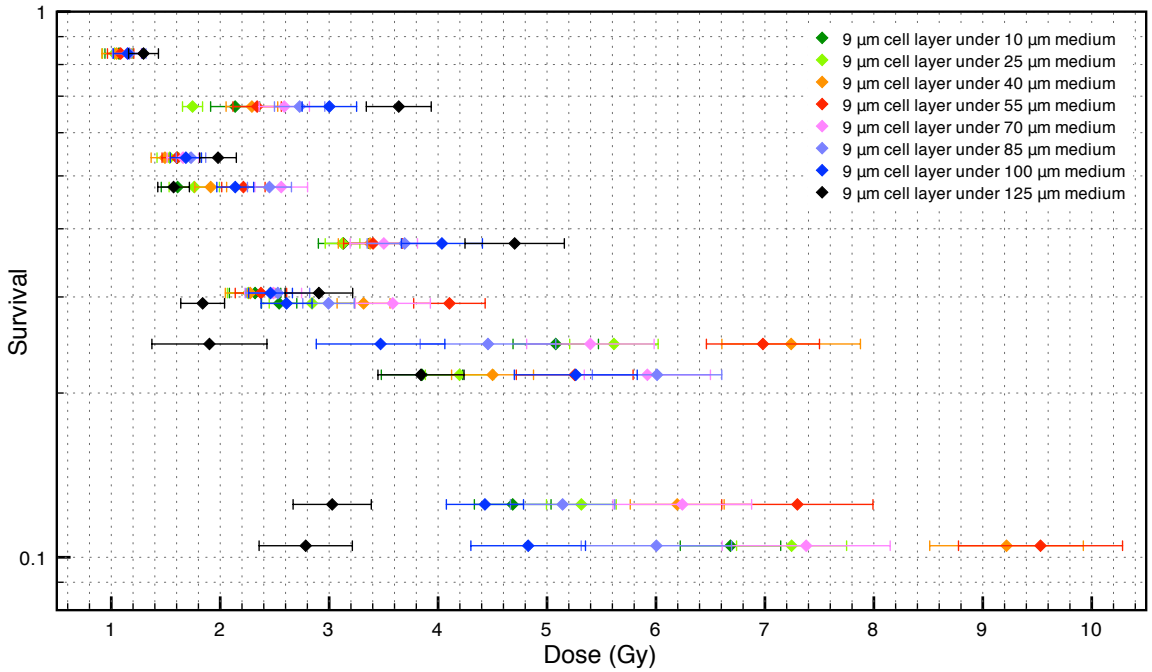

Figure 4.16 – Influence of medium thickness on the delivered dose. This graph shows how the doses, after the second correction, depend on the thickness of the medium above the cell monolayer spots.

from the 10 µm layer, the dose increases up to the 55 µm layer because the cells are irradiated by protons always less energetic: at ∼55 µm the Bragg peak produced by the proton beam with that initial proton energy is exactly on the cells; then the dose starts decreasing, because the lowest energy protons are stopped in the medium: the Bragg peak is almost in its entirety in the medium, and the cells are irradiated by a lower number of protons. Thus, the uncertainty in the medium thickness, as well as the cell layer thickness (if it is not a monolayer), should always be kept at minimum, and in particular when working with very low energy protons.

The detail of using very thin Gafchromic films is preferable, but even when it is not possible, the method described here can still be used. In this case the use of the simulations will be more important, because the correction factors to determine the dose absorbed by the cell layer will vary over a much larger range. Also, the first part of the method regarding the dose edge relation between simulated and

experimental films will require more attention. In particular at very low energies, the number of dose edges will be smaller (due to the larger thickness of the films) making less space for comparison. If the proton energy is much higher, then, there is no necessity for very thin films.

The dosimetry method and the subsequent spectral analysis are therefore well tested and can be applied in any other similar radiobiological experiment using laser-driven proton beams under the condition that the initial laser-driven proton spectrum is reasonably well known. Following all the steps of this method, even for the shots where the proton spectrum is uncertain, it is possible to approximate the spectra on the cells and strip because the comparison between the experimental and simulated dose edges and the dose distribution on the films, provides the necessary additional information. For this reason, it is preferable to use as many films as possible in the stack for each shot, so that it is possible to detect any potential incongruence between the simulated and the experimental dose edges or the presence of peaks in the experimental spectrum.

4.1.8 Comparison with other proton sources

In order to understand whether this new kind of high dose-rate radiation causes different biological consequences from the well known effects of conventionally accelerated beams, the same method of handling the cells should be applied to irradiations non involving laser sources and then the obtained survival curves should be compared.

A first try to obtain a preliminary comparison using the proton beam accelerated by the cyclotron of the University of Birmingham was conducted. Unfortunately, after a week of irradiation and after the due wait time needed to the seeded cells to form their colonies, all the dishes were found completely contaminated by some kind of bacterium. The survival could not be determined because the contamination

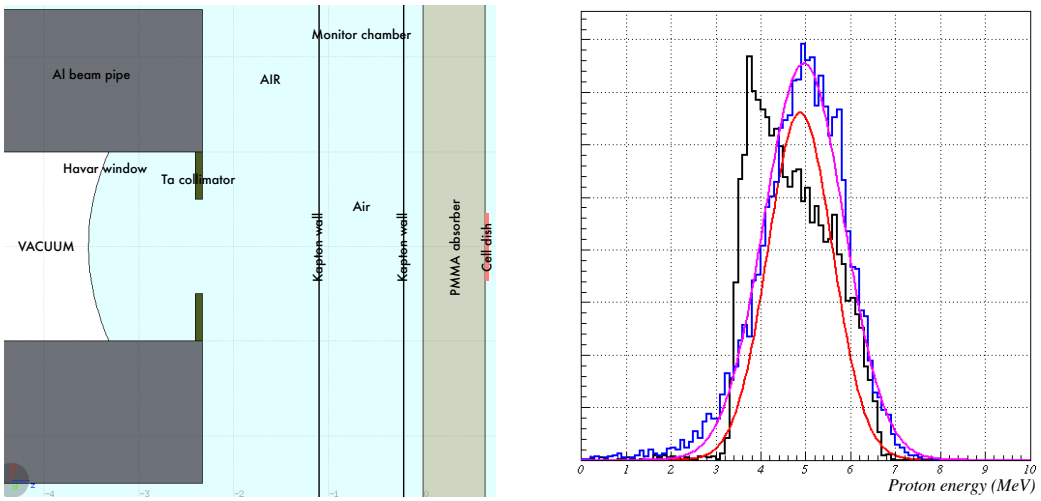

(a) (b)

Figure 4.17 – (a) Simulated final part of the cyclotron-accelerated proton beam line used at the University of Birmingham for the comparison. (b) Comparison between the spectrum obtained with the laser-driven protons in the middle of cell spot C (black line) and the spectrum obtainable in the middle of an equal cell monolayer using 29 MeV protons accelerated by the cyclotron of the University of Birmingham and a 0.651 mm thick PMMA absorber (blue line). The pink and the red line are the gaussian fits of respectively the blue and the black spectrum.

affected the health of the survived cells. Even if the desired results could not be obtained, what was done during the irradiation is here reported. The first aim was to approximately recreate the proton spectra in figure 4.10 and 4.12 using a system of absorbers to decrease the proton energy from the initial 29 MeV coming out from the cyclotron to the energy necessary for the comparison.

Since it was a preliminary test, it was decided to do the comparison only for the cases where the average energy in the middle of the thickness of C cell spots was 5 MeV. In order to do this a Fluka simulation of the experimental setup was run. The simulated final part of the beam pipe is shown in figure 4.17 (a), where the inserted PMMA absorber was chosen in order to obtain a spectrum similar to the one in figure 4.10 (c) for C spot. The required thickness was found to be 0.651 cm. The comparison between the two spectra is shown in figure 4.17 (b). As it can be seen the

agreement between the two spectra is not ideal: the blue spectrum has a gaussian trend while the black spectrum still maintains part of the initial exponential trend of the laser accelerated proton beam. Applying to both the curves a gaussian fit it is possible to find the average energy, and as it can be seen from the red (gaussian fit of the laser accelerated beam) and pink line (cyclotron accelerated beam) that the average energy delivered to the cells was the same: 5 MeV. At the beginning of each day of irradiation, the ratio between the reading from the Markus and Monitor chamber, $R\left(\frac{Ch_{Mark}}{Ch_{mon}}\right)$, was calculated, then the Markus chamber was removed and the doses to deliver to the cells were calculated using the equation 2.14. The doses varied in the range 0.5 – 10 Gy.

A subsequent work would be the construction of several different modulators able to reproduce exactly the same proton spectra obtained using the TARANIS laser for all the cell spots. A study has been conducted again for C cell spot simulating a PMMA modulator wheel made of as many differently thick absorbers as needed to reproduce the required exponential-like spectrum. Since the 29 MeV proton beam when decelerated though absorbers creates a spectrum more spread than the laser-driven one, an initial 15 MeV cyclotron accelerated proton beam was chosen. The comparison between the obtained spectrum and the one delivered with the TARANIS laser is shown in figure 4.18 (a). Figure 4.18 (b) shows the components of the final spectrum: each component represents the effect of each single step in the modulator. The percentage of each step and so the actual portion of the straight angle in the modulator has been decided in dependence on the coefficients which multiplied by the single spectra minimise the difference between the final modulated spectrum and the laser-driven one. Otherwise they can be seen as the normalised number of particles necessary to be run in the simulation of each single step to produce a the final red spectrum. The wheel could be built in a single 360° slice divided in 9 steps or as in $4 \times 90°$slices divided in 36 steps: 4 for each thickness. Table 4.2 shows the

thicknesses, percentages and angles of the required steps (where the $4 \times 90°$ case has been chosen). The rotation of the wheel would be fast enough to deliver, in a few

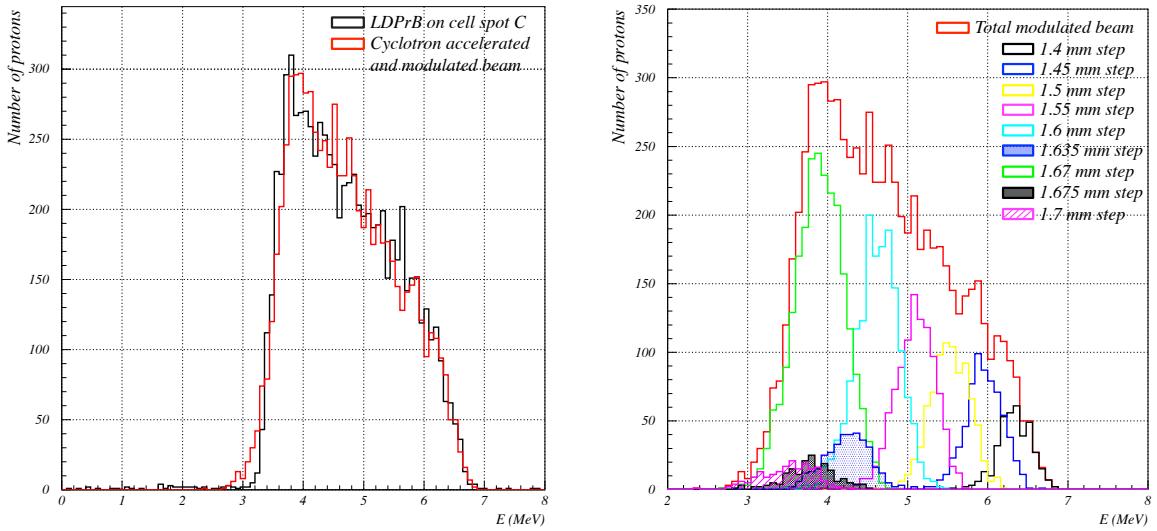

(a) (b)

Figure 4.18 – (a) Comparison between the TARANIS proton spectrum on C cell spot and the 15 MeV cyclotron accelerated proton spectrum modulated by a PMMA wheel. (b) Modulated spectrum with its components: each component represent a different step on the modulator wheel.

Step thickness (mm)	Percentage of total angle (%)	Angle in $1 \times 90°$ slices
1.4	4.88	4.4°
1.45	8.54	7.7°
1.5	10.98	9.9°
1.55	13.41	12°
1.6	20.73	18.7°
1.635	4.88	4.4°
1.67	31.71	28.5°
1.675	2.44	2.2°
1.7	2.44	2.2°

Table 4.2 – Modulator wheel components: thicknesses and percentages of angle are shown in the first two columns for each step. Each 90° slice of the wheel will comprehend the 9 steps with the angles in the third column.

seconds of irradiation, low doses as well as high doses to the cells and to always irradiate them with the same chosen uniform spectrum. The same can be obtained in order to recreate the laser-driven proton spectrum on B and D cell spots respectively using thinner and thicker steps.

Even if the kind of measurements just described would provide the most accurate RBE comparison between the laser-driven and conventional proton sources, since the biologist availability was very limited, we could not do the experiment using the wheel. A simpler comparison is here reported using data in literature for V79 cells irradiated by proton beams conventionally accelerated and other data we obtained using 225 kV X-ray beam (from PXI Inc.) using the same radiobiology procedure as the experiment at the TARANIS facility.

Figure 4.19 shows the comparison between the TARANIS survival data for cell spot B irradiated by protons with 3.7 MeV mean energy (green points) and the proton data published by Belli et al.[91] (red data and fitting curve) and Folkard et al.[92] (blue points and fitting curve). As it can be seen our experimental data are in good agreement with the conventionally accelerated proton data at 3.2 and 3.66 MeV, but in order to have an even better comparison the number of points at higher doses need to be improved as already mentioned. Improving these data would also help to better calculate the RBE at 10% survival, which is usually used to define the effectiveness of the irradiation. By fitting the X-ray data (black points) with:

$$S(D) = e^{-(\alpha D + \beta D^2)} \tag{4.4}$$

I obtained $\alpha = (0.123 \pm 0.008)$ Gy^{-1} and $\beta = (0.030 \pm 0.002)$ Gy^{-2} which give the black curve in figure 4.19. Both these values are in good agreement with the values for X-ray data published by Belli and Folkard, meaning that the comparison done between our and their proton data is actually meaningful. By fitting the data from B cell spot at 3.7 MeV, I obtained $\alpha = (0.40 \pm 0.18)$ Gy^{-1} and $\beta = (0 \pm 0.08)$ Gy^{-2}

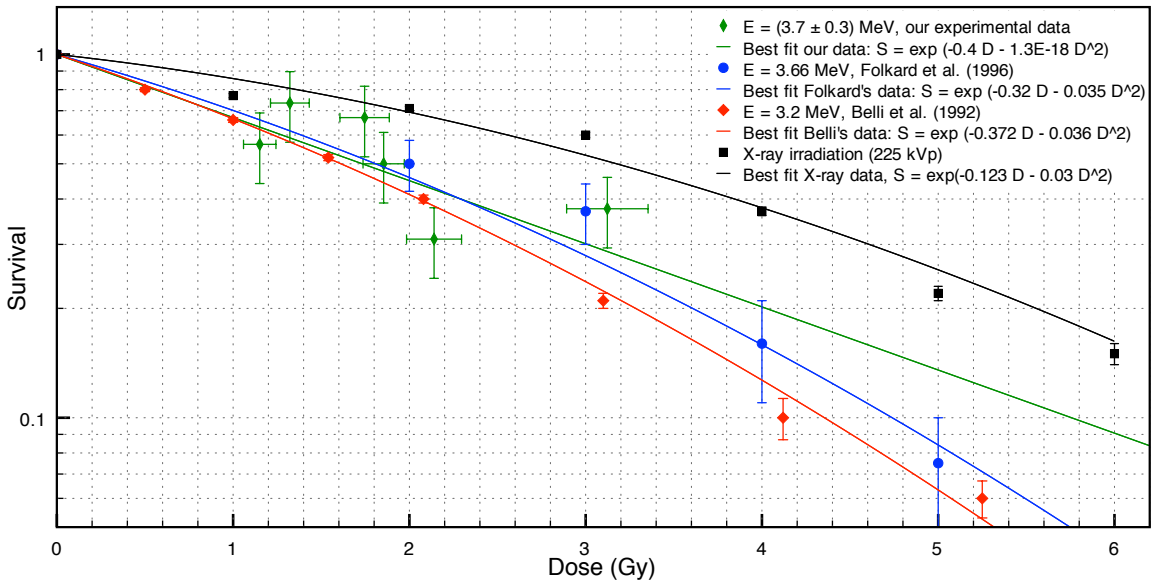

Figure 4.19 – Comparison of V79 survival curves between our experimental data at 3.7 MeV and other data in literature where the protons are conventionally accelerated.

which give the green curve in figure 4.19. Even if the accuracy on these parameters is not optimal, it has been possible to calculate another useful parameter, $\mathrm{RBE}_{\alpha_p/\alpha_X}$, normally called RBE_{max}, which is used to define the overall radiobiological effectiveness of a treatment. The obtained $\mathrm{RBE}_{\alpha_p/\alpha_X}$ is 3.3 ± 1.7, which shows that this kind of irradiation, even if complex and still needed of massive improvements, is worth to be investigated because:

- its radiobiological effectiveness is higher than the effectiveness provided by X-ray beams;
- its radiobiological effectiveness is similar to that of conventional accelerated proton beams, so that it can be assumed that the high dose–rate does not cause substantial different effects on the irradiated cells;
- if in future the maximum delivered energy is improved as well as the possibility to irradiate the cells with monoenergetic beams, the cost of a particle therapy treatment will be reduced as well as the sizes of the delivering facility.

4.1.9 SUMMARY OF THE METHOD

The procedure to obtain the dosimetry deeply involves the use of Gafchromic films and Monte Carlo simulations. To summarise: the cell dish is placed in front of a stack of Gafchromic films and behind an energy and charge selection system (figures 4.2-4.5). A film strip can be placed at the same distance from the source as the cell layer (see figure 4.4) in order to make a first estimate of dose which is as near as possible to the actual dose absorbed by the cells. This is the approach adopted here, but it is not strictly necessary. In fact, even without using it, applying the second correction, the dose measured from the first film of the stack will be corrected for the different position and thickness of the cell layer. The films need then to be scanned (example in figure 4.6 (b)) and the grey values of the regions corresponding to the cell spots on the strip identified, as well as the dose edge positions on the films of the stack. Using the calibration (equation 4.1) the grey values are translated to a first estimates of dose, d_{ij} (example in figure 4.7). Using the known initial spectrum of the protons accelerated by the laser, several simulations are performed. One is necessary to find the translation value between the reference system of the simulation and of the experiment and so to locate the cell spots in the simulated experiment. Another is to determine the spectrum of protons crossing the strip in the cell spot regions (examples in figure 4.9 (a)) in order to apply the first correction, $\overline{g}_{Q,Q_{0ij}}$, due to the variation of dose response of the films as a function of proton energy (curve in figure 4.9 (b)). With this correction the real dose that should have been measured from the active layer of the strip is found: $Ds_{ij} = d_{ij}\,\overline{g}_{Q,Q_{0ij}}$. The final simulation is necessary to obtain the correction, R_{ij}, due to the different thickness and position of the active layer of the strip and of the cell layer, and so to calculate the actual dose absorbed by the cell spots: $Dc_{ij} = Ds_{ij}\,R_{ij}$. This simulation is also needed to determine the spectra of the protons crossing the cell spots (examples in figure 4.10, 4.11 and 4.12).

CHAPTER 5

NUCLEAR ACTIVATION AS A DETECTOR OF LDPB

As showed in several papers [10, 7], the energetic ions accelerated by a laser can induce nuclear reactions in secondary activation targets placed in the beam.

One of the results of the interaction is the fusion of projectile and target with the creation of compound nuclei that de-excite emitting evaporation particles: α, protons, neutrons and photons. If the evaporation residues, the nuclei remaining after the evaporation emissions, are not stable isotopes, they decay emitting γ and β. Through the γ decays, it is possible to obtain information about the reactions occurred and so about the particles accelerated by the laser.

Other possible reactions are direct reactions where scattering between the incident particle and the nucleons of the target nucleus take place. The target nucleus can acquire or emit some nucleons and if it is left in an excited state and, if radioactive, it will emit gamma. As with the fusion reactions, from the decay photons, it is

possible to obtain some information about the incident particles.

The difficulties with this kind of measurement are mainly as follows:

- usually the energy spread of the accelerated beam is large, so, by detecting only the decay products of the residual isotopes, finding the spectrum of the incident beam on the activation target is not trivial: the same residual nuclei can be created by incident particles with different energies (this occurs mainly if the cross section of production has a broad distribution);
- if particles of similar mass are accelerated (for example ^{12}C and ^{16}O), by interacting with the activation target, these may produce the same residual nuclei, but with different evaporation emissions.

Detecting only the decay photons of the residual nuclei could give misleading results. From the activation of an Al target [10], an example of fusion reactions is:

$$^{12}C + {}^{27}Al \rightarrow {}^{38}K + n \tag{5.1}$$

$$^{16}O + {}^{27}Al \rightarrow {}^{38}K + n + \alpha \tag{5.2}$$

an example of direct reactions is instead:

$$^{12}C + {}^{27}Al \rightarrow {}^{24}Na + 3\alpha + 2p + n \tag{5.3}$$

$$^{16}O + {}^{27}Al \rightarrow {}^{24}Na + 4\alpha + 2p + n. \tag{5.4}$$

In these cases the detection of the decay photons of ^{38}K (for the fusion case) or of ^{24}Na (for the direct case) is not sufficient to define the yields of both the accelerated Carbon and Oxygen ions.

The technique of obtaining the ion yields from the activation of the target has already been applied in the past, but employing for the majority of the cases the same activation targets, Cu or Al [10, 7, 69]. With this work I investigated the possibility

of enlarging the group of usable isotopes making the activation targets, in particular researching those that could be employed for the detection of reactions induced by low energy protons (part of the results from this study has been published in the Radiation Measurements Journal, [93]). My aim was also looking for isotopes, the reactions of which were correctly simulated by Fluka, so that a simulation of a future experiment could give important support to discover the initial reactions originated in the target and so the spectrum of the incident particles.

I started testing the technique using the already well used Cu target in order to show the pros and cons of the method and then I investigated other isotopes. All the tests have been performed using the proton beam accelerated by the cyclotron of the University of Birmingham. A test using laser-driven proton beam has not been possible due to two main reasons:

- limited beam time at RAL, where the majority of the LIBRA time has been spent to characterise the accelerated beams, trying to increase the maximum energy of protons and ions;

- low energy of the proton beam accelerated at Queen's University Belfast. In fact, even if this proton beam can be accelerated up to 12 MeV (see figure 4.1), this energy was too low to test the chosen targets (Cd and Ti).

In the case of a cyclotron-accelerated monoenergetic beam, it is possible to obtain the number of particles in the beam, fundamentally because a given beam energy corresponds to a cross section of production of the parental isotopes which emit the detected photons. The protons could be absorbed by the target nuclei inducing (p,xn), (p,α), (p,d)... reactions, or be elastically or inelastically scattered away.

5.1 TEST WITH MONOENERGETIC PROTON BEAMS

During the irradiation the number of radioactive isotopes in the activation target increases according to:

$$N_{iso_i}(t \leq t_0) = \frac{RR_i}{\lambda_i}(1 - e^{-\lambda_i t}) \tag{5.5}$$

where t_0 is the final instant of irradiation, λ_i is the inverse of the decay time of the i-th radioisotope and RR_i is its reaction rate of production. After the irradiation the number of radioisotopes decreases according to:

$$N_{iso_i}(t > t_0) = N_{0iso_i} e^{-\lambda_i (t - t_0)} \tag{5.6}$$

where N_{0iso_i} is the number of the i-th radioactive isotopes at the end of the irradiation. The trend of N_{iso_i} curve during the irradiation and during the decay is shown in figure 5.1.

Choosing to count in a time interval ($t_1 \leq \Delta t \leq t_2$) only the photons, with a specific energy, emitted by a particular decaying radioactive isotope, and knowing its pro-

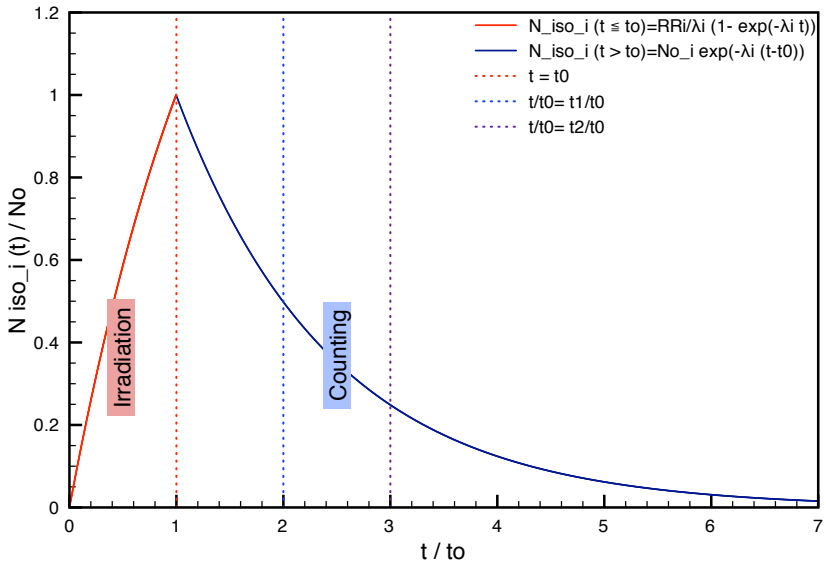

Figure 5.1 – Trend of the number of the i-th radioactive isotopes curve during irradiation and counting.

duction cross section, it is possible to re-obtain the number of bombarding particles using the equation 5.7:

$$N_{p_{beam}} = \frac{\lambda_i N_{\gamma_{ij}} \Delta t_{irr}}{P_{\gamma_{ij}} \sigma_i(E_p) \varepsilon_{tot}(E_{\gamma_j}, d) N_t} (e^{\lambda_i t_0} - 1)^{-1} (e^{-\lambda_i t_1} - e^{-\lambda_i t_2})^{-1} \tag{5.7}$$

where: $N_{p_{beam}}$ is the number of beam particles; $N_{\gamma_{ij}}$ is the number of the photons with energy E_{γ_j} emitted by the i-th decaying isotopes and $P_{\gamma_{ij}}$ their emission probability; $\sigma_i(E_p)$ is the production cross section of the i-th isotope; $\varepsilon_{tot}(E_{\gamma_j}, d)$ is the total efficiency of the used detector to count the decay photons (dependent on the energy of the detected photons and on the geometry of the detector) and N_t is the number of nuclei in the metal target.

In order to use equation 5.7, it is necessary either to obtain $\sigma_i(E_p)$ from a simulation, or, if achievable, to find it from literature [94] knowing the corresponding proton energy. If the target is thin (thickness $\sim$100 μm for proton beams) and the particle spectrum almost monochromatic, it can reasonably be chosen as the energy in the middle of the target, so that $\sigma_i(E_p)$ can easily be considered as $\sigma_i(\overline{E_p})$ and found from literature. In the case of laser-driven beams, if there are no energy selection systems in use, the incident proton spectrum has the characteristic exponential trend, so that the use of a Monte Carlo program becomes more necessary to find the $\overline{\sigma_i}(E_p)$ due to the particles reaching the activation target.

In this test Fluka simulations have been implemented to recreate the geometry of the experiments, not only to have information about the mean energy of the beam in the middle of the targets, but also to understand whether Fluka could be a feasible program to determine $\overline{\sigma_i}(E_p)$ in the energy range of in interest.

To detect the decay photons, a HpGe detector was used (GEM 28195, by ORTEC). Its total efficiency (i.e. the product of the intrinsic efficiency, energy dependent, and of the geometric efficiency) has been accurately studied using point radioactive sources placed at different distances from the detector. The geometric efficiency

in the presence of a point source has been firstly calculated using Fluka through simulations of the target and of the detector geometry. In particular the target has been simulated as a point source emitting in 4π a special kind of Fluka *pseudoparticles* called RAY. These particles have been implemented by Fluka developers appositely for this kind of study since they do not interact with matter but can be detected as normal particles. Knowing the number of emitted RAYs (decided by the user) and detecting the RAYs reaching the active surface of the detector, it is possible to calculate the geometric efficiency simply dividing the number of detected RAYs by the number of initial emitted RAYs in 4π. The simulation and the calculation have been repeated for different distances target–detector in the range 0–20 cm, each one giving $\varepsilon_{geo}(d)$, where d represents the distance.

Using several testing sources emitting photons with different characteristic energies in the range 0.1–1.4 MeV, the total efficiency of the detector has been measured. This measurement has been repeated for different distances target–detector in the same range as the simulations, 0–20 cm. Dividing each measured total efficiency $\varepsilon_{tot}(E_{\gamma_j}, d_h)$, one per photon energy (E_{γ_j}) and distance target-detector (d_h), by the geometric efficiency simulated at the same distance target-detector, $\varepsilon_{geo}(d_h)$, it is possible to obtain the intrinsic efficiency, $\varepsilon_{int}(E_{\gamma_j})$ according to:

$$\varepsilon_{int}(E_{\gamma_j}) = \frac{1}{n} \sum_{h=1}^{n} \frac{\varepsilon_{tot}(E_{\gamma_j}, d_h)}{\varepsilon_{geo}(d_h)} \tag{5.8}$$

where *n* is the number of times for which the measurement has been repeated changing (or not) the distance target-detector and without changing the photon energy. The same average must, then, be calculated for each E_{γ_j} proper of the emitting sources.

By plotting and finding the best fit of $\varepsilon_{int}(E_\gamma)$ as a function of E_γ (see figure 5.2), it is possible to find the relation between the two quantities. The best fit equation

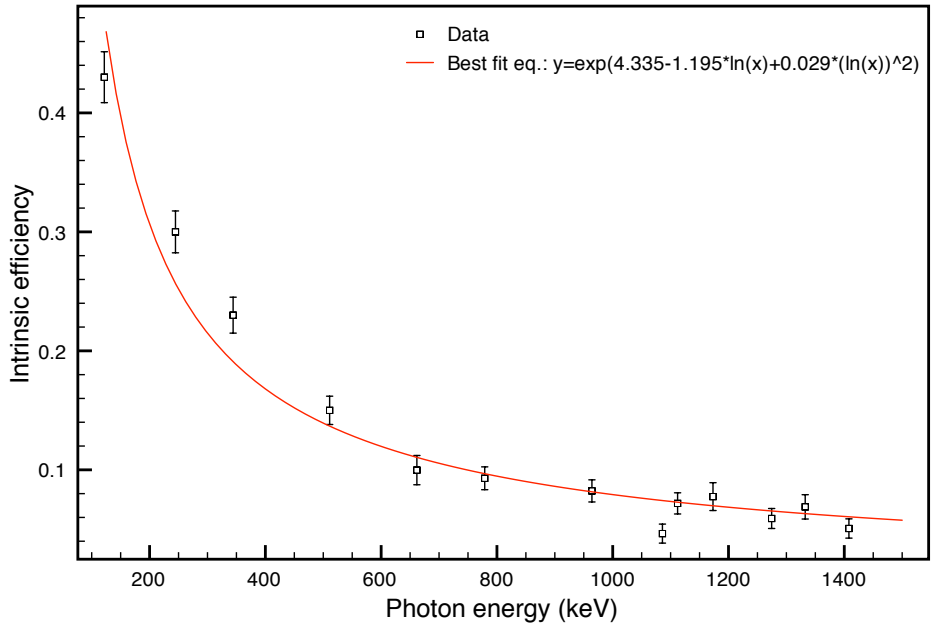

Figure 5.2 – Intrinsic efficiency of the HpGe detector used to measure the activation of the irradiated foils.

was:

$$\varepsilon_{int}(E_{\gamma_j}) = \exp\left(-a_0 + a_1 \ln(E_{\gamma_j}) + a_2 (\ln(E_{\gamma_j}))^2\right) \tag{5.9}$$

where $a_0 = (-4.335 \pm 0.008)$, $a_1 = (1.195 \pm 0.009)$ and $a_2 = (0.029 \pm 0.005)$. This function has subsequently been used to find the intrinsic efficiency for the energies of the photons emitted by the activated foils. The geometric efficiency in the presence of an extended source (our irradiated foils) is not the same as in the presence of a point source, so new simulations of target and detector have to be performed: the source is again 4π RAY emitting from a given distance from the detector, but its size is the size of the real foils: a disc with a radius of 0.3 cm. The final total efficiency, $\varepsilon_{tot}(E_{\gamma_j}, d)$, to be used in equation 5.7 will be the product of this geometric efficiency for extended sources and of the calculated $\varepsilon_{int}(E_{\gamma_j})$.

5.1.1 Determination of the number of protons from the monitor chamber

The setup of the experimental test is shown in figure 5.3. In order to provide a comparative measure of the beam intensity, other simulations have been performed to reveal the number of protons reaching the target. The number of protons calculated with this method provides a valuable comparison to asses the correctness of the activation method. After having determined the initial experimental proton energy (as described in section 2.1.2), and simulated the monitor chamber as a kapton cylinder filled with dry air, it is possible to obtain the average energy deposition of the particles crossing the chamber. The initial energy was estimated to be ∼29.2 MeV, which corresponds to an average energy deposition $\Delta E_{1p} = (18.486 \pm 0.003)$ keV per proton in the monitor chamber air (the actual energy of the protons reaching the monitor chamber would be slightly lower than 29.2 MeV and this is taken into account by the

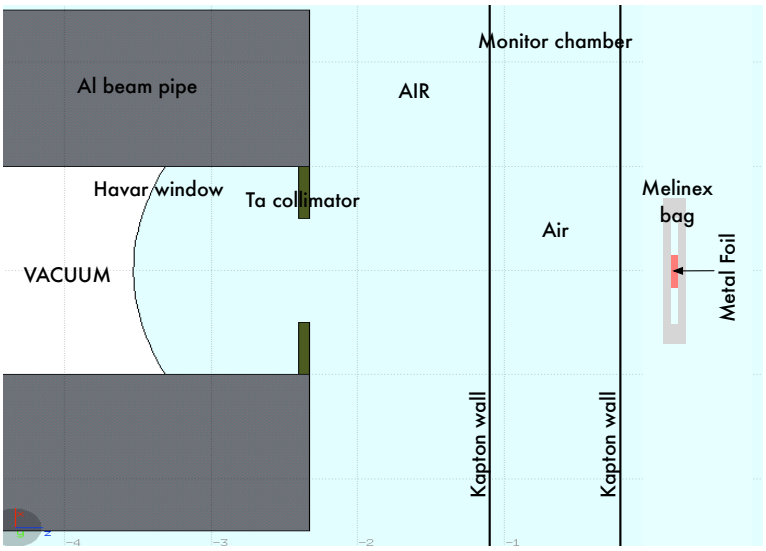

Figure 5.3 – Simulated experimental setting: the proton beam, coming from the cyclotron, travels in vacuum until the havar window. Then, in air, it passes through the final part of the aluminium beam pipe, the tantalum collimator, the monitor chamber and the target with its supporting plastic bag. In this image, for reasons of good visualisation, metal foil and melinex bag are not in scale with the other objects of the setup.

Monte Carlo code to give that energy deposition). Knowing the ionisation potential of air due to protons, $W_{air} = (34.23 \pm 0.14)$ J/C, and the total charge measured by the monitor chamber during irradiations, Ch_{exp}, the number of bombarding particles can be derived from:

$$Ch_{1p} = \frac{\Delta E_{1p}}{W_{air}} = (8.65 \pm 0.03) \times 10^{-17} C \tag{5.10}$$

$$N_{MC} = \frac{Ch_{exp}}{Ch_{1p}} \tag{5.11}$$

where Ch_{1p} is the charge created in the monitor chamber air by one proton and N_{MC} is the number of proton generating the measured experimental charge. Assuming that the number of protons crossing the chamber is the same as the number of protons reaching the target level (condition true as long as there are no thick objects between the chamber and the target stopping part of the beam) the only correction to be applied to N_{MC} to obtain the number of protons crossing the target is due to the difference between the size of the beam spot and the target:

$$Np_{MC} = N_{MC} \frac{A_{target}}{A_{beam}} \tag{5.12}$$

The size of the target has always been chosen to be smaller than the beam spot (in particular the beam radius was 0.5 cm and the target radius was 0.3 cm, so that $\frac{A_{target}}{A_{beam}} = 0.36$). On the other hand, if the target area were larger than the beam size, the correction to be applied would have been $\frac{A_{beam}}{A_{target}}$. In any case it is of great importance to have a uniform beam spot, or at least to know its intensity on X and Y axes in order to be able to apply the due corrections to calculate the number of crossing protons.

5.1.2 CHOICE OF THE TARGET

As the production cross section is a function of the beam energy, in order to use the equation 5.7 it is necessary that the beam is monochromatic or at least strongly peaked in energy, so that the uncertainty of the chosen $\sigma_i(\overline{E_p})$ is small. Moreover the target must be chosen according to the characteristics of at least one particular produced radioactive isotope. It must have:

- a large $\sigma_i(E_p)$ so that the detection of its decay photons is possible above the background noise;
- a unique decay channel as it should be the only isotope to produce photons with a specific energy, so that it is possible to associate those photons with the production of that isotope;
- a large probability of producing those photons ($P_{\gamma_{ij}}$);
- a suitable decay time ($T_{1/2}$ of the order of few hours), so that the photons are well visible even after a short time of counting which however must not be too short otherwise the photons would be lost before the counting begins.

According to these limitations, the chosen targets were, other than the widely used copper: natural titanium and natural cadmium.

Copper

Since at 29 MeV (one of the proton energies achievable from the cyclotron of the University of Birmingham) the cross section of production of the chosen daughter isotope of natural Cu+p is low, I preferred to decrease the energy of the beam using a 5 mm thick polystyrene absorber placed on the beam line in front of the target. The energy of the protons entering and escaping from the 100 μm natural Cu target is shown in figure 5.4 (a).

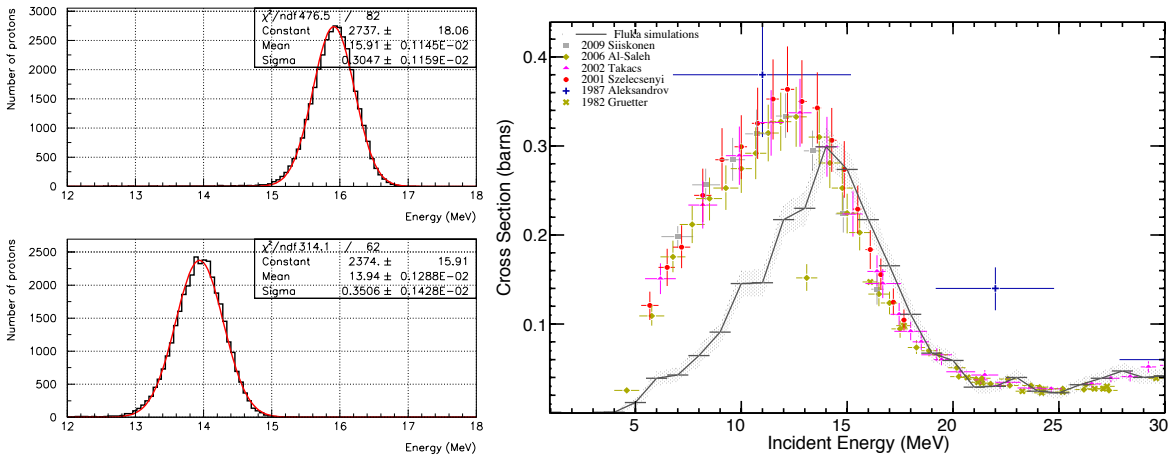

(a) (b)

Figure 5.4 – (a) Spectra of the protons incident (top) and escaping (bottom) the target. (b) Cross section for the production of ^{63}Zn created in the reaction of natural copper and protons: data in literature and results from Fluka simulations.

The reaction of interest is $^{63}\mathrm{Cu} + \mathrm{p} = {}^{63}\mathrm{Zn} + \mathrm{n}$ with Q-value = – 4.149 MeV and threshold[1] = 4.215 MeV (the abundance of ^{63}Cu in natural Cu is 69.15%). ^{63}Zn (with half life $t_{1/2}$ = 38.47 min) decays by electron capture to ^{63}Cu emitting the gamma peak at 669.62 keV (with probability of emission $P\gamma_{669.62\mathrm{keV}}$ = 8%) satisfying the requirements listed above. The estimated average energy in the middle of the thickness of the target was 14.93 MeV and its standard deviation was 0.33 MeV. The other possible reaction producing ^{63}Zn is $^{65}\mathrm{Cu} + \mathrm{p} = {}^{63}\mathrm{Zn} + 3\mathrm{n}$, which at the energy of this test was not energetically possible, since its Q-value is -21.976 MeV. At this energy, the corresponding cross section for production of ^{63}Zn from natural copper is (0.22 ± 0.02) barns.

For a comparison with the cross section data in literature, simulations with Fluka were performed (see Appendix 3.2 for nuclear activation in Fluka). The simulated

[1]The threshold of a reaction is defined as the minimum kinetic energy of an impinging particle that makes the reaction energetically possible. For reactions induced by charged incident particles, the real threshold, i.e. the energy at which the reaction has a nonzero cross section, will be at a value somewhat greater than the difference between the rest masses of the initial interacting particles and final products (Q-value) because of coulomb effects. The Q-value is positive for exothermal reactions and negative for endothermal reactions. If the mass of the impinging particle is m, then the threshold for reactions having negative Q-values can be approximately calculated with $-[(\mathrm{A}+\mathrm{m})/\mathrm{A}]\mathrm{Q}$, where A is the mass of the target.

data were obtained simulating a uniform intensity beam crossing in vacuum a natural copper target (100 μm thick). Changing the energy of the incident beam between 0 and 30 MeV in steps of 1 MeV and detecting all the decay photons at 669.62 keV escaping the target (in the time required for all the created ^{63}Zn to totally decay to ^{63}Cu), the cross section was calculated according to:

$$\sigma_{^{63}Zn}(E_p) = \frac{N\gamma_{669.62keV}}{P\gamma_{669.62keV}\ N_p\ N_t} \tag{5.13}$$

where $N\gamma_{669.62keV}/P\gamma_{669.62keV} = N_{^{63}Zn}$ is the number of ^{63}Zn isotopes created during the irradiation, N_p is the number of protons crossing the foil (chosen by the user) and N_t is the number of Cu nuclei per cm^2 in the target. In figure 5.4 (b) the data in literature for the cross section of production of ^{63}Zn from natural copper and protons and the cross sections simulated with Fluka are shown. As can be seen the agreement is not good for energies lower than 13 MeV. This is a bug of the current (Fluka 2011.2) and previous versions of the code and, while some inconsistencies between the cross sections calculated by Fluka and those in literature were already known [82], this bug was not documented and it has been signalled to the Fluka developers. While waiting for a correction to be made to the code, Fluka cannot be used to accurately predict activation of Cu for those low proton energies.

Experimentally, four copper foils (Δt_{irr}=100 s) were irradiated using different proton currents. Detecting the decay photons for a $\Delta t_{count} = 1000$ s (see figure 5.5) using the HpGe detector, counting those at 669.62 keV and subtracting the background (acquired for the same Δt_{count} without any foil) and the Compton component of the spectrum, the number of protons has been calculated through equation 5.7. The results and the comparisons with the measurements from the monitor chamber are shown in table 5.1.

So as already known, natural copper can be easily used for nuclear activation to obtain the number of initial particles crossing the target. Its main advantage is the

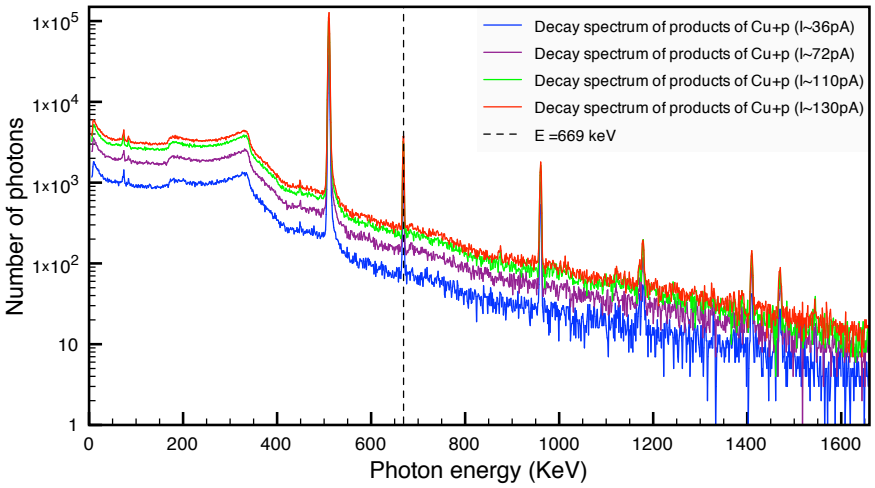

Figure 5.5 – Acquired spectrum of the decay photons emitted by the irradiated Cu foils. The useful gamma peak is at 669.62 keV due to the decay of ^{63}Zn to ^{63}Cu.

Target	$Np_{MC} \times 10^{10}$	$Np_{Cu} \times 10^{10}$	I_{MC}(pA)	I_{Cu}(pA)
1	2.256 ± 0.008	2.3 ± 0.4	36.1 ± 0.1	36 ± 6
2	4.46 ± 0.02	4.5 ± 0.8	71.5 ± 0.3	71 ± 12
3	6.84 ± 0.03	6.6 ± 1.2	109.5 ± 0.4	106 ± 18
4	7.97 ± 0.03	7.8 ± 1.3	127.7 ± 0.5	120 ± 20

Table 5.1 – Comparison of the number of protons in the beam and current using the measurements and the simulation of the monitor chamber (MC) and the nuclear activation of the copper foils.

fact that it can be used even with proton beams with low energies given the low threshold (∼4 MeV) of the reaction producing ^{63}Zn. All of this makes this material a very good candidate for laser-driven proton activation at low energies and explains why so far it has been the preferred material for this kind of measurement.

Titanium

Using a natural titanium foil (thickness 55 µm) irradiated by protons with an initial energy of 29.2 MeV, the useful gamma peak is at 1.157 MeV, produced by the decay of ^{44}Sc ($t_{1/2}$=3.97 h and $P\gamma_{1157keV}$ = 99.9%) to ^{44}Ca by electron capture. The reactions

Reaction	Q-value (MeV)	Threshold (MeV)	isotopic abundance in ^{nat}Ti
$^{46}Ti + p = ^{44}Sc + ^{3}He$	-13.95	14.26	8%
$^{47}Ti + p = ^{44}Sc + \alpha$	-2.25	2.30 [2]	7.3%
$^{48}Ti + p = ^{44}Sc + n + \alpha$	-13.88	14.17	73.8%
$^{49}Ti + p = ^{44}Sc + 2n + \alpha$	-22.02	22.45	5.5%
$^{50}Ti + p = ^{44}Sc + 3n + \alpha$	-32.96	33.63	5.4%

Table 5.3 – Reactions producing ^{44}Sc from ^{nat}Ti irradiated by protons with related Q-values, thresholds and abundances of the Ti isotope involved in each reaction.

producing ^{44}Sc from natural Ti are listed in table 5.3.

From the gaussian fit of the spectrum of the proton beam in the middle of the thickness of the titanium foil obtained from the simulation of the experimental setting (in figure 5.3), the average energy was 27.9 MeV (with σ=0.3 MeV). This implies that the reaction in the last row of table 5.3 does not take part in the production of ^{44}Sc. The cumulative corresponding cross section for ^{44}Sc production from natural Ti at 27.9 MeV is $(4.4 \pm 0.4)\times10^{-2}$ barns, chosen as an average of the values in literature (see figure 5.6).

Exactly as for ^{nat}Cu, simulations were performed to compare the cross sections in Fluka with the ones available from literature. By detecting the decay photons at 1.157 MeV escaping the target and calculating the cross sections according to:

$$\sigma_{^{44}Sc}(E_p) = \frac{N\gamma_{1.157MeV}}{P\gamma_{1.157MeV}\, N_p\, N_t} \tag{5.14}$$

with $N\gamma_{1.157MeV}/P\gamma_{1.157MeV} = N_{^{44}Sc}$ created during the irradiation, N_p the number of protons in the incident beam and N_t the number of Ti nuclei per cm^2 in the target, the results shown in figure 5.6 were obtained. The agreement with the existing data

[2] Even if this threshold is low enough to allow activation of a Ti target irradiated by a proton beam accelerated by the TARANIS laser beam, the ratio signal-noise would have been too low given the low cross section of production of ^{44}Sc at this energy.

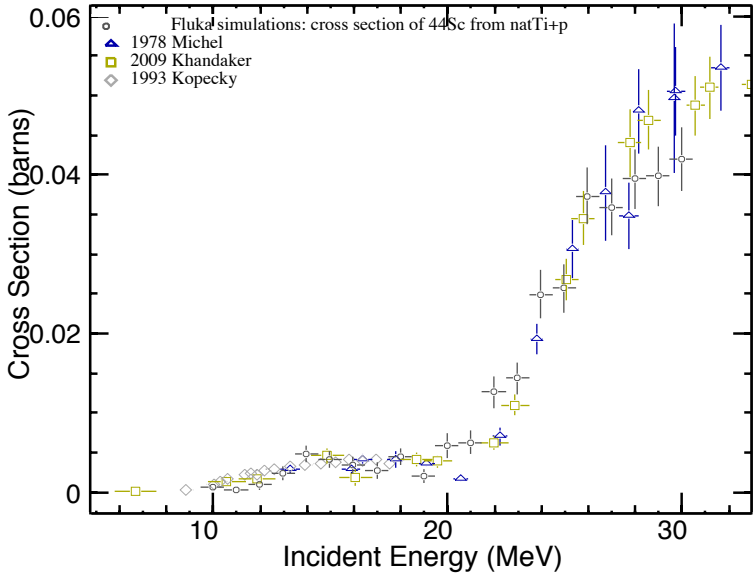

Figure 5.6 – Cross section for the production of ^{44}Sc from the reaction of natural Ti and protons: data in literature and results of the simulation with Fluka

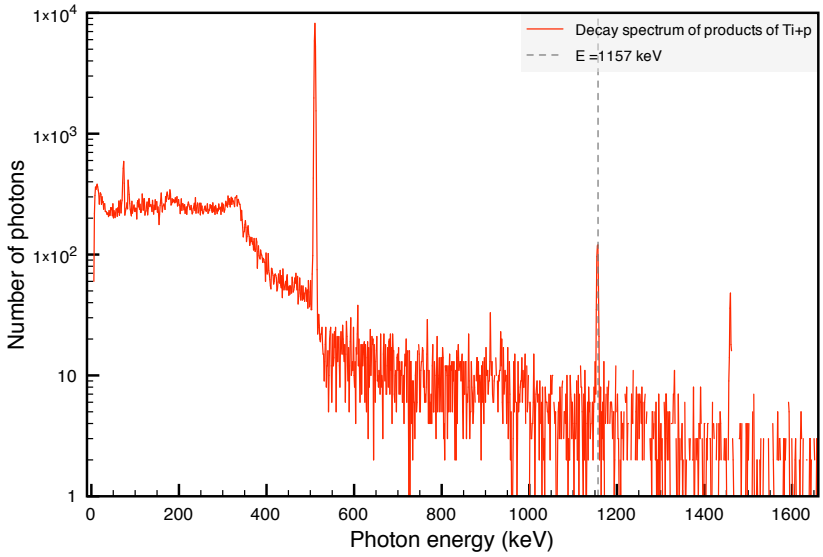

Figure 5.7 – Acquired spectrum of the decay photons emitted by the irradiated Ti foil. The useful gamma peak is at 1157 keV due to the decay of ^{44}Sc to ^{44}Ca.

is this time very good.

After the irradiation ($\Delta t_{irr} = 100$ s) and photon counting ($\Delta t_{count} = 4000$ s), see figure 5.7, the number of protons in the beam could be calculated using equation 5.7. The results and comparison with the measurement and simulation of the monitor

chamber are shown in table 5.4.

Target	$Np_{MC} \times 10^{10}$	$Np_{Ti} \times 10^{10}$
1	11 ± 1	12 ± 2

Table 5.4 – Comparison of the number of protons in the beam using the measurement and the simulation of the monitor chamber (MC) and the nuclear activation of the Ti foil.

Cadmium

Using natural cadmium targets (thickness ∼125 µm) irradiated by protons at 29 MeV, one of the useful gamma peaks satisfying all the necessary conditions is at 203 keV produced by the decay of ^{109}In ($t_{1/2}$=4.17 h and $P\gamma_{203keV}$ = 73.5%) to ^{109}Cd by electron capture (see table 5.6).

From the gaussian fit of the spectrum of the beam in the middle of the Cd foil obtained from the simulation of the experimental setting, the average energy was 27.7 MeV (with σ=0.6 MeV). The corresponding cross section in literature for the production of ^{109}In from nat Cd+p is (0.150 ± 0.013) barns. This value does not include the cross sections of the last two reactions in table 5.6 since their thresholds are higher than the maximum experimental proton energy.

Reaction	Q-value (MeV)	Threshold (MeV)	isotopic abundance in ^{nat}Cd
$^{108}Cd + p = {}^{109}In + \gamma$	4.53	0	0.89%
$^{110}Cd + p = {}^{109}In + 2n$	-12.72	12.83	12.49%
$^{111}Cd + p = {}^{109}In + 3n$	-19.69	19.87	12.8%
$^{112}Cd + p = {}^{109}In + 4n$	-29.09	29.35	24.13%
$^{114}Cd + p = {}^{109}In + 6n$	-44.67	45.07	28.73%

Table 5.6 – Reactions producing ^{109}In from ^{nat}Cd irradiated by protons. The related Q-values, thresholds and abundances of the Cd isotope involved in each reaction are also listed.

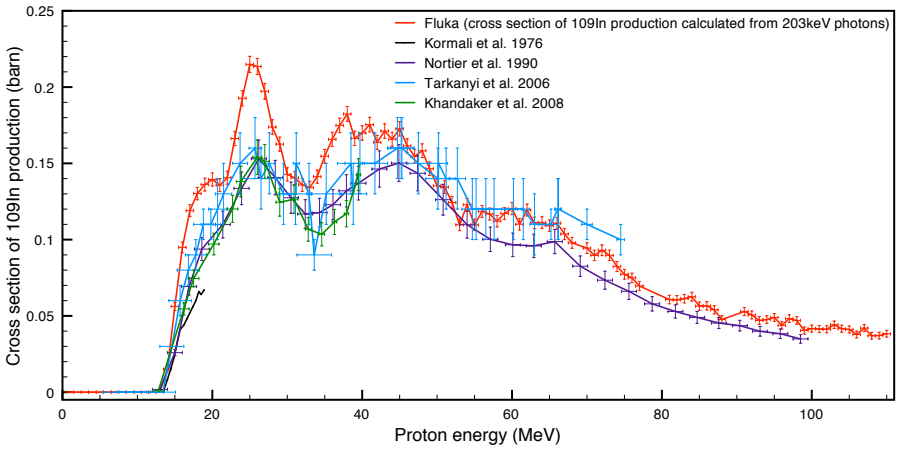

Figure 5.8 – Cross section for the production of ^{109}In from ^{nat}Cd+p: data in literature and results of the simulations with Fluka.

Again a comparison between the cross sections achievable with Fluka and those in literature was performed. I simulated a uniform proton beam (energy range 0-110 MeV) irradiating a 100 μm thick ^{nat}Cd target and detected all the emitted photons with 203 keV energy. The comparison is shown in figure 5.8. Except for the peak at ∼25 MeV the simulated cross sections and the data in literature are in reasonable good agreement.

Two different sets of tests using cadmium foils were carried out. In the first, changing the current of the proton beams, nine targets were irradiated one at a time (Δt_{irr}= 100 s) and then the spectra of the emitted photons were acquired (Δt_{count}= 1000 s), see figure 5.9 (a). After having subtracted the background and the Compton component of the spectra, the number of protons in the beams were calculated as well as the current. The comparison with the measurements of the monitor chamber can be seen in table 5.7. In the second test, the current of the beam was fixed and only one cadmium foil was irradiated (Δt_{irr}= 100 s). At the end of the irradiation the photon spectrum was acquired in four different counting times. The spectra are shown in figure 5.9 (b) and in table 5.8 is the comparison with the monitor chamber measurement.

Simulations of the two tests were also conducted. A comparison between the

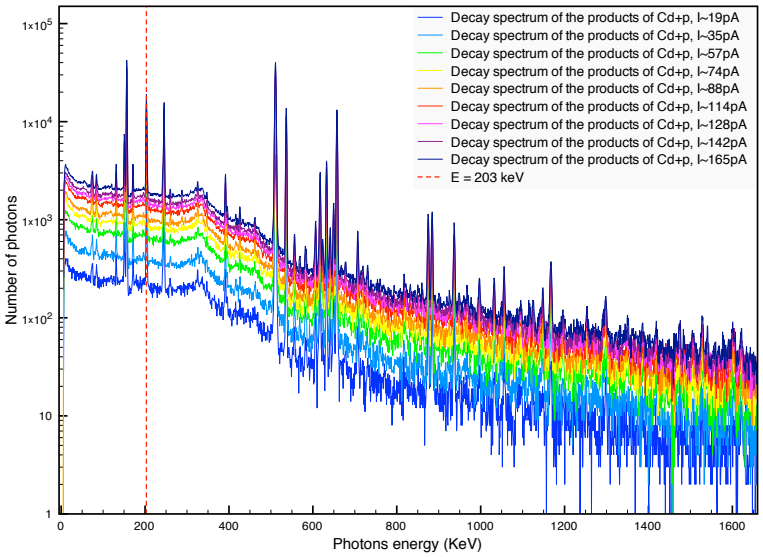

(a)

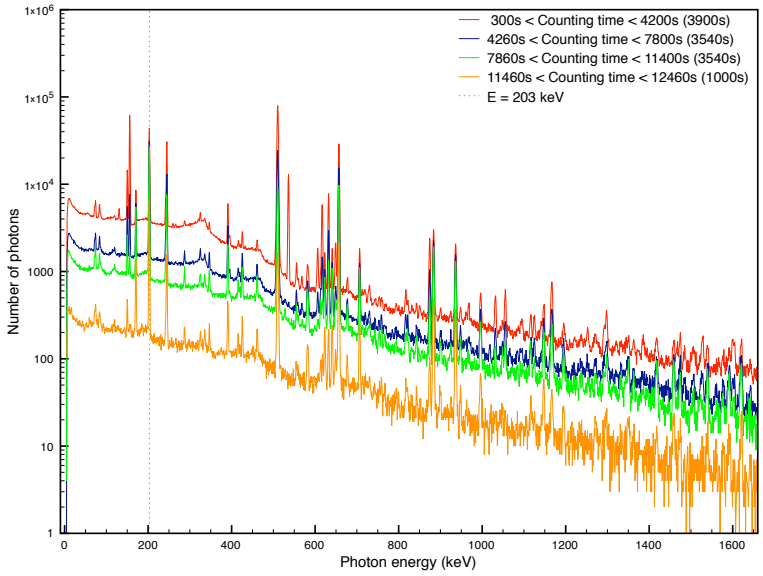

(b)

Figure 5.9 – (a) Photon spectra of nine irradiated Cd foils: each spectrum corresponds to an initial beam current. (b) Photon spectra of one irradiated Cd foil: each spectrum corresponds to a different counting time. In both the graphs, the photons useful to calculate the number of incident protons are at 203 keV produced by the decay of ^{109}In to ^{109}Cd.

number of photons at 203 keV detected experimentally and simulated with Fluka is shown in figure 5.10 (a) for the current test and (b) for the temporal evolution test. From the agreement of results between these simulations and the experimental

Target	$Np_{MC} \times 10^{10}$	$Np_{Cd} \times 10^{10}$	I_{MC}(pA)	I_{Cd}(pA)
1	1.188 ± 0.004	1.3 ± 0.2	18.69 ± 0.07	20 ± 3
3	4.61 ± 0.02	5.0 ± 0.8	73.8 ± 0.3	79 ± 12
8	7.12 ± 0.05	7.7 ± 1.2	114.0 ± 0.5	120 ± 20
9	10.30 ± 0.04	11.3 ± 1.8	164.3 ± 0.6	180 ± 30

Table 5.7 – Current test: results and comparisons of the number of protons in the beam and of the current using the measurements and the simulation of monitor chamber (MC) and the nuclear activation of some of the irradiated Cd foils.

Δt_{count} (s)	$Np_{MC} \times 10^{10}$	$Np_{Cd} \times 10^{10}$
$300 \leq \Delta t_{count} \leq 4200$	6.80 ± 0.03	7.8 ± 1.2
$4260 \leq \Delta t_{count} \leq 7800$	6.80 ± 0.03	7.6 ± 1.2
$7860 \leq \Delta t_{count} \leq 11400$	6.80 ± 0.03	7.5 ± 1.2
$11460 \leq \Delta t_{count} \leq 12460$	6.80 ± 0.03	7.6 ± 1.2

Table 5.8 – Temporal evolution test: results and comparisons of the number of protons in the beam using the measurement and the simulation of monitor chamber (MC) and the nuclear activation of one irradiated Cd foil. In each row, the number of protons is calculated using the photons counted in the corresponding Δt_{count}.

results, it is seen that Fluka, calculates correctly not only the cross section of production of ^{109}In at the energy of the incidental beam, but also the probability of emission of the 203 keV photons ($P\gamma_{203keV}$). Moreover, the assumption of using the energy in the middle of the target to calculate the number of protons is seen to be reasonable.

The same cannot be said for other isotopes which, in the reactions of natural cadmium and protons, are produced not only in the ground state, but also in the metastable state. An example is the case of the production of ^{110}In described in detail in the Appendix B. In the Appendix it is shown that simulated and experimental yields of ^{110}In in any of its possible states created from ^{nat}Cd+p are not in agreement. In principle the chosen photon peaks (at 657 and 884 keV) due to the decay of ^{110}In to ^{110}Cd by electron capture can be experimentally used to calculate the number of

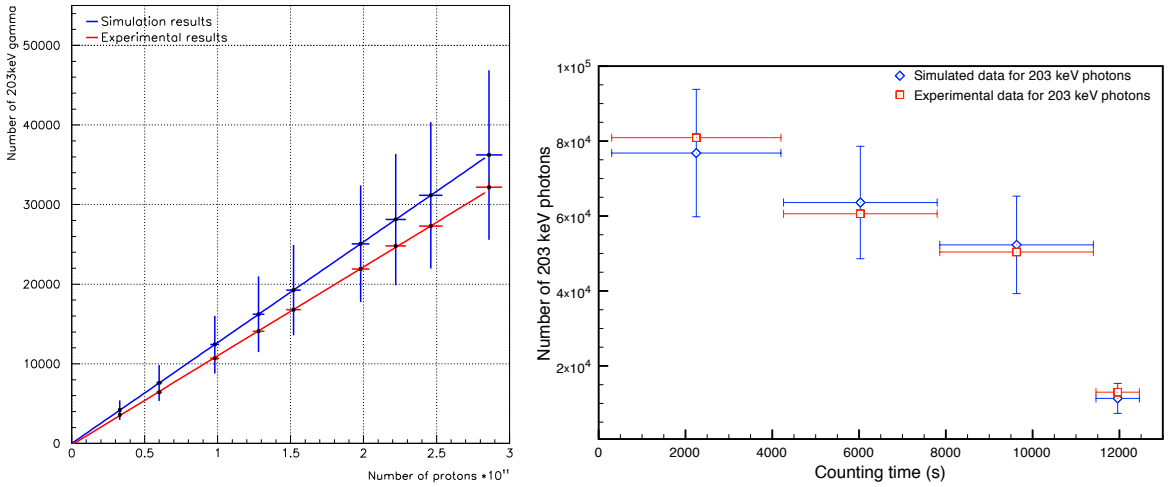

(a) (b)

Figure 5.10 – Experimental (red) and simulated (blue) results of the number of detected 203 keV photons emitted by the decay of ^{109}In to ^{109}Cd. In (a) each point was obtained changing the number of incident protons for each irradiated foil (Δt_{irr}= 100 s and 300s $\leq \Delta t_{count} \leq$ 1000s). In (b) the temporal evolution of the 203 keV photon emission is shown: the points were obtained irradiating only one foil and counting photons in four different counting times.

incident protons, but if the user wanted to use Fluka to support the analysis (for example if the beam is not monoenergetic, but has a broad spectrum), then those photons peaks should be avoided and preference given to the use of 203 keV peak from the decay of ^{109}In to ^{109}Cd.

5.2 CONCLUSIONS DEDUCTED FROM THE TESTS WITH MONOENERGETIC BEAMS

The level of accuracy obtained with the activation of the metal foils due to proton irradiation at 15 and 28 MeV has been found to be ∼17% compared to measurements made with the ionisation chamber. This was mainly due to the systematic uncertainty in the cross section ($\Delta\sigma \sim 9\%\ \sigma$) and in the detector efficiency ($\Delta\varepsilon_{tot} \sim 5\%\ \varepsilon_{tot}$) and to the fact that the experimental beam was not always perfectly uniform in particular near the edge.

Nuclear activation of a metal foil placed on the laser-driven proton or ion beam line, thus, seems to be a promising technique to identify any major faults of more standard dosimetric techniques, since the radiation proceeds very rapidly and does not saturate. Moreover this technique can in principle be used with any other ion beam always being careful to choose the γ peak satisfying the requirements listed in section 5.1.2. In this case, though, the only real limitation is that the cross section of production of the parental photon-emitting radioisotopes is not always available from the literature.

On the other hand, this method can be used any time the intensity of the incident beam is very high and in particular higher than or on the edge of what the conventional detection instruments can tolerate or it can simply be used as a validation.

Since laser-driven proton and ion beams produced so far have broad spectra, in order to use this technique as simply as it has been explained in this chapter an energy selection system should be employed. It would be, in fact, much easier to separate the entire beam energy in single energy bins (exactly as was performed for the radiobiological experiment described in chapter 4) and analyse the activation due to each bin rather than modifying the method and risking the deconvolution of the data becoming too difficult.

However, if it is not possible to use an energy selection system, the user will have to find metals with a cross section of production of radioactive isotopes strongly peaked at a particular energy. In fact, if the cross section has a large energy spectrum response, using a single foil it will not be possible to recover the initial beam energy. If, instead, the cross section is peaked in a certain energy with a small spread, the user will know that in the beam there was a number $X \pm x$ particles with an energy $E_{min} \leq E \leq E_{max}$ both depending on the width of the cross section distribution. Except for this quality, the other characteristics of the target should remain the same as in the monoenergetic case.

Another opportunity could be the use of a mixed metal foil or stacks of different metals. This could be useful not only for energy reasons, but also because at high laser intensities the accelerated beam could be a mix of protons and ions. In the case of a mixed metal foil, the requirements will be exactly the same as in the case previously explained, but with the advantage that, using more than one metal, there will be the possibility of detecting more than one proton or ion energy in just one irradiation. In the case of a stack, the first metal on the beam line will be a metal useful to detect the radioactive isotopes produced by the reactions with the ions (in first position because the ions are created with very low energy) and then the others useful to detect the radioactive isotopes (more than one species in dependence on the cross section response) produced by the protons.

CHAPTER 6

FLUKA SIMULATIONS OF LDXRB

At present, simulation programs capable of predicting exactly what happens in matter when a laser pulse hits a target are few. Experiments at high intensity have been often simulated using collisionless particle-in-cell (PIC) codes. They are called collisionless, because they assume that the 'hot' electrons generated by the laser beam interacting with the target have a high energy that they can travel through the target (generally with thicknesses of the order of μm or less) without interact with the target matter. This means that in case of simulation of real cases, collisionless PIC simulation codes can be an approximative source of comparison with real experiments only for high MeV electron beams accelerated in very, very thin targets, where the real energy loss is negligible, but they become very unsatisfactory in the case of thick targets where it is obvious that the energy of the beam lost crossing the target is not negligible.

At the same time Monte Carlo codes used in particle and nuclear physics, are not able to simulate laser-matter or laser-plasma interactions, but they are well capable

of simulating a general 'cold' electron beam moving inside matter.

In advance of a simulation code able to reproduce laser-matter as well as particle-matter interactions, I have implemented a simulation study of a simplified electron refluxing scheme in several different thick targets to investigate the X-ray production, which would be otherwise clearly impossible using collisionless PIC codes. Theoretical hot electron spectra have been involved and changing material and thickness of the perpendicularly irradiated targets, it was possible to obtain combinations (kT-material-thickness) giving the maximum photon yield. Part of this work has been published in the CLF annual report 2010-2011 (Fiorini et al. [95]).

6.1 Simulation implementation

The simulations presented in this work have been performed using Fluka. Given its aims, Fluka is not meant to simulate the reactions produced by lasers, but it can simulate the electron interactions producing the photon beam in cold matter. The reactions due to the electric field occurring in the target cannot be simulated using Fluka, so:

- since the laser interacts with a plasma created on a very thin layer (few micrometers) of the target, the produced electron spectrum is only dependent on the laser characteristics and not on the target material;
- the electron reflux is simulated by 'hand'. The electron beam exiting the target is forced to re-enter the target: the spectrum of the outgoing electrons is saved and while X% of the most energetic electrons can escape, (100-X)% of them are forced to re-enter the target. The chosen X for this study is 10 [96];
- each refluxing electron is reinserted in the target from the same point where it escaped and its direction cosines are inverted [5];

- second and third points above are repeated until the number of exiting electrons at the end of one of the reflux processes is null;
- the spectra of the photons emitted forward at the end of each reflux process is saved. The sum of all the 'forward' photon spectra is the result of this simulation study for each used target.

Figure 6.1 (a) and (b) show a schematic view of the simulation approach. In section 6.2 a more detailed explanation of the cards and user routines used in Fluka to perform the simulations is reported.

The initial electron spectrum follows a quasi Maxwellian distribution. The distribution findable in literature to describe the same process are several: some authors [97] use $dN_e/dE = E^2 \exp(-E/k_BT)$, others [98] use $dN_e/dE = E\exp(-E/k_BT)$, some others [99] $dN_e/dE = \sqrt{E}\exp(-E/k_BT)$ and others [100] even only $dN_e/dE = \exp(-E/k_BT)$. The only relation among them is the k_BT, taken from the ponderomotive acceleration or resonance absorption theory, but none of them really detected the initial electron beam (which is impossible to detect but at maximum to derive), so none knows what is the best equation of the spectrum to use. As a results of this ambiguity in the spectrum some authors saw the expected k_BT to be respected, while some others did not.

Since for the same k_BT the differences among these distributions are quite remarkable (as shown in figure 6.2), I decided to study at least two of them:
$dN_e/dE = E^2 \exp(-E/k_BT)$ and $dN_e/dE = E\exp(-E/k_BT)$, with N_e the number of electrons and E their energy. For simplicity from now on the first distribution will be identified with $(E^2\exp)$ and the second one with $(E\exp)$. The hot temperature (k_BT) depends on the intensity and on the wavelength of the main laser pulse and on the acting force. In particular in this study only perpendicularly irradiated targets are considered, so that the ponderomotive force should be the only acting force, but it is still valid also in the case where the resonance absorption is the main acting

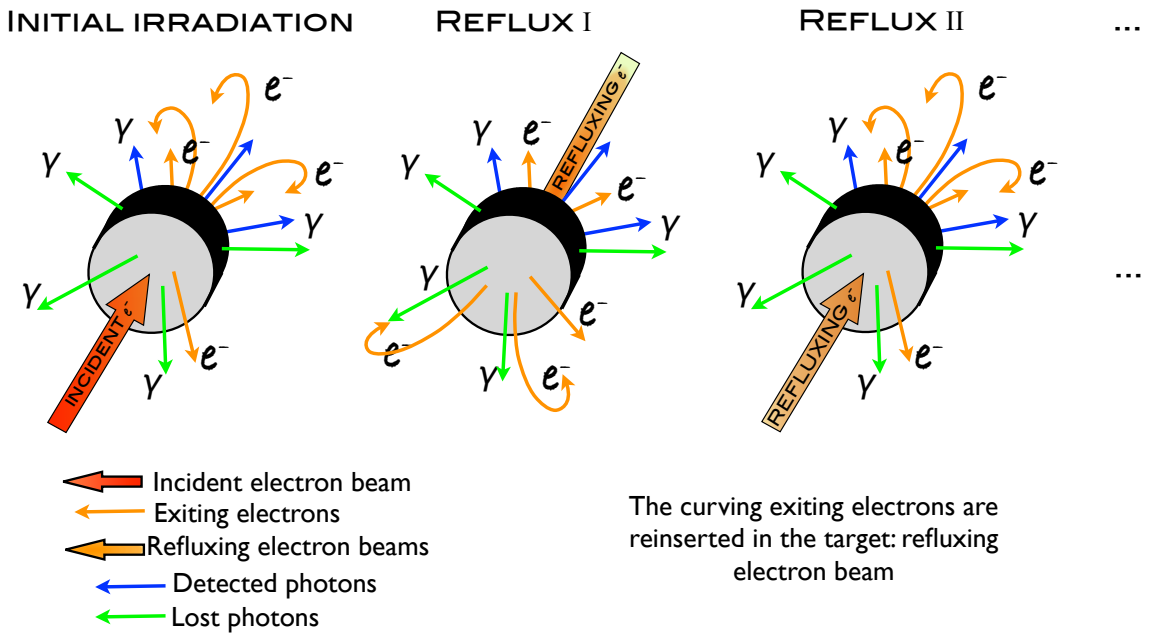

(a)

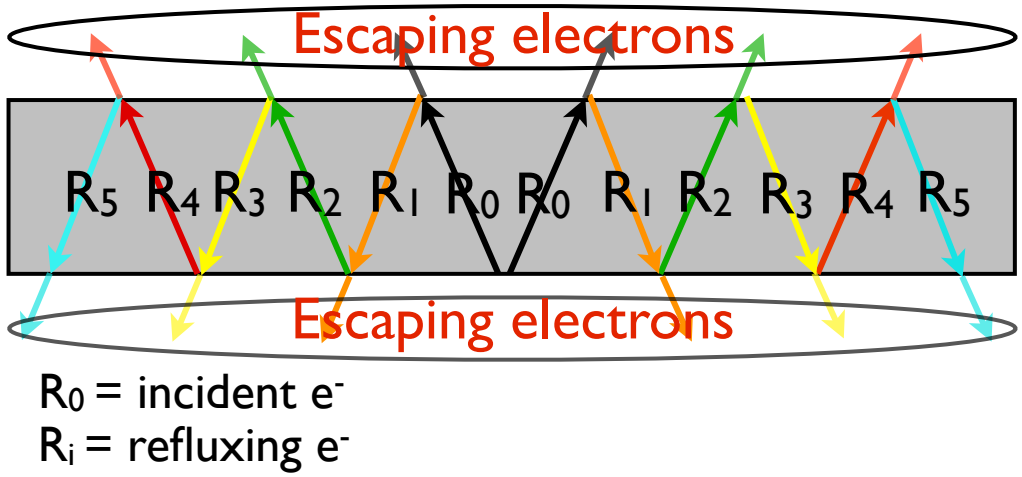

(b)

Figure 6.1 – Schematic view of simulation approach of the laser-driven electron and X-ray beams. (a) The refluxing electrons, 90% of the exiting electrons with lower energy (curving orange arrows), are reinserted with their energy in the target as many times as needed to stop all of them in the target. The photon spectra are saved only for the photons emitted forward (blue arrows) where one can expect real detectors are placed. (b) The refluxing electrons are reinserted from the same point where they got out and their direction cosines on X, Y and Z axes are inverted.

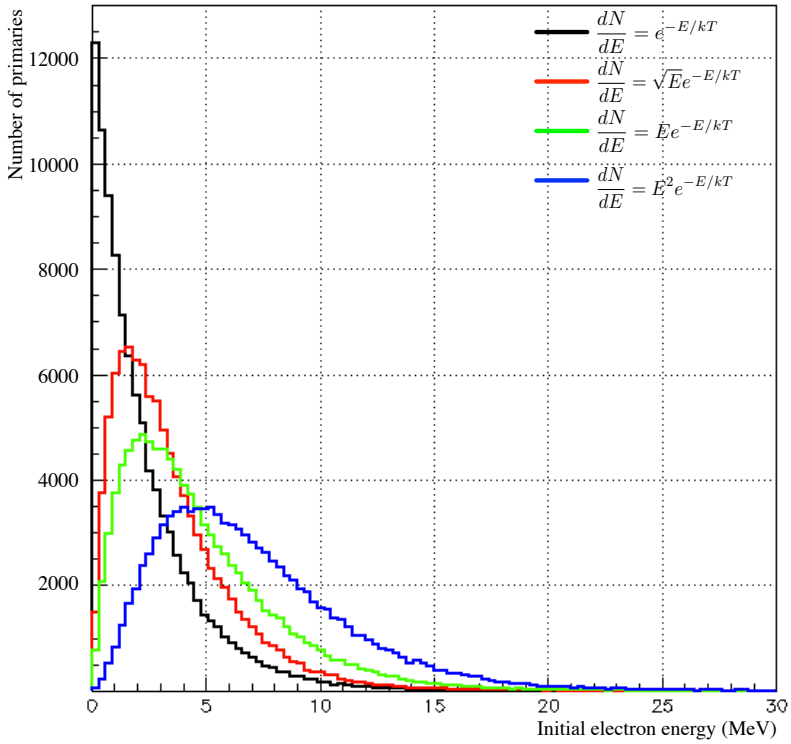

Figure 6.2 – Initial electron spectra findable in literature for the same k_BT value (2.3 MeV) and same number of simulated particles.

force because the yield results are expressed as a function of k_BT and not of the laser intensity. In fact, as seen in section 1.1.1, the main practical differences between the two forces are in the temperature of the accelerated electron beam and in its direction. Considering several possible k_BT and detecting all the photons emitted forward, this study can well represent the case when the two forces are acting separately creating, two different and separable electron beams or when one of the two acts more than the other. In the case the two forces act together in the target generating a single out coming beam, the user will need to combine the results of two different temperatures, but obviously they will need to know the right percentage of the acting forces. For this same reason, in the simulation the initial electron beam propagates into the target without any initial divergence: the divergence is seen to be a parameter dependent on the main acting force [18].

Targets made of different materials and with different thicknesses were simulated: Au, Ta, Cu, SiO_2 and PMMA. This selection was used to find out which thickness of each material maximised the number of produced X-rays and to compare the produced X-ray spectra.

6.2 CARDS AND USER ROUTINES USEFUL FOR THE SIMULATIONS

6.2.1 INPUT FILE

The input file is pretty basic and involves mainly an initial part where Fluka default card is defined, then a part to describe the beam parameters and the geometry and then a final part for the detection details and the number of input particles. Since these simulations involve refluxing electrons, similar input files were written to be used for each electron cycle. In particular one was written for the initial electron beam and one for the refluxes. The difference was only in the SOURCE card definition.

CALORIME is the chosen default for this kind of simulation, because, among other things, it enables:

- the Electro Magnetic Fluka (EMF) package (useful to request a detailed transport of electrons, positrons and photons);
- Compton scattering package, for the full treatment of electron binding and motion in Compton scattering. It is particularly important for low energies and/or heavy materials, and in general for all cases where the best accuracy for photon transport is requested;
- multiple scattering threshold at minimum allowed energy, for both primary and secondary charged particles.

The card MULSOP is used, for the lowest electron temperatures, to activate the single scattering given the fact that the Molière multiple scattering model becomes

unreliable below 20-30 keV. By activating the single-scattering option satisfactory results can be obtained in any material also in this low energy range (but with a noticeable increment of CPU time spent to do the simulations for the heaviest materials). The cards BEAM and BEAMPOSition are used, but their values are overwritten once Fluka reads the *source* routine. This routine is invoked by the SOURCE card, where some parameters of the beam are defined and then passed to the routine. In the case of the input for the initial electron beam in the SOURCE card were defined: k_BT of the initial electron spectrum, the radius of the beam (=0 for pencil beams) and its origin. In the case of the input for the refluxes, the SOURCE card was only used to give to the user routine the amount of escaping electrons (most of the times (100-refluxing electron)%=X%=10% was used, but also other percentages of escaping and refluxing electrons can be used). In the geometry and media part of the file, a sphere for the BLACKHOLE (the material surrounding the user geometry and determining the end of the transport for each particle entering in it) and one for the vacuum are as well defined as two cylinders one for the target (made of the one materials between Au, Ta, Cu, SiO_2 or PMMA) and two made of vacuum useful for the detection of the X-rays and electrons. The detection of the X-rays was performed using the *mgdraw* user routine invoked in the input file by the USERDUMP card. The USRICALL and USROCALL cards were also used in order to invoke the routines useful to *mgdraw* to write the output file, *usrini* and *usrout*. In fact, the particular output file I wanted was not an ASCII file, but a binary file called *ntuple* which is a particular matrix file read by the program PAW (Physics Analysis Workstation, CERN, http://paw.web.cern.ch/paw/reference_manual/) containing the requested characteristics of the detected particles. To conclude the input file, the initial random seed (used to start the pseudo random number sequence of the Monte Carlo) and the number of initial electrons were defined.

6.2.2 SOURCE ROUTINES

Two different set of *source* routines were written in fortran: one for the initial electron beam and one for the refluxing beams. Both of them, in the first few lines of the code, include the 'initialisation' where the parameters passed from the SOURCE card and other parameters useful for the simulation are read and saved. The initialisation is read only once, during the creation of the first particle of the beam, the characteristics of which are defined in the code lines following the initialisation. Then Fluka enters again in this routine (jumping the initialisation) anytime another primary particle is generated.

Source routines for the initial beam

In order to define the energy of each generated particle, one of the possible ways (the most elegant and accurate) is inverting the known statistical equation of the spectrum, so that instead of N as a function of E, one has E as a function of N (with N the number of particles and E their energy).

Since in this particular case it is not possible to invert the functions of the distribution, $dN_e/dE = E^2 \exp(-E/k_B T)$ or $dN_e/dE = E \exp(-E/k_B T)$ with N_e the total number of electrons and E their energy, it is necessary to find another way. A gamma distribution and its properties are used.

A random variable x is gamma-distributed with scale θ and shape *n* if its distribution is denoted by the equation 6.1:

$$\Gamma(n, \theta) = \int_0^\infty x^{n-1} e^{-x/\theta} dx \tag{6.1}$$

with $x \geq 0$ and $n, \theta > 0$. The exponential distribution is a particular case of gamma distribution with $n = 1$. In our case $n - 1$ is 2 for $(E^2 \exp)$ and 1 for $(E \exp)$, $x = E$ and $\theta = k_B T$.

The equation 6.1 for $(E^2 \exp)$ becomes:

$$\Gamma(3, k_B T) = \int_0^\infty E^2 e^{-E/k_B T} dE = N_e \tag{6.2}$$

and for $(E \exp)$:

$$\Gamma(2, k_B T) = \int_0^\infty E e^{-E/k_B T} dE = N_e \tag{6.3}$$

For integer n, if x_1, x_2, ... x_n are independent aleatory variables, each one following a gamma distribution with scale θ and shape α_i, then the property in equation 6.4 is valid:

$$\sum_{i=1}^{n} \Gamma(\alpha_i, \theta) = \Gamma(\alpha, \theta) \quad \text{with} \quad \alpha = \sum_{i=1}^{n} \alpha_i \tag{6.4}$$

Therefore in the case of $(E^2 \exp)$, $\Gamma(3, k_B T)$ can be rewritten as the sum of three independent exponential distributions:

$$\Gamma(3, k_B T) = \Gamma(1, k_B T) + \Gamma(1, k_B T) + \Gamma(1, k_B T) \tag{6.5}$$

and in the case of $(E \exp)$ as:

$$\Gamma(2, k_B T) = \Gamma(1, k_B T) + \Gamma(1, k_B T) \tag{6.6}$$

where each $\Gamma(1, k_B T)$ defines the distribution of an independent random variable E. The inverse of an exponential distribution is given by:

$$F^{-1}(\Gamma(1, \theta)) = -\theta \ln u \tag{6.7}$$

being u a variable uniformly distributed on $(0, 1]$. Thus the inverse of $\Gamma(3, k_B T)$ can be rewritten as in equation 6.8:

$$F^{-1}(\Gamma(3, k_B T)) = -k_B T (\ln(N_1) + \ln(N_1) + \ln(N_3)) \tag{6.8}$$

and the inverse of $\Gamma(2, k_B T)$ as in equation 6.9:

$$F^{-1}(\Gamma(2, k_B T)) = -k_B T\,(\ln(N_1) + \ln(N_2)) \tag{6.9}$$

with N_1, N_2 and N_3 independent variables uniformly distributed on $(0, 1]$. For fractional n, the algorithms explained in [101] can be used.

Equations 6.8 and 6.9 have been used in the *source* routine to define the inverse of the energy distributions. Each time Fluka generated a new primary particle, the natural logarithms of three (for $(E^2 \exp)$) or two (for $(E \exp)$) independent random numbers (N_1, N_2 and N_3 generated using the Fluka subroutine FLRNDM) were calculated, summed to each other and then multiplied by the $k_B T$ coming from the SOURCE card, to assign an energy E to the particle. The initial position of the beam is also defined in this routine. At the end of a run, in dependence on the $k_B T$ chosen in the input, the created initial beam had one of the spectra shown in figure 6.5 (a) for $(E^2 \exp)$ or one of the spectra shown in figure 6.7 (a).

Source routines for the refluxing beams

As explained later in this section, during each target crossing the *mgdraw* routine creates an ASCII file containing the properties (energy, position and direction cosines) of each electron exiting the target in the main motion direction. This means that in the case of an electron emitted after the first crossing in a forward direction, its properties will be saved, otherwise, if emitted backward it will be lost, because in this assumption only the bulk electrons (i.e. those moving as a body carrying the electric field) can do the reflux. In the case of an electron emitted after the first reflux, the bulk electrons will be directed backward, so in this case only the electrons emitted backward will be saved in the ASCII file. And so on for all the other refluxes. Since the name of the file created by *mgdraw* is specific to each reflux, each *source* routine will read one file at a time. Therefore, several *source*s have been writ-

ten, one for each reflux, where the only difference is the name of the file to read.

In the initialisation part, the routine reads the number for the amount of escaping electrons passed by the SOURCE card, reads the electron file (saving the number of lines: each line is an electron), sorts partially the energy using a Bubble sort algorithm rewriting in the same file. All of this, being in the initialisation, is done only once at the beginning of the specific reflux run. The Bubble sort is a sorting algorithm that works by repeatedly stepping through the list to be sorted, comparing each pair of adjacent values and swapping them if they are in the wrong order. After the first iteration the last energy value in the list (as well as the exiting position and direction cosines of that electron) will be the highest one and it will not be compared again; after the second iteration the second highest energy value will be the second-last (and it will not be compared again) and so on until there are no more values to be compared and the list is completely sorted. Since the assumption requests that only X% of the highest energy electrons can escape the reflux, the routine does not need to sort all the entire file, but only until X% of all the energy values in the file have been placed deeper in the file. The number of electrons to be reinserted in the target and so to start the simulation will be most of the times (100-X)%=90% of the number of lines in the first ASCII file. This new number is saved again in a counter array, N_e. Energy, position and direction cosines are saved in arrays, where the number of each line represents an electron. The initialisation ends here.

The first time Fluka enters in the part following the initialisation an electron is created with the energy, the position and the inverted direction cosine of the first line of the arrays saved in the initialisation and then it fixes $N_e = N_e - 1$. For the second electron Fluka will read the second lines in the arrays and another 1 will be subtracted from N_e; and so on until $N_e = 0$. At this point the routine will overwrite the NOMORE flag, changing it from 0 to 1, which forces Fluka to end the run.

6.2.3 MGDRAW ROUTINES

mgdraw is a user routine useful to detect particles in a particular region of space. In my case I decided to detect electrons and photons using the BXDRAW subroutine of the fortran file, necessary to detect particles crossing a chosen boundary between two different geometry regions. In general, photons will be always detected forward (where a real detector could be placed), while electrons will be detected forward and backward depending on the number of reflux. After the first crossing the electrons will be detected on the boundary between the target and another region made of vacuum placed on the right of the target (as seen in figure 6.3). After the first reflux, the electrons will be moving backward and for this reason they will be detected in a region adjacent to the target but this time placed on the left. After the second reflux, the reentering electrons will be moving forward again and so they will be detected on the boundary between the target and the region on its right. And so on for all the other refluxes: odd refluxes will correspond to a detection on the left of the target, while even refluxes and first incident beam (which could be thought as reflux 0) will correspond to a detection on the right of the target (see figure 6.3). This means that two different *mgdraw* routines has to be written with the only difference being the boundary used for the electron detection.

During each reflux cycle *mgdraw* will open two files: one necessary to detect the photon beam emitted forward with its properties and one necessary to detect the electron beam in its own direction. The first file will be an ntuple initialisation file: a sort of matrix file (to be passed to other routines in order to be written in the right format) where each line represents a photon and each column one of the chosen scored variables: position on X, Y and Z axis, number identifying the reflux (0 if the photons come from the initial electron beam, 1 if the photons come from the first refluxing electron beam and so on) and energy in MeV. The information created by this file are then passed to other three routines *usrini*, *usrout* and *histin* which cre-

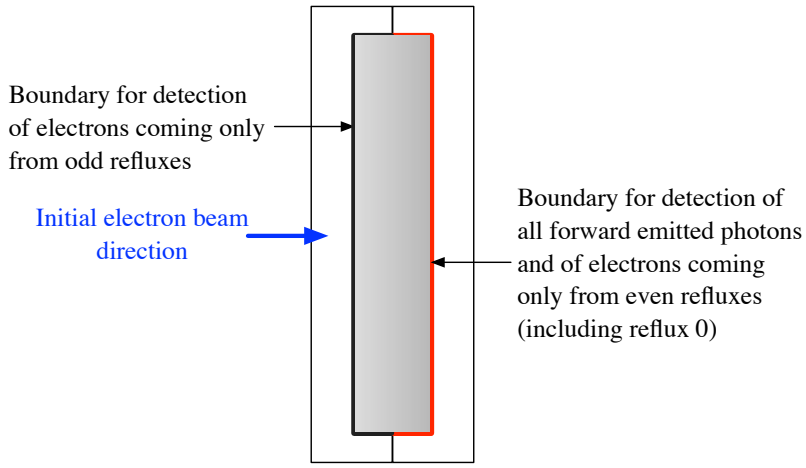

Figure 6.3 – Schematic view of the target and of the surrounding vacuum regions. Two boundaries between the target and each vacuum region are highlighted: the red boundary on the left is used for the detection of photons and electrons coming from even refluxes and from the first target crossing and the black boundary on the right for the detection of the electrons coming from odd refluxes.

ate the final ntuple file (called *xxx_hbk.his*) which can be opened and analysed with PAW. The second file is an ASCII file (called *xxx_ele.dat*) which contains the properties of only the electrons crossing the chosen boundary: energy in GeV, position on X, Y and Z axis and direction cosines on X, Y and Z are the information written. Both the created files will have the first part of their names (the *xxx*) depending on the name of the input file (only the second part is chosen in *mgdraw*). For this reason the input files to be written will be as many as the number of refluxes expected for the chosen initial electron energy, each one with a different name to avoid overwriting a created output file by a subsequent one. Moreover as already mentioned to allow the reflux also the *source* files will be as the number of refluxes expected, so that each one of them can read the proper *xxx_ele.dat*.

In my case, because of the energies involved in the simulations, the average number of refluxes would have been seven (and in particular fewer for the thickest target and more for the thinnest). So in total eight input (one for the initial beam and seven for the refluxes), eight *source* (one for the initial beam and seven for the refluxes), two

mgdraw (one for the left and one for the right detection), one *usrini*, one *usrout* and one *histin* routines were the necessary files to allow the complete function of one set of simulation for each target, thickness, distribution and k_BT used.

6.2.4 Compiling and run

All the files needed to complete a full run with all the refluxes are compiled and run by a single executable program appositely written to make the entire simulation totally automatic. This program firstly compiles all the fortran routines, then creates as many Fluka executables as the number of single simulations requested in a full cycle of refluxes (eight in total). During the creation of the executables it also calls the CERN libraries necessary for Fluka to create the output files readable by PAW (ntuple). Running this program, if the compiling does not give any message of error, the full simulation starts and there is no need to do anything else until it ends.

6.3 Simulation results

For each set of simulations, the eight created ntuples where merged in a single ntuple file and analysed using PAW. The number of produced photons was saved and their spectrum was plotted. By dividing the number of photons by the number of initial electrons the yield of the photons emitted forward was calculated.

As already mentioned the reflux is not very effective for thick targets and low temperatures, because the majority of the electrons are stopped in the target after the initial crossing. A difference in the yields, instead, can be seen for thin targets even at low k_BT. Examples of photon yields for irradiated targets with and without reflux for the $(E^2 \exp)$ distribution is shown in figure 6.4.

Some of the photon spectra obtained for the different k_BT simulated and for the $(E^2 \exp)$ spectrum are shown in figure 6.5. Integrating the obtained spectra the total number of forward emitted photons can be found. The thicknesses of the tar-

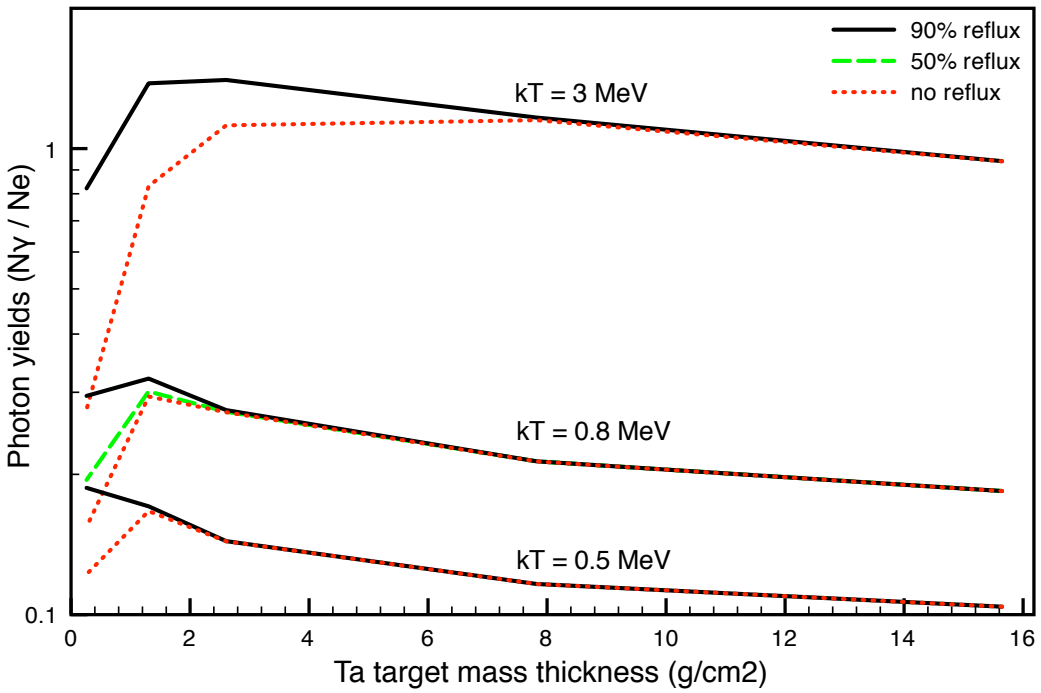

Figure 6.4 – Simulated photon yields (number of photons detected forward in 2π normalised by the number of initial simulated electrons) with and without reflux for (E^2 exp) distribution from tantalum targets. As can be seen, at the used energies (0.5, 0.8 and 3 MeV), the photon yields are higher for the cases where 90% reflux is used and lower where no reflux is used only for the thinnest thicknesses, while there are no differences for the thickest targets.

gets shown in figure 6.5 are those or close to those which maximise the number of forward emitted photons for the corresponding initial electron temperature. The spectra giving the largest numbers of photons are always produced by the high Z materials (as expected from the bremsstrahlung effect) as well as the highest energy photons. The peak of the energy of the photons emitted from SiO_2 and PMMA targets is in both the cases below 100 keV and it does not change much its position increasing the initial electron energy even for the highest studied k_BT (22.5 MeV). The tails in the spectra at high energies are always shorter for these materials than the tails created by the high Z targets. The K_α and K_β peaks are visible only for Au (energies between 66 and 80 keV) and Ta (energies between 55 and 67 keV) targets: this is because the energy threshold for particle transport in Fluka is close to 30 keV

and the K_α and K_β peaks for the other materials have energy lower than this threshold. From k_BT=1.85 MeV, also annihilation photons are visible: their production is, in fact, unlikely for the other lower temperatures because of the low number of photons with energy greater than 1.2 MeV (necessary for pair production).

Repeating the simulations for several target thicknesses it was possible to determine the thickness maximising the photon yields for each simulated k_BT and for both the initial electron energy distributions. Figure 6.6 and 6.7 show the photon yields plotted as a function of the mass thickness for each material and initial electron temperature studied respectively for $(E^2 \exp)$ and $(E \exp)$ distribution. Plotting the initial electron temperatures used in the simulations as a function of the mass thicknesses giving the maximum photon yields for each material, the graphs in figure 6.8 and 6.9 are obtained respectively for $(E^2 \exp)$ and $(E \exp)$ distribution.

These results were used to guide the selection of target materials and thicknesses for the laser experiments reported in chapter 7.

6.4 CONCLUSIONS

In order to obtain the largest photon yields, not only the material (or better its atomic number Z or Z_{eff}) is important but also its thickness. Several applications can use laser generated X-ray beams and knowing the material and the thickness which maximise the yields or the ones giving a certain spectrum is always preferable. But this study, if the approach well approximates the refluxing process, can be used as a method to estimate the initial temperature of the laser-driven electron beam. The important experimental step is the irradiation of targets (selecting one material between the studied ones) changing, shot after shot, its thickness choosing it in a 'wide' range. Detecting the number of photons (or even the dose due to photons) and looking at the maximum production in 2π forward, it will be possible to estimate the initial electron energy and so also the energy of the exiting electrons. This is

a test that could be implemented whenever there is an interest in using laser-driven electron and/or photon beams. In fact, it could be performed during the first day of an experiment to check that the electron energy is as expected according to the laser parameters (so that also the main driving force could be evaluated), or what is wanted for the experiment purposes, and once it is estimated carry on with the experiment.

Unfortunately the fact that there is ambiguity in the initial electron energy distribution to use does not help. A proof that one of them is better than the other has not be found yet, but a sort of evidence is given in chapter 7. A benchmark of the simulations explained in this chapter is given in section 7.3, where these results are used to estimate the initial energy of experimental electron beams produced by the Vulcan laser [102]. The comparison of these results with the theoretical electron energy expected for the experiment will be seen to be quite good despite all the assumptions made to simplify the simulation approach.

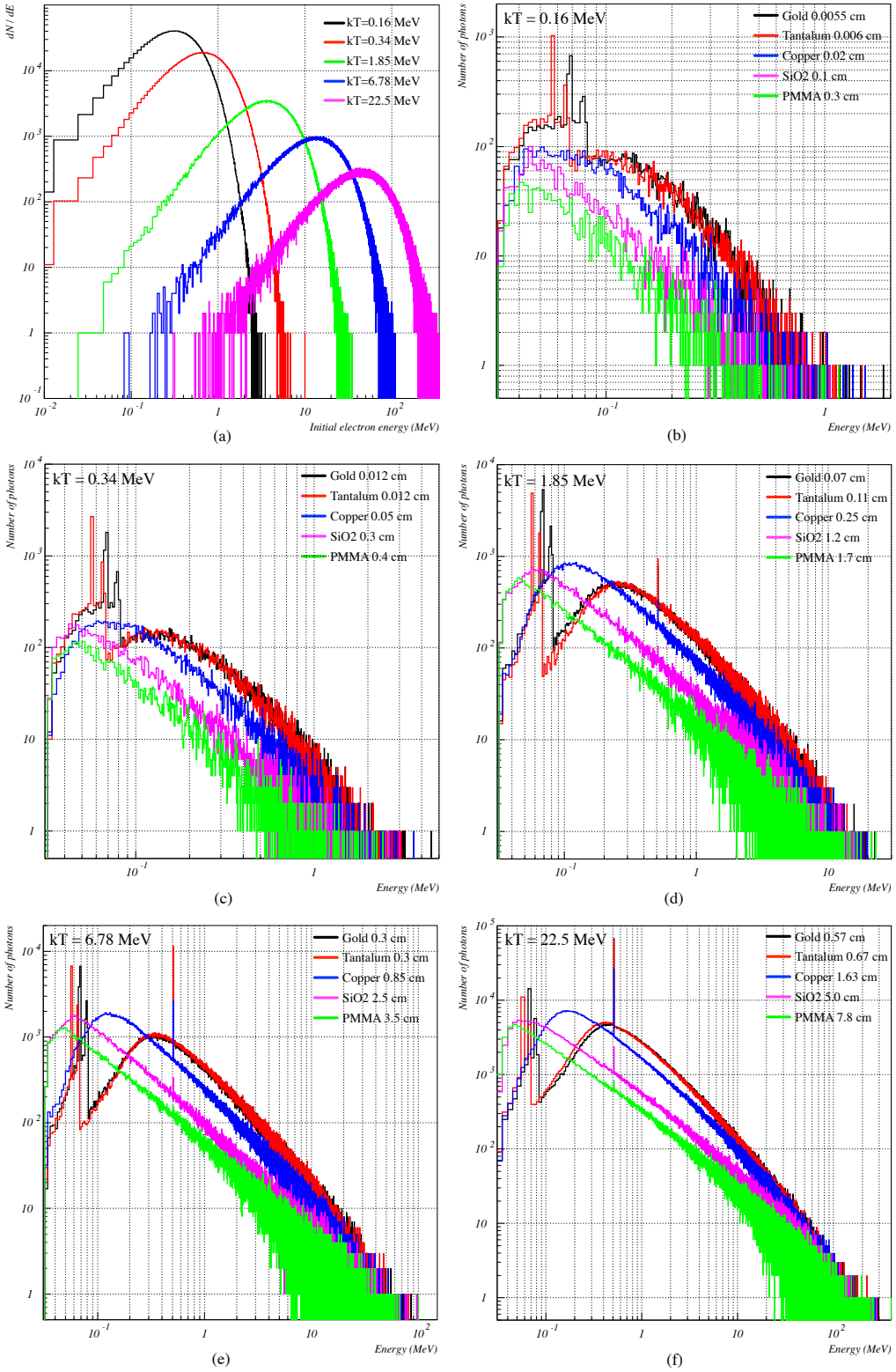

Figure 6.5 – (a) Simulated initial electron spectra with (E^2 exp) distribution. From (b) to (f) simulated spectra of the photons emitted forward from the irradiated targets for each studied initial temperature. The thicknesses of the targets shown here are those or close to those which maximise the number of forward emitted photons. The number of initial electrons for these simulations was 3×10^5.

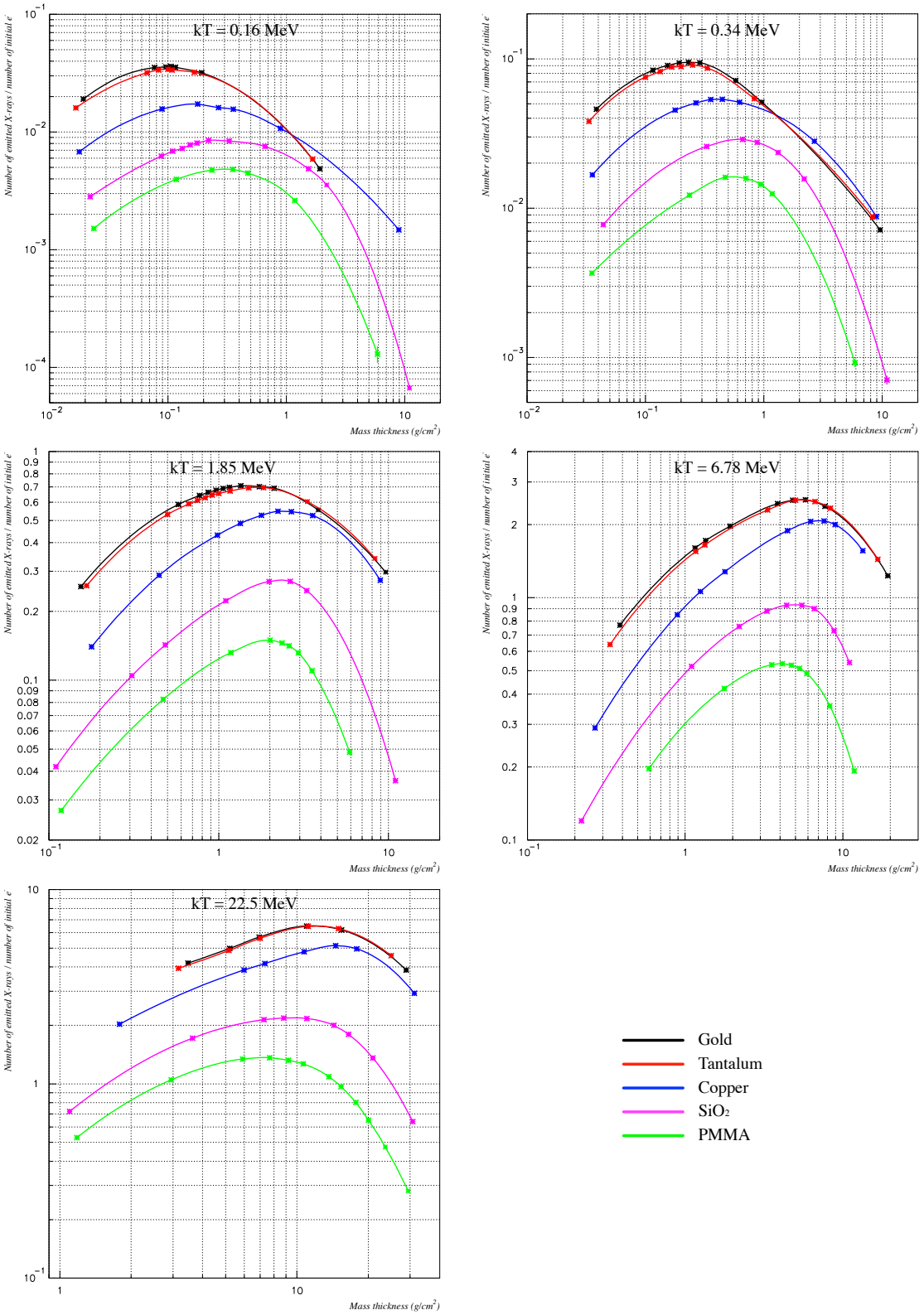

Figure 6.6 – Simulated photon yields as a function of the target mass thickness for gold, tantalum, copper, SiO_2 and PMMA for each studied initial electron temperature for the (E^2 exp) distribution.

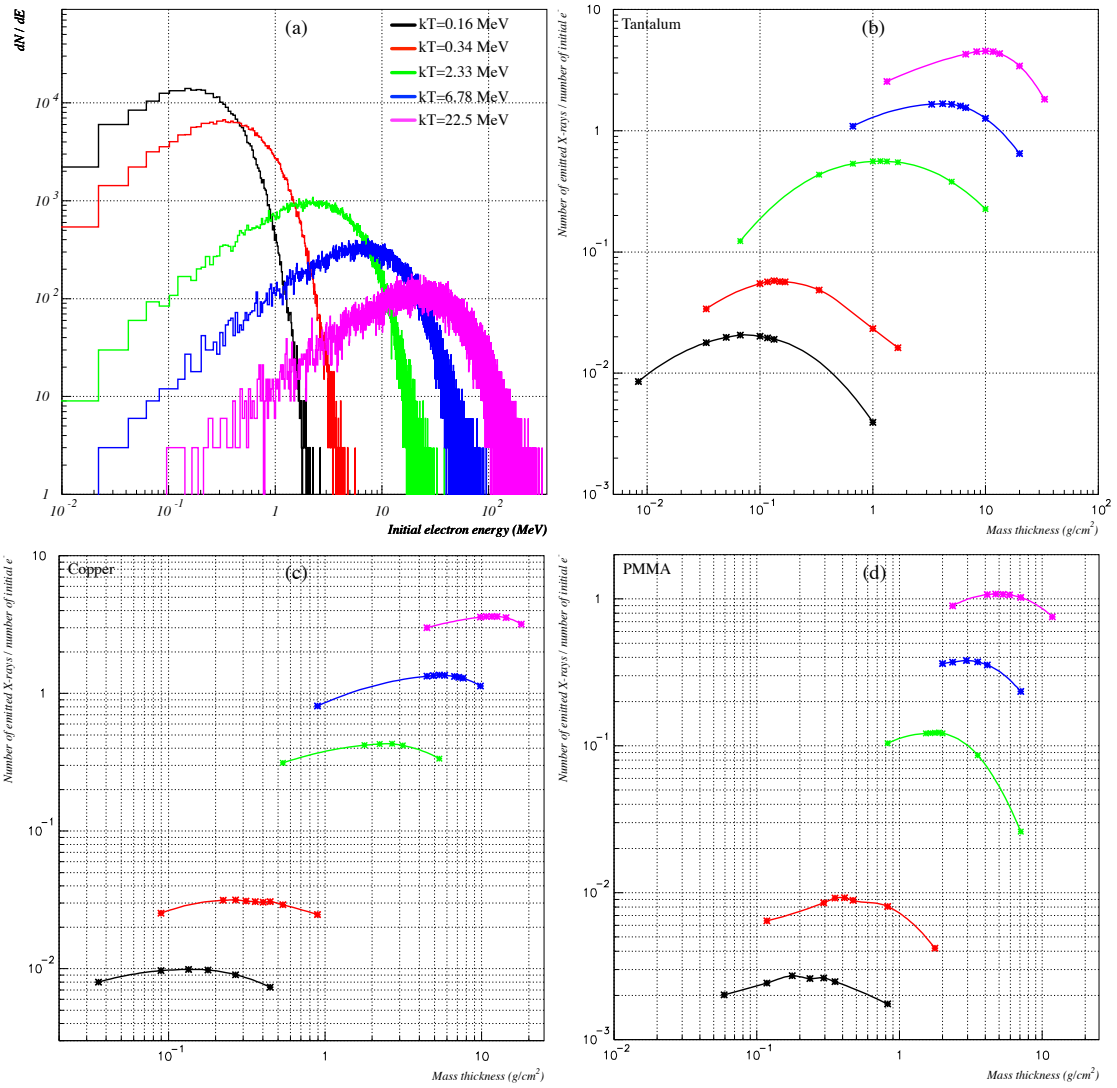

Figure 6.7 – Simulated photon yields as a function of the target mass thickness for tantalum (b), copper (c) and PMMA (d) for each studied initial electron temperature for the (Eexp) distribution. Each graph includes the yields for one material target and all the studied temperatures. The colour representing each kT is written in graph (a) where the initial spectra are shown.

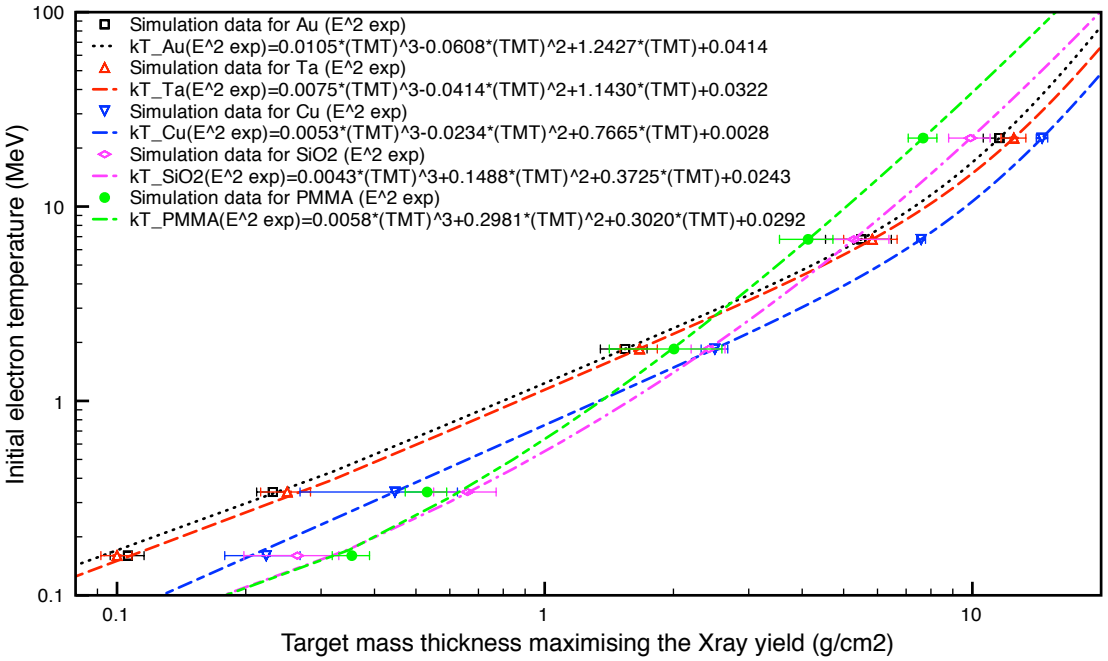

Figure 6.8 – Initial electron temperature of the $(E^2 \exp)$ distribution as a function of the target mass thickness giving the maximum X-ray yields for each studied material.

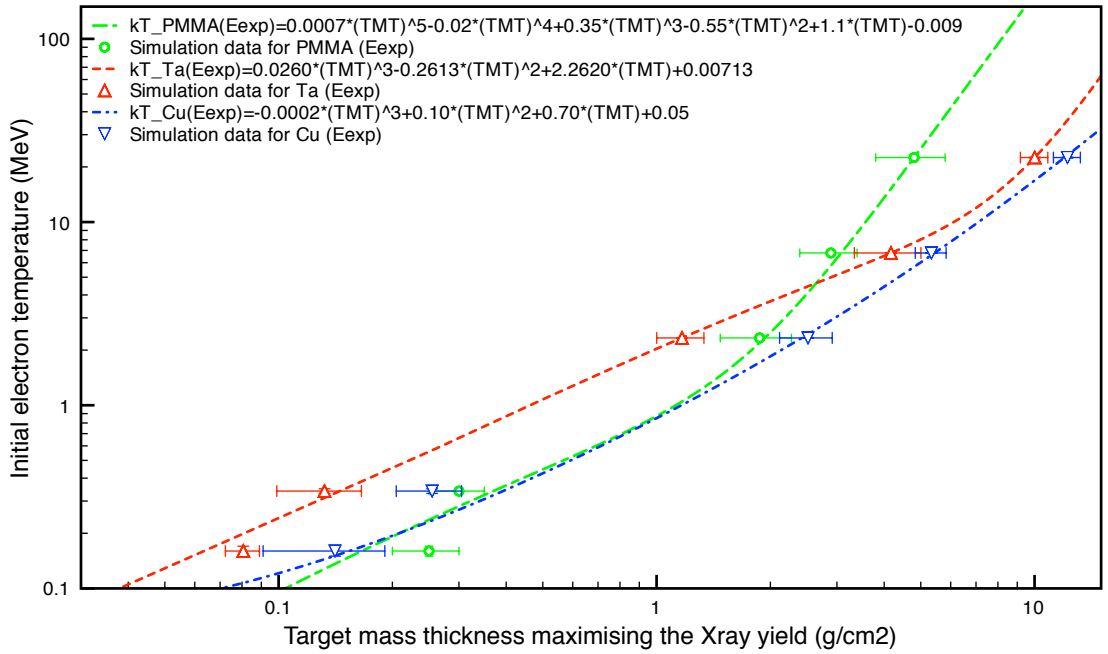

Figure 6.9 – Initial electron temperature of the $(E\exp)$ distribution as a function of the target mass thickness giving the maximum X-ray yields for each studied material.

CHAPTER 7

GEMINI AND VULCAN EXPERIMENTS WITH LDXRB

In order to determine the correctness of the simulations explained in chapter 6, but also to characterise the laser-driven photons and electron beams a series of experiments was performed at RAL using Astra Gemini and Vulcan lasers.

Astra is a high power, ultra-short pulse, high repetition-rate laser. It uses titanium-doped sapphire (TiS) as its active material, and works at 800 nm [103]. Astra Gemini is an extension of Astra that, in each of its two twin laser beams, can deliver an energy up to 15 J to target in pulses of minimum duration of 30 femtoseconds (i.e. a peak power of 0.5 PW). The maximum focused intensity from each beam is $\sim 10^{22}$ W/cm^2, higher than the 10^{21} W/cm^2 achieved with the Vulcan Petawatt system. This makes Gemini one of the most intense lasers in the world [104]. Vulcan is a high power laser system composed of a Nd:glass amplifier chain capable of delivering more than 300 J of laser energy in long pulses (ns duration) and up to 50 J

in short pulses (500 fs duration) at 1054 nm. It has 8 beam lines: two of them can operate either short pulse mode or long pulse mode and the remaining 6 operate on a long pulse mode [102]. The shot rate of Gemini is one shot every 30 seconds, while for Vulcan the time between two consecutive shots can reach even few hours.

The first experiment was performed at Gemini mainly to compare the simulations with real data, but given the unexpected results obtained a second less complex experiment was repeated at Vulcan.

The results of the experiment conducted at Astra Gemini have been published on the CLF annual report (Fiorini et al. 2011 [105]). Another paper, in which also the results of the experiment conducted at Vulcan are included, is in preparation.

7.1 Experiment at Astra Gemini

This experiment was conducted during a radiological commissioning of the Astra Gemini laser upon installation of a new tight-focusing off-axis parabola (F/2 OAP) in the laser system. It was performed by several components of the LIBRA group: most of them worked with the laser (setting up the optics in the laser chamber, focusing the laser on the targets, choosing the laser parameters useful for the experiment...) while I worked entirely on the dosimetry part of the experiment (setting up the TLD stack, reading, wiping and analysing the TLD chips and doing the analysis of the acquired data).

About half of the data was taken using a set of plasma mirrors on the laser beam line which increased the contrast between the main pulse and the pedestal/prepulses, and the other half was taken without using any plasma mirror. Several effects can be associated with prepulse and pedestal in dependence on their intensity. Examples are: destruction of thin foil targets by the shock generated by the laser prepulse, creation of pre-plasma on the target front side affecting laser absorption, deformation of the target rear side, and whole displacement of foil targets affecting

the focusing condition. Plasma mirrors are devices made of dielectric materials, on which the laser is focused before hitting the target: pedestal and pre-pulses are absorbed by the crystal because they are not intense enough to ionise it, while, when the much more intense main pulse arrives, it rapidly ionises the material and it is reflected by the over-critic plasma it creates. The reflectivity of the dielectric and the much higher reflectivity it acquires when it becomes over-critic plasma are the main factors to investigate to improve the pedestal-main pulse contrast. On the other hand, though, the ionisation of the dielectric material requires an expenses in energy, therefore, the main pulse energy on the final target will be lower.

During the measurements without plasma mirrors (low contrast data, LC) the contrast (main pulse intensity/pre-pulse intensity) could reach 10^5 and the average energy of the laser hitting the target was (7.6±0.4) J. During the measurements with a couple of plasma mirrors installed in the beam line (high contrast data, HC), the contrast was kept at 10^9 and the average energy (4.5±0.4) J, around 60% of the low contrast energy. The main pulse duration for both the cases was ∼50 fs and the diameter of the focal spot ∼2.5 μm. The estimated laser intensity for the low contrast case was $(1.41 \pm 0.07) \times 10^{21}$ W/cm^2 and for the high contrast $(8.3 \pm 0.7) \times 10^{20}$ W/cm^2.

7.1.1 Experimental set-up

In the experiment Thermo Luminescent Dosimeter (TLD-700) chips were used to record the dose carried by electrons and photons produced by the interaction the Gemini laser and solid targets. Their size was $(3.2 \times 3.2 \times 0.89)$ mm^3, and they were inserted between absorbers to form a stack. The minimum photon energy that could be detected was approximately 30 keV. The TLDs were calibrated by AWE using ^{60}Co gamma rays, as already mentioned in section 2.3.1. In the Astra Gemini target chamber the TLD stacks were positioned around the target as shown in figure 7.1

(a) and (b) where the simulated geometry of the experiment is reported. Each stack was composed of an alternating arrangement of TLD chips and filters made of aluminium and stainless steel (see figure 7.1 (c)). Two images of the real setup are also included in figure 7.2.

The nine inner ring stacks contained three TLD chips each and covered an angular range between -124° and 60° (where 0° is the laser direction), the five outer ring stacks instead contained six TLD chips and covered an angular range between -33° and 50°. In the majority of cases each outer ring stack had on its front a dipole magnet (object on the top in figure 7.1 (c)) to deviate the electrons and therefore measure only the dose due to the photons emitted by the target. Two stacks of the outer ring were placed under the laser axis (∼5°). The inner and outer stack rings were placed at distances of 20 cm and 45 cm, respectively, from the centre of the target. Targets made of different materials and with different thicknesses were irradiated: Ta (0.1 mm, 1 mm and 3 mm), Cu (3 mm), PMMA (3 mm) and SiO_2 (6 mm). The angle between laser axis and target was kept constant at 35°.

In order to achieve good signal to noise levels on the TLD, multiple shots under identical conditions were fired on the same target (different positions on it, see image (b) in figure 7.2) until the accumulated energy on each target was approximately 150 J. Since the same target was shot several times (∼33 shots per target during HC measurements and ∼20 during LC measurements), the dose measured represents an average. Even if the target and laser characteristics were kept constant during the irradiations, stochastic phenomena could affect the produced electron and X-ray beams, causing a lower or higher dose on the TLDs in a single shot. By collecting more shots per target, these random effects still affect the measured dose at any angle, but the final contribution is minimised. Moreover, since the accumulated energy on the target was slightly different from target to target, each acquired dose was divided by the total accumulated energy and then multiplied by the average

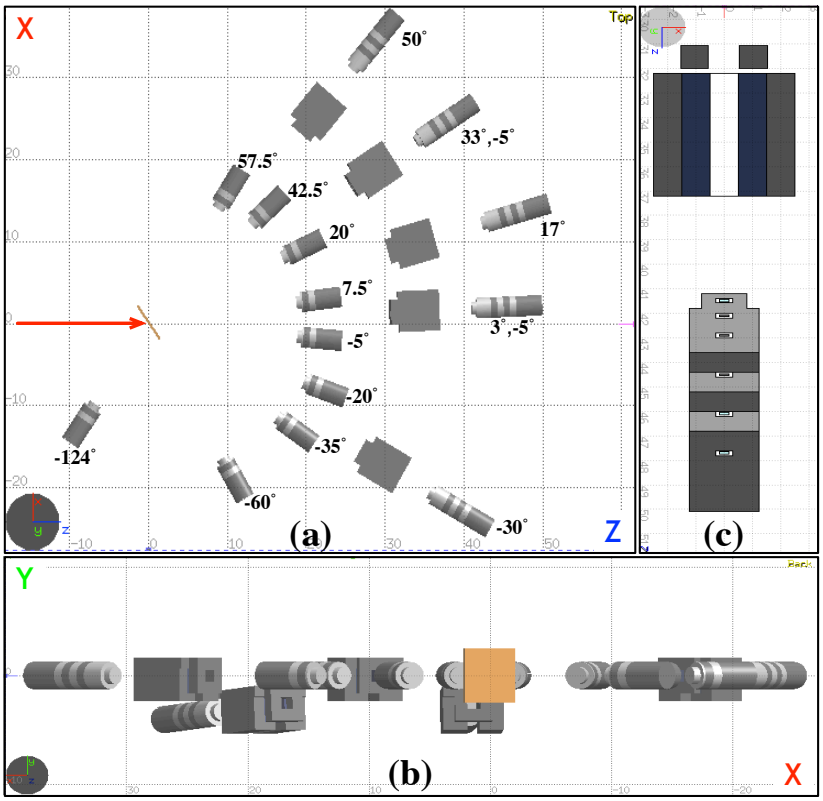

Figure 7.1 – Experimental setup of the experiment performed at Astra Gemini. Stack disposition around the target: (a) on ZX plane and (b) on XY plane, with Z the laser axis, Y the vertical axis and X from the right hand system. (c) Stack of the outer ring showing the magnet on the top and the sequence of absorbers and TLD chips on the bottom.

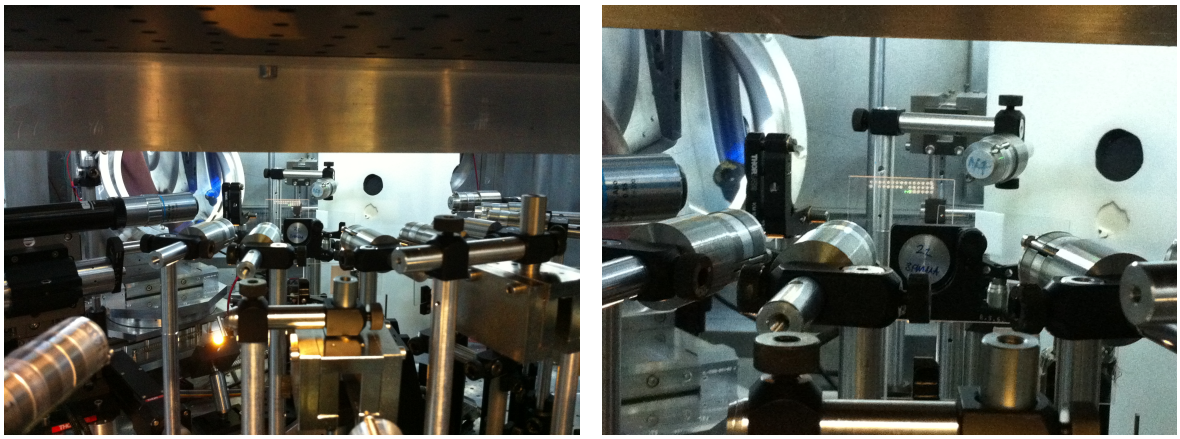

(a) (b)

Figure 7.2 – Photographs of the Astra Gemini experimental set-up inside the vacuum target area: (a) inner ring and part of the outer ring stack during setting up, (b) zoom on the PMMA target surrounded by the inner ring stacks.

energy per shot, so that the small differences due to different accumulated energy could also be minimised. The background dose (read from non-irradiated TLDs) was subtracted to the doses read from the irradiated TLDs before doing any other calculation. The uncertainty of the acquired total doses was estimated to be close to 3%. Due to the over response of the this TLD type to photon irradiation at energies lower than 1 MeV, an additional 10% uncertainty was considered for the doses read from the first TLDs of the stack irradiated by only photons. Considering also the under response for electrons with energy between 2 and 20 MeV, another 10% of uncertainty was added to the reading of the TLDs irradiated also by electrons.

7.1.2 RESULTS

The demonstration that the laser energy per shot was higher for LC than it was for HC is possible looking at the doses accumulated on the TLD chips. From figure 7.3 where the absorbed doses per shot are converted in doses at 1 meter and plotted as a function of the angle of detection, it is possible to understand how different the angular distribution and the doses due to electron and photon beams in each TLD of the inner ring stacks were in the two cases.

The data acquired with low contrast were significant only for the radiological commissioning. Using the F/2 OAP parabola and no plasma mirrors it was measured that the ambient dose at 1 m is between 2 to 50 times (depending on the irradiated material) higher than it is in the case where two plasma mirrors are used. In particular the highest differences in dose were measured for PMMA and SiO_2 targets. For the characterisation of the beams, instead, LC data were not taken into consideration, because, for the reasons already explained, the laser might have produced a more unpredictable electron beam.

The HC data from the outer ring stacks are shown in figure 7.4. Here the dose, not normalised by the distance of the TLD chips from the target, and due only to

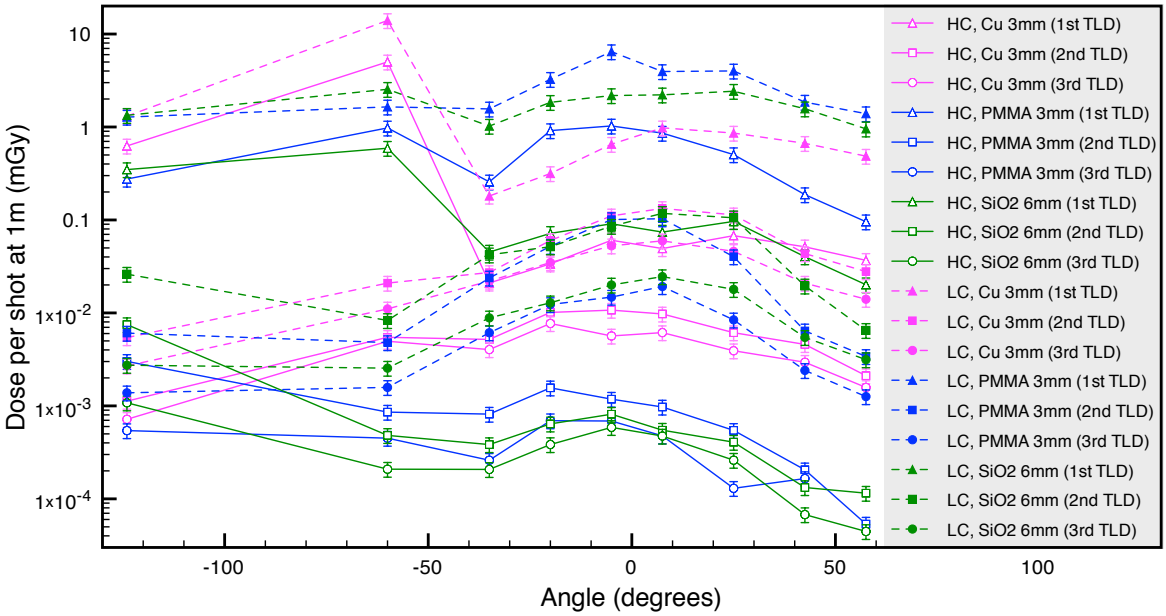

(a)

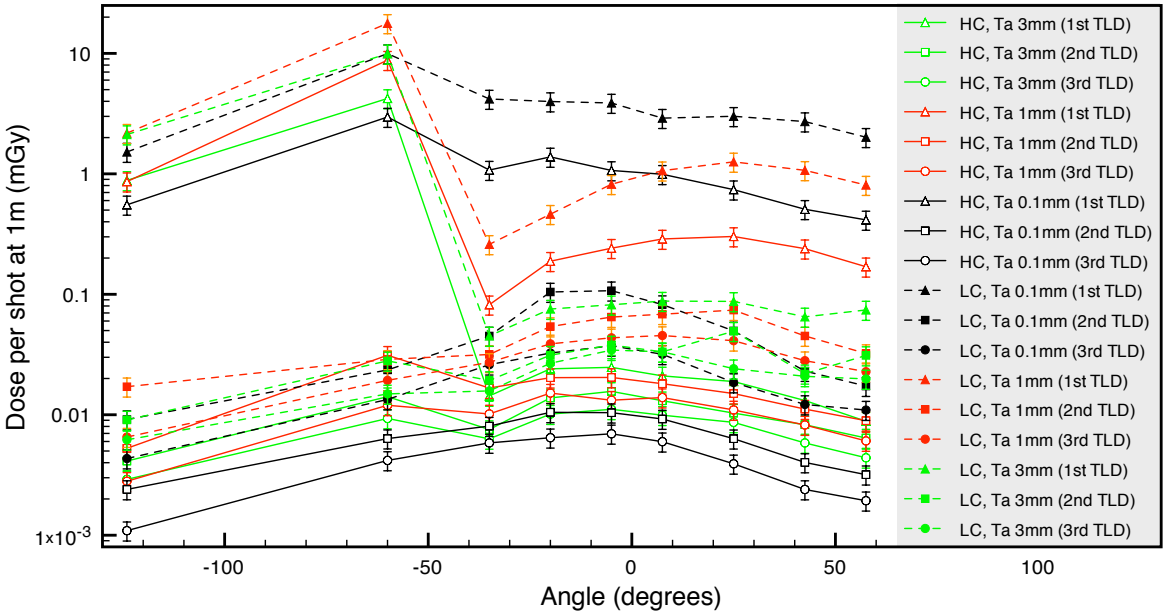

(b)

Figure 7.3 – Comparison between LC and HC data: dose per shot at 1m as a function of the angle of detection for the stack of the inner ring. The dashed lines represent the LC data and the full lines the HC data for all the irradiated targets: (a) 3 mm Cu, 3 mm PMMA and 6 mm SiO_2 and (b) 0.1, 1 and 3 mm Ta

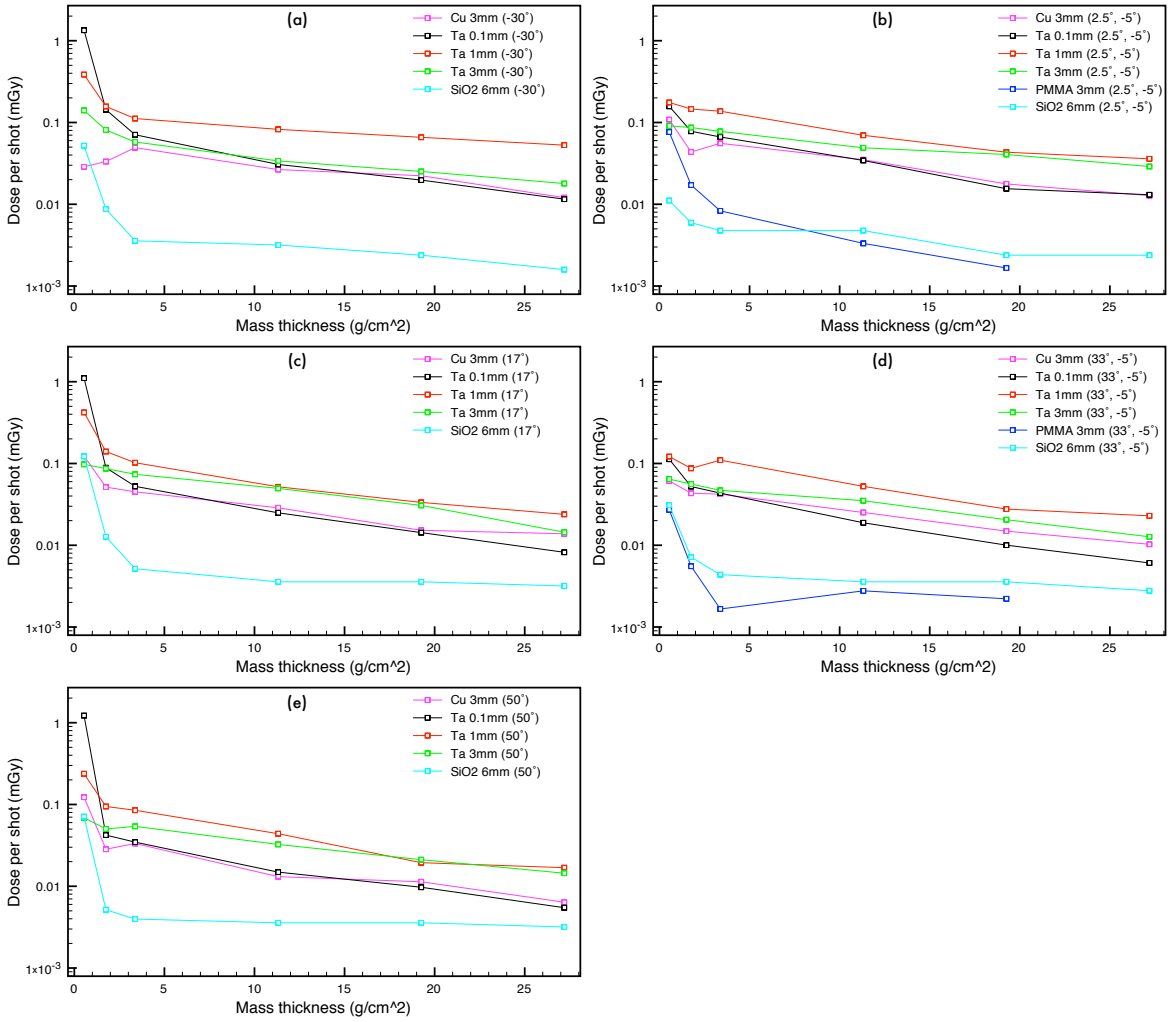

Figure 7.4 – High contrast data. Experimental dose per shot accumulated in the TLD chips of the outer ring stacks as a function of the mass thickness in the stack for each irradiated target. Doses from the stack at: (a) -30° on laser plane, (b) 2.5° and 5° below laser plane, (c) 17° on laser plane, (d) 33° and 5° below laser plane and (e) 50° on laser plane.

the emitted photons, are plotted against the mass thickness of the absorbers in each stack. The graphs on the left come from the stacks placed on laser plane, while those on the right from the stacks placed 5° below laser plane. As can be seen from the doses measured from the first TLD chips of the stacks, the TLDs on laser plane detected more low energy photons than the TLD chips below the plane. The doses due to the highest energy particles are instead seen to be almost similar at any angle, sign of a wide angular distribution.

The divergence along the X-axis of both electron and photon beams is better shown in figure 7.5, where the doses per shot (not normalised by the TLD distance from the target) due to the two beams are plotted as a function of the detection angle. Focusing on the data from -40° to 60°, these graphs show a large angular distribution of dose for all the TLDs in the stacks, but the dose trend changes with the depth in the stack. In plot (a) representing the dose measured from the fist TLD chips of the inner ring stacks we can see that the targets producing the highest dose are 0.1 mm Ta and 3 mm PMMA, meaning that these target were probably emitting the highest number of lowest energy electrons stopped mainly in the first millimetres of the stack. The least emitting target was instead the 3 mm Ta. Looking at the dose measured from the second and third TLD chips ((b) and (c) graphs), the situation changes: 1 mm Ta was the most emitting target at all angles and SiO_2 was the least emitting one. This can be explained with the fact that the largest number of electrons was stopped before reaching the second TLD and that the intensity of the remaining X-ray beam was gradually decreasing crossing the absorbers of the stack. The provenance of the very high peak at -60° and the higher doses at angles lower than -60° is not at all clear. They could have been caused by a very large quantity of backscattering electrons, or it could be that the electron beam was not mainly accelerated forward.

The irradiation of the 3 mm PMMA target was repeated twice only at HC conditions. In one case all the magnets in front of the outer ring stacks were removed and in the other the magnets were installed only in front of the stacks at 2.5° and 33°, both 5° under laser plane. This allowed to determine the contribution to the dose due to the electrons and also to derive an estimate of the maximum electron energy at those angles. The comparison of the doses measured in presence and absence of magnets is shown in figure 7.6 (a) and (b). The plot in (c) underlines the fact that the laser conditions and the absorbed doses from the stacks without mag-

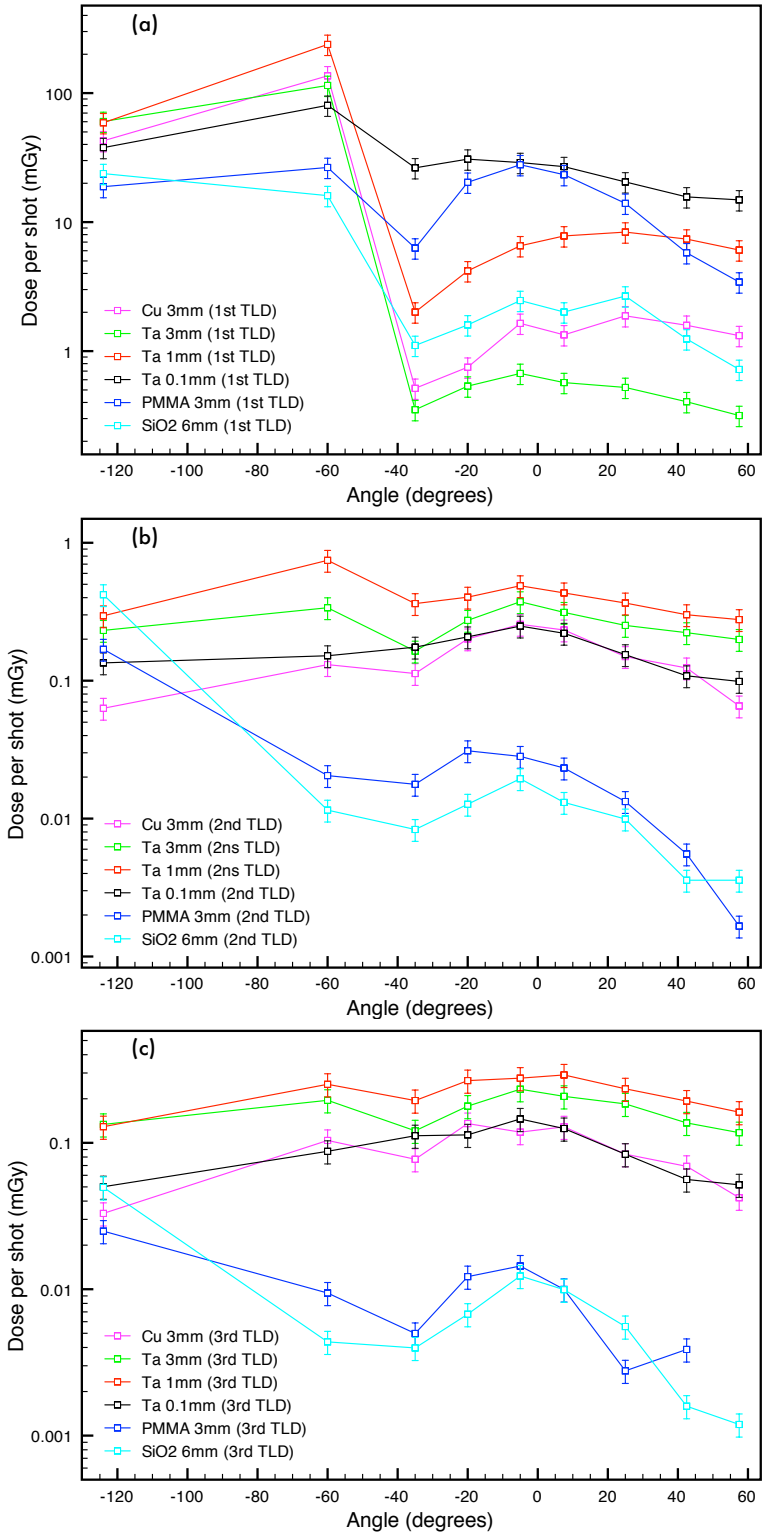

Figure 7.5 – High contrast data. Experimental dose per shot accumulated in the TLDs of the inner ring stacks as a function of the angle of detection for each target: (a) fist TLD of the stacks (mass thickness=0.54 g/cm^2), (b) second (mass thickness=8.615 g/cm^2)and (c) third TLD (mass thickness=16.555 g/cm^2).

nets were the same for both the irradiations, so that the comparison between the dose absorbed with and without magnets is justified. The doses due to electrons and X-rays measured in the first TLD of the stack at about laser axis (2.5°) appear to be almost 60 times higher than the dose measured in the case where the dose was due to only photons. In the case of the stack at about target normal, instead, the difference was almost an order of magnitude. This means that the electron beam divergence was lower than the divergence of the X-ray beam, because the black curve is much higher in (a) than in (b), but the red one does not show such a large reduction. Moreover, since for both the angles from the 4th TLD the dose due to electrons and X-rays is equal to the one due to only X-rays, we can assume that starting from somewhere in between the 3rd and the 4th TLD the totality of the electron beam and their secondary particles were stopped, at least for these stacks placed under laser plane. Running a Fluka simulation of a monoenergetic electron beam crossing an outer ring stack, it was possible to determine the maximum energy of the electron beam created by the interaction of the laser with the plastic target. According to the simulations, using an incident energy of (1.6 ± 0.2) MeV, the e^- beam and its secondary particles stop before hitting the middle of the 3rd TLD chip. Using instead an incident energy of (3.6 ± 0.1) MeV, the e^- beam and its secondary particles stop just before hitting the 4th TLD chip, so that there is no deposited energy on the 4th TLD of the stack.

If what is true for the stacks under laser plane (i.e. that the maximum electron energy was lower than 3.6 MeV) can be approximated also for the stacks on laser plane, not having electrons reaching the 4th TLD (at 11.315 g/cm^2) of the outer stacks means that there are very few electrons reaching the 2nd TLD chips of the inner ring stacks (at 8.615 g/cm^2) and no electrons at all reaching the 3rd TLDs (at 16.555 g/cm^2), so that the hypothesis previously done about the provenance of the dose absorbed by the TLDs of the inner ring stacks can be considered correct. Look-

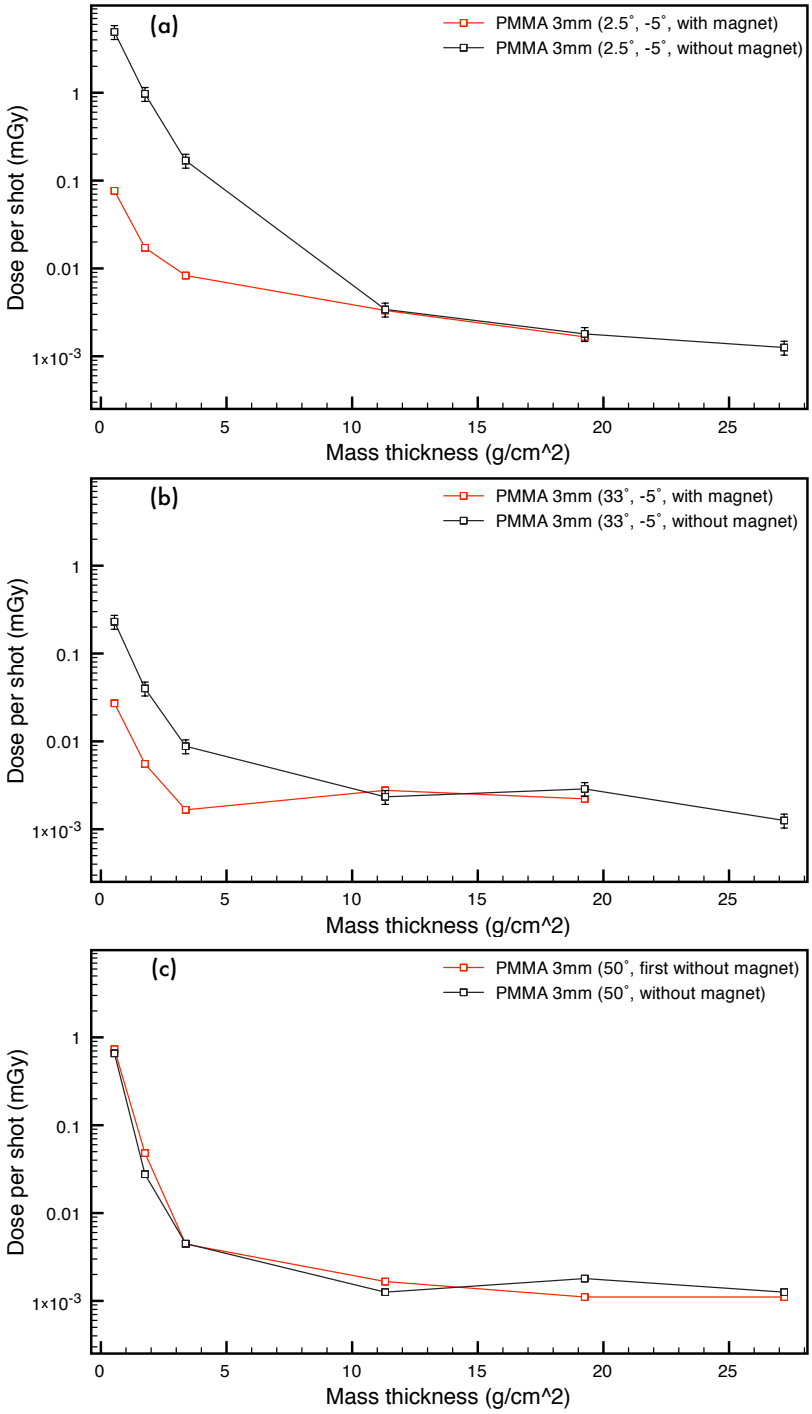

Figure 7.6 – Comparison between the dose accumulated irradiating 3mm PMMA with and without magnet in front of two stacks of the outer ring. Dose per shot from the stack at (a) 2.5° and (b) 33° (both 5° under laser plane) irradiated firstly without magnet and then with magnet in front. To check that the conditions were the same during the two irradiation, in both the cases the magnets in front of the other 3 stacks of the outer ring were removed: the graph in (c) shows the perfect agreement of the dose per shot from the TLDs of the stack at 50° for both the irradiations.

ing also at the amount of the deposited dose, we can assume that at low mass thickness the deposition of energy is highly dominated by the electrons while at higher mass thickness ($\geq$10 g/cm^2) the energy deposition is dominated by the photons.

Running another Fluka simulation of the PMMA target and of an electron beam with a Maxwellian (E^2exp) spectrum, it was possible to estimate the k_BT of the initial electron beam reaching the stacks under laser plane, knowing that the very maximum initial energy of the escaping electrons would have been close to 3.6 MeV. All of this assumes that the real electron distribution was actually approximated by a (E^2exp) distribution. Assuming that 90% of the electrons exiting the target would contribute to the reflux and that the other 10% escape, in the simulation I set the escaping electrons to have an energy between 1.6 and 3.6 MeV. Figure 7.7 (a) shows in black a simulated Maxwellian electron spectrum with k_BT = 0.38 MeV generated by the laser on the front surface of a 3mm PMMA target, and in red is the distribution of the simulated electrons at the rear surface of the target after having crossed the target thickness. This red spectrum satisfies the energy conditions about the number of refluxing and escaping electrons: the electrons with energy higher than 1.6 MeV (which are close to 10% of the total number of exiting electrons) escape and the other with lower energy would be reinserted in the target. Therefore the initial temperature of the laser induced electron reaching the stacks under laser plane can be estimate to be $\sim$0.38 MeV. As can be seen most of the initial electron beam is stopped in the target. (If the analogous study is repeated using the (Eexp) energy distributions, the k_BT would be $\sim$0.6 MeV.) This analysis assumes that the observed lower energy of the emitted electrons under laser plane is accompanied by an electron energy on laser plane lower than what is expected if the driving force of the electrons was the ponderomotive force. In fact, looking at the graphs in figure 7.4 and comparing the doses from the stacks on laser plane (on the left) and those under laser plane (on the right), it is possible to see that except for the first TLDs (which

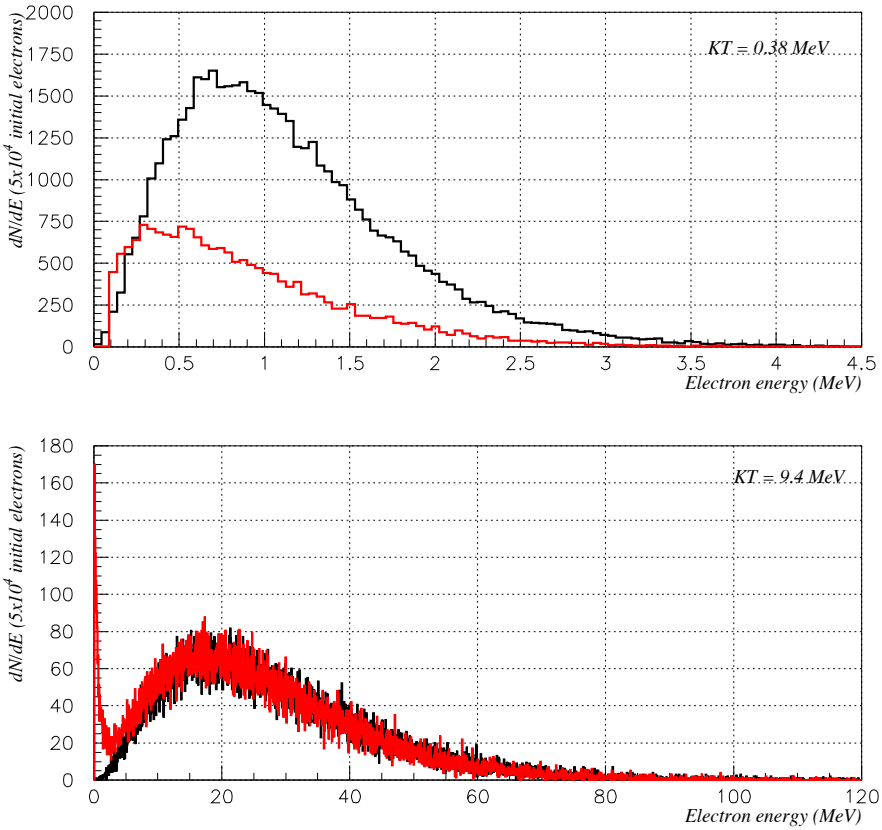

Figure 7.7 – (a) In black it is shown the supposed Maxwellian spectrum of the laser-driven electron beam at the front surface of the target (k_BT=0.38 MeV) obtained from the fact that the escaping electrons had a maximum initial energy between 1.6 and 3.6 MeV. The spectrum in red is the spectrum of the electrons at the rear surface of the target after having crossed the target. (b) In black it is shown the spectrum that according the ponderomotive theory the laser-driven electron beam should have had: k_BT=9.4 MeV. In red it is shown the consequent spectrum of the electrons at the rear surface of the target after having crossed the target.

mainly absorbed the doses delivered by the lower energy photons) the dose does not really change with the angle along X and Y-axis.

Because of the fact the dose distribution peaked on the laser axis direction and given the theory of the laser–solid target interactions explained in section 1.1.1, one would expect to have an initial electron beam with a hot temperature (k_BT_{PM}) given by Wilks' formula (equation 1.1). For the laser intensity estimated for this experiment, $I = (8.3 \pm 0.7) \times 10^{20}$ W/cm^2, the expected temperature of the generated electron beam would have been 9.4 MeV. Figure 7.7 (b) shows in black a (E^2 exp) energy

distribution with k_BT = 9.4 MeV and in red the distribution of the electrons reaching the rear surface of the target after having crossed the target thickness. If it is assumed a 90% reflux, the escaping electrons would have an energy between 40 and 120 MeV which is definitely too high to explain the experimental results from the stacks at 2.5° and 33°.

Summarising, from the dose released in the TLD chips, it has been found out that the angular distribution does not match that reported in the literature: the divergence along X-axes is different if compared to that reported in [106] where the initial conditions of laser and target were similar to those of this experiment. Moreover and more importantly, from the measurements with and without magnets a discrepancy on the expected ponderomotive electron temperature was found. A comparison between these experimental data and the simulation data in chapter 5, is also very inconclusive. Assuming that the trend of the dose is a direct consequence of the trend of the number of photons, the only trend that could be compared is that of the dose from the Tantalum targets, 0.1, 1 and 3 mm thick. If the initial electron beam was really peaked on laser axis direction, the real thickness of the inclined Ta targets would be respectively 0.174, 1.74 and 5.23 mm, which correspond to mass thickness of 0.29, 2.9 and 8.7 g/cm^2. Using the fit for Ta targets in figure 6.8 and knowing that the dose appeared to be higher when 1 mm target was irradiated, it is possible to conclude that the initial electron temperature had to be between 0.3 and 12 MeV and possibly close to 3 MeV (corresponding to 1.74 g/cm2). As already mentioned this comparison is inconclusive, not only because there are not enough experimental data to establish a precise electron temperature or because the suggested possible temperature is not comparable with the one estimated using and not using magnets with the PMMA target and the stacks under laser axis, but mainly because there are serious doubts about the experimental data. Several causes could have badly affected the measurements, what seems really suspicious is the strange

similarity between the data at low and high contrast (see figure 7.3) and the fact that the highest doses were detected at angles lower than -60° (where it was not supposed to be any dose at all). So another set of measurements was performed using the Vulcan laser, making sure that what could have affected the data at Gemini was this time well checked.

Even if the origin of the lower electron energy lay in an unusual laser acceleration, with this experiment it was possible to define another method to check the initial electron beam energy by using and not using magnets to separate the X-ray and electron contribution to the total deposited dose in TLD stacks. The method can be improved replacing the heavy absorber in the stacks with a higher number of lighter absorbers and TLD chips, so that a more detailed trend of dose due to electrons and photons can be reached. At this point by placing these stacks all around the target and repeating the shot on each target using and not using the magnets it is not only possible to locate the initial electron temperature, but also determine the more precisely the angular distribution of the two beams.

7.2 Experiment at Vulcan

Like the experiment at Gemini, this experiment was also inserted in a radiological commissioning session upon the installation of a new parabola at one of the long pulse mode chamber at the Vulcan laser facility. The reason for this was that this beam time was the closest beam time our group could use after discovering the discrepancy on the electron temperature with the Wilks' theory. Exactly as in the commissioning at Gemini, the detectors useful for the commissioning could be used also for the characterisation of the laser-driven beams, so our group did not have to wait a long time before performing a new experiment appositely for the characterisation. I was not involved in taking the data, but they were given to me to be analysed. Since I was not there during the experiment and the commissioning in

itself last for a very short time, I could not have the opportunity to chose how to arrange the TLD stacks around the target or how many times to repeat the same measurement using (and not using) magnets.

The average laser energy deposited on the targets was (357 ± 19) J in a main pulse duration of $\sim$1 ps. The diameter of the focal spot was $\sim$5 μm, so that the estimated laser intensity was $(8.3 \pm 0.4) \times 10^{20}$ W/cm^2. The contrast of this Vulcan laser is known to be much higher than the Gemini laser, so that it was not even necessary to use plasma mirrors.

From the amount of X-rays emitted from the differently thick Ta targets, it was possible to relate the experimental data to the simulations in chapter 6 and also perform new ones with the experimental setting to refine the comparison.

7.2.1 Experimental set-up

The experimental setup is shown in figure 7.8. The TLDs used were the same as in the experiment at Gemini. The composition of the stacks was also the same as the outer ring stacks of the previous experiment already shown in figure 7.1 (c). Five tantalum targets with different thicknesses were irradiated: 0.1, 0.5, 1, 3 and 6 mm. The inclination of the targets respect to the laser axis was 40°, so that the stack placed at 50° was normal to the target surface (for this reason called TN). Other three stacks were also used and placed on laser axis (at 0° and called LA) and on the two edges of the laser beam, at 10° (BEM) and at -10° (BENM). Only three magnets were installed in front of the stacks. One stack, BENM, was always used without magnet in order to also have some information about the electron beam.

7.2.2 Results

The doses detected by the TLD chips are shown in figure 7.9 and 7.10 where they are plotted respectively against the mass thickness of the stacks where the TLDs were

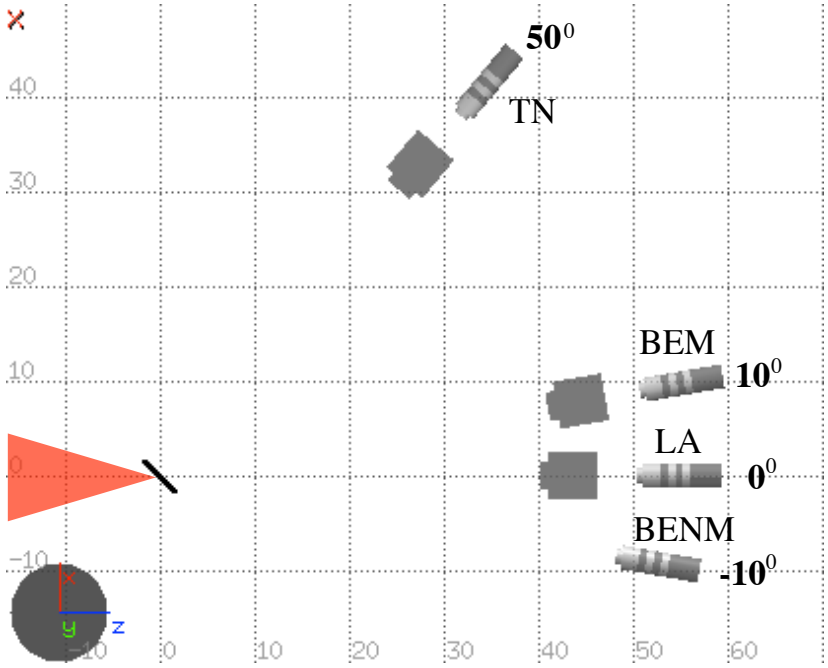

Figure 7.8 – Stack disposition around the target of the experiment performed at Vulcan. The stack composition is exactly the same as the stack of the outer ring used at Gemini and shown in figure 7.1 (c). The red object impinging on the target represents the Vulcan laser which had a divergence of 20°.

placed and against the thickness of the target irradiated to obtain them. On both the figures the data from the stack on target normal (TN) are represented by the blue lines and the data from the stack on laser axis (LA) are represented by the green lines. BEM and BENM are respectively red and black.

As it is visible from figure 7.9, for the lowest thickness targets (0.1 and 0.5 mm) the doses from BENM are higher than the doses from all the other stacks up to the 5th TLD. Nevertheless, the presence of electrons is still possible also in the 6th TLD, because of the large inclination of BENM with respect to the supposed direction of the beam (∼50°, see the explanation in section 7.3). If BENM had a magnet on its front, it is probable that its doses would have been always lower than the doses from all the other stacks. This is also visible in the other graphs of figure 7.9. Increasing the thickness of the target, the number of electrons reaching BENM decreases, and so does their energy, because of the large path they have to travel before exiting the

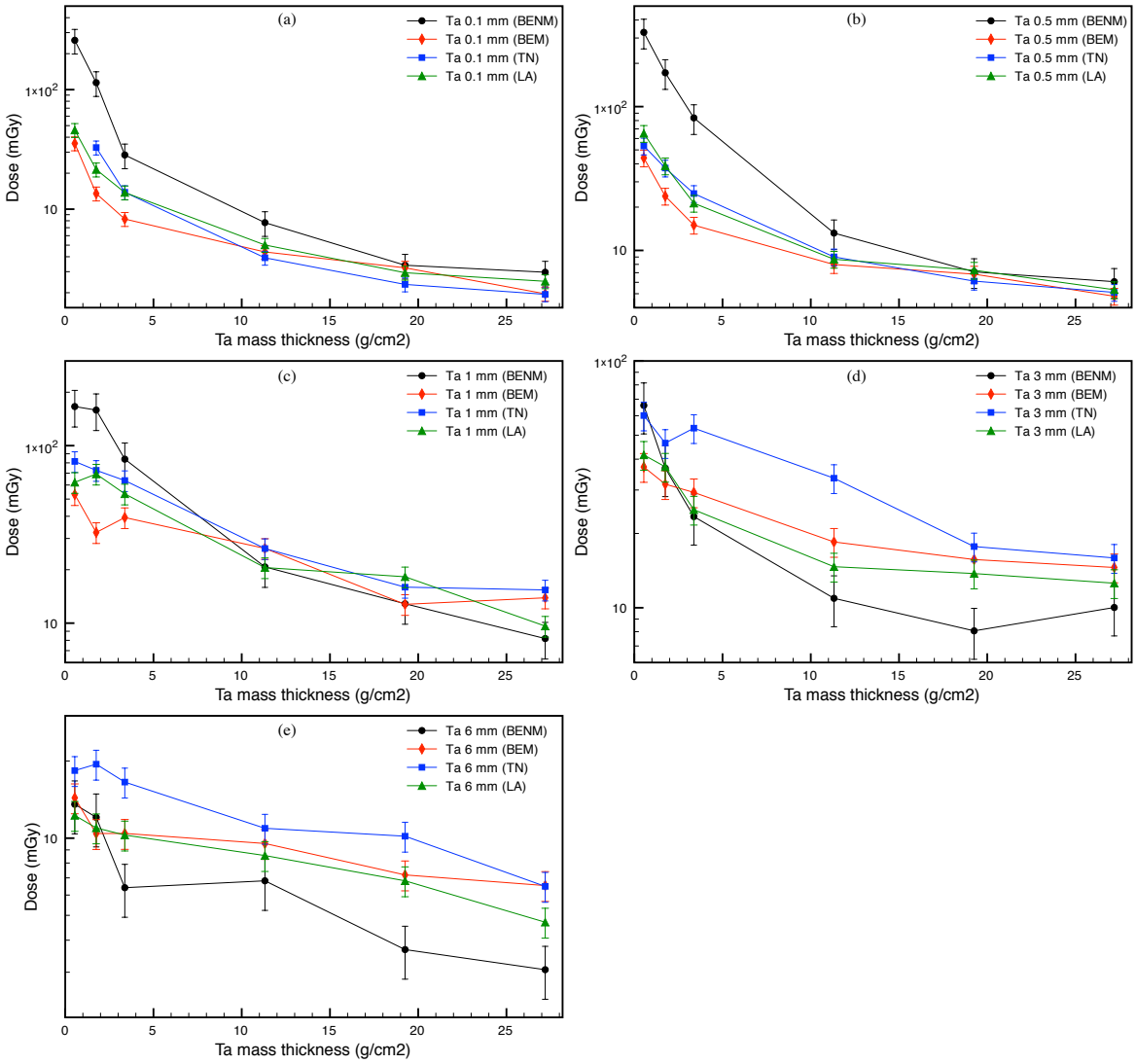

Figure 7.9 – Detected doses as a function of the mass thickness of the stacks. Each plot contains the doses detected from the 4 stacks for one irradiated target.

target. As a consequence the doses detected from BENM gradually decreases for all its TLDs. For this reason it is not possible to estimate the maximum energy of the escaping electrons, and consequently k_BT, by simply comparing the data from BENM and the data from any other stack as was done for the experiment at Gemini.

From figure 7.10 (b), (c) and (d) it is possible to see that the maximum dose was mainly detected when 1 mm target was irradiated. For very few TLDs the maximum could be found when 3 mm target was irradiated. From the graph in (a), instead,

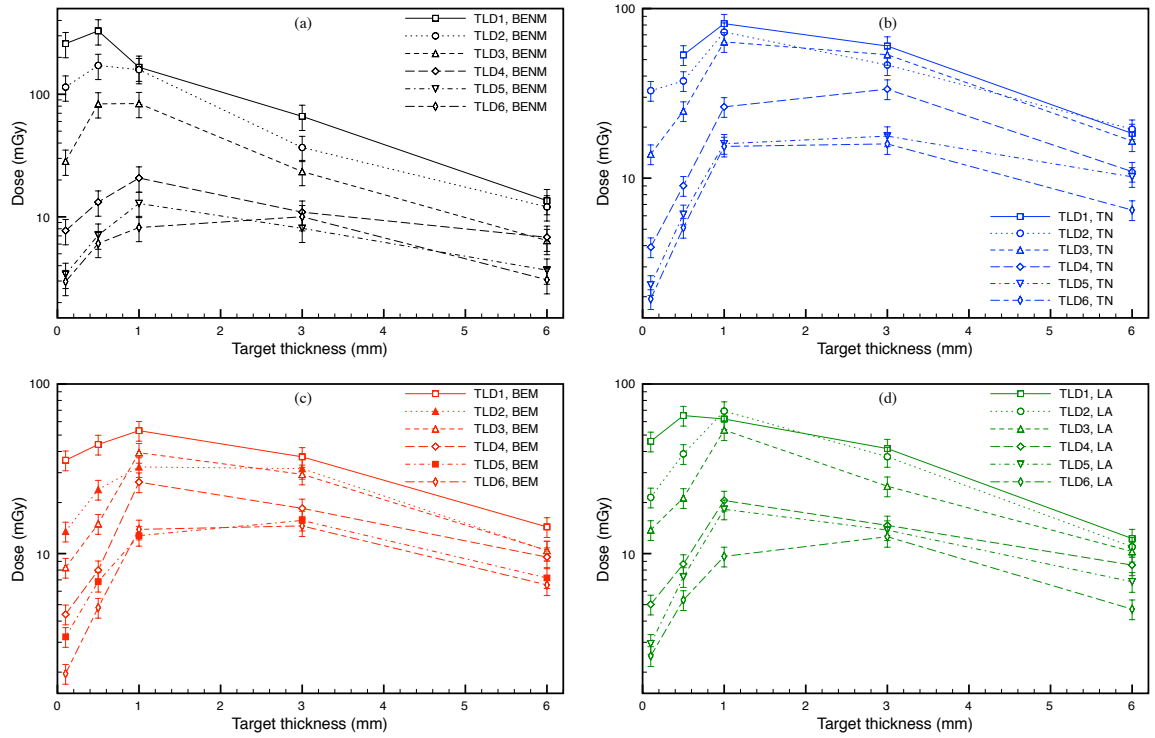

Figure 7.10 – Detected doses as a function of the thickness of the target. Each plot contains the doses detected from one stack for all the irradiated target.

it can be noticed that starting from the 4th TLD photons are mainly detected. In fact, it looks like that there are two different trends for the doses deposited in the TLDs. In particular while the first three curves (coming from the more superficial TLDs) have a maximum at 0.5 mm, the other three have a trend which is more flat with a maximum between 1 and 3 mm. So, the first trend could be dominated by electron deposition while the second by photon deposition, given its similarity with the trend of the doses coming from the TLDs detecting only photons.

As already discussed in the introduction Cho et al. were able to detect contemporarily two electron beams from targets irradiated at 45 degrees by a laser with intensity of 2×10^{19} W/cm^2 [18]. These two beams were seen to have different divergence (higher for the beam emitted at target normal), energy (two times higher for the beam emitted at laser axis) and intensity (one order of magnitude higher for the beam emitted at target normal). In particular the authors found that the estimated

energies of the two beams were in perfect agreement with the temperature given by Wilks due to the ponderomotive force (on laser axis direction) and by Beg due to the resonance absorption (on target normal direction).

In 2000 Santala et al. using photonuclear activation of Cu foils placed around the target and irradiated by the high energy X-rays emitted from Ta targets shot at 45 degrees by one of the Vulcan laser beams (I$\sim 2\times 10^{19}$ W/cm^2, energy incident on target 2050 J and main pulse duration 11.5 ps), detected the two beams, but in dependence on the pre-plasma scale length (given by the expansion of the plasma cloud created by the prepulse) they saw that the two electron beams (and so the X-ray beam created by them) could merge together generating a single beam exiting the target [107]. They found that for intermediate plasma scale lengths the photonuclear activation due to the exiting X-ray beam could either have a wide distribution with a peak between the laser axis and target normal, or have a double-peak distribution, where the two peaks were at laser normal (higher peak) and target normal (lower peak). They explained the formation of the wider distribution with the fact that at plasma scale lengths closer to the laser wavelength, resonance absorption is the dominant mechanism and so the electrons are mainly accelerated along the target normal. At high plasma scale lengths the ponderomotive force becomes the main mechanism and the electrons are mainly accelerated along the laser axis. In neither case the beam was seen to have a distribution properly peaked in one of the two directions, meaning that the two forces were both present, but one was much stronger than the other. The FWHM for the distribution were measured to be $\sim 40^\circ$. At intermediate plasma scale lengths the two forces were more balanced creating either a wider peak (FWHM$\sim 56^\circ$) or a double-peaked distribution. 2D PIC simulations for a 40° off-axis target irradiated by a laser with an intensity of 10^{20} W/cm^2 reported in the same article corroborated the experimental results, showing that the electron distribution was never peaked at laser axis, and so the ponderomotive force

was never the only acting force. Only for large plasma scale length the electron distribution moved towards laser axis. In particular in the first case the peak of the simulated electron distribution was seen to be at 10 degrees from the target normal and in the second at 10 degrees from laser axis. The electrons on the peaks were more energetic than those on the tails for both the recreated cases, but the slightly more energetic one where seen when the peak was closer to the target normal. This is not in clear contrast with that explained by Cho et al. because in their experiment they only were witnesses of on the two cases saw by Santala and in particular the case where the ponderomotive force was the main active force. Moreover their irradiated target was thin enough to allow the detection of two beams instead of the combination of the two.

Looking at the data from Vulcan in figure 7.9 and 7.11, it is clear that the dose distribution is different from that obtained from Gemini (which was peaked on laser axis). Excluding the data from the stack without magnet, the doses measured from the stack at target normal are always higher than the doses detected on the other stacks, meaning that the peak in the dose was not on the laser axis direction but closer to the target normal direction, or that a double peaked distribution was present. The important fact to note is that looking at the plots in figure 7.11, the dose at TN is not only higher, which could mean a higher intensity, but the peak is generally present at the same thickness as for the other stacks. At this point it is important to remember the simulation graphs in figures 6.6 and 6.7 where the simulated X-ray yield is plotted as a function of the mass thickness of the irradiated targets for both the electron energy distributions. In these graphs it is shown that increasing the temperature of the initial electron distribution, the peak in the number of X-rays moves towards higher thicknesses. The same would happen if instead of the number of X-rays the dose in an absorber was plotted. From this and from the fact that the peak in dose for TN data is between 1 and 3 mm (as it is for the

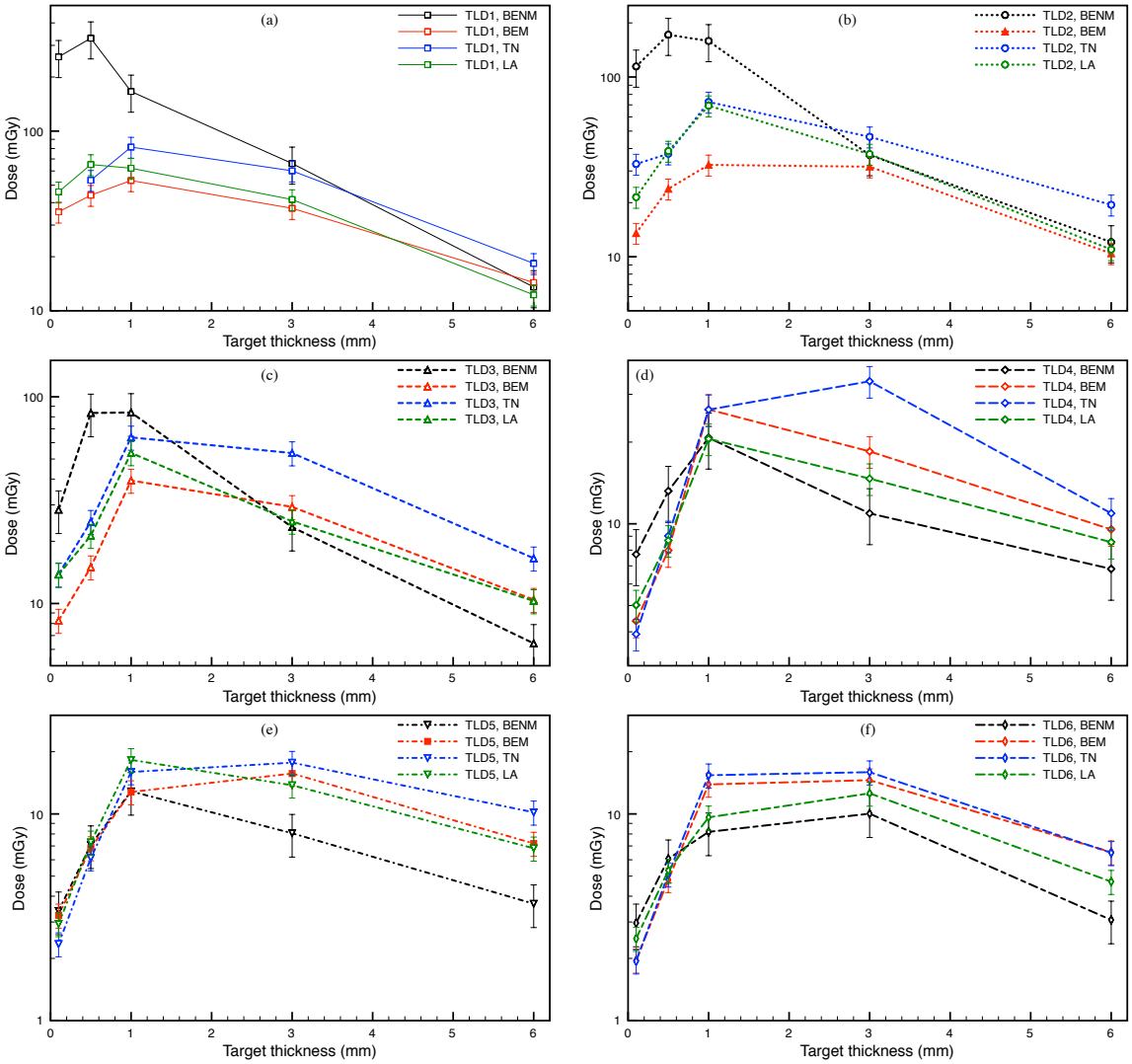

Figure 7.11 – Detected doses as a function of the thickness of the target. Each plot contains the doses detected from all the stacks for one irradiated target.

other stacks), it is possible to conclude that the energy of the electrons emitted along TN was equal or slightly higher than the energy of the electrons emitted along LA. Therefore resonance absorption was in this case the main acting force. It could be assumed that either there were two electron beams with very similar energies, or that there were two beams and the one accelerated by the resonance absorption had an energy which was much higher than the one accelerated by the ponderomotive force. This second case would correspond to the small pre-plasma scale case de-

scribed by Santala, who not only used one of the Vulcan lasers but also irradiated targets which were quite thick (1.75 mm) as those used in this experiment. In fact, even if there were a low energy electron beam accelerated by the ponderomotive force, it is possible that because of the large target thickness, its secondary particles could not escape from the target. For this reason I assumed that there was only one out-coming beam peaked in a direction closer to TN. The inclination of the incident electron beam was chosen to be 40° respect to the Z axis (i.e. at 10° from TN) which is in perfect agreement with what reported on Santala's paper. The initial beam divergence was a parameter to be determined also because it is dependent on the laser intensity [108].

Given the assumption of having only one beam peaked in a direction close to TN and so mainly driven by resonance absorption, it was also obvious to presume that the initial hot electron temperature was obtainable from equation 1.2 by Beg: $k_B T_{res} = (2.33 \pm 0.04)$ MeV.

7.3 Comparison with Fluka simulations

From the simulations described in chapter 6, from the fact that the Vulcan experimental dose peaks appear when 1 or 3 mm Ta targets were irradiated and since the beam inclination can be supposed to be 40° and so 10° respect to the target inclination, it is possible to estimate an initial electron temperature using the fit in figure 6.8 and 6.9 for Ta and reported in figure 7.12 for a better view. If the photon yields were maximum during the irradiation of 1 mm Ta target, which at 10° would have a thickness of 1.015 mm (1.694 g/cm^2), according the fits in figure 7.12, the initial electron beam would have $k_B T$=2.37 MeV for $(E^2 \exp)$ and $k_B T$=3.22 MeV for $(E \exp)$. If instead the photon yield were maximum with the irradiation of 3 mm Ta target (5.08 g/cm^2), $k_B T$ would be 7.21 MeV for $(E^2 \exp)$ and $k_B T$=8.16 MeV for $(E \exp)$. So that, assuming that photon yields and doses would have a similar trend,

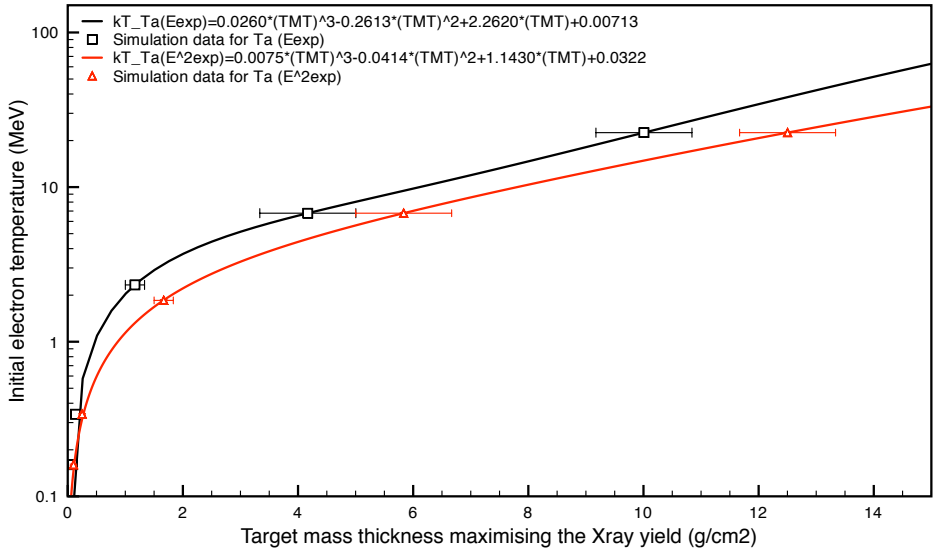

Figure 7.12 – Simulation results for Ta target from chapter 6. Initial electron temperature as a function of the Tantalum target mass thickness giving the maximum X-ray yields for both the simulated electron distributions (Eexp) in black and (E^2exp) in red.

according to the study in chapter 6, temperatures between 2 (also because the actual peak could have been at thicknesses in the range (0.5, 1] mm) and 8 MeV could have been possible. By irradiating more targets with thickness between 0.5 and 3 mm the peak in dose would be determined more precisely and so also the k_BT of the initial beam and potentially also some information about the equation of the electron distribution describing the process could be evaluated.

In addition some more information could be obtained looking at the dose deposition in the TLDs of each stack. So, in order to estimate more precisely the initial electron temperature new Fluka simulations were performed. The experimental setting was carefully simulated using Fluka (figure 7.8 comes from these Fluka simulations) and using the same approach used for the simulations described in chapter 6, this time the doses in the TLD chips of each stack were also detected. Some parameters of the beam had to be determined, first of all the temperature of the electron distribution and then the divergence. The amount of reflux was kept constant at 90%, as well as the inclination of the beam (40° respect to the Z-axis and so 10° respect to the

target normal). By changing the unknown parameters and comparing the obtained simulated doses from both the electron distributions to the experimental ones, it was possible to fix those parameters when a best fit was achieved.

7.3.1 CARDS AND USER ROUTINES USEFUL FOR THE SIMULATIONS

The input files and the user routines used for these simulations are slightly different from those described in section 6.2: the simulation approach is the same, but this time the electrons escaping the target needed to be detected in the TLD stacks. In the simulations in chapter 6, the out-coming electrons were transported up to the end of each run but not detected. In these simulations, instead, only the escaping electrons had to be transported up the end of each single run and others had to be 'killed' and then reused for the reflux in the following run. This was due to the presence of the TLD stack without magnet (BENM) which could detect both photons and the escaping electrons.

Input file

The input files used in these simulations are more complex than those described in chapter 6, not only because the geometry and media part also includes the description of the experimental set-up (using several transformations to rotate target and stacks) and materials, but also because there are more vacuum regions surrounding the target which are necessary to detect electrons and photons and to 'kill' the electrons. The cards, which are different from those already described in section 6.2.1, are:

- the MAT-PROP card with SDUM 'userdire' used to call the routines *usrmed* useful to kill the electrons exiting the target;
- the MGNFIELD card used to activate the magnetic field in the magnets and useful to call the *magfld* routine where each magnetic field is described;

- several USRBIN cards (one for each TLD chip) used to score the dose equivalent absorbed by the TLD chips and to save them in a ASCII file.

Moreover the MULSOPT card was removed in order to allow a lowest CPU time spent for the simulations. This has been possible because the simulated initial electron energies even if low were not lower or close to the multiple scattering threshold and in any case the lowest energy detectable with the TLDs was $\sim$30 keV.

To conclude a new input file is created without the MAT-PROP card for the simulation of only the escaping electrons (which will not be killed by the *usrmed* routine).

Source routines

The *source* routines are very similar to those described in section 6.2.2. One of the differences is in the *source* for the initial electron beam. This time the direction cosines of each created particle are modified in order for the beam to have a precise divergence, the value of which is written in the input file and passed to the routine through the SOURCE card.

The other main difference for the *refluxing sources* is that after the Bubble sort algorithm another ASCII file (called *xxx_esc_ele.dat*) containing only those 10% electrons with highest energy is written. Again the 90% of electrons are reinserted in the target inverting their direction cosines from the point of exit.

At the end of the simulations of incident and refluxing electrons all the created *xxx_esc_ele.dat* are merged in one ASCII file and then used by a new input file, a new source (*escaping source*) and a new mgdraw routine (*escaping mgdraw*) to transport and detect the escaping electrons. These electrons are not reinserted into the target, but simply re-created with their own energy, their own direction cosines and with origin the point of exit from the target and transported as a normal beam without being killed. The detection of the doses they cause in the TLDs will be possible through the USRBIN cards in the input file and the calculation of photon yields

through the *escaping mgdraw*.

Mgdraw routines

As for the simulations in section 6.2, two sets of *mgdraw* routines (*mgdraw even* and *mgdraw odd*) were used for the even refluxes and first crossing electrons and one for the odd refluxes. Moreover another one was created to be used for the simulation of the escaping electrons.

In *mgdraw even* an ntuple is created to detect photons emitted backwards and forwards and electrons only backwards. An ASCII file is created to save energy, position and direction cosines of the forward emitted electrons.

In *mgdraw odd* an ntuple is created to detect photons emitted backwards and forwards and electron only forwards. An ASCII file is created to save energy, position and direction cosines of the backward emitted electrons.

In *escaping mgdraw* an ntuple is created to detect the escaping electrons everywhere around the target.

Usrmed routines

Two *usrmed* routines have been used: one to kill the electrons coming from even refluxes and from the initial beam and one to kill the electrons coming from odd refluxes. The method to kill particles consists in changing their weight to 0 once they cross a determined boundary. For the initial crossing electrons and for the even refluxing electrons this boundary is on the right of the target, so that the backscattering electrons can be detected. For the odd refluxing electrons the 'killing' boundary is on the right of the target, so that the backscattering electrons (i.e. the backscattering with respect to the motion of the main beam) can be detected. The *usrmed* routine was obviously not used during the simulation of the escaping electrons.

A schematic view of where *usrmed odd*, *usrmed even*, *mgdraw odd* and *mgdraw even*

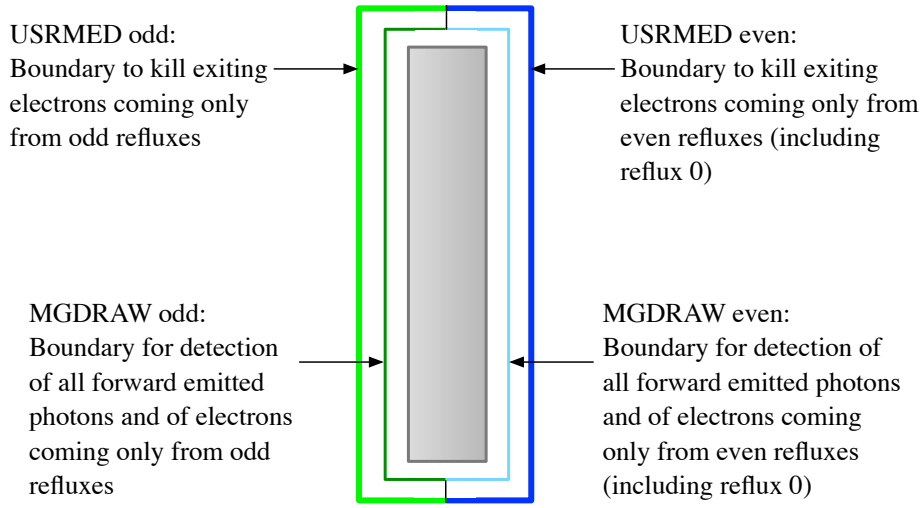

Figure 7.13 – Schematic view of the target and of the surrounding vacuum regions used in the *usrmed* and *mgdraw* routines.

were applied is given in figure 7.13.

Compiling and run

Exactly like in the previous simulations, an executable program is written to automatically compile and run an entire cycle of simulations, but this time the number of single simulations to run will be nine: one incident beam, seven refluxing beam, and one escaping beam. In order to have enough statistic, in particular for the doses detected in the stacks, at least one million particles were used in the simulation of the incident beam and then the entire cycle was repeated other 15 times using different random numbers.

When single runs are repeated at least twice, the executable file used to merge the binary files created by USRBIN (called *usbsuw* and available from the Fluka folder), not only merges the scored quantities in each run, but also calculates the averages and standard deviations. So in this case, for the dose detected in each TLD chip, the final result will be an average absorbed doses with associated a standard deviation. Obviously, increasing the number of particles in a run and the number of runs, the standard deviation decreases.

Analysis of the results

All the ntuples created during a complete set of simulations were merged together and analysed with PAW. This time not only the characteristics of the photons could have been investigated, but also those of the backscattering electrons (i.e. those emitted in the direction opposed to the main beam motion) and of the escaping electrons.

In order to compare the simulation data with the experimental data from Vulcan, the doses detected in the simulated and experimental TLD chips had to be compared. The merge of all the data coming from the USRBIN scoring is not possible directly, since each dose detected is normalised by the number of primaries in the simulation. This means that the doses coming from the first crossing electrons are normalised by the number of electrons chosen by the user in the input, but the doses coming from each reflux are normalised by the number of refluxing electrons. Thus, in order to know the total dose absorbed by the TLDs due to each reflux, it was necessary to firstly know the number of refluxing electrons. Remembering that in the *xxx_ele.dat* files each line corresponded to an electron, each file was scanned using the unix command *wc -l*, which in few seconds gives the number of lines in a file. Multiplying the number given by *wc -l* from each electron reflux file by the corresponding doses, the total dose absorbed by each TLD in each single reflux was calculated. In order to have the cumulative dose absorbed in a total set of simulations by each TLD, the doses calculated for each reflux and initial beam had to be summed. The values of these total dose were in pSv, so to be compared with the experimental doses they had to be transformed in mGy, which for electrons and photons is straight forward, being Sv=Gy.

Experimental and simulated doses were compared and plotted using MATLAB (The MathWorks Inc., Natick, MA, 2000). A normalisation factor had to be applied to the simulated doses in order to relate the small number of electrons simulated

to the large number generated by the laser in a shot. Each simulated k_BT required a separate normalisation factor. Once the best normalisation factor was chosen the trend of the experimental and simulated data were compared: when the agreement looked good, the k_BT and divergence used in the simulation could be assumed to best model the initial experimental laser-driven electron beam.

7.3.2 Comparison results

For reasons of space, all the different tries (simulating different divergences from 20 to 60° and k_BT from 0.5 to 12 MeV) to obtain the best fit are not shown here. Only the ones giving reasonable best fits for $(E\,\mathrm{exp})$ and for $(E^2\,\mathrm{exp})$ are shown in figure 7.14 and 7.15 respectively.

The best fits for both the studied initial electron distributions were obtained using k_BT=2.33 MeV and 50° of half angle divergence. Most of the simulated doses agree with the experimental ones considering the uncertainties, while for others, such as in the graph for the 6 mm target in figure (a), the comparison does not give good results mainly for the doses from TN and BEM stacks. The reason of this disagreement could lie in a shorter electron energy tail, but it is also necessary to remember that the experimental data from shot to shot could be different and in the case of the experiment with the Vulcan laser the measured doses were not an average of doses from several shots. This disagreement reflects also in the disagreement of the final points for most of the curves in the graphs in (b): all those points come from the 6 mm target graph in (a).

The large divergence could be explained with the expansion of the pre-plasma. The larger the duration of the laser pedestal (before the main peak arrives), giving time to the pre-plasma cloud to expand around the target surface, the larger the divergence of the produced electron beam will be.

So despite some small disagreements, the graphs in figures 7.14 and 7.15 could

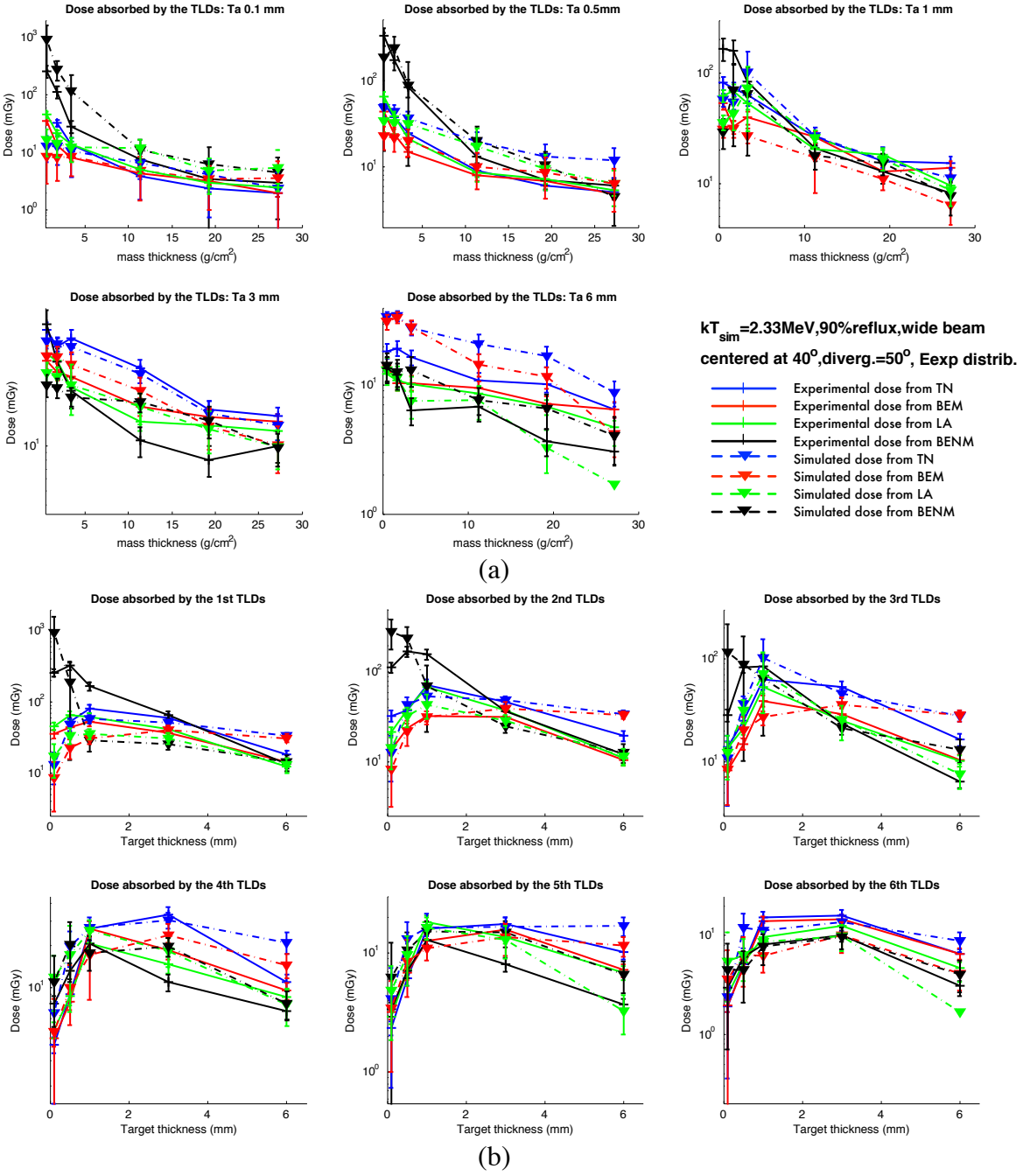

Figure 7.14 – Best fit of the experimental doses with the simulated doses using (Eexp) distribution with k_BT =2.33 MeV and 50° half angle divergence. In (a) the doses in each stack are plotted as a function of the mass thickness of the stack; in (b) the doses from each TLD number of each stack are plotted as a function of the target thickness.

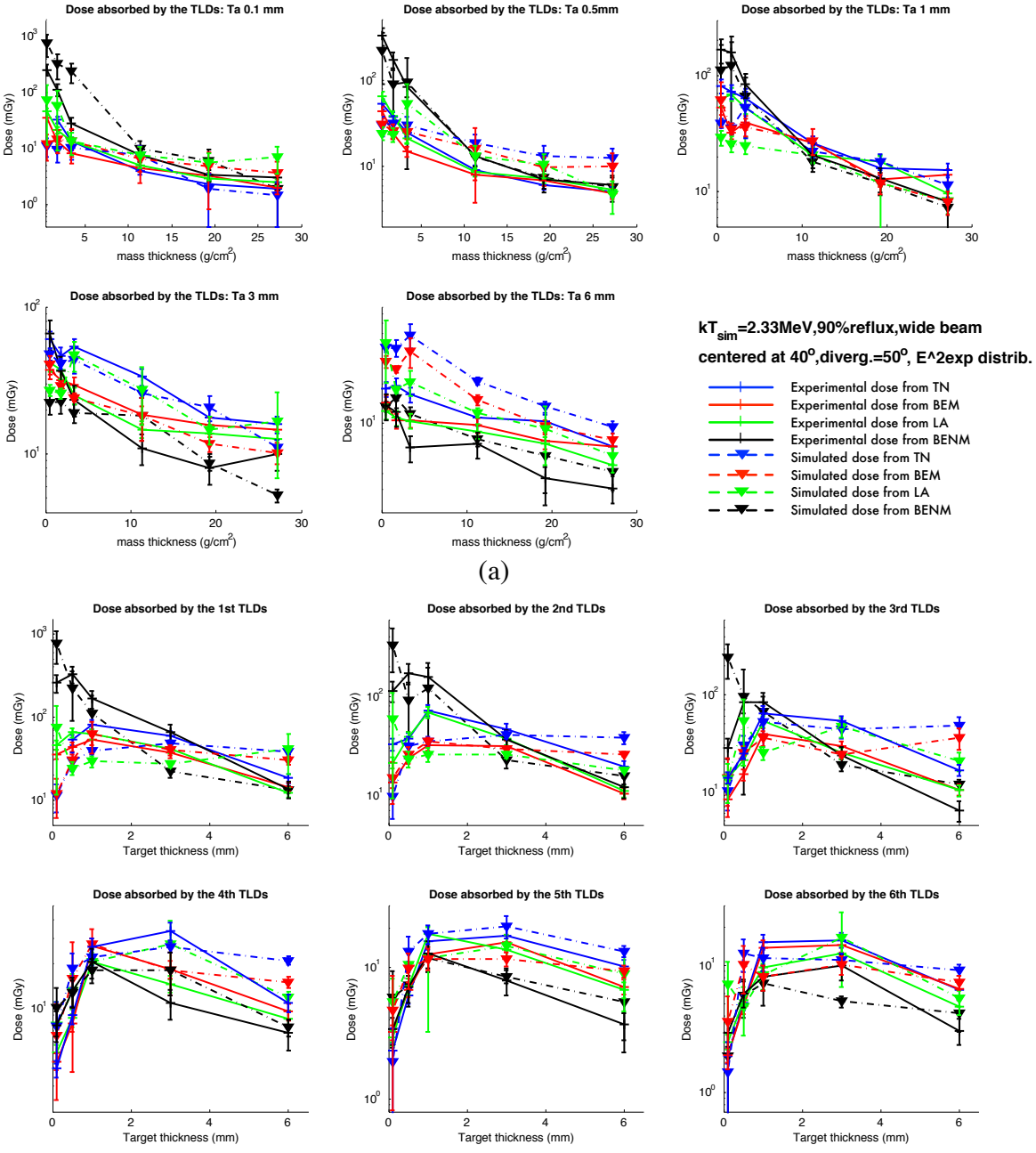

Figure 7.15 – Best fit of the experimental doses with the simulated doses using (E^2 exp) distribution with k_BT =2.33 MeV and 50° half angle divergence. In (a) the doses in each stack are plotted as a function of the mass thickness of the stack; in (b) the doses from each TLD number of each stack are plotted as a function of the target thickness.

represent the experimental data demonstrating not only that the approach used for the simulations well approximates real laser-driven electron beams created and accelerated from the irradiation of thick targets, but also that the experiment obeys the theory of the resonance absorption with the k_BT of the best fit being the one expected using equation 1.2 by Beg. In figure 7.16 and 7.17, examples of spectra of emitted forward escaping electrons, photons and positrons obtainable from the simulations are shown for the 1 mm thick target and for both the initial distributions. The main differences are in the number of emitted particles, higher for the $(E^2 \exp)$ distribution and in the shape of the electron spectrum, which has a longer tail and a peak at higher energies for the $(E^2 \exp)$ distribution. Also the positions of the spikes in the electron distributions are different: spikes at higher energies are noticeable in the $(E^2 \exp)$ distribution, which is due to the dependence on the electron energy of the method used to simulated the reflux mechanism. In the graphs in black in figure 7.16 and 7.17 only one peak and one spike are visible: they are respectively due to the first electron crossing and to the second reflux. The escaping electrons due to the first reflux are not visible because they are emitted in the backward direction, but they would be visible if the spectra of the electrons emitted in 4π were plotted. With regard to the forward emitted photon spectra, there is no profound difference between the shapes of the two graphs in red.

The choice on which initial electron spectrum best approximated the real beam is not easy: for some graphs, and in particular for the BENM stacks detecting also electrons, it looks that $(E^2 \exp)$ is the best, while for others, in particular for low mass thicknesses, $(E \exp)$ is better. It could be that none of them really represent the real electron distribution or, since for both the distributions the best fit was obtained using the same k_BT, that a distribution of the type $(E^{3/2} \exp)$, which is in between the two considered distributions, is closer to the real case. In order to find this out an experiment where the spectra of electrons and photons emitted are detected all

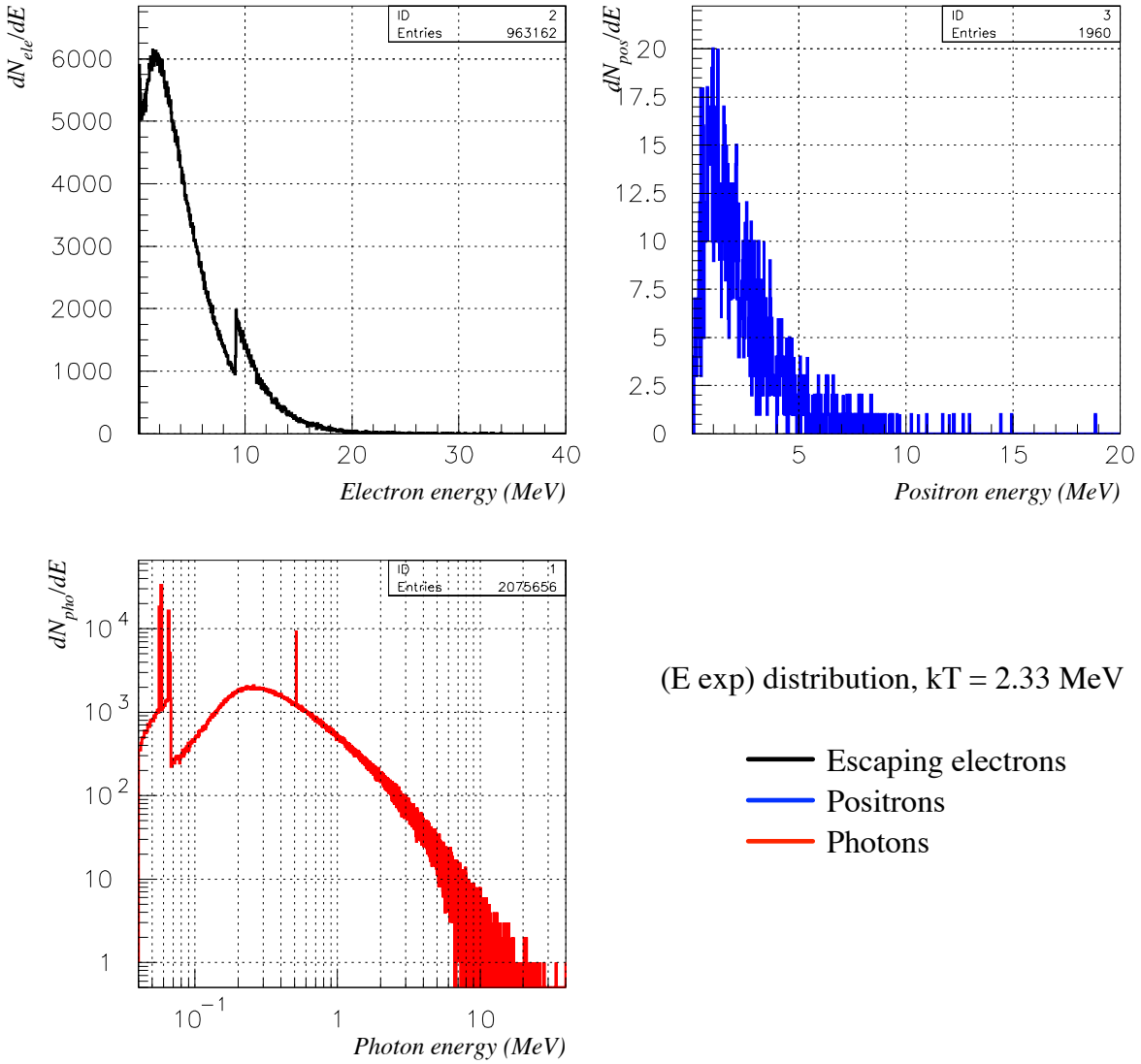

Figure 7.16 – Simulated spectra of the forward emitted particles for the (Eexp) distribution with kT=2.33 MeV

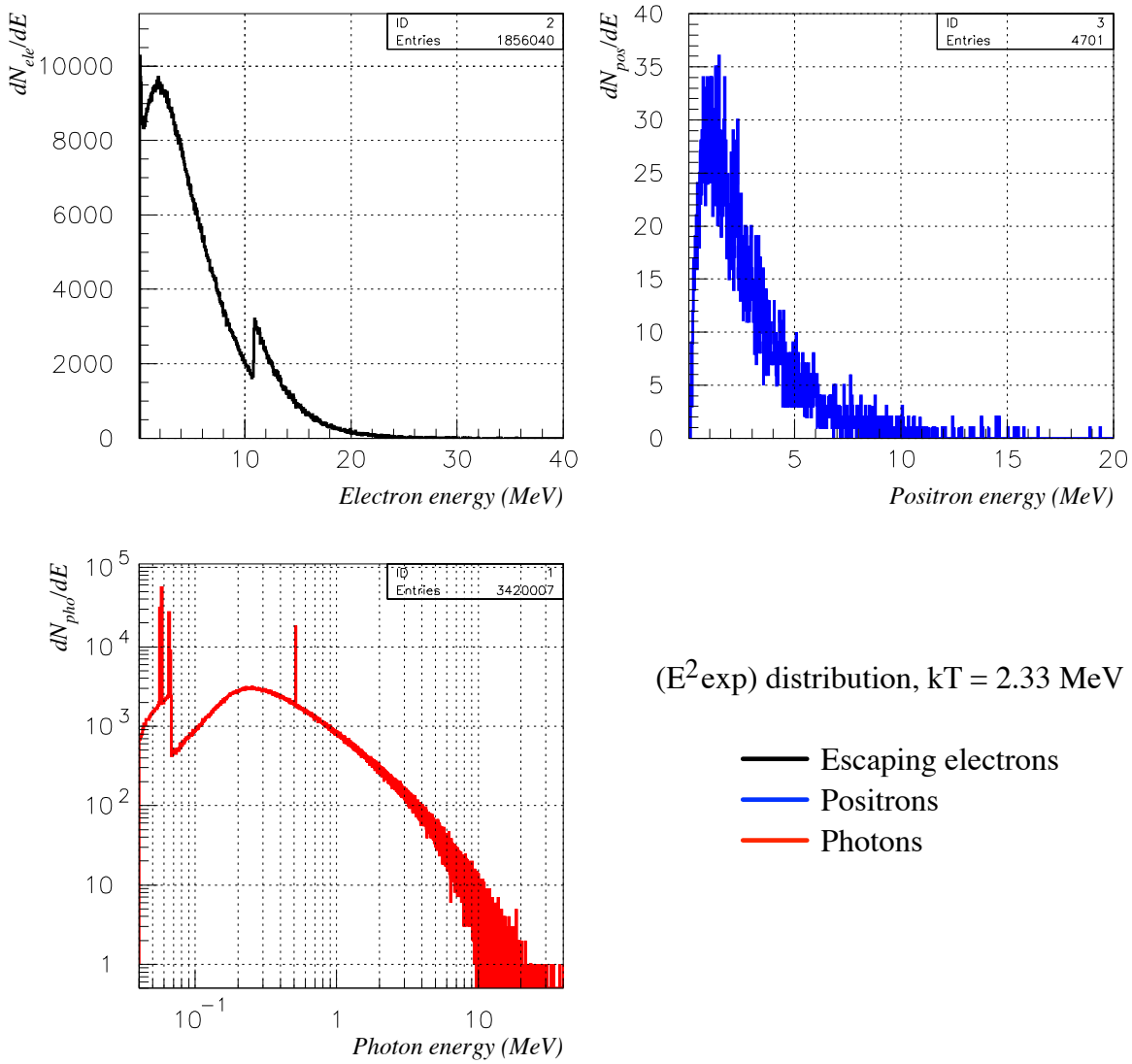

Figure 7.17 – Simulated spectra of the forward emitted particles for the $(E^2 exp)$ distribution with kT=2.33 MeV

around the target is necessary. Even doses, as in this experiment, could be used, but it is vital that more target thicknesses and more TLD chips inside each stack are used, that the stacks are placed around the target on X and Y axis to exactly determine the distribution of the beams, and more importantly that the same data are acquired using and not using magnets in front of the stacks.

7.4 CONCLUSIONS

The difference in the distribution of the dose, and so in the main acting force, in the very similar experiments performed at Gemini and Vulcan could be due to the different characteristics of the two used lasers and in particular in the pulse duration (much longer for Vulcan) and contrast ratio (higher for Vulcan) which could have produced different pre-plasma conditions. But given the unusual features of the data obtained using the Gemini laser, it is more likely to be that some error was made during setting the laser parameters. The measurements with and without magnets in front of the stacks could detect this strangeness because the maximum energy of the emitted electrons was lower than what expected given the intensity of the laser.

Further studies extending the covered angular range along the X and Y-axis are required to characterise completely the electron and photon beams. The angular distribution is an important factor that should be determined in any experiment given that the direction of the beam and its initial k_BT determine the main accelerating force. As already mentioned measurements should be done to to separately resolve the angular distribution and spectrum of photons and escaping electrons.

From the simulations of the Vulcan experiment, it is seen that the approach used to perform the electron reflux well approximates the real situation of irradiated thick targets notwithstanding all the assumptions made (see chapter 6) and the fact that there is no plasma in the simulations: the simulated target is a cold solid target and

does not explode after the irradiation.

Several applications can be found for these beams and in particular for the photon one. Imaging is one of the proposed applications, in particular tomography of objects for security purposes. Medical imaging is not possible using the Gemini and Vulcan laser with their nominal intensities because the created beams are too energetic. Medical imaging is usually performed with X-ray spectra with 200-300 keV as maximum energies, while the maximum energy obtained from Vulcan was $\sim$30 MeV.

CHAPTER 8

CONCLUSIONS AND POSSIBLE FUTURE WORKS

This final chapter is intended to rapidly summarise the results obtained during the PhD which have been discussed in more detail throughout this thesis. Each section also contains a description of the possible research which could follow from the work explained in the main chapters.

8.1 DOSIMETRY OF LDPRB USING GAFCHROMIC FILMS AND FLUKA SIMULATIONS

In chapter 4 a radiobiological experiment using laser-driven proton beams is explained as well as the dosimetry method employed to calculate the doses absorbed by the irradiated V79 cells. This dosimetry method has been developed using GafChromic films and Fluka simulations in order to compensate for the fact that conventional dosimetry cannot be used in the presence of these high dose-rate beams. The method, even if developed appositely for the experiment, can easily be adapted

to any other radiobiology experiment involving laser-driven beams with the limitation that the shape of the spectrum of the particles accelerated by the laser is at least roughly known so that Fluka simulations can be performed to obtain the dose absorbed by the cells. Starting from the first estimate of dose, measured from the films conveniently placed beyond the cell dish, two corrections to this dose have to be calculated. The first is due to the fact that radiochromic films are LET dependent, so, depending on the energy of the protons irradiating them, the response in dose will be altered. The second is due to the fact that even if conveniently placed, films and cells were not at the same distance from the origin of the beam and that they also did not have the same equivalent thickness. Both the corrections have been calculated using accurate Fluka simulations of the experimental set-up. Results of the dosimetry method are the proton spectra shown in figures 4.10, 4.11, 4.12 and 4.13. Result of the experiment and demonstration of the good suitability of the applied dosimetry method is the graph in figure 4.15, where the cell survivals are plotted against the calculated doses.

In order to show that laser-driven proton therapy is feasible the obtained data have been compared to data for V79 found in literature. The agreement between the data is shown to be very good. Another comparison has also been done using conventional accelerated X-ray beams and the results obtained are good as well (see figure 4.19), giving an RBE_{max} close to 3. Despite the fact that better statistics are necessary for the laser-driven data in order to calculate a good estimate of RBE, an $RBE_{max} \geq 1$ still means that laser-driven proton therapy is not only possible (or will be possible when the proton beam energies are increased) but also more radiobiologically effective than conventional radiotherapy using X-ray beams.

A study was also performed in order to compare the laser-driven results with the results which could be obtained using the same method of handling the cells and a conventional proton beam, like the one accelerated by the cyclotron of the

University of Birmingham. The study was carried out to create a wheel made of absorbers with different thicknesses in order to recreate, using the cyclotron, a proton spectrum similar to the one generated by the TARANIS laser. The simulations and the calculations of the thicknesses and angles to actually build the wheel are ready (see figure 4.18 and table 4.2), but an experiment has not yet been conducted. So a future work is, not only to repeat the experiment using the TARANIS laser to have better statistics and reach higher doses and lower survivals and then calculate the RBE, but also to perform the irradiation with the cyclotron accelerated beam using the designed wheel. The results from both the experiments, then, will be compared in order to provide a more accurate evaluation of the difference between a conventionally accelerated and a laser-driven proton beam.

8.2 Nuclear activation as a detector of LDPB

The nuclear activation study described in chapter 5 shows that activation of foils irradiated by particle beams (laser-driven or not) can be used as a reliable detector of beam current. This method could be useful not only for the detection of laser-driven beams, but also for any occasion when the conventional dosimetry techniques fail or could fail because of possible saturation or damage.

Other than copper foils which have been widely used previously, other two materials, cadmium and titanium, have been tested using the proton beam accelerated by the University of Birmingham. The only limitation to this method, in which a specific reaction is chosen depending on the characteristics of the daughter isotope created, is that the cross section of this chosen reaction has to be known in order to calculate the number of initial particles starting from the number of detected gamma rays.

The method and the selected materials have been tested using a conventional proton beam, but they still need to be applied to laser-driven proton or ion beams.

Starting from the description of the method and from the suggestions in section 5.2 a future researcher should be able to perform a test with a laser-driven beam. The main suggestion is due to the fact that laser-driven proton or ion beam are not monoenergetic, so in order to know the number of particles with a specific energy, an energy selection system should be used. If, instead, it is not possible to use an energy selection system, the researcher will have to find metals with cross sections of production of radioactive isotopes which are strongly peaked at a particular energy. In this way the user will know that the beam consists of a number $X \pm x$ of particles with an energy $E_{min} \leq E \leq E_{max}$ both depending on the width of the cross section distribution. Another opportunity could be the use of a mixed metal foil or stacks of different metals. This could be useful not only for energy reasons, but also because at high laser intensities the accelerated beam could be a mix of protons and ions.

8.3 FLUKA SIMULATIONS OF LDXRB AND EXPERIMENT AT VULCAN

The simulations described in chapter 6 have been performed in the context of the fact that, at present, there are no simulation programs capable of predicting exactly what happens in matter when a laser pulse hits a thick target. Starting from supposed distributions of electron beams accelerated by petawatt laser pulses, Fluka simulations have been used to study the X-ray beam produced by the electrons crossing the irradiated target and its dependence on the temperature of the electron distributions. The simulation approach makes several assumptions to simplify the way the refluxing electron beam is simulated using a program which is not designed to simulate a laser or its interactions with matter. First of all, since the laser interacts with a plasma created on a very thin layer (few micrometers) of the target, the produced electron spectrum is only dependent on the laser characteristics and not on the target material and the used distribution is $dN_e/dE = E^2 \exp(-E/k_B T)$

(called $(E^2 exp)$) or $dN_e/dE = Eexp(-E/k_BT)$ (called $(Eexp)$). Secondly, the electron beam exiting the target is forced to re-enter the target: the spectrum of the outgoing electrons is saved and while X% of the most energetic electrons can escape, (100-X)% of them are forced to re-enter the target. Each refluxing electron is reinserted in the target from the same point where it escaped and its direction cosines are inverted, and this is repeated until there are no more emitted electrons. The target is simulated as a solid target and not a sort of solid-plasma mix which it becomes in reality when it is irradiated by a petawatt laser. Detailed information about the code written to implement the simulation is given in section 6.2.

The results of this simulation study are shown in figures 6.6 (for $(E^2 exp)$ distribution) and 6.7 (for $(Eexp)$ distribution), where the yields of the photons emitted forward are plotted against the mass thickness of the targets, for each material and each k_TB simulated. Plotting the initial electron temperatures used in the simulations as a function of the mass thicknesses giving the maximum photon yields for each material, the graphs in figure 6.8 and 6.9 are obtained respectively for $(E^2 exp)$ and $(Eexp)$ distribution.

The results of the comparison between the experimental data and the simulation performed for the Vulcan experiment (figures 7.14 and 7.15 respectively for $(Eexp)$ and $(E^2 exp)$ and detailed explanation about the code in section 7.3.1) show that this approach, even if with some imprecision, quite well approximates what actually happens in the interaction of petawatt lasers and thick solid targets. The best fits were obtained for temperatures perfectly in agreement with those expected from resonance absorption which is believed to be the main force accelerating the electrons.

This demonstrates that these simulations can be used as a method to estimate the initial electron temperature of electron beams. Detecting the number of photons emitted forward into 2π (or even the dose due to these photons) and looking at the

maximum yield, it will be possible to estimate the initial electron energy and so also the energy of the exiting electrons. This is a test that could be implemented whenever there is an interest in using laser-driven electron and/or photon beams.

There are still characteristics which are not clear related to these created electron and photon beams, so that further studies extending the covered angular range along the X and Y-axis and using different laser intensities are required to characterise completely the electron and photon beams and their dependence on the laser properties.

8.4 OTHER WORKS

Other project have been started during the PhD but not completed. One of these is the study of treatment plans for patients with metal and non-metal implants. The presence of these implants causes artefacts in the CT, so that the treatment plan based on the CT is compromised. The study also includes an estimate of the activation that the implants acquire after sessions of particle therapy. All of this should be implemented with Fluka simulations and then, irradiating the implants in a water phantom according to the simulated treatment plan, compare the activation. A microCT was carried out using the microCT of the School of Dentistry of the University of Birmingham and using the images from each CT slide the geometry part of the simulation involving only the implant was performed. The particular implant firstly taken into consideration was a spinal support made of peek (Polyether ether ketone) with titanium inserts. The simulated geometry, the real object and the frontal microCT are shown in figure 8.1. The aim of this study is to prove that implanting plastic supports is better for all those patients who could benefit of radiotherapy treatments (conventional or non). The disadvantage to this is that usually plastic implants are less resistant and durable than the traditional metallic ones. Improved materials such as peek are being developed helping surgeons in the deci-

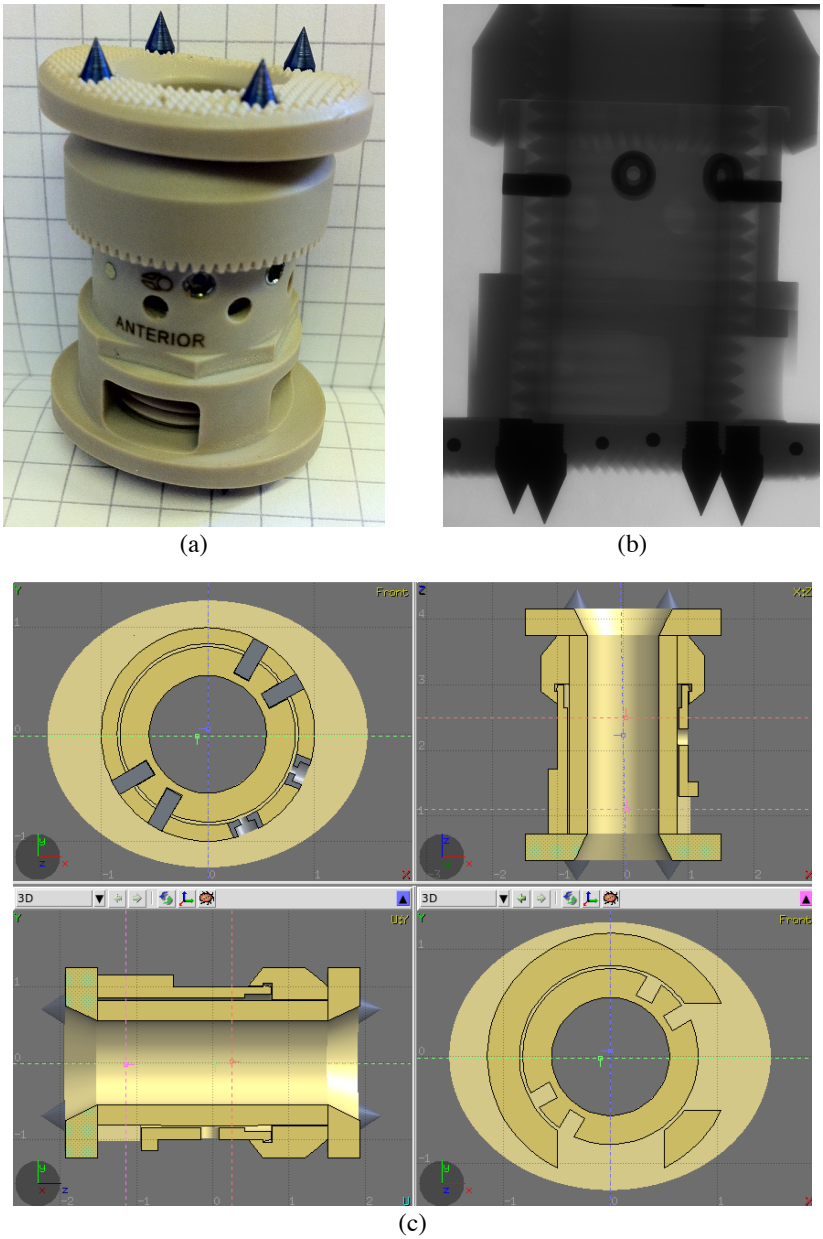

(a) (b) (c)

Figure 8.1 – (a) Spinal support implant made of peek and titanium, (b) frontal microCT and (c) simulate geometry using Fluka. The darkest object in (b) are the titanium inserts.

sion of which implant use. Also another spline cage (made by Creaspine®) entirely made of peek has been considered for this study and given its reduced geometric complexity a normal CT has been performed at the Queen Elisabeth University Hospitals Birmingham.

Another simulation has been started to determine the calibration of an NPL

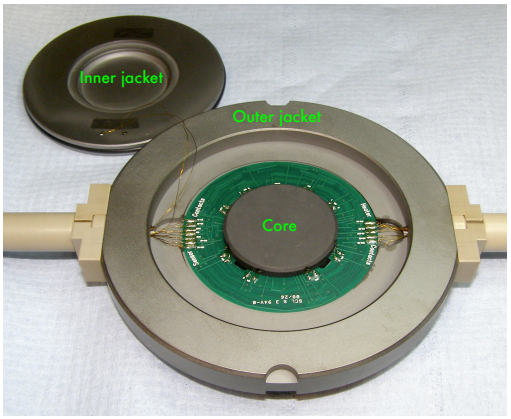

(a)

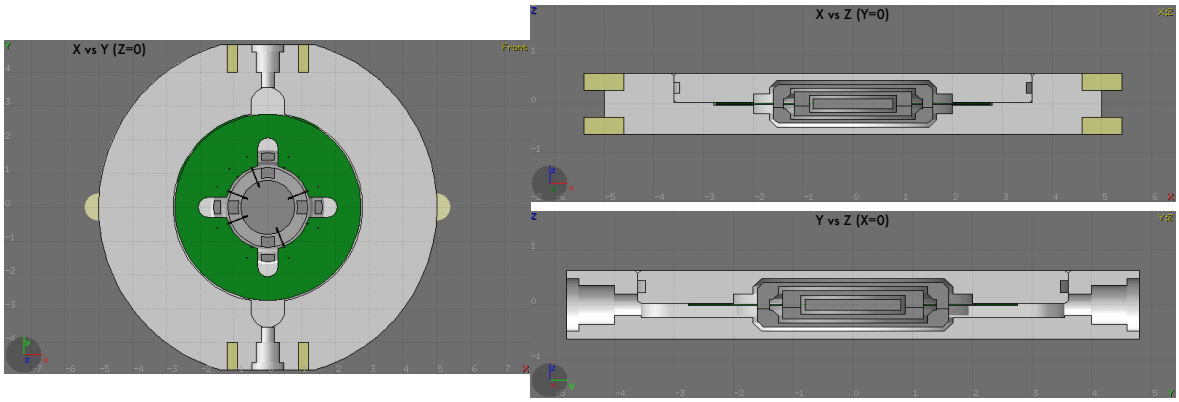

(b)

Figure 8.2 – (a) Photograph of the NPL graphite calorimeter, where the main three objects, core, unmounted inner jacket and outer jacket are clearly shown. (b) Geometry of the calorimeter simulated with FLUKA.

calorimeter. Images of the device and the simulated geometry are shown in figure 8.2. Because of the inhomogeneities of the calorimeter (holes, wires and thermistors) the relationship between the rise of temperature and dose to water has to be calculated using equation 2.18 and so through the simulation the determination of the effects due to these inhomogeneities, $\prod_{i=1}^{n} k_i$, can be evaluated.

APPENDIX A

A BRIEF INTRODUCTION TO PARTICLE THERAPY

Therapy using protons and heavier ions has two main advantages compared to the conventional X-ray radiotherapy. The first advantage is the large ballistic efficiency of hadrons due to the different energy-loss mechanisms compared to photons and electrons. In particular, hadrons lose most of the energy at the end of their penetration path instead of at the beginning, exhibiting a peak in the energy loss spectrum known as the Bragg peak. This can be seen in figure A.1, where the dose is depicted in function of penetration depth for carbon ions. That this peak could be useful for the treatment of tumours was first proposed by Wilson in 1946 [109]. Another noticeable feature is that the energy loss is relatively small before the peak and almost nil after, resulting in the possibility to localise the effect of the ion beam to a small spot. The position of the Bragg peak depends on the energy of the incident ions and can be controlled by changing the energy of the incident ion beam. The size of the Bragg peak is of the order of millimetres, smaller than that of a typical tumour (which is in the centimetre range), so that beam modulation is used to conform the

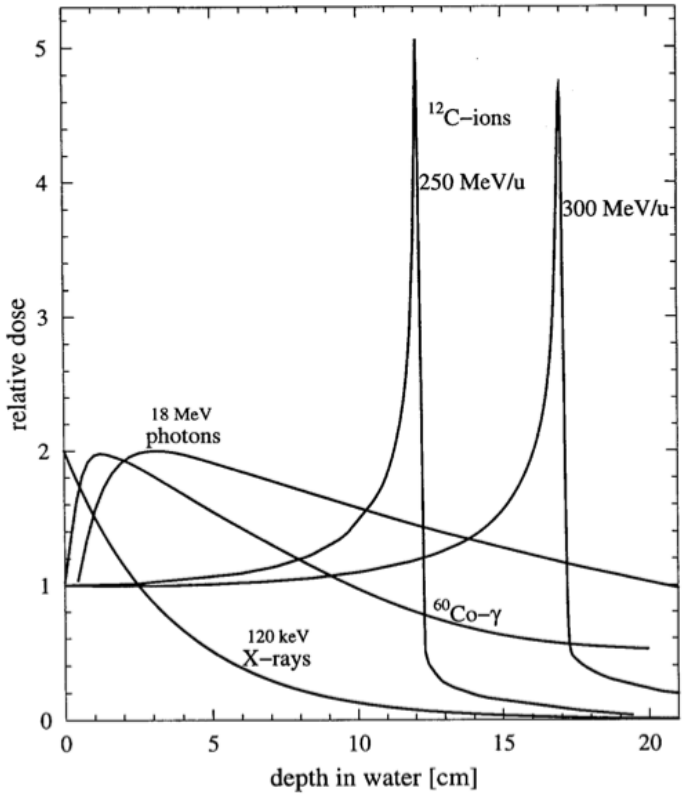

Figure A.1 – Depth doses curve comparison for different beams used in radiotherapy

beam to the size of the target, creating a spread peak generally referred to as Spread Out Bragg Peak (SOBP).

A.1 BETHE-BLOCK FORMULA

The principal effects which characterise the passage of particles through matter are the energy dissipation of incident particles and the particle deflection from the incident beam direction. These two effects are due to inelastic collisions between the particles from the beam with atomic electrons in the material and to the elastic scattering between nuclei. However, there are also other processes which may be observed, in primis, nuclear reactions.

The energies relevant for therapeutical purposes are those determined by the necessity to have a penetration range in water of up to about 25 cm. This translates

into an energy interval from about 50 to 250 MeV for proton therapy and from 50 to 400 MeV/n for carbon ion treatment. The most probable process of energy dissipation is represented by collisions with the electrons of the target atoms. In these collisions, the energy is transferred from the incident particles (hadrons in this case) to the target atoms, causing ionisation. This energy loss is described by the Bethe-Block formula [28]:

$$-\frac{dE}{dx} = \frac{4\pi e^4 n_e Z^2 Z_{eff}^2}{m_e v^2}\left[\ln\left(\frac{2m_e v^2}{I}\right) - \beta^2 - \frac{\delta}{2} - \frac{C}{Z}\right] \tag{A.1}$$

where n_e is the electron density in the target, Z is the atomic number of the target, v the velocity of the particles in the incident beam, $I = \langle V \rangle$ is the average excitation potential of the target atoms V, $\beta = v/c$ and γ is the Lorentz factor. Z_{eff} represents the effective charge of the projectile, which can be calculated through the Barkas approximation [110]:

$$Z_{eff} = Z\left(1 - e^{-125\beta Z^{\frac{2}{3}}}\right) \tag{A.2}$$

The β^2 term in equation (A.1) is due to the consideration of relativistic effects. $\delta/2$ is the density term, important at high incident energies, and is due to the electric field screening by the electrons. The term C/Z is important only for low velocities of the incident particles and must be considered when their velocity is comparable to the average velocity of electrons in an atom.

In the therapy case, the beam energy is relatively low and the relativistic and density terms can be neglected. The Bethe-Block formula then reduces to:

$$-\frac{dE}{dx} = \frac{4\pi e^4 n_e Z^2 Z_{eff}^2}{m_e v^2}\left[\ln\left(\frac{2m_e v^2}{I}\right) - \frac{C}{Z}\right] \tag{A.3}$$

so that the Bragg peak shown in figure A.1 can be easily understood in terms of the factor $1/v^2$ in the Bethe-Block equation. This term is inversely proportional to the kinetic energy of the impinging particles, producing a plateau in the energy loss for

fast ions and a peak at the end of the ion penetration depth.

The range of a particle is defined as the distance it covers in a material before losing all of its kinetic energy. This quantity is given by:

$$R = \int_0^E \left(\frac{dE}{dx}\right)^{-1} dE \tag{A.4}$$

Since the energy dissipation is a random statistical process, the energy spectrum is broadened to take-on a gaussian distribution, centred at the range R [27]:

$$S(z) = \frac{1}{\sqrt{2\pi}\sigma_z} e^{-\frac{(z-R)^2}{2\sigma_z^2}} \tag{A.5}$$

with a standard deviation given approximately by:

$$\sigma_z = 0.012 \frac{R^{0.961}}{\sqrt{A}} \tag{A.6}$$

where A is the mass number of the particles. Some standard deviations for several types of projectiles in water, with a fixed range of 20 cm, are given in table A.1.

ion	p	α	C	Ne
σ_z	2 mm	1 mm	0.6 mm	0.46 mm

Table A.1 – Range standard deviation for different particle beam.

These examples show that the broadening of the distribution falls off with increasing mass number, improving the probability that the ion beam releases its maximum energy in the pre-estabilished region.

Multiple Coulomb scattering of hadrons with the nuclei of the target causes lateral broadening of the beam. This phenomena is well described by Molière theory [111], according to which, for small angles α, the particles acquire an angular

distribution given by:

$$f(\alpha) = \frac{1}{\sqrt{2\pi}\sigma_\alpha} \exp\left(\frac{-\alpha^2}{2\sigma_\alpha^2}\right) \tag{A.7}$$

$$\sigma_\alpha = \frac{14.1\text{MeV}}{\beta pc} Z_p \sqrt{\frac{d}{L_{rad}}\left(1 + \frac{1}{9}\log_{10}\frac{d}{L_{rad}}\right)} \tag{A.8}$$

where σ_α is the standard deviation of the gaussian distribution, p is the impulse of the particles, L_{rad} the radiation length and d the thickness of the target. As can be seen from the top graph in figure A.2, photons and protons are more affected by multiple scattering than ^{12}C ions and their lateral distributions are larger. Understandably, this phenomenon is very important during treatment planning for an actual tumour, since it is strongly desirable to be able to avoid unnecessary damage of critical structures along the main direction of the beam before the tumour is reached.

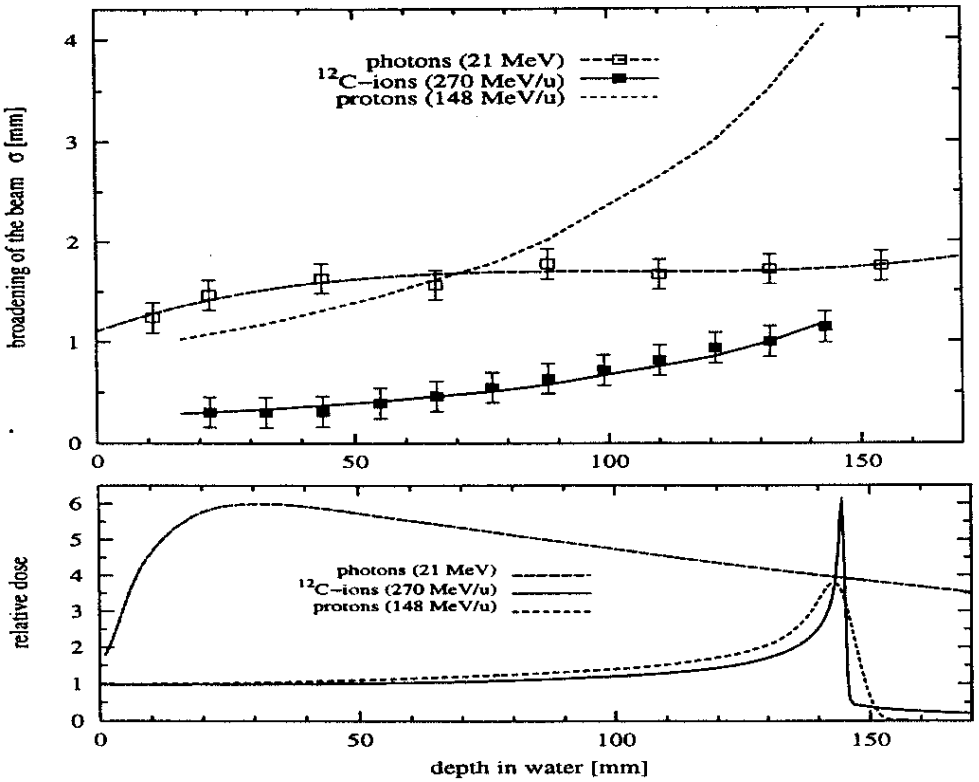

Figure A.2 – Comparison between lateral scattering (top) and the relative doses (bottom) for photons, protons and ^{12}C ions. Image taken from [27].

Summarising, in term of physical dose, the presence of a Bragg peak in the energy loss spectrum and the restricted lateral distribution of a ^{12}C ion beam compared to a photon or proton beam, indicated that the use of heavy ions has considerable advantages over photons or protons for cancer therapy.

A.2 Nuclear Reactions

When a hadron beam crosses a material, nuclear reactions may occur. There are two basic types of such reactions: the so-called direct reactions and the reactions of the compound nucleus [80]. Nuclear reactions take place when the projectile collides with the nucleus target, an event which occurs on time-scales of the order of 10^{-22} s. Upon collision, the projectile can interact with a nucleon, with a group of nucleons, or with the whole nucleus, after which it is ejected. The simplest example of a direct reaction is elastic scattering, which leaves the target nucleus in its ground state. In inelastic reactions on the other hand, the nucleus is left in an excited state, because consecutive scattering events between the incident particle and the nucleons of the target nucleus take place. These initially cause the excitation of single particle states, followed by collective excitations of the nucleus

Alternatively the projectile can be caught by the target nucleus and its energy divided between all the nucleons of the new compound nucleus. Compound nucleus reactions then take place until statistical equilibrium is reached (which is not necessarily equal to the ground state energy). After fusion and the creation of the compound nucleus, a large part of its energy is converted in collective translational motion of the nucleons. This motion, following a cascade of nucleonic interactions, transforms into thermal chaotic motion, which gives the thermalisation of the compound nucleus. Prior to thermal equilibrium, nucleons, or clusters of nucleons, with energy greater than that of other nucleons, may be emitted in continuum, giving rise to a process called pre-equilibrium emission.

If the energy of the incident ion is below a certain threshold, $E_{inc} \leq 25$ MeV/n, the particles are emitted in coincidence with the residual nucleus, i.e. the nucleus after the pre-equilibrium emissions. Since the ejected particles have a very small mass compared to the residual nucleus, the residual and compound nuclei have approximately the same mass. The residual nuclei are then emitted in very small angles and with velocities similar to those of the compound nuclei. At high incident energies, the excitation energy is high enough to cause the ejection of multiple particles, some of which will not necessarily have low kinetic energy or mass. In this case the velocity of the residual nucleus will be smaller than the velocity of the compound nucleus.

If the compound nucleus has a high excitation energy and a high angular momentum, it may split into two fragments immediately after its formation. In fact, having a considerable angular momentum J, the nucleus will begin to deform along the axis perpendicular to the rotational axis of the nucleus. If the angular momentum is high enough, the ellipsoid of rotation will become so elongated that the scission in two big fragments will be inevitable.

A nucleon or a group of nucleons dwelling on the surface of the nucleus may be able to escape due to statistical energy fluctuations. This statistical process is called evaporation, being very similar to the evaporation of molecules from liquid drops. Only particles with sufficient energy to cross the Coulomb barrier can evaporate. If the excitation energy of the compound nucleus is high enough, the evaporation may occur sequentially for several particles giving rise to what is known as chain evaporation. The most abundant particle types emitted in such processes are alpha particles, especially at the end of the chain evaporation. This is due to the fact that nucleons in alpha particles are more tightly bound between themselves than to the other nucleons in the nucleus. Evaporation continues also after fission, until the nucleus reaches the threshold energy for particle evaporation. Beyond this

threshold, the nucleus emits photons until its ground state is reached. In contrast to pre-equilibrium emissions, evaporation occurs only for lower energy particles which are always ejected isotropically in space. While evaporation emission takes place as soon as the Coulomb barrier is surpassed, pre-equilibrium emission occurs whenever there is a difference between energies of the compound and residual nucleus.

In the case of light incident ions, the ejected particles will prevalently have a smaller mass than that of the projectiles and a velocity very similar to that of the incident beam. This is a sign that a binary break-up processes have taken place. Fragments are emitted in very small angles preferentially forward. There are three different kinds of break-ups:

- elastic break-up, where two fragments are emitted and the target nucleus is not excited;
- inelastic break-up, where two fragments are emitted, but one has interacted with the target nucleus, exciting it. The nucleus must then de-excite emitting particles or photons;
- fusion break-up, also called incomplete fusion, where even if a binary fragmentation has occurred, only one of the fragments is emitted, because the other is absorbed by the target nucleus, that ends up in a highly excited state [112].

At sufficiently high incident energies, every fragment of the projectile preserves the initial, forward, velocity, with the addition of an angular spread due the internal motion of the nucleons. This spread is observed experimentally in the angular distribution of the fragments, which are not detected only in the forward direction, but also at very small angles. The nuclear field of the target nucleus, despite being strong enough to cause the division of the projectile in two fragments does not modify appreciably their motion. In the case of incomplete fusion, this statement is valid

for the single fragment that is detected.

The effect of all these reactions is fragmentation, which produces new particles with different mass, atomic number and velocity with respect to the initial incoming beam. The production of such fragments may be a problem for therapy since these new particles have a different energy loss spectrum and therefore exhibit different Bragg peaks and dose distributions. Particles with mass and charge smaller than the primary beam but with similar velocity have longer ranges in materials (see figure A.3 (a)): this causes a spread of the Bragg peak. For some heavy ions, the tail due to fragments can even be larger than the peak itself. These effects are illustrated in figure A.3 (b), where the dose beyond the peak position increases with the mass of the primary nuclei in the beam.

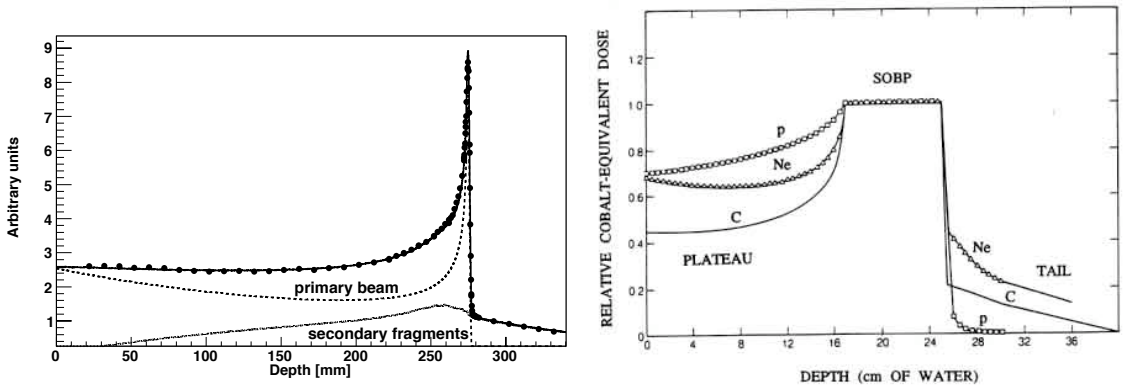

(a) (b)

Figure A.3 – (a) Bragg curve as a function of depth in water for a 400 MeV/n carbon beam. The points and the solid line represent the experimental data and the Fluka calculations, respectively. The dose contribution from primary ^{12}C ions and secondary fragments is also reported. Both the experimental data and the MC results are normalised by the integral of the Bragg curve calculated between the entrance region and the BP. Image taken from [113]. (b) By varying the energy during the irradiation in a controlled way, it is possible to superimpose many narrow Bragg peaks and obtain a Spread-Out Bragg Peak (SOBP). The dose release due to various different nuclei is shown, with the region beyond the SOBP due to fragmentation. The dose due to fragmentation is 1-2% for protons, $\sim$ 15% for ^{12}C and $\sim$ 30% for ^{20}Ne.

A.3 RELATIVE BIOLOGICAL EFFECTIVENESS

In the previous sections it has been found that heavier ions are preferable for therapy due to their kinematic properties. However, this advantage is contrasted by fragmentation issues as the ion mass increases. It is therefore necessary to find a compromise in choosing ions for particle therapy that takes into account the dose due to primary particles, as well as the dose due to their fragmentation in the patient tissue.

The target of protons or ions in particle therapy is the DNA contained in the core of the cancer cells, because it is only by causing irreparable damage to the DNA that the functions of these cells and their reproduction capabilities are inhibited. Hadrons cause a larger biological damage compared to photons for a given dose. However, the absorbed dose alone does not prove to be a satisfactory parameter to evaluate the radiation efficiency on biological tissue. What is used instead, is the relative biological effectiveness (RBE), defined as the ratio between the X-ray dose and the particle dose necessary to give the equivalent biological effect:

$$\mathrm{RBE} = \frac{D_X}{D_p} \tag{A.9}$$

The images in figure A.4 show the difference between the structure of a proton and a carbon track in nanometre resolution compared with a schematic representation of a DNA molecule. The higher density of secondary electron production for carbon ions will create a larger amount of DNA damage.

At low absorbed doses, the logarithmic biological response to X-rays can be related to the level of cell survival S by the approximate relation:

$$S = S_0 \, e^{\alpha D + \beta D^2} \tag{A.10}$$

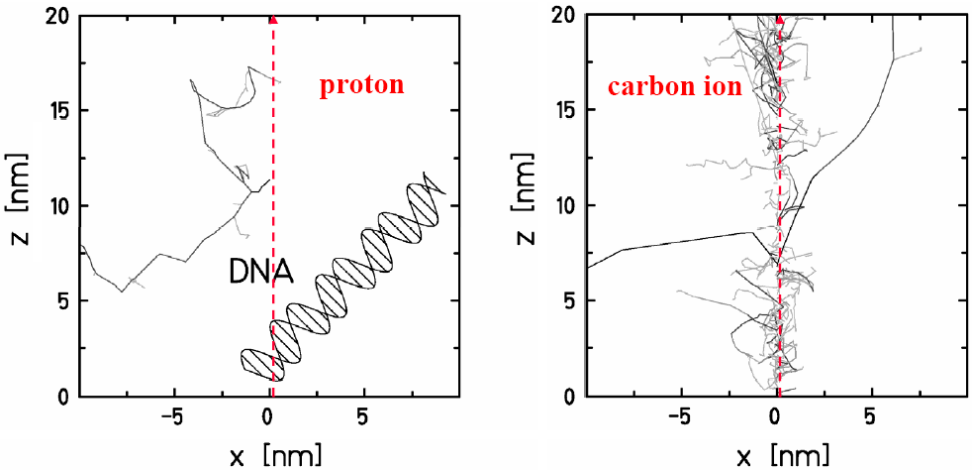

Figure A.4 – Comparison between the amount of secondary electrons produced by a proton and by a carbon ion in nanometre resolution which is the resolution comparable with the DNA molecule. Image taken from [29].

In the case of ions or protons irradiating cells in the Bragg peak region of their depth-dose curve, the β parameter is very small and may be neglected. The logarithmic biological response then becomes a linear function of the dose. This effect is shown in figure A.5. Asymptotically, the RBE tends to 1, since at very high doses the death of cells is certain.

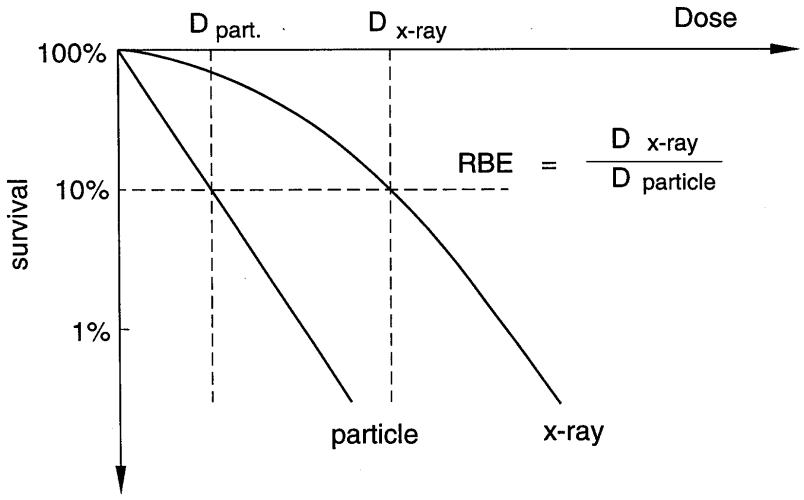

Figure A.5 – Survival of cancer cells: for a given dose, the survival after irradiation by photons is larger than the survival after ion irradiation.

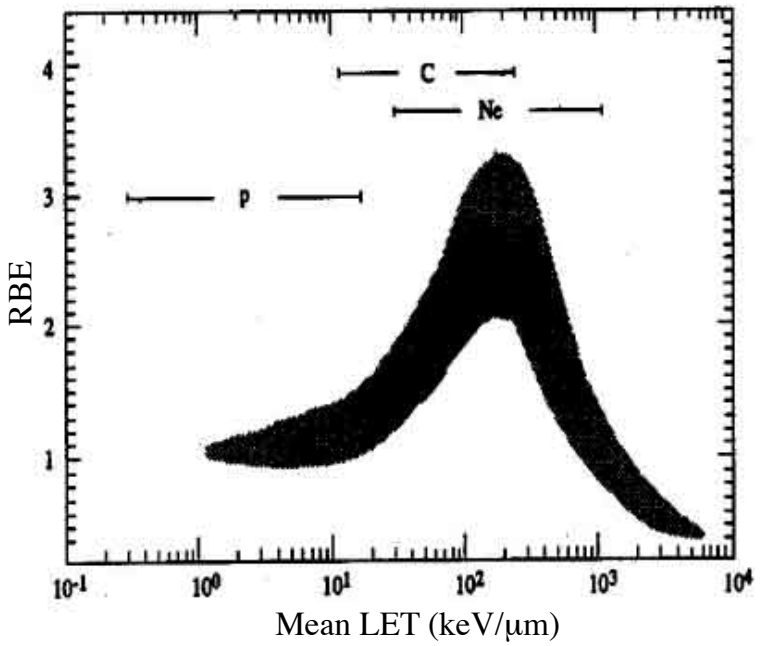

Figure A.6 – Relative Biological Efficiency (RBE) in function of the Linear Energy Transfer (LET) for protons and neon and carbon ions. Image readapted from [114], where results from experiments using different energies and cell types were plotted.

The RBE depends on several factors, most importantly on the linear energy transfer per unit path (LET). This depends on the dose level and on the type of the irradiated tissue. RBE as a function of LET is shown in figure A.6. At the energies used in therapy, at the maximum LET, protons have an RBE of 1.3 (figure A.6). This means they are 30% more efficient with respect to photons, for which the RBE values is by definition always 1. The RBE for ^{20}Ne is very high, however due to fragmentation issues it is unsuitable for therapeutic use. The best compromise turns out to be ^{12}C, which has an RBE from 1.5 to 3.5 and produces a reasonable amount of fragmentation (figure A.6 and figure A.3 (b) respectively).

In conclusion, an ion treatment not only allows a much more accurate dose distribution due to the ballistic efficiency of ions, but is also much more efficient in terms of biological effects than therapies based on photons or protons. In any case, since the energy of the laser-accelerated carbon ions is still too low for therapeutic purposes, proton beams were used for the radiobiological experiment in chapter 7.

APPENDIX B

EXPERIMENTAL AND SIMULATED YIELDS OF NUCLEAR ACTIVATION OF NATURAL CADMIUM WITH PRODUCTION OF ^{110}IN

This Appendix is related to chapter 5, and in particular to the discussion started at the end of section 5.1.2 explaining why the reaction ^{nat}Cd+p=^{110}In+xn cannot be used for nuclear activation measurements in the case the user wanted to support the analysis with Fluka simulation. In fact, in principle the chosen photon peaks (at 657 and 884 keV) due to the decay of ^{110}In to ^{110}Cd by electron capture can be experimentally used to calculate the number of incident protons, but simulating the reaction with Fluka does not give good results, because ^{110}In is produced not only in the ground state, but also in the metastable state.

When asked, Fluka developers said that Fluka should be able to simulate correctly the production of ^{110}In (G+M), but not the production of the two single states

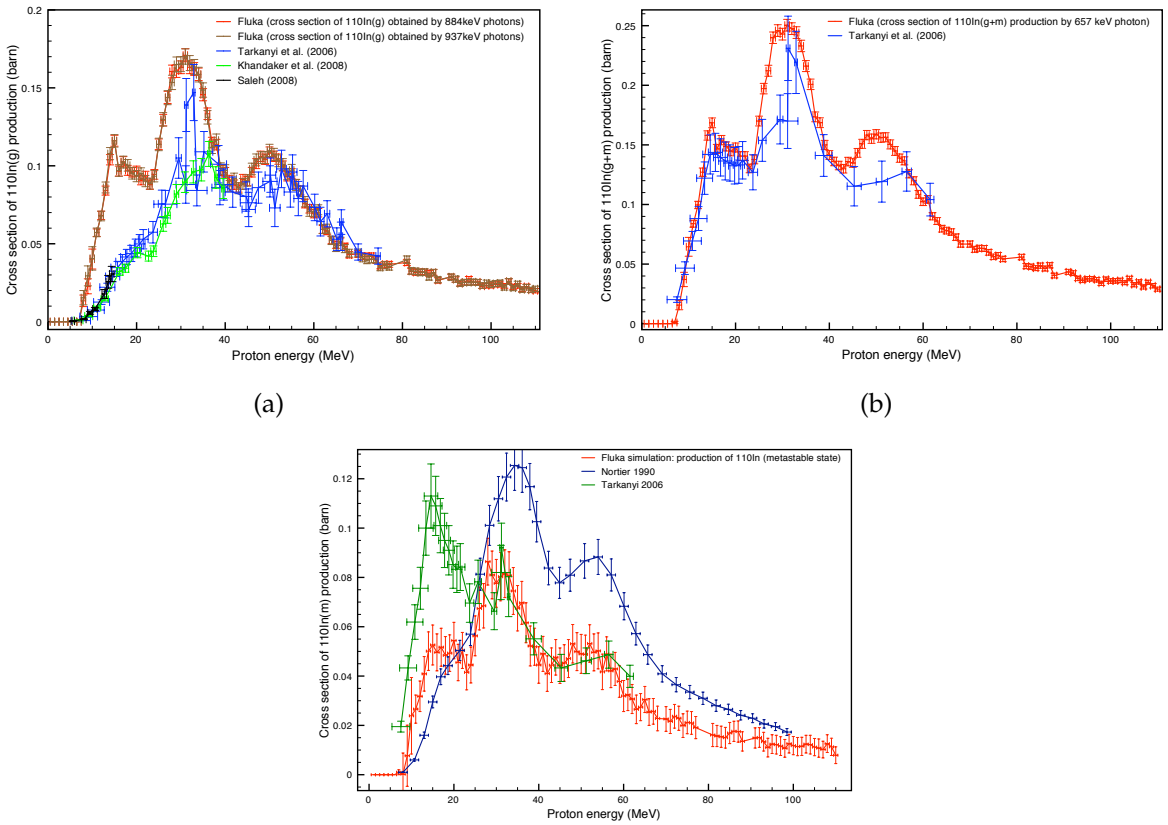

Figure B.1 – Comparison between simulated and literature cross section for the production of: (a) ^{110}In(G) obtained counting the photons at 884 or 937 keV (emitted only by ^{110}In(G)); (b) ^{110}In(G+M) obtained counting the photons at 657 keV (emitted by the isotopes in both the states); and (c) ^{110}In(M) obtained as subtraction between the graph in (b) and the graph in (a).

separately, because the production of isotopes which can be created in an isomeric state is not yet implemented in the code. According to them, the total production of (G+M) states should be correct, but the relative abundance of the isomeric and ground state isotopes is arbitrarily chosen to give the correct sum (see figure B.1). This can be also seen from the graphs in figure B.2, which shows the comparison between simulated and experimental results of the number of photons at: (a) 884 keV emitted in the decay of ^{110}In(G) and (b) at 657 keV emitted in the decay of ^{110}In(G+M). For both 300s $\leq \Delta t_{count} \leq$ 1000s.

In spite of the apparent correctness of the graph in figure B.2 (b), and despite

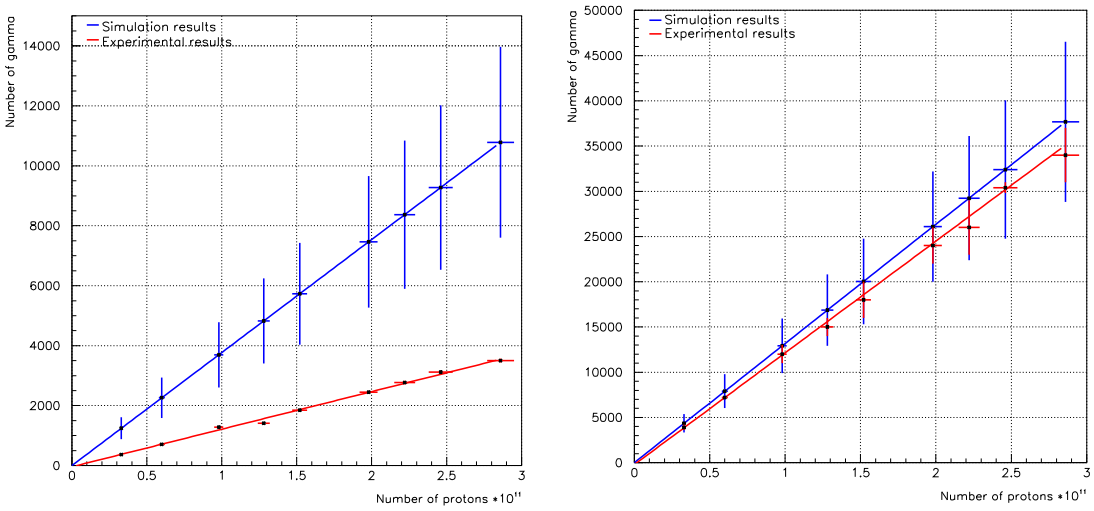

(a) (b)

Figure B.2 – (a) Experimental (red) and simulated (blue) results of the number of detected photons at: (a) 884 keV emitted in the decay of ^{110}In(G) to ^{110}Cd and (b) 657 keV emitted in the decay of ^{110}In(G+M) to ^{110}Cd. Each point in (a) and (b) has been obtained changing the number of protons in the incident beam for each irradiated foil.

what Fluka developers say, there are also problems with the production of ^{110}In(G+M) due to the fact that the isotopes with different states have also different decay times: $t_{1/2}(^{110}\text{In(G)})$ = 4.9 h and $t_{1/2}(^{110}\text{In(M)})$ = 69.1 min. Looking at the temporal evolution of the photon emission in figure B.3 (a) the simulation seems to be almost correct only for long counting times, when in reality only ^{110}In(G) is emitting, but in figure B.3 (b), which shows the photon emission of ^{110}In(G+M), the simulation appears correct for short (both the states are still emitting) and long counting times (when practically only the isotopes in the ground state are emitting), but not in the intermediated times (the isotopes in the ground state are emitting much more than the isotopes in the isomeric state which are decaying faster). Note that the graphs in figure B.2 were obtained counting photons in $300\text{s} \leq \Delta t_{\text{count}} \leq 1000\text{s}$, while the points in the graphs in figure B.3 were obtained counting in irregular intervals: first point in $300\text{s} \leq \Delta t_{\text{count}} \leq 4200\text{s}$ (4200 s is just a bit larger than $t_{1/2}(^{110}\text{In(M)})$), second in $4260\text{s} \leq \Delta t_{\text{count}} \leq 7800\text{s}$, third in $7860\text{s} \leq \Delta t_{\text{count}} \leq 11400\text{s}$ and fourth in $11460\text{s} \leq \Delta t_{\text{count}} \leq 12460\text{s}$

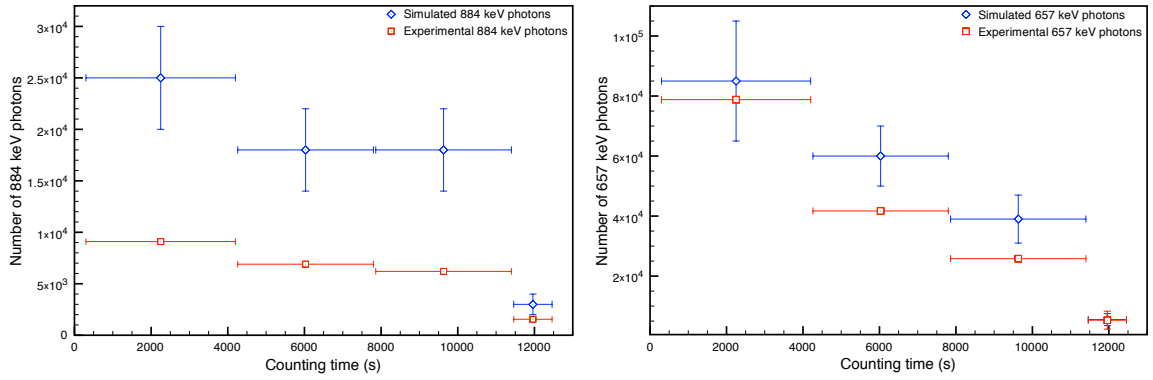

(a) (b)

Figure B.3 – Temporal evolution of the 884 keV (a) and the 657 keV (b) photon emission: from the simulation in blue and from the experiment in red. The points have been obtained irradiating only one foil and counted photons in the same intervals in figure 5.10 (b). The correctness of the simulated results in the graph in figure B.2 (b) is reflected in the good agreement between simulation and experiment in the first point of the graph in figure B.3 (b)

(around 3 times the $t_{1/2}(^{110}In(M))$). So the apparent correctness of the graph in figure B.2 (b) is reflected only in the first point of the graph in figure B.3 (b).

Without doing this set of tests with ^{nat}Cd, studying the temporal evolution of γ emissions, it could not be possible to discover the anomaly in the yields of $^{110}In(G+M)$ in Fluka, which, instead, according to Fluka developers should have been right and which appears in good agreement with literature data, if only the cross section (figure B.1 (b)) is observed[1].

This demonstrates that in Fluka the sum of all the simulated emitted photons, $N\gamma_{tot},$) is correct, but $\frac{dN\gamma}{dt}$ is not if these γ are emitted by the same isotopes in different energetic states (ground and metastable) with different half lives. Obviously this problem become of particular importance when the user is interested in looking at the temporal evolution of the radiation emitted by a radioactive isotopes, given that in the reality he/she does not have an "infinite" time to wait for the emitting

[1]During the cross section calculation the temporal evolution of the emission is not taken into account because all the photons in the time necessary for the complete decay of all the radioactive isotopes in exam are counted.

isotopes to be totally decayed (and so $\frac{dN\gamma}{dt}$ or better $\frac{\Delta N\gamma}{\Delta t}$ is more significant than $N\gamma_{tot}$). Fortunately, in the case of cadmium irradiation the radiation emitted by ^{110}In(G+M) and ^{110}In(G) is always overestimated by Fluka, so would not constitute a health risk for the user who is not aware of the real temporal evolution of those isotopes.

APPENDIX C

PUBLISHED WORK

During the course of my PhD I have published two peer-reviewed papers as first author. The first, *Nuclear activation as a current detector for ion beams produced by a high intensity laser*, was published in 2010 in Radiation Measurements [93]. The second, *Dosimetry and spectral analysis of a radiobiological experiment using laser-driven proton beams*, was published in 2011 in Physics in Medicine and Biology [86].

I have co-authored an additional two peer-reviewed articles: *Radiochromic film spectroscopy of laser-accelerated proton beams using the FLUKA code and dosimetry traceable to primary standards* published in 2011 in Laser and Particle Beams [115], and *Biological effectiveness on live cells of laser-driven protons at dose rates exceeding* 10^9 *Gy/s* published in 2012 in AIP Advances [85].

I have also been the main author of two papers published in the CLF 2011 Annual Report. One is on the simulations of laser-driven X-ray beams, *Fluka simulations of laser irradiated targets: thickness study for production of X-ray beams* [95], and the other is on the experiment conducted at Gemini, *TLD measurements of electron and X-ray*

emission from different materials irradiated by the Gemini laser [105]. I am co-author of another two papers in the Annual Report: *An assessment of the reproducibility of the Gemini retro focusing system* [116] and *Maximising the dynamic range of radiochromic film through novel scanning techniques* [117].

Several posters have also been presented in international and national conferences.

BIBLIOGRAPHY

[1] S. Eliezer, *The interaction of high-power lasers with plasmas*. Taylor & Francis, 2002.

[2] S. Wilks, W. Kruer, M. Tabak, and A. Langdon, "Absorption of ultra-intense laser pulses," *Physical review letters*, vol. 69, no. 9, pp. 1383–1386, 1992.

[3] A. Bell, J. Davies, S. Guerin, and H. Ruhl, "Fast-electron transport in high-intensity short-pulse laser-solid experiments," *Plasma physics and controlled fusion*, vol. 39, p. 653, 1997.

[4] J. Myatt, W. Theobald, J. Delettrez, C. Stoeckl, M. Storm, T. Sangster, A. Maximov, and R. Short, "High-intensity laser interactions with mass-limited solid targets and implications for fast-ignition experiments on omega ep," *Physics of plasmas*, vol. 14, p. 056301, 2007.

[5] M. Quinn, X. Yuan, X. Lin, D. Carroll, O. Tresca, R. Gray, M. Coury, C. Li, Y. Li, C. Brenner, *et al.*, "Refluxing of fast electrons in solid targets irradiated by

intense, picosecond laser pulses," *Plasma Physics and Controlled Fusion*, vol. 53, p. 025007, 2011.

[6] S. Wilks, A. Langdon, T. Cowan, M. Roth, M. Singh, S. Hatchett, M. Key, D. Pennington, A. MacKinnon, and R. Snavely, "Energetic proton generation in ultra-intense laser–solid interactions," *Physics of Plasmas*, vol. 8, p. 542, 2001.

[7] P. McKenna, K. Ledingham, J. Yang, L. Robson, T. McCanny, S. Shimizu, R. Clarke, D. Neely, K. Spohr, R. Chapman, *et al.*, "Characterization of proton and heavier ion acceleration in ultrahigh-intensity laser interactions with heated target foils," *Physical Review E*, vol. 70, no. 3, p. 036405, 2004.

[8] B. Hegelich, B. Albright, J. Cobble, K. Flippo, S. Letzring, M. Paffett, H. Ruhl, J. Schreiber, R. Schulze, and J. Fernandez, "Laser acceleration of quasi-monoenergetic MeV ion beams," *Nature*, vol. 439, no. 7075, p. 441, 2006.

[9] R. A. Snavely, M. H. Key, S. P. Hatchett, T. E. Cowan, M. Roth, T. W. Phillips, M. A. Stoyer, E. A. Henry, T. C. Sangster, M. S. Singh, S. C. Wilks, A. MacKinnon, A. Offenberger, D. M. Pennington, K. Yasuike, A. B. Langdon, B. F. Lasinski, J. Johnson, M. D. Perry, and E. M. Campbell, "Intense high-energy proton beams from petawatt-laser irradiation of solids," *Phys. Rev. Lett.*, vol. 85, pp. 2945–2948, Oct 2000.

[10] P. McKenna, K. Ledingham, T. McCanny, R. Singhal, I. Spencer, M. Santala, F. Beg, K. Krushelnick, M. Tatarakis, M. Wei, *et al.*, "Demonstration of fusion-evaporation and direct-interaction nuclear reactions using high-intensity laser-plasma-accelerated ion beams," *Physical review letters*, vol. 91, no. 7, p. 75006, 2003.

[11] Y. Fukuda, A. Y. Faenov, M. Tampo, T. A. Pikuz, T. Nakamura, M. Kando, Y. Hayashi, A. Yogo, H. Sakaki, T. Kameshima, A. S. Pirozhkov, K. Ogura,

M. Mori, T. Z. Esirkepov, J. Koga, A. S. Boldarev, V. A. Gasilov, A. I. Magunov, T. Yamauchi, R. Kodama, P. R. Bolton, Y. Kato, T. Tajima, H. Daido, and S. V. Bulanov, "Energy increase in multi-mev ion acceleration in the interaction of a short pulse laser with a cluster-gas target," *Phys. Rev. Lett.*, vol. 103, p. 165002, Oct 2009.

[12] E. Clark, K. Krushelnick, M. Zepf, F. Beg, M. Tatarakis, A. Machacek, M. Santala, I. Watts, P. Norreys, and A. Dangor, "Energetic heavy-ion and proton generation from ultraintense laser-plasma interactions with solids," *Physical Review Letters*, vol. 85, no. 8, pp. 1654–1657, 2000.

[13] M. Borghesi, A. Bigongiari, S. Kar, A. Macchi, L. Romagnani, P. Audebert, J. Fuchs, T. Toncian, O. Willi, S. Bulanov, *et al.*, "Laser-driven proton acceleration: source optimization and radiographic applications," *Plasma Physics and Controlled Fusion*, vol. 50, p. 124040, 2008.

[14] K. Ledingham, P. McKenna, and R. Singhal, "Applications for nuclear phenomena generated by ultra-intense lasers," *Science*, vol. 300, no. 5622, p. 1107, 2003.

[15] J. Freidberg, R. Mitchell, R. Morse, and L. Rudsinski, "Resonant absorption of laser light by plasma targets," *Physical Review Letters*, vol. 28, no. 13, pp. 795–799, 1972.

[16] W. Kruer, "The physics of laser plasma interactions," 1988.

[17] F. Beg, A. Bell, A. Dangor, C. Danson, A. Fews, M. Glinsky, B. Hammel, P. Lee, P. Norreys, and M. Tatarakis, "A study of picosecond laser-solid interactions up to 1019 w cm-2," *Physics of Plasmas*, vol. 4, no. 2, pp. 447–457, 1997.

[18] B. Cho, J. Osterholz, A. Bernstein, G. Dyer, A. Karmakar, A. Pukhov, and T. Ditmire, "Characterization of two distinct, simultaneous hot electron beams

in intense laser-solid interactions," *Physical Review E*, vol. 80, no. 5, p. 055402, 2009.

[19] A. Robinson, M. Zepf, S. Kar, R. Evans, and C. Bellei, "Radiation pressure acceleration of thin foils with circularly polarized laser pulses," *New Journal of Physics*, vol. 10, p. 013021, 2008.

[20] O. Lundh, F. Lindau, A. Persson, C. Wahlström, P. McKenna, and D. Batani, "Influence of shock waves on laser-driven proton acceleration," *Physical Review E*, vol. 76, no. 2, p. 026404, 2007.

[21] K. Krushelnick, E. Clark, R. Allott, and F. Beg, "Ultrahigh-intensity laser-produced plasmas as a compact heavy ion injection source," *IEEE Transactions on Plasma Science*, vol. 28, Jan 2000.

[22] M. Roth, T. Cowan, M. Key, and S. Hatchett, "Fast ignition by intense laser-accelerated proton beams," *Physical Review Letters*, vol. 86, Jan 2001.

[23] S. Bulanov and V. Khoroshkov, "Feasibility of using laser ion accelerators in proton therapy," *Plasma Physics Reports*, vol. 28, no. 5, pp. 453–456, 2002.

[24] I. Spencer, K. Ledingham, R. Singhal, T. McCanny, P. McKenna, E. Clark, K. Krushelnick, M. Zepf, F. Beg, M. Tatarakis, *et al.*, "Laser generation of proton beams for the production of short-lived positron emitting radioisotopes," *Nuclear Instruments and Methods in Physics Research Section B: Beam Interactions with Materials and Atoms*, vol. 183, no. 3, pp. 449–458, 2001.

[25] M. Nishikino, K. Sato, S. Ohshima, N. Hasegawa, M. Ishino, T. Kawachi, Y. Okano, H. Numasaki, T. Teshima, and H. Nishimura, "Development of focused laser plasma x-ray beam for radiobiological applications," in *Conference on Lasers and Electro-Optics/Pacific Rim*, Optical Society of America, 2009.

[26] Y. Glinec, J. Faure, L. Dain, S. Darbon, T. Hosokai, J. Santos, E. Lefebvre, J. Rousseau, F. Burgy, B. Mercier, *et al.*, "High-resolution γ-ray radiography produced by a laser-plasma driven electron source," *Physical review letters*, vol. 94, no. 2, p. 25003, 2005.

[27] G. Kraft, "Tumor therapy with heavy charged particles," *Progress in Particle and Nuclear Physics*, vol. 45, pp. S473–S544, 2000.

[28] W. Leo, *Techniques for nuclear and particle physics experiments: a how-to approach*. Springer Verlag, 1994.

[29] U. Amaldi and G. Kraft, "Radiotherapy with beams of carbon ions," *Reports on progress in physics*, vol. 68, p. 1861, 2005.

[30] A. Peeters, J. Grutters, M. Pijls-Johannesma, S. Reimoser, D. De Ruysscher, J. Severens, M. Joore, and P. Lambin, "How costly is particle therapy? cost analysis of external beam radiotherapy with carbon-ions, protons and photons," *Radiotherapy and Oncology*, vol. 95, no. 1, pp. 45–53, 2010.

[31] C. Ma, I. Veltchev, E. Fourkal, J. Li, W. Luo, J. Fan, T. Lin, and A. Pollack, "Development of a laser-driven proton accelerator for cancer therapy," *Laser Physics*, vol. 16, no. 4, pp. 639–646, 2006.

[32] M. Krämer, O. Jäkel, T. Haberer, G. Kraft, D. Schardt, and U. Weber, "Treatment planning for heavy-ion radiotherapy: physical beam model and dose optimization," *Physics in medicine and biology*, vol. 45, p. 3299, 2000.

[33] M. Murakami, Y. Hishikawa, S. Miyajima, Y. Okazaki, K. Sutherland, M. Abe, S. Bulanov, H. Daido, T. Esirkepov, J. Koga, *et al.*, "Radiotherapy using a laser proton accelerator," in *Laser-Driven Relativistic Plasmas Applied for Science, Industry, and Medicine:(AIP Conference Proceedings Volume 1024)*, vol. 1024,

pp. 275–300, American Institute of Physics, 2 Huntington Quadrangle, Suite 1 NO 1, Melville, NY, 11747-4502, USA,, 2008.

[34] P. Bolton, T. Hori, H. Kiriyama, M. Mori, H. Sakaki, K. Sutherland, M. Suzuki, J. Wu, and A. Yogo, "Toward integrated laser-driven ion accelerator systems at the photo-medical research center in japan," *Nuclear Instruments and Methods in Physics Research Section A: Accelerators, Spectrometers, Detectors and Associated Equipment*, vol. 620, no. 1, pp. 71–75, 2010.

[35] P. Andreo, D. Burns, K. Hohlfeld, M. Saiful Huq, T. Kanai, F. Laitano, V. Smyth, and S. Vynckier, "IAEA TRS-398," *Absorbed dose determination in external beam radiotherapy: An international code of practice for dosimetry based on standards of absorbed dose to water. IAEA, Vienna*, 2004.

[36] P. Andreo, "IAEA TRS-277," *Absorbed dose determination in photon and electron beams: an international code of practice*, 1987.

[37] P. Almond, P. Andreo, O. Mattsson, A. Nahum, and M. Roos, "IAEA TRS-381," *The use of plane-parallel ionization chambers in high-energy electron and photon beams. An international Code of Practice for dosimetry*, 1997.

[38] P. Andreo, "Chamber-dependent wall correction factors in dosimetry," *Physics in Medicine and Biology*, vol. 31, p. 1189, 1986.

[39] M. Niatel, A. Perroche-Roux, and M. Boutillon, "Two determinations of w for electrons in dry air," *Physics in Medicine and Biology*, vol. 30, p. 67, 1985.

[40] D.T.L Jones, "The w-value in air for proton therapy beams," *Radiation Physics and Chemistry*, vol. 75, pp. 541–550, 2006.

[41] H. Palmans and F. Verhaegen, "Monte carlo study of fluence perturbation effects on cavity dose response in clinical proton beams," *Physics in medicine and biology*, vol. 43, p. 65, 1998.

[42] H. Palmans, F. Verhaegen, J. Denis, S. Vynckier, and H. Thierens, "Experimental pwall and pcel correction factors for ionization chambers in low-energy clinical proton beams," *Physics in Medicine and Biology*, vol. 46, p. 1187, 2001.

[43] J. Boag, "Ionization chambers," *Radiation dosimetry*, vol. 2, pp. 1–72, 1966.

[44] H. Palmans, R. Thomas, and A. Kacperek, "Ion recombination correction in the clatterbridge centre of oncology clinical proton beam," *Physics in medicine and biology*, vol. 51, p. 903, 2006.

[45] G. Battistoni, S. M. P. R, Sala, F. Cerutti, A. Ferrari, S. Roesler, A. Fassò, and J. Ranft, "The FLUKA code: Description and benchmarking," *Proceedings of the Hadronic Shower Simulation Workshop 2006, Fermilab 6–8 September 2006, M. Albrow, R. Raja eds., AIP Conference Proceeding*, vol. 896, pp. 31–49, 2007.

[46] A. Fassò, A. Ferrari, J. Ranft, and P. R. Sala, "FLUKA: a multi-particle transport code, CERN-2005-10," *INFN/TC_05/11, SLAC-R-773:* , 2005.

[47] A. Mack, G. Mack, D. Weltz, S. Scheib, H. Böttcher, and V. Seifert, "High precision film dosimetry with gafchromic films for quality assurance especially when using small fields," *Medical physics*, vol. 30, p. 2399, 2003.

[48] A. Rink, D. Lewis, S. Varma, I. Vitkin, and D. Jaffray, "Temperature and hydration effects on absorbance spectra and radiation sensitivity of a radiochromic medium," *Medical physics*, vol. 35, p. 4545, 2008.

[49] B. Lynch, J. Kozelka, M. Ranade, J. Li, W. Simon, and J. Dempsey, "Important considerations for radiochromic film dosimetry with flatbed CCD scanners and EBT GAFCHROMIC film," *Medical physics*, vol. 33, p. 4551, 2006.

[50] D. Kirby, S. Green, H. Palmans, R. Hugtenburg, C. Wojnecki, and D. Parker, "LET dependence of GafChromic films and an ion chamber in low-energy proton dosimetry," *Physics in Medicine and Biology*, vol. 55, p. 417, 2010.

[51] M. Martišíková and O. Jäkel, "Dosimetric properties of gafchromic® ebt films in monoenergetic medical ion beams," *Physics in Medicine and Biology*, vol. 55, p. 3741, 2010.

[52] W. McLaughlin, M. Al-Sheikhly, D. Lewis, A. Kovacs, and L. Wojnarovits, "Radiochromic solid-state polymerization reaction," in *ACS Symposium Series*, vol. 620, pp. 152–166, ACS Publications, 1996.

[53] W. Rasband, "ImageJ. US National Institutes of Health, Bethesda, MD."

[54] Y. Furuta and S. Tanaka, "Response of 6lif and 7lif thermoluminescence dosimeters to fast neutrons," *Nuclear Instruments and Methods*, vol. 104, no. 2, pp. 365–374, 1972.

[55] Y. Horowitz, "The theoretical and microdosimetric basis of thermoluminescence and applications to dosimetry," *Physics in Medicine and Biology*, vol. 26, p. 765, 1981.

[56] S. Miljanic, M. Ranogajec-Komor, B. Vekic, *et al.*, "Main dosimetric characteristics of some tissue-equivalent tl detectors," *Radiation protection dosimetry*, vol. 100, no. 1-4, p. 437, 2002.

[57] A. Lakshmanan, C. Raffnsře, and J. Tuyn, "Photon energy dependence of sensitized lif (tld-700) phosphor," *The International journal of applied radiation and isotopes*, vol. 35, no. 5, pp. 418–420, 1984.

[58] C. Edwards, P. Mountford, S. Green, J. Palethorpe, and A. Moloney, "The low energy x-ray response of the lif: Mg: Cu: P thermoluminescent dosemeter: a comparison with lif: Mg: Ti," *British journal of radiology*, vol. 78, no. 930, pp. 543–547, 2005.

[59] S. Davis, C. Ross, P. Mobit, L. Van der Zwan, W. Chase, and K. Shortt, "The response of LiF thermoluminescence dosemeters to photon beams in the energy

range from 30 kV X-rays to ^{60}Co gamma rays," *Radiation protection dosimetry*, vol. 106, no. 1, pp. 33–43, 2003.

[60] O. Geiß, M. Krämer, and G. Kraft, "Efficiency of thermoluminescent detectors to heavy charged particles," *Nuclear Instruments and Methods in Physics Research Section B: Beam Interactions with Materials and Atoms*, vol. 142, no. 4, pp. 592–598, 1998.

[61] B. Ruden *et al.*, "Tld measurements of dose distribution around a beta-ray applicator," *Physics in Medicine and Biology*, vol. 19, p. 186, 1974.

[62] J. Holt, G. Edelstein, and T. Clark, "Energy dependence of the response of lithium fluoride tld rods in high energy electron fields," *Physics in Medicine and Biology*, vol. 20, p. 559, 1975.

[63] W. Schöner, N. Vana, and M. Fugger, "The let dependence of lif: Mg, ti dosemeters and its application for let measurements in mixed radiation fields," *Radiation protection dosimetry*, vol. 85, no. 1-4, p. 263, 1999.

[64] B. Mukherjee, D. Makowski, and S. Simrock, "Dosimetry of high-energy electron linac produced photoneutrons and the bremsstrahlung gamma-rays using tld-500 and tld-700 dosimeter pairs," *Nuclear Instruments and Methods in Physics Research Section A: Accelerators, Spectrometers, Detectors and Associated Equipment*, vol. 545, no. 3, pp. 830–841, 2005.

[65] C. Karzmark, J. White, and J. Fowler, "Lithium fluoride thermoluminescence dosimetry," *Physics in Medicine and Biology*, vol. 9, p. 273, 1964.

[66] I. Spencer, K. Ledingham, R. Singhal, T. McCanny, P. McKenna, E. Clark, K. Krushelnick, M. Zepf, F. Beg, M. Tatarakis, *et al.*, "Laser generation of proton beams for the production of short-lived positron emitting radioisotopes,"

Nuclear Instruments and Methods in Physics Research Section B: Beam Interactions with Materials and Atoms, vol. 183, no. 3, pp. 449–458, 2001.

[67] J. Yang, P. McKenna, K. Ledingham, T. McCanny, S. Shimizu, L. Robson, R. Clarke, D. Neely, P. Norreys, M. Wei, *et al.*, "Nuclear reactions in copper induced by protons from a petawatt laser-foil interaction," *Applied physics letters*, vol. 84, p. 675, 2004.

[68] P. McKenna, K. Ledingham, T. McCanny, R. Singhal, I. Spencer, E. Clark, F. Beg, K. Krushelnick, M. Wei, J. Galy, *et al.*, "Effect of target heating on ion-induced reactions in high-intensity laser–plasma interactions," *Applied physics letters*, vol. 83, p. 2763, 2003.

[69] R. Clarke, K. Ledingham, P. McKenna, L. Robson, T. McCanny, D. Neely, O. Lundh, F. Lindau, C. Wahlström, P. Simpson, *et al.*, "Detection of short lived radioisotopes as a fast diagnostic for intense laser-solid interactions," *Applied physics letters*, vol. 89, p. 141117, 2006.

[70] J. Frenje, C. Li, F. Séguin, D. Hicks, S. Kurebayashi, R. Petrasso, S. Roberts, V. Glebov, D. Meyerhofer, T. Sangster, *et al.*, "Absolute measurements of neutron yields from dd and dt implosions at the omega laser facility using cr-39 track detectors," *Review of scientific instruments*, vol. 73, p. 2597, 2002.

[71] A. Maksimchuk, S. Gu, K. Flippo, D. Umstadter, and V. Bychenkov, "Forward ion acceleration in thin films driven by a high-intensity laser," *Physical review letters*, vol. 84, no. 18, pp. 4108–4111, 2000.

[72] K. Krushelnick, E. Clark, Z. Najmudin, M. Salvati, M. Santala, M. Tatarakis, A. Dangor, V. Malka, D. Neely, R. Allott, *et al.*, "Multi-mev ion production from high-intensity laser interactions with underdense plasmas," *Physical review letters*, vol. 83, no. 4, pp. 737–740, 1999.

[73] Y. Hayakawa, Y. Amemiya, J. Tada, K. Hosono, and T. Arimoto, "Application of an imaging plate to dose distribution measurement of proton beam," *Nuclear Instruments and Methods in Physics Research Section A: Accelerators, Spectrometers, Detectors and Associated Equipment*, vol. 378, no. 3, pp. 627–628, 1996.

[74] A. Nohtomi, T. Terunuma, R. Kohno, Y. Takada, Y. Hayakawa, A. Maruhashi, and T. Sakae, "Response characteristics of an imaging plate to clinical proton beams," *Nuclear Instruments and Methods in Physics Research Section A: Accelerators, Spectrometers, Detectors and Associated Equipment*, vol. 424, no. 2, pp. 569–574, 1999.

[75] I. Paterson, R. Clarke, N. Woolsey, and G. Gregori, "Image plate response for conditions relevant to laser–plasma interaction experiments," *Measurement Science and Technology*, vol. 19, p. 095301, 2008.

[76] S. Gales and C. Bentley, "Image plates as x-ray detectors in plasma physics experiments," *Review of scientific instruments*, vol. 75, no. 10, pp. 4001–4003, 2004.

[77] J. Green, M. Borghesi, C. Brenner, D. Carroll, N. Dover, P. Foster, P. Gallegos, S. Green, D. Kirby, K. Kirkby, *et al.*, "Scintillator-based ion beam profiler for diagnosing laser-accelerated ion beams," in *Proceedings of SPIE*, vol. 8079, p. 807919, 2011.

[78] J. Ranft and S. Ritter, "Particle production in hadron-nucleus collisions in a multi-chain fragmentation model," *Zeitschrift für Physik C Particles and Fields*, vol. 20, no. 4, pp. 347–355, 1983.

[79] H. Sorge, "Flavor production in Pb (160 AGeV) on Pb collisions: Effect of color ropes and hadronic rescattering," *Physical Review C*, vol. 52, no. 6, pp. 3291–3314, 1995.

[80] P. Hodgson, E. Gadioli, and E. Erba, *Introductory nuclear physics*. Oxford University Press New York, 1997.

[81] M. Cavinato, E. Fabrici, E. Gadioli, E. Gadioli Erba, and G. Riva, "Monte carlo calculations of heavy ion cross-sections based on the boltzmann master equation theory," *Nuclear Physics, Section A*, vol. 679, no. 3-4, pp. 753–764, 2001.

[82] M. Brugger, A. Ferrari, S. Roesler, and P. Sala, "Calculation of radionuclide production cross sections with fluka and their application in high energy hadron collider studies," 2008.

[83] A. Yogo, K. Sato, M. Nishikino, M. Mori, T. Teshima, H. Numasaki, M. Murakami, Y. Demizu, S. Akagi, S. Nagayama, *et al.*, "Application of laser-accelerated protons to the demonstration of DNA double-strand breaks in human cancer cells," *Applied Physics Letters*, vol. 94, p. 181502, 2009.

[84] S. Kraft, C. Richter, K. Zeil, M. Baumann, E. Beyreuther, S. Bock, M. Bussmann, T. Cowan, Y. Dammene, W. Enghardt, *et al.*, "Dose-dependent biological damage of tumour cells by laser-accelerated proton beams," *New Journal of Physics*, vol. 12, p. 085003, 2010.

[85] D. Doria, K. Kakolee, S. Kar, S. Litt, F. Fiorini, H. Ahmed, S. Green, J. Jeynes, J. Kavanagh, D. Kirby, K. Kirkby, M. Merchant, G. Nersisyan, R. Prasad, K. Prise, G. Schettino, M. Zepf, and B. M., "Biological effectiveness on live cells of laser driven protons at dose rates exceeding 10^9 Gy/s," *accepted for publication in AIP Advances*, 2012.

[86] F. Fiorini, D. Kirby, M. Borghesi, D. Doria, J. Jeynes, K. Kakolee, S. Kar, S. Litt, K. Kirkby, M. Merchant, and S. Green, "Dosimetry and spectral analysis of a radiobiological experiment using laser-driven proton beams," *Physics in Medicine and Biology*, vol. 56, pp. 6969–6982, 2011.

[87] T. Dzelzainis, G. Nersisyan, D. Riley, L. Romagnani, H. Ahmed, A. Bigongiari, M. Borghesi, B. Doria, D. andDromey, M. Makita, S. White, S. Kar, D. Marlow, B. Ramakrishna, G. Sarri, M. Zaka-Ul-Islam, M. Zepf, and C. L. S. Lewis, "The TARANIS laser: A multi-Terawatt system for laser-plasma investigations," *Laser and Particle Beams*, vol. 28, pp. 451–461, July 2010.

[88] M. Hegelich, S. Karsch, G. Pretzler, D. Habs, K. Witte, W. Guenther, M. Allen, A. Blazevic, J. Fuchs, J. Gauthier, *et al.*, "Mev ion jets from short-pulse-laser interaction with thin foils," *Physical review letters*, vol. 89, no. 8, p. 85002, 2002.

[89] G. Schettino, M. Folkard, K. Prise, B. Vojnovic, K. Held, and B. Michael, "Low-dose studies of bystander cell killing with targeted soft X rays," *Radiation research*, vol. 160, no. 5, pp. 505–511, 2003.

[90] P. Thévenaz, U. Ruttimann, and M. Unser, "A pyramid approach to subpixel registration based on intensity," *IEEE Transactions on Image Processing*, vol. 7, pp. 27–41, January 1998.

[91] M. Belli, F. Cera, R. Cherubini, A. Haque, F. Ianzini, G. Moschini, O. Sapora, G. Simone, M. Tabocchini, and P. Tiveron, "Inactivation and mutation induction in v79 cells by low energy protons: Re-evaluation of the results at the lnl facility," *International journal of radiation biology*, vol. 63, no. 3, pp. 331–337, 1993.

[92] M. Folkard, "Inactivation of v79 cells by low-energy protons, deuterons and helium-3 ions," *International journal of radiation biology*, vol. 69, no. 6, pp. 729–738, 1996.

[93] F. Fiorini, D. Kirby, S. Green, and D. Parker, "Nuclear activation as a current detector for ion beams produced by a high intensity laser," *Radiation Measurements*, vol. 45, no. 10, pp. 1103–1104, 2010.

[94] "Experimental nuclear reaction data (EXFOR)."
Webpage: www-nds.iaea.org/exfor/exfor.htlm.

[95] F. Fiorini, R. Clarke, D. Neely, Z. Najmudin, and S. Green, "Fluka simulations of laser irradiated targets: thickness study for production of x-ray beams," *CLF Annual Report 2010-2011*, vol. High Power Laser Science - Femptosecond Pulse Physics, pp. 20–22, 2011.

[96] P. M. Nilson, J. R. Davies, W. Theobald, P. A. Jaanimagi, C. Mileham, R. K. Jungquist, C. Stoeckl, I. A. Begishev, A. A. Solodov, J. F. Myatt, J. D. Zuegel, T. C. Sangster, R. Betti, and D. D. Meyerhofer, "Time-resolved measurements of hot-electron equilibration dynamics in high-intensity laser interactions with thin-foil solid targets," *Phys. Rev. Lett.*, vol. 108, p. 085002, Feb 2012.

[97] K. Ledingham and W. Galster, "Laser-driven particle and photon beams and some applications," *New Journal of Physics*, vol. 12, p. 045005, 2010.

[98] J. Galy, M. Maučec, D. Hamilton, R. Edwards, and J. Magill, "Bremsstrahlung production with high-intensity laser matter interactions and applications," *New journal of Physics*, vol. 9, p. 23, 2007.

[99] M. Perry, J. Sefcik, T. Cowan, S. Hatchett, A. Hunt, M. Moran, D. Pennington, R. Snavely, and S. Wilks, "Hard x-ray production from high intensity laser solid interactions," *Review of scientific instruments*, vol. 70, p. 265, 1999.

[100] H. Chen and S. Wilks, "Evidence of enhanced effective hot electron temperatures in ultraintense laser-solid interactions due to reflexing," *Laser and Particle Beams-Pulse Power and High Energy Densities*, vol. 23, no. 4, pp. 411–416, 2005.

[101] J. Ahrens and U. Dieter, "Computer methods for sampling from gamma, beta, poisson and bionomial distributions," *Computing*, vol. 12, no. 3, pp. 223–246, 1974.

[102] "Vulcan laser."
Webpage: www.clf.rl.ac.uk/Facilities/Vulcan/Vulcan+laser/12250.aspx.

[103] "Astra laser."
Webpage: www.clf.rl.ac.uk/Facilities/Astra/Astra+Laser/12256.aspx.

[104] "Astra Gemini."
Webpage: www.clf.rl.ac.uk/Facilities/Astra/Astra+Gemini/12258.aspx.

[105] F. Fiorini, S. Green, J. Green, R. Clarke, D. Carroll, M. Coury, G. Scott, P. McKenna, M. Streeter, D. Neely, and other, "Tld measurements of electron and x-ray emission from different materials irradiated by the gemini laser," *CLF Annual Report 2010-2011*, vol. High Power Laser Science - Femptosecond Pulse Physics, pp. 5–8, 2011.

[106] R. Edwards, M. Sinclair, T. Goldsack, K. Krushelnick, F. Beg, E. Clark, A. Dangor, Z. Najmudin, M. Tatarakis, B. Walton, *et al.*, "Characterization of a gamma-ray source based on a laser-plasma accelerator with applications to radiography," *Applied physics letters*, vol. 80, p. 2129, 2002.

[107] M. Santala, M. Zepf, I. Watts, F. Beg, E. Clark, M. Tatarakis, K. Krushelnick, A. Dangor, T. McCanny, I. Spencer, *et al.*, "Effect of the plasma density scale length on the direction of fast electrons in relativistic laser-solid interactions," *Physical review letters*, vol. 84, no. 7, pp. 1459–1462, 2000.

[108] P. Norreys, R. Scott, K. Lancaster, J. Green, A. Robinson, M. Sherlock, R. Evans, M. Haines, S. Kar, M. Zepf, *et al.*, "Recent fast electron energy transport experiments relevant to fast ignition inertial fusion," *Nuclear Fusion*, vol. 49, p. 104023, 2009.

[109] R. R. Wilson, "Radiological use of fast protons," *Radiobiology*, vol. 47, p. 487, 1946.

[110] H. Barkas, *Nuclear Research Emulsion*, vol. I. Accademic Press New York and London, 1963.

[111] G. Molière, *Theorie der Streuung schneller geladener Teilchen. II. Mehrfach-und Vielfachstreuung*. Z. Naturforsch 3a, 1948.

[112] B. Neumann, J. Buschmann, H. Klewe-Nebenius, H. Rebel, and H. Gils, "Transfer of ^{6}Li break-up fragments at ^{6}Li projectile energies far above the coulomb barrier," *Nuclear Physics A*, vol. 329, pp. 259–270, Oct. 1979.

[113] G. Battistoni, F. Broggi, M. Brugger, M. Campanella, M. Carboni, and C. et al, "The FLUKA code and its use in hadrontherapy," *Il Nuovo Cimento C*, vol. 31, pp. 69–75, 2008.

[114] IAEA and ICRU collaboration, "Relative biological effectiveness in ion beam therapy," *IAEA TRS-461*, 2008.

[115] D. Kirby, S. Green, F. Fiorini, D. Parker, L. Romagnani, D. Doria, S. Kar, C. Lewis, M. Borghesi, and H. Palmans, "Radiochromic film spectroscopy of laser-accelerated proton beams using the fluka code and dosimetry traceable to primary standards," *Laser and Particle Beams*, vol. 29, no. 02, pp. 231–239, 2011.

[116] D. Carroll, M. Coury, G. Scott, P. McKenna, M. Streeter, H. Nakamura, Z. Najmudin, F. Fiorini, S. Green, J. Green, D. Neely, *et al.*, "An assessment of the reproducibility of the gemini retro focusing system," *CLF Annual Report 2010-2011*, vol. High Power Laser Science - Femptosecond Pulse Physics, pp. 1–2, 2011.

[117] G. Scott, J. Green, D. Neely, M. Mitchell, P. McKenna, F. Fiorini, D. Kirby, S. D. Green, and J. Rickman, "Maximising the dynamic range of radiochromic film through novel scanning techniques," *CLF Annual Report 2010-2011*, vol. Laser

Science and Development - Instrumentation and Plasma Diagnostics, pp. 4–6, 2011.